PONTIFICIA UNIVERSIDAD CATOLICA DE CHILE

ESCUELA DE INGENIERIA

A NEW TYPE OF TUNED LIQUID DAMPER AND ITS EFFECTIVENESS IN ENHANCING SEISMIC PERFORMANCE; NUMERICAL CHARACTERIZATION, EXPERIMENTAL VALIDATION, PARAMETRIC ANALYSIS AND LIFE-CYCLE BASED DESIGN

RAFAEL O. RUIZ

Thesis submitted to the Office of Research and Graduate Studies in partial fulfillment of the requirements for the Degree of Doctor in Engineering Sciences

Advisors:

DIEGO LÓPEZ-GARCÍA

ALEXANDROS TAFLANIDIS

Santiago de Chile, (August, 2015)

PONTIFICIA UNIVERSIDAD CATOLICA DE CHILE
ESCUELA DE INGENIERIA

A NEW TYPE OF TUNED LIQUID DAMPER AND ITS EFFECTIVENESS IN ENHANCING SEISMIC PERFORMANCE; NUMERICAL CHARACTERIZATION, EXPERIMENTAL VALIDATION, PARAMETRIC ANALYSIS AND LIFE-CYCLE BASED DESIGN

RAFAEL O. RUIZ

Members of the Committee:

PROFESOR DIEGO LÓPEZ-GARCÍA

PROFESOR ALEXANDROS TAFLANIDIS

PROFESOR JOSÉ LUIS ALMAZÁN

PROFESOR DIEGO CELENTANO

PROFESOR TRACY KIJEWSKI-CORREA

PROFESOR GEORGE MAVROEIDIS

PROFESOR CRISTIÁN VIAL

Thesis submitted to the Office of Research and Graduate Studies in partial fulfillment of the requirements for the Degree of Doctor in Engineering Sciences

Santiago de Chile, (August, 2015)

ACKNOWLEDGEMENTS

I would like to thank my supervisors, Dr. Alexandros Taflanidis and Dr. Diego Lopez-Garcia for their technical guidance through my doctoral studies. I have no words to express the important role that you played in my personal and professional life.

To the staff at Pontificia Universidad Catolica de Chile and at University of Notre Dame, your support was vital for conducting this dual PhD program.

I would like also to express my appreciation to the members of my workgroup, especially to Jose Ignacio Colombo, Juan Carlos Obando, Ioannis Gidaris, Gaofeng Jia, Christopher Vetter and Juan Camilo Medina. Special thanks goes to Christopher Vetter for his help in developing the hazard-compatible stochastic ground motion model that is used for describing seismic risk for the Chilean region and VBM Ingenieria Estructural for provide the dynamic properties of the structure used in Chapter 6.

Finally, thank you to Vicerrectoria de Investigacion at Pontificia Universidad Catolica de Chile and to Ministerio de Educacion Superior de Chile for supporting this research and the dual PhD program.

A NEW TYPE OF TUNED LIQUID DAMPER AND ITS EFFECTIVENESS IN ENHANCING SEISMIC PERFORMANCE: NUMERICAL CHARACTERIZATION, EXPERIMENTAL VALIDATION, PARAMETRIC ANALYSIS AND LIFE-CYCLE BASED DESIGN

Abstract

by

Rafael Ruiz

In the last decades the use of seismic protection devices in Chilean buildings has gained popularity for reducing earthquake losses. Mass dampers (also referenced as inertia dampers), with the most popular representative being the Tuned Mass Damper (TMD), are a potential device for facilitating these tasks; they consist of a secondary mass attached to the primary structure through an equivalent spring and dashpot. Through proper tuning of frequency/damping characteristics, the movement of this secondary mass counteracts the vibration of the primary mass (structure) providing the desired energy dissipation for this vibration. Among the general class of mass damper devices, Tuned Liquid Dampers (TLDs), which consist of a tank filled with some liquid (typically water) whose sloshing within the tank provides the mass damper effect, have some attractive characteristics such as low cost, easy installation and tuning, bidirectional control capabilities and alternative use of the secondary mass (liquid in this

case). Their popularity, though, has been hindered by the facts that (i) their dynamic behavior is highly non-linear due to wave breaking and (ii) their inherent damping is usual lower than the optimal one, requiring the introduction of submerged elements (to increase this damping) that make the overall behavior even more complex. Other type of liquid dampers that share some of the TLD advantages, the liquid column dampers, offer a simpler modeling but their dynamic behavior is still non-linear since their damping ends up being amplitude dependent, whereas they are strictly restricted to one-directional applications. Additionally, the advantages of any such type of mass dampers particularly for seismic applications in the Chilean region have not been clearly demonstrated; this pertains to both their efficiency, acting as an inertia device, to allow significant energy dissipation for the ground motions common in the region but more importantly to an explicit discussion of the life-cycle cost improvement they can facilitate.

The research presented here introduces a new type of liquid mass damper, called Tuned Liquid Damper with Floating Roof (TLD-FR) which combines the favorable characteristics of both TLDs and liquid column dampers, and further examines its efficiency for seismic applications for Chile. The TLD-FR consists of a traditional TLD (liquid tank filled with liquid) with the addition of a floating roof. The sloshing of the liquid within the tank is what still provides the inertia damper effect, but the roof prevents wave breaking phenomena and introduces a practically linear response and a dynamic behavior in a dominant only mode. This creates a vibratory behavior that resembles other types of a linear mass dampers and a framework is developed to

characterize this behavior with a simple parametric description that can facilitate an easy comparison to such dampers. Within this framework, focus is given on a theoretical/computational characterization of the new device, coupled with an experimental validation of its capabilities and of the established numerical tools. To support these advances an efficient computational approach is formulated to describe the dynamic behavior of liquid tanks and is then extended to describe the behavior of the TLD-FR (address the inclusion of the roof). The aforementioned parametric formulation is then used to develop an approach that facilitates a direct design in the parametric space, as well as an efficient mapping back to the different tank geometries that correspond to each parametric configuration. During this process the efficiency of mass dampers for seismic applications in Chile is also examined by comparing the performance across different types of ground motions, representing different regions around the world. Finally, a versatile life-cycle assessment and design of the new device is established considering risk characterizations appropriate for the Chilean region, so that the cost-benefits from its adoption can be directly investigated. This involves the development of a multi-criteria design approach that considers the performance over the two desired goals: (i) reduction of the total life-cycle cost considering the upfront damper cost as well as seismic losses and (ii) reduction of the consequences, expressed through the repair cost, for low likelihood but high impact events. Through this approach the financial viability of the TLD-FR (competitiveness against TMDs) for enhancing seismic performance is demonstrated.

CONTENTS

FIGURES

TABLES

1 INTRODUCTION

1.1 Motivation

In modern urban areas there is an increasing trend to build light and flexible structures. In order to enhance the performance of such structures addition of supplemental devices is frequently promoted to control undesirable vibrations due to exposure to dynamic excitations such as winds or earthquakes (Housner et al. 1997; Zemp et al. 2011). Earthquake-induced (short-duration and large amplitude) vibrations may result in significant damages to structural and non-structural components and building-contents. Recent examples of such damages are discussed in Inokuma and Nagayama 2013 or Saatcioglu et al. 2013. Additionally, wind-induced (longer-duration but smaller amplitude) vibrations can also contribute to failure for serviceability limit states (cladding damage, elevator malfunction) as well as to fatigue damage (large number of lower amplitude oscillations) and, to some extreme cases (very strong winds or errors in designs/construction), even to structural failure (Sain and Kishen 2007).

To alleviate such impacts, different techniques have been proposed to control natural hazard induced-vibration of structures, with one of the most popular being the

introduction of passive devices, i.e. devices that require no external power supply. These devices impart forces counteracting directly the motion of the structure. Examples include viscous and viscoelastic dampers, friction dampers, hysteretic dissipaters, base isolation systems or inertial-type of dampers generally referenced as mass dampers (Soong and Dargush 1997; C. Christopoulos and A. Filiatrault 2006; Gutierrez Soto and Adeli 2013). They have prevailed in structural control applications, including in control application in Chile (Zemp et al. 2011; De la Llera et al. 2004), over active devices due to the large power demand of the latter (Housner et al. 1997) that cannot be reliably provided, and the fact that a significant life-cycle cost improvement arguing for the adoption of active devices has never been comprehensively proven. Note, furthermore that some of these passive devices can be extended to operate in semi-active mode by controlling in real-time their characteristics, such as orifice openings for viscous dampers that alter the viscosity coefficient of spring characteristics for TMDs (Housner et al. 1997; Sun et al. 2014).

1.2 Mass Dampers and the Tuned Mass Damper (TMD)

Perhaps the most commonly used passive device are mass dampers (frequently also referenced as inertia dampers), which consist of an inertial element (secondary mass) attached to a higher floor of the structure to be controlled (primary mass). Through appropriate tuning of its vibratory characteristics (meaning typically tuning to a specific mode of vibration for the structure), the secondary mass resonates out-of-phase

with the point of connection to the structure, reducing through its own dynamic response the vibration level of the primary mass (Den Hartog 1985). When that secondary mass corresponds to a single degree of freedom oscillator then the device is known as a Tuned Mass Damper (TMD). An equivalent interpretation of TMDs is that they correspond to mass dampers for which the entire additional mass (of the inertia damper) responds in a single mode and therefore that entire mass ultimately participates in the suppression of the vibration of the primary mass.

It is well understood that mass dampers impact the vibratory characteristics only in the range close to their own frequency, meaning that (a) they can suppress only a specific mode and that (b) the aforementioned tuning is very important for their efficiency (Den Hartog 1985; Gutierrez Soto and Adeli 2013; Oberguggenberger and Schmelzer 2014). Implementation of mass dampers may take different forms, for example directly a mass-spring-damper configuration or a swinging pendulum with additional elements to provide a damping effect to its vibration. A more detailed description of such configurations can be found in (Matta and De Stefano 2009; Gutierrez Soto and Adeli 2013). Mass dampers have been proven particularly advantageous for flexible buildings since they are economical and can be relatively easily implemented as an add-on to existing or new structures. Application of multiple mass dampers can be also considered to provide more efficient vibration suppression or even control of different modes of vibrations (Abe and Fujino 1994; Yang et al. 2015; Park and Reed 2001). For example for Taipei 101, which stands 508 m above ground

level in a region which experiences strong winds, earthquakes, and typhoons, three different TMDs have been applied, one of which was, at that point, the largest TMD in the world with mass of 660 tons (Tamboli et al. 2008).

The first inertia damper application was actually presented by (Frahm 1911) to reduce hull motion of ships. Today it is commonly used in buildings, automobiles, antennas, and in general very diverse dynamical system where vibration suppression is desired. The modeling of all devices belonging in the mass damper category can be equivalently expressed as single-degree-of-freedom oscillator (Chang 1999) with a specified mass connected to the primary structure though a spring and a dashpot. The difference between the different type of inertia damper devices is how the spring/dashpot configuration is ultimately established with an additional distinction of whether the total mass participates in the vibration suppression (Chang 1999), whereas some exhibit nonlinear vibratory characteristics with respect to the damping (dashpot) properties (Rudinger 2007). Semi-active implementations further differentiate these dampers (Hrovat et al. 1983; Sun and Nagarajaiah 2014; Lin et al. 2015).

Such mass dampers have been proposed in the literature for improving the dynamic performance of structures under a variety of dynamic excitations, including seismic excitations, though at this case with a reduced overall effectiveness, an effectiveness which additionally greatly depends on the characteristics of the excitation (Gutierrez Soto and Adeli 2013; Lin et al. 2001). This should be attributed to the fact that earthquakes are short-duration, non-stationary excitations, frequently (in near-fault

regions) with impulsive characteristics (Mavroeidis and Papageorgiou 2003). On the other hand, mass dampers, being inertia devices, require typically some rise-time for their activation (Lin et al. 2010), so that their own vibration becomes large enough to facilitate the desired energy dissipation for the motion of the primary structure. If the characteristics of the ground motion are such that there is not sufficient time for this inertia mode of operation (meaning an impulsive rather than a gradual built-up of the excitation), then the efficiency of the mass dampers is expected to be small. Still, a variety of studies have demonstrated the potential of mass dampers in reducing seismic vibrations (Tributsch and Adam 2012; Hoang et al. 2008; Wong 2008; Miranda 2005). The caveat, though, that the discussion above demonstrates is that one needs to examine careful the characteristics of anticipated regional excitations before promoting such a solution.

The design, now, of mass dampers involves an optimization problem in which the spring/dashpot values are selected based on some performance criteria. For the spring this means, as discussed earlier, match to a specific modal frequency of the primary structure (impact to only a specific mode as discussed earlier). In this context, many researchers have addressed the optimal mass damper design under different excitation conditions (Soong and Dargush 1997; Gutierrez Soto and Adeli 2013) while examining different possible performance quantifications or even the implementation of multiple mass dampers (Abe and Fujino 1994). The most popular approaches correspond to reducing the response to (a) sinusoidal excitation [objective corresponds

to the maximum value of the amplification factor (Den Hartog 1985)] or (b) white noise excitation [objective corresponds to the area under the squared amplification factor giving the response-variance (Warburton 1982)]. The latter can easily be extended to minimization of the response to stationary excitation with any desired power spectrum (Yalla and Kareem 2000) [objective is related to the area of the squared amplification factor multiplied by the power spectrum of the excitation]. Approaches also exist that have looked at reliability definitions for the performance under stationary excitation, i.e. not just simple statistics such as the response-variance, by solving the so-called first-passage problem (Taflanidis et al. 2007; Marano et al. 2007).

Such procedures are definitely reasonable for wind excitation since the latter can be adequately described as stationary random processes (Simiu and Scanlan 1996). For seismic applications they might be problematic since the excitation does not have stationary characteristics. Still, they are popular even for design against earthquakes (Daniel and Lavan 2014; Moutinho 2012), the underlying assumption being that the strongest part of the ground motion can be described trough a stationary random process (Hoang et al. 2008) or that at least a design within this context will lead to a solution that is not far away from the optimal solution that would be obtained if a more faithful representation of the excitation and the performance of the structure was used. For mass dampers this seems a reasonable assumption since the fundamental requirement for proper design is the matching of its frequency to a modal frequency of the primary mass, which is to some degree independent of the excitation modeling as

has been demonstrated in (Taflanidis 2003) when comparing the design considering harmonic or white noise excitations. This design of course also provides an optimum equivalent dashpot; for this parameter it is well understood that the performance is quite insensitive to values of the dashpot higher than the actual optimum but exhibits very high sensitivity to lower values (Warburton 1982; Taflanidis 2003). This trend can be attributed to an inability to dissipate quickly-enough the vibration of the mass damper with kinetic energy ultimately being transferred back to the primary structure [with extreme case demonstrating beat-phenomenon behavior (Yalla and Kareem 2001)]. As long as lower values of the dashpot coefficient (from this optimal level) are avoided, good performance can be in general accomplished. It should be further stressed that for seismic applications, it is well understood that mass dampers will not necessarily reduce the peak vibration characteristics for all possible transient, seismic excitations, something that widely depends on the characteristics of the excitation itself (Giuliano 2013). Through a proper design, though, some contribution towards reduction of the seismic risk is anticipated (Tributsch and Adam 2012; Hoang et al. 2008; Wong 2008; Miranda 2005).

Of course other considerations do exist for mass damper design. An important one is the displacement of the secondary mass itself (secondary design goal), beyond the aforementioned vibration suppression of the primary mass (main design goal). This displacement ultimately imposes requirements of the clearance around the secondary mass to facilitate its vibration amplitude. Approaches have been proposed in the

literature to directly consider this displacement as design goal, typically through a multi-objective setting (Kim and Kang 2012; Chakraborty et al. 2012). Another important consideration is the effect of uncertainties related to properties of the primary structure (damping but more importantly factors affecting modal properties such as mass and stiffness). Poor estimation of the dynamic characteristics of the structure can lead to a significant mistune that translates into a loss of performance (Hoang et al. 2008; Mei et al. 2004; Oberguggenberger and Schmelzer 2014). This has motivated researchers to look into the robust design of mass dampers under excitation and structural uncertainties (Chakraborty and Roy 2011; Debbarma et al. 2010a; Debbarma et al. 2010b; Taflanidis et al. 2007), typically adopting stationary assumptions for the description of the excitation.

Despite the aforementioned efforts, limited attention has been given in the life-cycle assessment of the performance of mass dampers under seismic excitation adopting more comprehensive modeling frameworks to describe the excitation and addressing through a more meaningful approach the cost-benefit aspects of mass damper implementation. Larger dampers always provide greater benefits (bigger reduction for the vibration of the primary structure) but evidently have a larger associated cost that needs to be explicitly considered in the design process. Recent work (Lee et al. 2012) addressed the life-cycle benefits of adding TMDs but did not extend this approach to the more challenging aspects of design that requires direct incorporation of considerations about upfront cost. Even though such a framework for life-cycle cost

based design of other type of dissipative devices exist (Taflanidis and Beck 2009), it has never been applied to mass dampers. Furthermore this framework has only considered the design that directly minimizes the life-cycle cost without examining additional criteria such as losses for low likelihood but high impact events, representing more complex attitudes towards risk.

1.3 Special Mass Damper Case: Liquid Dampers

A special case of mass dampers are liquid dampers for which the secondary mass corresponds to a liquid (typically water) inside a (a) tank (Kareem and Sun 1987; Fujino et al. 1988) or a (b) U-shaped tube (Sakai et al. 1989). Implementation (a) is known as Tuned Liquid Damper or Tuned Sloshing Damper (TLD/TSD) and (b) as liquid column damper and has two different representatives the Tuned Liquid Column Damper (TLCD) (Sakai et al. 1989) and the Liquid Column Vibration Absorber (LCVA) (Hitchcock et al. 1997), the distinction between them being whether the U-tube has uniform or not, respectively, cross-section. These liquid dampers have some distinct advantages (A.1) lower installation costs, (A.2) easy tuning process for their fundamental frequency and (A.3) potential alternative use of the secondary mass which for this case is not simply a dead mass for the structure (for example water can be used during fire emergencies). Next each of the aforementioned type of liquid dampers is separately discussed

Tuned Liquid Dampers: TLDs have been demonstrated to effectively control vibrations induced by winds (Fujii et al. 1990; Tamura et al. 1995; Kareem 1990) while

also having the potential to mitigate earthquakes-induced vibrations (Banerji et al. 2000; Banerji and Samanta 2011; Zahrai et al. 2012). They consist of a tank filled with liquid (usually water), the sloshing of which counteracts the motion of the structure providing energy dissipation for the vibration of the latter. It is well-understood that not the entire liquid mass participates in this sloshing motion in a specific mode whereas additional challenges exist because of wave-breaking phenomena that impose a non-linear behavior (Sun et al. 1995; Reed et al. 1998). The oscillation characteristics (fundamental frequency) of the liquid are related to the dimensions of the tank and the depth of the liquid (Chen et al. 1996). Beyond the aforementioned advantages (A.1-A.3) TLDs are additionally attractive (over other type of mass dampers) because their bidirectional control capabilities (ability to tune liquid sloshing in both directions through appropriate selection of length). Their dynamic behavior, though, is typically highly nonlinear as explained above due to wave breaking phenomena, and their inherent level of damping (due to drag forces in the vibrating liquid) is typically much less than the level that would lead to an optimal suppression of the vibration of the structure (Soong and Dargush 1997). In other words the optimal equivalent dashpot coefficient cannot be achieved and the lower established damping will lead, as discussed earlier, to a significantly lower performance of the mass damper. While higher levels of damping can be attained by adding submerged obstacles, the resulting behavior is very difficult to model and, consequently, to reliably predict (Kaneko and Ishikawa 1999). It should be also stressed that even though TLDs have been primarily considered and widely

implemented to control wind-induced vibrations, many researchers are currently investigating how to develop practical TLDs than could be used to effectively control seismically induced vibrations. In general, the research efforts related to TLDs in recent years have primarily focused on: (a) developing relatively simple analytical tools to model wave breaking and damping (Tait 2008; Love and Tait 2010; Maravani and Hamed 2011); (b) establishing strategies to provide additional damping without introducing excessively complicated modeling issues (e.g. submerged screen, nets, baffles, etc.) (Modi and Munshi 1998; Modi and Akinturk 2002; Biswal et al. 2003; Kaneko and Ishikawa 1999); and (c) implementing active and semi-active control strategies (Zahrai et al. 2012; Shang and Zhao 2008).

Despite the aforementioned advantages and relevant research efforts, the popularity of TLDs has remained relatively low, something that should be attributed to the complexities in modeling both the wave breaking and the non-linearities related to the damping-enhancement elements. These complexities lead to numerical models that are difficult to implement, and to challenging design procedures.

Liquid Column Dampers: To address this barrier, liquid column mass dampers, namely the TLCD and the LCVA, have been introduced and given significant attention by various researchers (Chang and Hsu 1998; Sadek et al. 1998; Yalla and Kareem 2000; Won et al. 1997; Balendra et al. 1995; Taflanidis et al. 2007). As discussed before, these devices consist of a U-shaped tube, or, as can be equivalently considered, of two liquid containers interconnected at their lower part with a horizontal tube or pipe such that

the liquid is able to move from one container to the other. The motion of the liquid within the horizontal tube counteracts the motion of the structure and provides energy dissipation, resulting in an effectiveness of the TLCD/LCVA that is directly related to the mass in the tube and not to the overall liquid mass (Chang 1999). This may be equivalently considered as not the entire liquid mass participating in the horizontal mode of vibration. The frequency of oscillation of the liquid is directly related to the length of the liquid column, which is the only parameter that can be adjusted to establish the desired tuning characteristics. The horizontal tube can be also used to place an element (typically a valve or an orifice plate) that provides energy dissipation (damping) (Sakai et al. 1989), and the damping level can potentially be controlled in a passive or semi-active way (Yalla and Kareem 2003). The vibration of the liquid within the tube prevents any wave-breaking phenomena, thus leading to simpler models (single degree of freedom behavior) than those of TLDs. However, TLCD/LCVA devices are restricted to one-directional applications (Samali 1990), and their behavior is still nonlinear because damping is amplitude-dependent due to the presence of the orifice (Taflanidis et al. 2007).

1.4 Objectives

Motivated by the aforementioned limitations of TLDs and liquid column dampers but also the advantages that liquid mass dampers have to offer, the objective of this research is to propose a modification of the traditional TLD through a simple

introduction of a floating roof that addresses the aforementioned challenges that have restricted its popularity. This new device is termed TLD with floating roof (TLD-FR). Another objective is to establish a simplified framework for easy comparison of the new device to TLDs as well as TMDs. These goals include both a theoretical and experimental component, while they also involve the development of new numerical tools to facilitate a computationally simpler description of the behavior of TLDs. Additionally, the efficiency of mass dampers for seismic protection in the Chilean region is examined in detail and a life-cycle design of the new device (or as it will be demonstrated later generally of mass dampers) is developed that (a) provides a clear justification of the benefits offered by the adoption of such control measures and (b) considers risk criteria that are relevant to the Chilean region.

The specific objectives of the research are:

1) Develop a simplified, computationally efficient framework for describing the dynamic behavior of arbitrary geometry liquid storage tanks under base excitation.
2) Extend the previous framework to describe the dynamic behavior of TLDs-FR under base excitations as well as the coupling with the structure that supports them.
3) Validate the numerical models through scaled experiments and evaluate the accuracy of the proposed modeling framework to predict the behavior of TLDs-FR under seismic excitation.

4) Propose a parametric formulation to describe the TLD-FR dynamics only through its fundamental vibratory characteristics (participating mass, frequency and damping of equivalent mass damper) in order to establish a direct comparison with other mass dampers like TMDs, TLCDs and LCVAs.
5) Propose a methodology to establish a mapping between tank geometries and the resultant vibratory characteristics of the TLD-FR and through this approach establish a practical design methodology for selecting the tank characteristics of TLDs-FR.
6) Validate the potential of mass dampers for the Chilean region and establish a multi-objective life-cycle analysis/design process for the TLD-FR considering a risk-description that is relevant for this region. The latter refers to both an appropriate characterization of seismic hazard as well as the adoption of risk-criteria that beyond the total life-cycle cost incorporate risk-averse criteria for describing life-cycle performance.

The next chapter reviews some characteristics of mass dampers, including their equations of motion, and additionally presents the type of tank geometries that will be used throughout this dissertation. It also validates the potential of mass dampers for the Chilean region, providing a comparison for the level of seismic protection established between ground motions that are typical for the region and ground motions from other parts of the world for which potential effectiveness of mass dampers is regarded with

high degree of skepticism. Then the following chapters discuss the research advances to satisfy the established objectives. Chapter 3 presents a new numerical scheme for the dynamic analysis of liquid storage tanks. Chapter 4 discusses the numerical characterization of the dynamic behavior of the TLD-FR as well as an experimental validation of the proposed numerical framework. Then Chapter 5 establishes a parametric formulation for the equations of motion that simplifies the TLD-FR behavior and makes it directly comparable with other type of mass dampers. Based on this formulation the design in the parametric space as well as the efficient transformation of that design to the different tank geometries are discussed. Chapter 6 discusses the life-cycle based assessment and design of TLDs-FR (and more generally mass dampers) utilizing a simulation-based approach for the analysis and adopting hazard characterization and risk quantification appropriate for the Chilean region. Finally, Chapter 7 summarizes this work and its relationships to the stated above objectives and discusses potential future extensions of the research.

2 REVIEW OF COMMON MASS DAMPER EQUATIONS OF MOTION, DESCRIPTION OF TYPICAL TANK GEOMETRIES OF TLDS AND DEMONSTRATION OF EFFECTIVENESS FOR SEISMIC PROTECTION AGAINST CHILEAN EARTHQUAKES

In this chapter the equations of motion for common mass dampers (namely linear TMDs, TLCDs and LCVAs) and some general characteristics of their behavior are reviewed. This information will be used in later chapters to facilitate a direct comparison to TLDs-FR. Additionally, some common tank configurations that will be used for the analysis of TLDs and TLDs-FR throughout this dissertation are also presented. Finally the effectiveness of mass dampers for suppressing earthquake-induced vibrations for buildings in the Chilean region is demonstrated, providing a further motivation for the research presented within this dissertation.

2.1 Equation of Motion of TMDs, TLCDs and LCVAs

Consider a TMD or liquid column mass damper (LCVA or TLCD) attached to a SDOF oscillator as in Figure 2.1. The derivation of the equations of motion for the latter are discussed first with the ones for the former (TMD) presented also as a limiting case.

The displacement for the SDOF is denoted by u_o whereas the displacement for the liquid column (or secondary mass for the TMD case) by y_o.

Let ρ, B_o, and H_o denote the density, horizontal length and initial height of the liquid column, respectively, A_v and A_h the vertical and horizontal cross-sectional areas of the liquid column, respectively, and ζ the head-loss coefficient of an orifice plate attached in the middle of the horizontal tube to provide additional damping. These parameters fully define the damper's characteristics. Adapting the same parametric formulation as in (Taflanidis et al. 2007) define $m_d=\rho A_v(2H_o+B_o/r_a)$ as the mass of the damper, $L_{eff}=2H_o+r_aB_o$ as the effective length, $\omega_d=\sqrt{2g/L_{eff}}$ as the damper's natural frequency, $r_a=A_v/A_h$ as the area ratio, $\alpha_o=B_o/L_{eff}$ as the effective mass index, and $\lambda=(2H_o+r_aB_o)/(2H_o+B_o/r_a)$ as the effective length ratio. Note that for the TLCD, λ=1 whereas the effective mass index represents the portion of the total liquid mass that contributes in the vibration in the horizontal direction.

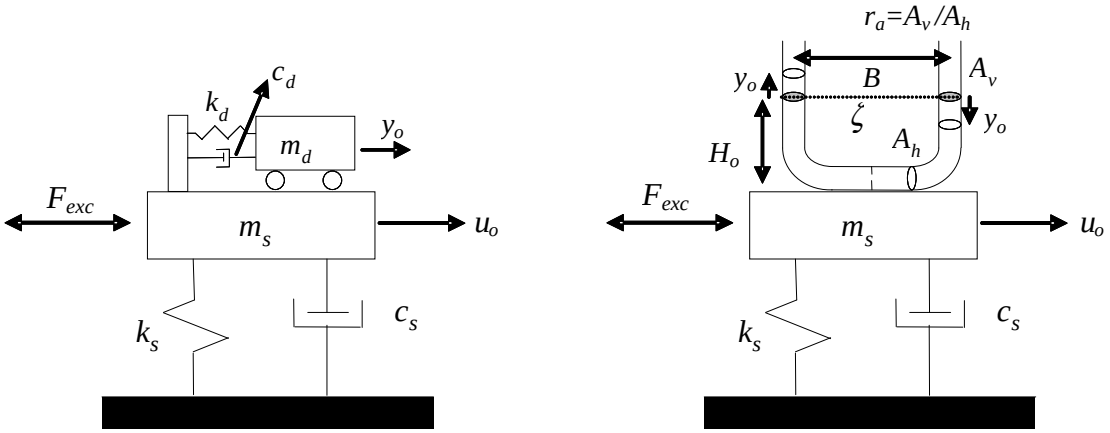

Figure 2.1 TMD (left) and LCVA (right) installed on a single degree of freedom oscillator

The equations of motion for the coupled system are (Chang, 1999):

$$\begin{aligned} &\left(m_s + m_d\right)\ddot{u}_o + \alpha_o \lambda m_d \ddot{y}_o + c_s \dot{u}_o + k_s u_o = F_{exc} \\ &\lambda m_d \ddot{y}_o + \alpha_o \lambda m_d \ddot{u}_o + \lambda m_d \omega_d^2 \frac{\zeta r_o}{4g} \left|\dot{y}_o\right| \dot{y}_o + \lambda m_d \omega_d^2 y_o = 0 \end{aligned} \tag{2.1}$$

where F_{exc} is the dynamic excitation on the SDOF, m_s, $c_s=2\xi_s\omega_s m_s$, $k_s=\omega_s^2 m_s$ are the mass, damping and stiffness for the SDOF with ω_s, ξ_s denoting its natural frequency and damping ratio, respectively. Let the normalized displacement of the liquid be $y_{n_o} = y_o / \alpha_o$, the orifice coefficient $d_o = \alpha_o \zeta r_a$ and define the efficiency index as in (Taflanidis et al. 2007) by

$$\gamma = \alpha_o^{\,2} \lambda = 1 / \left[\left(2H_o / B_o + r_a\right)\left(2H_o / B_o + 1/r_a\right)\right] \tag{2.2}$$

It is straightforward to prove (Taflanidis et al. 2007) that the efficiency index corresponds to $\gamma=\alpha_o^2/(1-r_a\alpha_o+\alpha_o/r_a)$, and so it combines the area and length ratio into one parameter. Also, note that $\gamma<1$. Equation (2.1) is finally transformed to:

$$\begin{aligned} &\left(m_s + m_d\right)\ddot{u}_o + \gamma m_d \ddot{y}_{n_o} + c_s \dot{u}_o + k_s u_o = F_{exc} \\ &\ddot{y}_{n_o} + \ddot{u}_o + \omega_d^2 \frac{d_o}{4g} \left|\dot{y}_{n_o}\right| \dot{y}_{n_o} + \omega_d^2 y_{n_o} = 0 \end{aligned} \tag{2.3}$$

This formulation indicates that the response of the coupled normalized damper-structure system is fully defined, with respect to the damper's characteristics, by the mass of the damper, m_d, the efficiency index, γ, the orifice coefficient, d_o, and the damper's natural frequency, ω_d. According to Equation (2.3), dampers that correspond to the same values for all four aforementioned parameters will exhibit the same response for the primary system and for the normalized liquid displacement. The actual

liquid displacement will be larger for dampers that are characterized by larger value of the effective mass index α_o. As long as only the primary system's response is of concern, the efficiency index allows the area and length ratios influence to be simultaneously addressed. Let the normalized damping force be $F_{dn} = \omega_d d_o \left|\dot{y}_{n_o}\right| / (8g)$, then Equation (2.3) leads to:

$$\begin{aligned} &\left(m_s + m_d\right)\ddot{u}_o + \gamma m_d \ddot{y}_{n_o} + 2\xi_s m_s \omega_s \dot{u}_o + m_s \omega_s^2 u_o = F_{exc} \\ &\ddot{y}_{n_o} + \ddot{u}_o + 2F_{dn}\omega_d \dot{y}_{n_o} + \omega_d^2 y_{n_o} = 0 \end{aligned} \tag{2.4}$$

This equation corresponds to the well-known TMD (right scheme presented in Figure 2.1) for γ=1 and F_{dn} equal to the damping ratio ξ_d of the damper. Note that for the TMD α_o=1, meaning that the entire mass contributes in the vibration in the horizontal direction and also $y_{n_o} = y_o$. Equation (2.4) can be used to model all three aforementioned mass dampers, simply by using the proper selection for F_{dn}.

Ultimately the behavior of these mass dampers can be described equivalently by the equation of motion for them, which is:

$$\ddot{y}_{n_o} + \ddot{u}_o + 2F_{dn}\omega_d \dot{y}_{n_o} + \omega_d^2 y_{n_o} = 0 \tag{2.5}$$

and by the force transferred to the primary mass which can be expressed as:

$$\begin{aligned} F &= -\gamma m_d \ddot{y}_{n_o} - m_d \ddot{u}_o \\ &= m_d \left[2F_{dn}\omega_d \gamma\right]\dot{y}_{n_o} + m_d \left[\gamma \omega_d^2\right] y_{n_o} - m_d \left[1-\gamma\right]\ddot{u}_o \end{aligned} \tag{2.6}$$

where $\ddot{u}_o$ is the acceleration of the base of the damper.

These two Equations (2.5) and (2.6) facilitate the modeling of the damper behavior as well as its coupling to the supporting structure, i.e. can extend the previous analysis to arbitrary structures with multiple degrees of freedom, not necessarily constrained to SDOF oscillators. For example, let's consider a linear and planar structure with a damper located in a particular floor described through the location vector $\mathbf{L}_s$ (vector of zeros with a single 1, at the floor of the damper). The equation of motion for the structure under ground-acceleration $\ddot{u}_g$ (which is the case that will be primarily used within this thesis) is then:

$$\mathbf{M}\ddot{\mathbf{u}} + \mathbf{C}\dot{\mathbf{u}} + \mathbf{K}\mathbf{u} - \mathbf{L}_s{}^T F = -\mathbf{M}\mathbf{D}_o \ddot{u}_g \tag{2.7}$$

where $\mathbf{M}$, $\mathbf{C}$ and $\mathbf{K}$ correspond to the mass, damping and stiffness matrices, while $\mathbf{D}_o$ is the vector of earthquake influence coefficients (vector of ones in this case) and $\mathbf{u}$ corresponds to the vector of displacements (relative to the ground) of each floor. The coupled system of equations for the structure equipped with a mass damper is then given by combining Equations (2.7) and (2.5) with F for the former given by Equation (2.6). Note that $\ddot{u}_o$ in Equation (2.5) corresponds to the absolute acceleration of the floor in which the mass damper is installed, therefore it should be substituted by $\ddot{u}_o = \mathbf{L}_s\,(\ddot{\mathbf{u}} + \mathbf{D}_o \ddot{u}_g)$, leading to:

$$\begin{aligned} &\begin{bmatrix} \mathbf{M} + \mathbf{L}_s^{\mathrm{T}} m_d \mathbf{L}_s & \mathbf{L}_s^{\mathrm{T}} \gamma m_d \\ \mathbf{L}_s & 1 \end{bmatrix} \begin{bmatrix} \ddot{\mathbf{u}} \\ \ddot{y}_{n_o} \end{bmatrix} + \begin{bmatrix} \mathbf{C} & 0 \\ \mathbf{0} & 2F_{dn}\omega_d \end{bmatrix} \begin{bmatrix} \dot{\mathbf{u}} \\ \dot{y}_{n_o} \end{bmatrix} + \begin{bmatrix} \mathbf{K} & 0 \\ \mathbf{0} & \omega_d^2 \end{bmatrix} \begin{bmatrix} \mathbf{u} \\ y_{n_o} \end{bmatrix} \\ &= -\begin{bmatrix} \left(\mathbf{M} + \mathbf{L}_s^{\mathrm{T}} m_d \mathbf{L}_s\right) \mathbf{D}_o \\ 1 \end{bmatrix} \ddot{u}_g \end{aligned} \tag{2.8}$$

2.2 Performance and Design Trends for TMDs, TLCDs and LCVAs

The performance characterization of the mass dampers discussed in the previous section can be further simplified by introducing two dimensional parameters, the tuning ratio α, defined as the ratio of damper frequency to fundamental frequency of the structure, and the mass ratio r, defined as the ratio of the damper mass to the total mass of the structure. For a single-degree of freedom oscillator these parameters are, respectively, $\alpha=\omega_d/\omega_s$ and $r=m_d/m_s$. The equations of motion for generalized force acting on the structure or for ground acceleration are then, respectively, transformed to

$$\begin{bmatrix} 1+r & \gamma r \\ 1 & 1 \end{bmatrix} \begin{bmatrix} \ddot{u}_o \\ \ddot{y}_{n_o} \end{bmatrix} + \omega_s \begin{bmatrix} 2\xi_s & 0 \\ 0 & 2F_{dn}\alpha \end{bmatrix} \begin{bmatrix} \dot{u}_o \\ \dot{y}_{n_o} \end{bmatrix} + \omega_s^2 \begin{bmatrix} 1 & 0 \\ 0 & \alpha^2 \end{bmatrix} \begin{bmatrix} u_o \\ y_{n_o} \end{bmatrix} = \begin{bmatrix} 1 \\ 0 \end{bmatrix} \frac{F_{exc}}{m_s} \tag{2.9}$$

$$\begin{bmatrix} 1+r & \gamma r \\ 1 & 1 \end{bmatrix} \begin{bmatrix} \ddot{u}_o \\ \ddot{y}_{n_o} \end{bmatrix} + \omega_s \begin{bmatrix} 2\xi_s & 0 \\ 0 & 2F_{dn}\alpha \end{bmatrix} \begin{bmatrix} \dot{u}_o \\ \dot{y}_{n_o} \end{bmatrix} + \omega_s^2 \begin{bmatrix} 1 & 0 \\ 0 & \alpha^2 \end{bmatrix} \begin{bmatrix} u_o \\ y_{n_o} \end{bmatrix} = -\begin{bmatrix} 1+r \\ 1 \end{bmatrix} \ddot{u}_g \tag{2.10}$$

For the linear TMD the amplitude of the transfer function for u_o and y_o for excitation on the structure [case presented in Equation (2.9)] are given, respectively, by (Taflanidis 2003):

$$\left|H_{u_o}(i\omega)\right| = \frac{1}{m_s\omega_s^2} \frac{\sqrt{[\alpha^2 - f^2]^2 + (2\xi_d \alpha f)^2}}{\sqrt{E_s^2 + D_s^2}} \quad \text{and} \quad \left|H_{y_o}(i\omega)\right| = \frac{1}{m_s\omega_s^2} \frac{f^2}{\sqrt{E_s^2 + D_s^2}}$$
$$E_s = [1-f^2][\alpha^2 - f^2] - 4\xi_s\xi_d\alpha f^2 - r\alpha^2 f^2 \tag{2.11}$$
$$D_s = 2f\left\{\xi_s[\alpha^2 - f^2] + [1-(1+r)f^2]\xi_d\alpha\right\}$$

where $f=\omega/\omega_s$ is the dimensionless ratio of excitation to SDOF frequency. A similar expression can be established for liquid column dampers by substitution of the

normalized damping force F_{dn} by an equivalent damping ratio ξ_d through some linearization approximation (Taflanidis 2003). The only difference is that E_s needs to be substituted by

$$E_s = [1 - f^2][\alpha^2 - f^2] - 4\xi_s\xi_d\alpha f^2 - \gamma r\alpha^2 f^2 \tag{2.12}$$

For ground excitation, [case presented in Equation (2.10)] the respective transfer functions are transformed to (Taflanidis, 2003):

$$\left|H_{u_o}(i\omega)\right| = \frac{1}{\omega_s^2}\frac{\sqrt{[(1+\mathrm{r})(\alpha^2 - f^2) + \gamma f^2]^2 + \left(2\xi_d\alpha f(1+r)\right)^2}}{\sqrt{E_s^2 + D_s^2}}$$
$$\text{and} \quad \left|H_{y_o}(i\omega)\right| = \frac{1}{\omega_s^2}\frac{\sqrt{1+2\xi_s f^2}}{\sqrt{E_s^2 + D_s^2}} \tag{2.13}$$

The optimal design for liquid column mass dampers refers to the determination of optimum values for the natural frequency (or tuning ratio) and the damping ratio, referred to herein as design variables, while the mass ratio and efficiency index are fixed based on architectural considerations and constraints for the damper mass. For the TMD the efficiency index is, of course, one. This design can be performed through any desired approach for the excitation description and the performance quantification as discussed in the introduction (harmonic excitation, white noise excitation, stationary response, first-passage problem, etc). Independent of the approach taken some general characteristics can be identified [detailed discussion on these trends can be found in (Chang 1999) or (Taflanidis 2003)]:

- Optimal design corresponds to tuning, i.e. to values for α close to 1. This leads to a transfer function for coupled system (for both the primary mass and the damper) having two separate peaks in the region close to its natural frequency. Effective design leads to suppressed peaks when compared to the initial single peak of the primary structure (this is what provides the vibration suppression).
- Larger values for the mass ratio r or efficiency index γ lead to larger optimal values for the tuning ratio α or the damping ratio ξ_d and to better performance under optimal design. In other words the TMD is always better than liquid dampers. This should be attributed to the fact that for the TMD the total mass is equal to its effective mass contributing to counteracting the vibration of the primary mass.
- Even though the optimum damping ratio is independent of the intensity of the excitation or the natural frequency of the primary system for the TMD, the nonlinear characteristics of the response of liquid column dampers introduce a dependence of the optimal orifice coefficient on these two parameters (Taflanidis et al. 2007). This means that the nominal optimal design for liquid column mass dampers, even when all other characteristics of the system are known, has to be based on a nominal intensity. Under different intensities than the nominal one, the design will always be sub-optimal.

- With respect to the optimal design variables great sensitivity exists for values of ξ_d smaller than the optimal ones.

This latter point, which is an important consideration for the damper design is demonstrated in Figure 2.2 that plots the maximum amplification factor, corresponding to a typical used performance objective for assessing performance of TMD applications, for a TMD with mass ratio 1% attached to a SDOF with damping ratio ξ_s=2% when the latter is excited by an external force. The objective function in this case corresponds to

$$H_{obj} = \max_f \frac{|H_x(i\omega)|}{m_s \omega_s^2} = \max_f \left[\frac{\sqrt{[\alpha^2 - f^2]^2 + (2\xi_d \alpha f)^2}}{\sqrt{E_s^2 + D_s^2}} \right] \quad (2.14)$$

Note that the amplification factor without the damper is 25. The plot exhibits a clear optimum that provides a significant performance improvement, whereas for values of the TMD damping (equivalently dashpot coefficient) lower than the optimum one the performance drastically deteriorates.

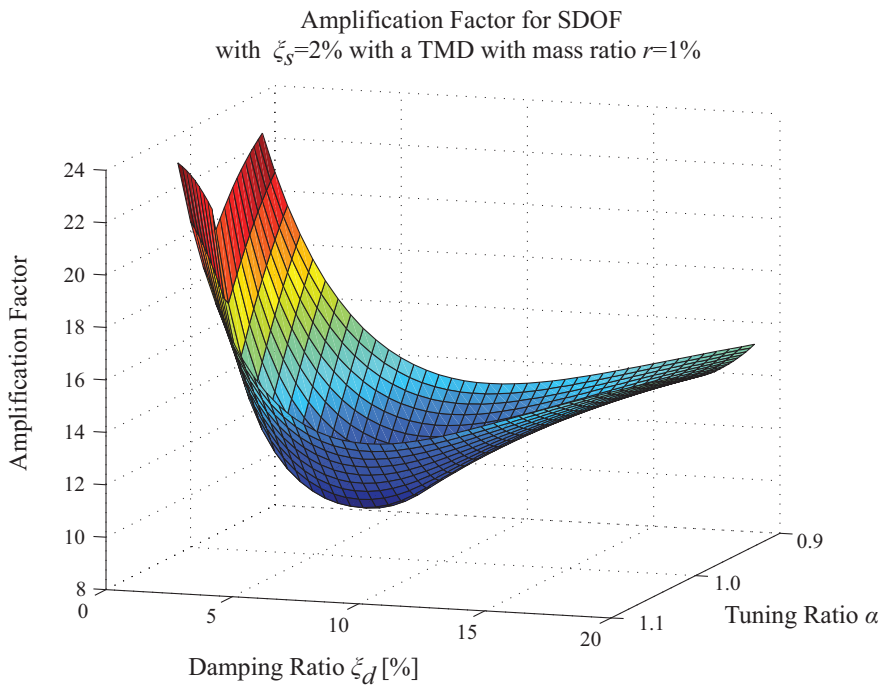

Figure 2.2 Maximum amplification factor for a SDOF equipped with a TMD as a function of TMD characteristics ξ_d and α for mass ratio of 1%. Damping ratio for SDOF is 2%.

2.3 Tank Geometries Used for TLD and TLD-FR

Within this dissertation different tank geometries will be considered. This section reviews the general geometrical characteristics of their cross-section (assumed constant along their width). The simplest configuration corresponds to a rectangular tank as shown in Figure 2.3 , which can be defined by two variables, the length L and the water depth H. Based on these two, the aspect ratio, $R= H/L$ can be defined to facilitate a simpler parametric investigation.

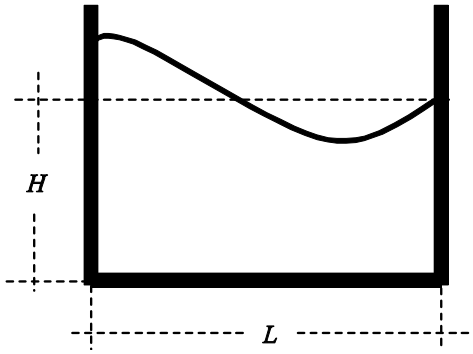

Figure 2.3 Scheme of a rectangular tank

The more complicated geometries are illustrated then in Figure 2.4. The first one is a W-Type Tank corresponding to a rectangular tank with a triangular obstacle located at the bottom, with its location and size defined by a and h as shown in the figure. The next two are the U-Type and V-Type Tanks, respectively, both corresponding to a tank with sloped walls, defined similarly through parameters a and h. The only difference is that the U-Type Tank satisfies the condition of $h<H$ while the V-Type Tank satisfies the condition of $h>H$. The final one is the T-Type that corresponds to a tank where the inferior corners are rounded by semicircles defined by an eccentricity e_o and a radius r_o. Note that for all cases, H is the non-perturbed water depth and L is the length of the tank. Therefore the aspect ratio $R= H/L$ can still be used to parameterize the tanks, establishing a uniformity with respect to the rectangular tank discussed earlier. Additionally, two new ratios are introduced for each type of tank to facilitate this parameterization corresponding to a normalization with respect to the external

dimensions L and H: $\bar{h} = h / H$ and $\bar{a} = a / L / 2$ for V-Tank, U-Tank and W-Tank, while $\bar{r} = r_o / H$ and $\bar{e} = e_o / r_o$ for T-Tank.

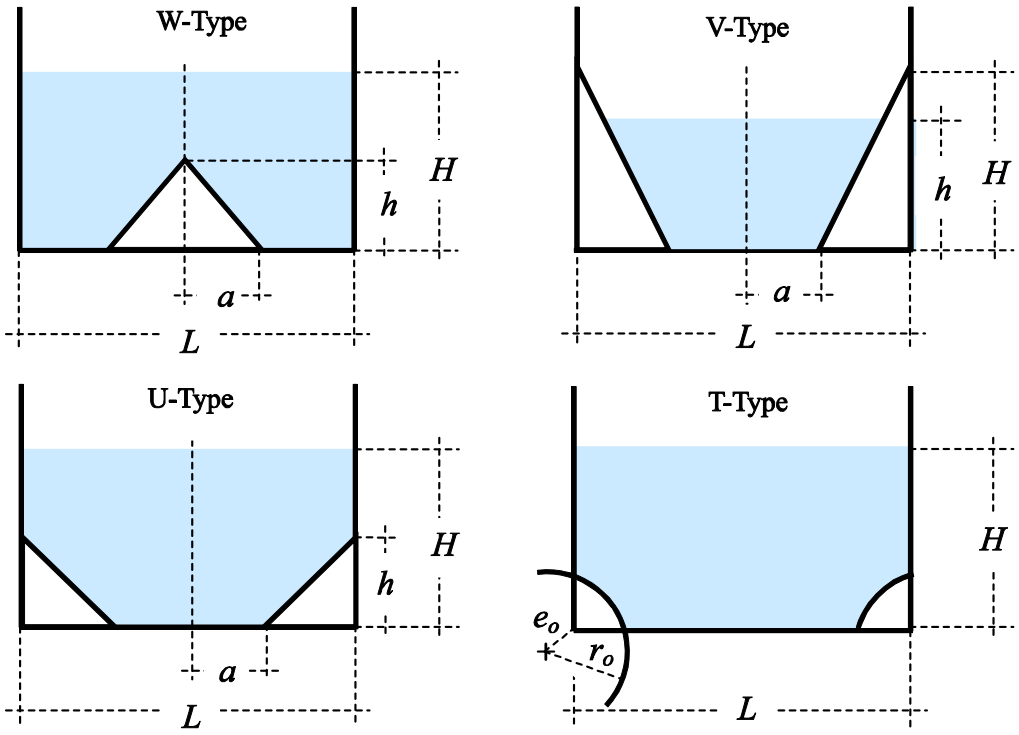

Figure 2.4 Description of four different non-rectangular tank geometries, termed as W-type, V-type, U-type and T-type tanks

In general, the cross-section shape is defined by the following dimensionless ratios: (R) for rectangular tanks, ($\bar{h}$, $\bar{a}$, R) for V-W-U-Tanks and ($\bar{r}$, $\bar{e}$, R) for T-Tanks. Then, the incorporation of the length L allows scaling the shape to a particular size such that it is feasible to have tanks with the same shape but different sizes. The width of the tank (dimension out of plane) then sizes the overall liquid mass.

2.4 Effectiveness of TMDs to suppress earthquakes-induced vibrations for common earthquakes for the Chilean region

As it was mentioned in the introduction, the effectiveness of mass dampers in controlling seismic vibrations of buildings is an open question, since depending upon the characteristics of the excitation a variety of performance-levels have been reported, ranging from significant to little or no reductions in the structure´s response (Lin et al. 2001; Lin et al. 2010). It is well understood that mass dampers, due to their operation as inertia devices, and independent of the design approach taken, are not always efficient in suppressing transient seismic responses (Giuliano 2013). In particular they are less effective in reducing the response of buildings excited by near-fault (rather than far-field) earthquakes (Lin et al. 2010) due to the impulsive characteristics of the former (not sufficient rise-time for inertia devices to become fully operational). In that sense, a correct optimization and tuning of the TMD characteristic is mandatory but not sufficient to guarantee a good performance in seismic applications.

A question then rises related to how effective can mass dampers be for the Chilean region? This is a critical topic for properly motivating the research in the latter chapters of this dissertation. Existing applications of mass dampers in the region (Lu et al. 2014) are definitely a strong indication of their potential effectiveness, but further justification is required to demonstrate why mass dampers can be effective for seismic applications for Chilean buildings. The answer to this question is directly related to the seismicity of the region and the characteristics of typical seismic ground motions these

buildings are exposed to over their lifetime. This seismicity is associated with the subduction zones at the Chilean coast which result in strong and long-duration excitations (Leyton et al. 2009), with far-field characteristics (a) rupture distances for major events greater than 30 km for most important cities (Boroschek and Contreras 2012), (b) ground motion records that lack pulse-like waveforms in the velocity time histories and (c) large durations. With respect to the latter it is interesting to note that the significant duration of the "El Maule" 2010 earthquake in Chile ranged from 30-80s while the perceptible durations were longer than 2-3 min (Boroschek et al. 2012). These characteristics of regional ground motions indicate that the implementation of mass dampers to control the seismic response on buildings can indeed provide substantial benefits.

To further demonstrate this a comparative study is established considering different sets of ground motions and evaluating the effectiveness of mass damper implementation at the top of a 9-story building corresponding to the benchmark structure discussed in (Ohtori et al. 2004). The first set, representing typical Chilean earthquakes, corresponds to 11 ground motions taken from the RENADIC (National Accelerograph Network at the Department of Civil Engineering, Universidad de Chile) database (Boroschek et al. 2015), associated with different important seismic events in Chile the past 30 years Some important characteristics for these ground motion are reviewed in Table 2.1. The second set, representing earthquakes from other parts of the world, corresponds to an additional 11 ground motions, most of them from the US West

coast and many of them including a pulse-like components (seismic events at near-fault region). This set is similarly reviewed in Table 2.2. The third, and final, set of ground motions are synthetic ones, obtained employing the stochastic ground motion modeling procedure that will be described later in Chapter 6 and provides excitations compatible with the Chilean seismic hazard. The reason for including these synthetic motions, whose characteristics are reviewed in Table 2.3, is to establish a further comparison of the trends obtained from this ground motion modeling approach to the regional motions (set 1). A total of 33 ground motions are therefore considered, and each ground motion is characterized by a unique ID number, reported also in the Tables 2.1-2.3.

As mass damper a TMD is considered with mass equal to 1% of the total mass of the building, frequency ratio 0.983 and damping ratio 4.98%. The latter two values correspond to the optimal design configuration under stochastic, stationary, base-excitation utilizing the approach that will be discussed in more detail later in Section 5.4. Performance for the mass damper implementation is evaluated through time-history analysis under the different sets of ground motions and two different metrics are utilized for quantifying this performance: maximum instantaneous inter-story drift and maximum instantaneous story acceleration. These correspond to representative engineering demand parameters for quantifying damages to structural components and building contents, respectively (Taflanidis and Beck 2009). The percentage reduction through the introduction of the damper (reduction of the maximum responses over the

entire building obtained by the installation of the mass damper) is used as measure to quantify the damper-efficiency and results are presented in Figure 2.5.

Table 2.1 Characteristics of the chosen Chilean earthquakes

Location	ID	Earthquake Name	Station Name	Year	M	Epicentral Distance (km)	PGA (g)
Chile	1	Valparaiso	Melipilla	1985	7.9	76.2	0.687
	2	Valparaiso Aftershock	Llolleo	1985	7.3	41	0.191
	3	Antofagasta	Tocopilla	1995	8	169.5	0.51
	4	January 30th	Antofagasta UCN	1998	7	62.2	0.053
	5	Sur del Peru	Arica Cementerio	2001	8.4	431.2	0.269
	6	Sur del Peru Aftershock	Arica Chalcalluta	2001	7.6	187.3	0.069
	7	June 20th	Puente Amolanas	2003	6.8	63.9	0.094
	8	April 30th	Copiapo	2006	6.5	101.2	0.054
	9	Tocopilla	Tocopilla	2007	7.7	66.7	0.502
	10	Tocopilla Aftershock	Mejillones Puerto	2007	6.7	25.3	0.394
	11	Maule	Concepcion Centro	2010	8.8	62.3	0.401

Table 2.2 Characteristics of earthquakes chosen from other regions of the world

Location	ID	Earthquake Name	Station Name	Year	M	Epicentral Distance (km)	PGA (g)
US west coast	12	Landers	Joshua Tree	1992	7.3	11.03	0.284
	13	Loma Prieta	Corralitos	1989	6.9	3.85	0.479
	14	Northridge	Newhall	1994	6.7	5.92	0.59
	15	Imperial Valley	Holtville	1979	6.5	5.35	0.248
	16	Parkfield	Fault zone 7	2004	6	2.67	0.228
	17	Cape Mendocino	Shelter Cove	1992	7	28.78	0.177
Japan	18	Kobe	KJMA	1995	6.9	0.96	0.599
Taiwan	19	Chi-Chi	CHY024	1999	7.6	9.62	0.277
Turkey	20	Kocaeli	Arcelik	1999	7.5	13.49	0.147
Italy	21	Irpinia	Sturno	1980	6.9	10.84	0.247
Iran	22	Tabas	Tabas	1978	7.4	55.24	0.852

Table 2.3 Characteristics of the chosen synthetic ground motions compatible with Chilean hazard

ID	M	Rupture Distance (km)	PGA (g)
23	6.9	125.6	0.047
24	7.5	60.8	0.191
25	7.9	65.7	0.226
26	7.5	122.7	0.083
27	6.8	77.8	0.081
28	8.0	127.8	0.153
29	8.4	61.9	0.345
30	7.3	125.55	0.078
31	6.2	65.5	0.060
32	8.2	105.8	0.183
33	6.6	214.7	0.010

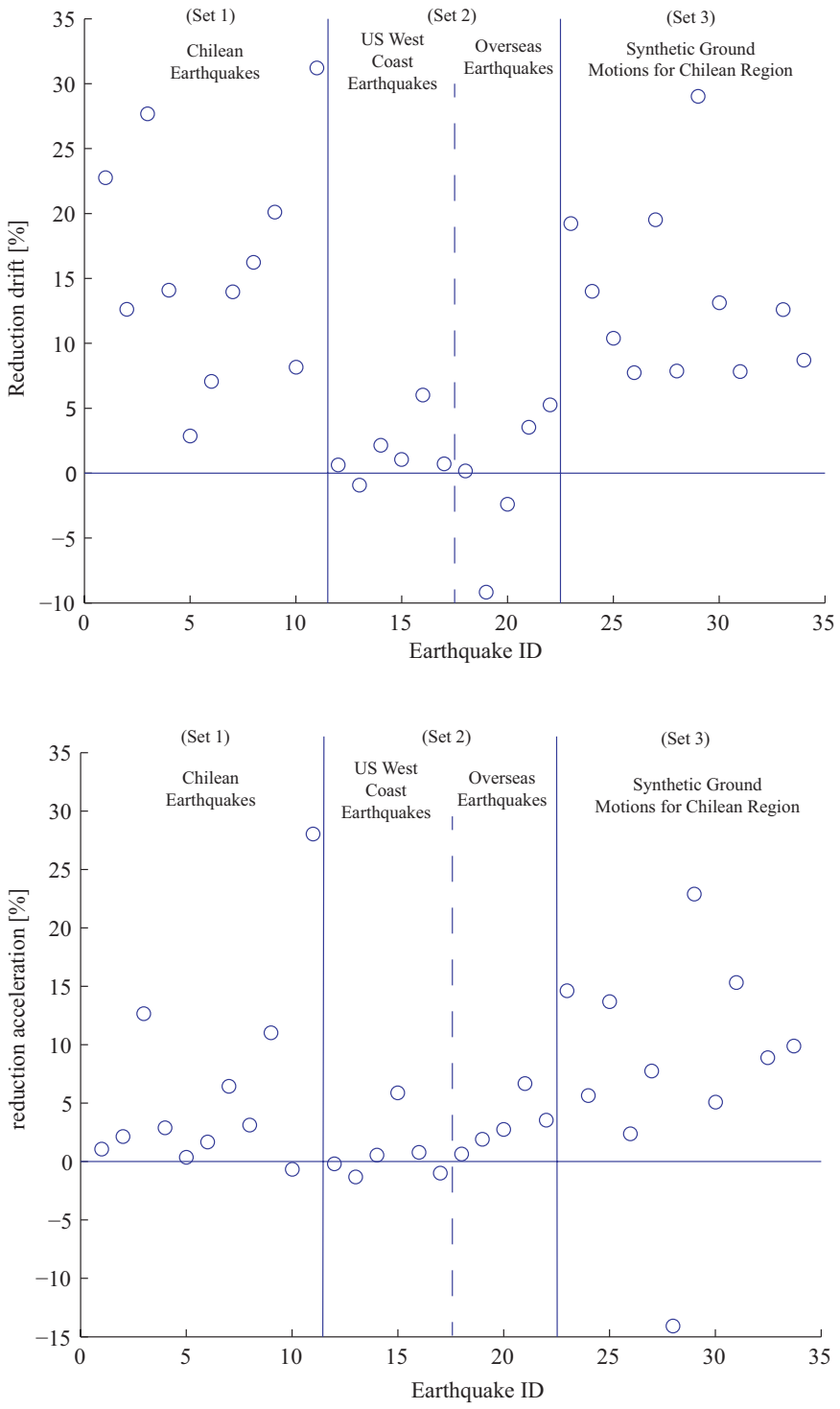

Figure 2.5 Mass damper efficiency (maximum inter-story drift and acceleration reduction) for 9-story building under different ground motions

The most important comparison is between the first two sets of ground motions. It is evident that for drift-responses significant reduction is established for set 1 over all examined ground motions, with values as high as 30%, whereas for set 2 minimal improvement is overall reported (or even amplification of the response for some instances). This validates the arguments made above: earthquakes that are typical in Chilean region accommodate the reduction of seismic responses though inertia devices. The reason for this should be attributed to the fact that these excitations allow sufficient time for mass damper to respond and dissipate energy. This characteristic is further examined in Figure 2.6, which reports the normalized RMS response using a 3 s time-window for the TMD (output) and its input, i.e. the acceleration at the top of the structure (base of TMD), for four indicative ground motions: two from set 1 and two from set 2. The normalization is established with respect to the max value of the RMS response. Figure 2.7 shows the time-history of the responses for these cases. In both figures, the first and second rows show the response of the building under two different Chilean earthquakes, while the third and fourth rows show the response under two ground motions with pulse-like characteristics. In the later cases the maximum of the structural response occurs before the TMD has sufficient time to build-up its own response and therefore provide the desired energy dissipation. The inertia device is effective only after the maxima of the acceleration response has occurred, therefore providing limited improvement in the seismic performance. This is particularly evident for ID19 excitation. On the other hand, for the longer-duration and without strong

pulse-component Chilean motions, the TMD is provided the opportunity to dissipate sufficient energy (larger RMS response values for TMD) before the maximum of the structural response occurs. These results agree with the discussion related to sufficient rise-time for TMD efficiency provided in (Lin et al. 2010) when evaluating the potential of mass dampers for protection against near-fault excitations, and are the reason for the improvement that is reported by the addition of the mass dampers in Figure 2.5 for these ground motions. Note that this improvement is relatively smaller for the acceleration responses when compared to the drift responses. This should be attributed to fact that the acceleration responses have higher bandwidth and are impacted by higher modes which the TMD cannot control. This feature has on its own important implications: even for excitations for which TMDs can provide improvement of structural responses, this improvement is expected larger for drift demands rather than acceleration demands. Therefore, TMDs are expected to be more effective in improving the performance of drift-sensitive components rather than acceleration-sensitive components or building contents.

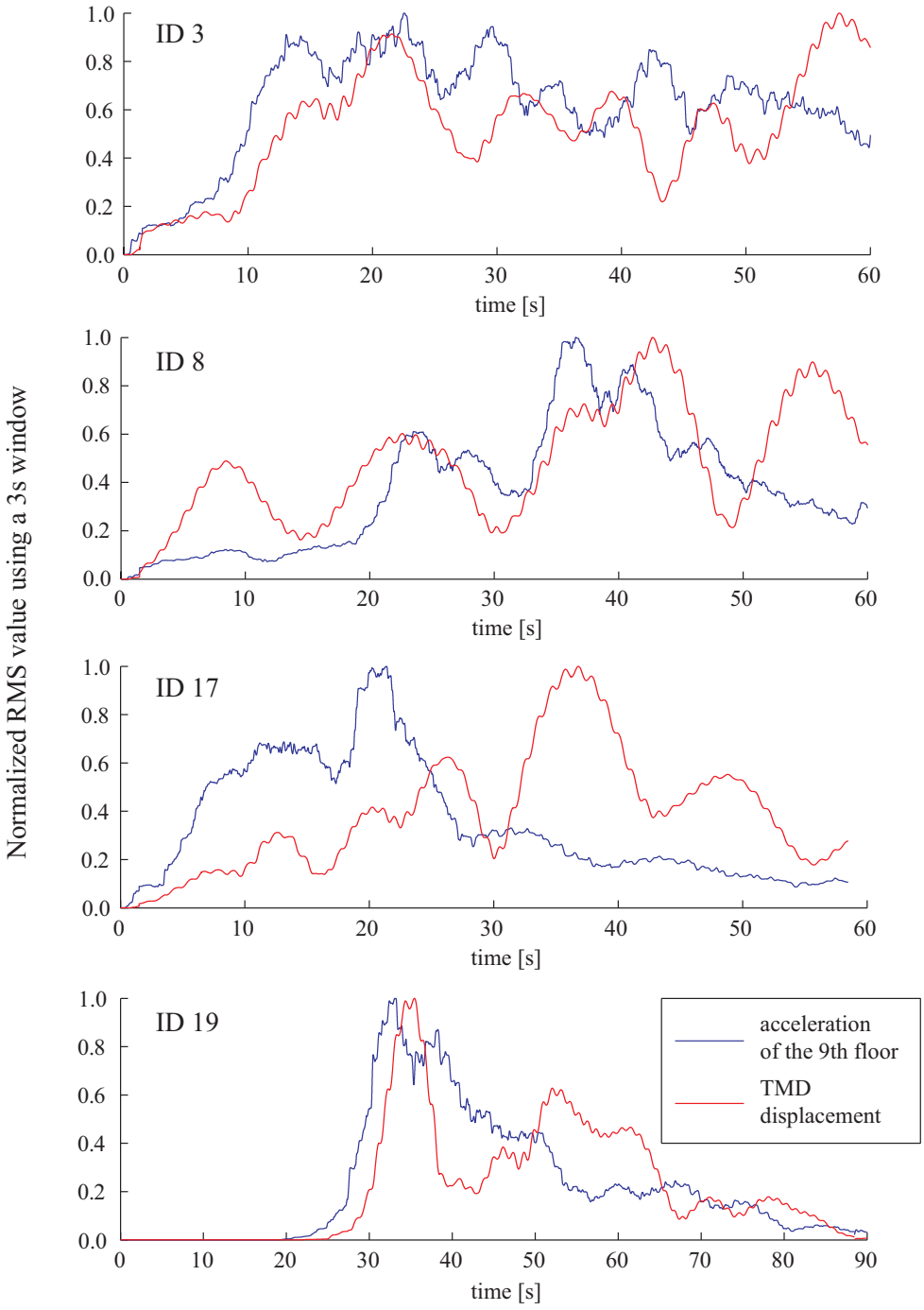

Figure 2.6 Comparison of the acceleration of the 9th floor of the building with the response of the TMD in terms of the rms values using a 3s window. Results for four different excitations are reported (characterized through the ID numbers)

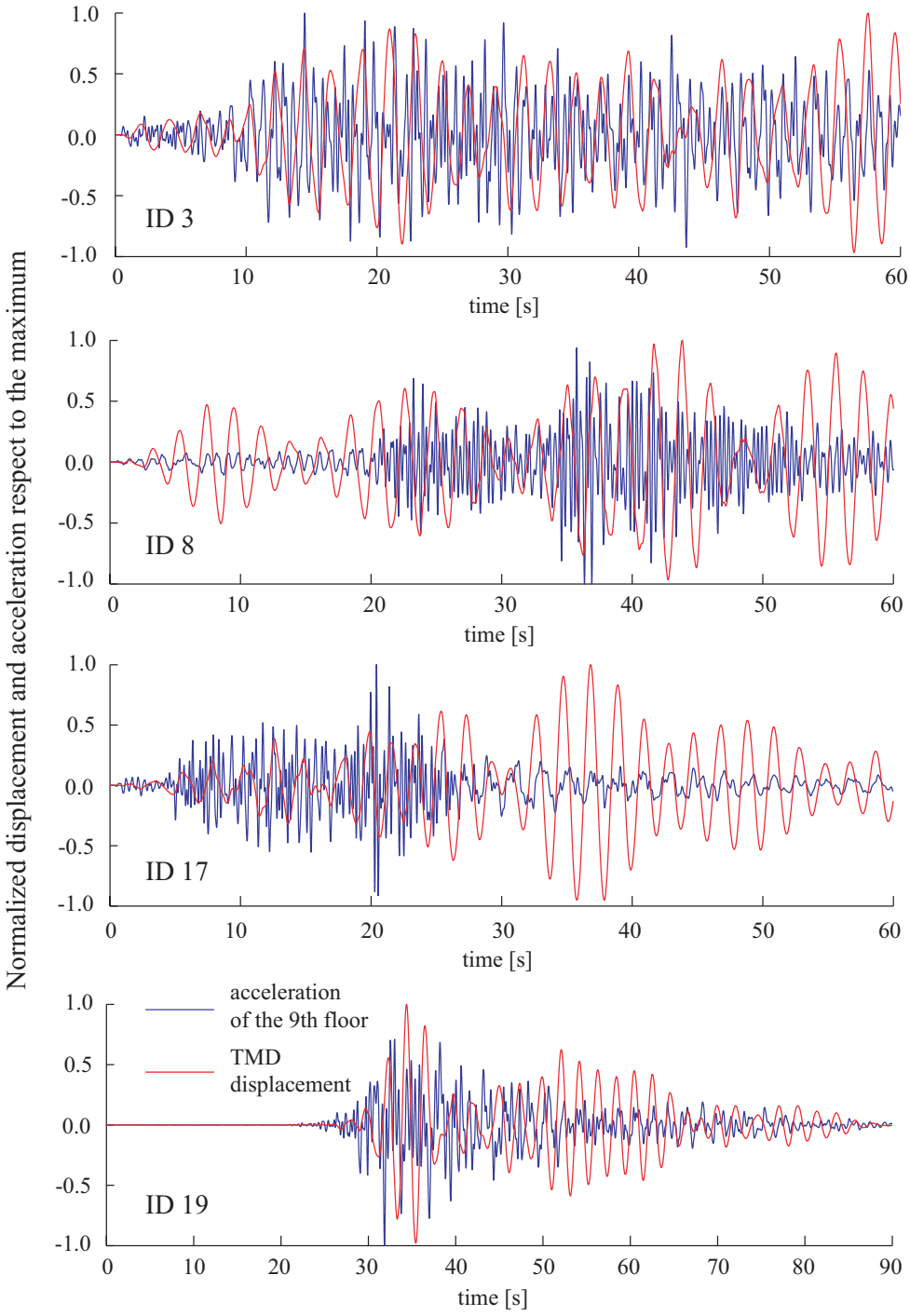

Figure 2.7 Time-histories for the acceleration of the 9th floor of the building and the displacement of the TMD. Results for four different excitations are reported (characterized through the ID numbers)

A final comparison in the results in Figure 2.5 can be made between the first and third set of ground motions. The trends reported for the synthetic ground motions (set 3) are very similar to the trends for the real ground motions (set 1). This shows that the stochastic ground motion model provides excitations with waveform characteristics similar to Chilean earthquakes, at least when evaluating efficiency of mass dampers. The importance of this will be further discussed in Chapter 6 when more information is provided for the stochastic ground motion modeling approach.

Overall the discussion in this section demonstrates the potential for mass dampers to control seismic-induced vibration for buildings in the Chilean region. The lack of pulse-like excitation, and perhaps more importantly, the longer duration of typical Chilean seismic events provide sufficient time in most instances for the mass damper to operate in its inertia mode and absorb energy from the primary structure.

3

EFFICIENT DYNAMIC ANALISYS OF LIQUID STORAGE TANKS

This chapter discusses a new numerical procedure for dynamic analysis of liquid storage tanks. Though the interest in the context of this thesis stems from analysis of TLDs the procedure is more general and is presented as such. Some discussion on the state-of-the-art in the field is first presented before moving on to the new computational procedure.

3.1 Review and Motivation

Several approaches have been proposed to model the dynamical behavior of liquid storage tanks. In earlier studies, the fluid was taken into account by adding a mass to the structure, with characteristics computed by an analytical solution based on simplified geometries (Hoskins and Jacobsen 1934). Later, Housner developed an analysis and design procedure, primarily for cylindrical and rectangular storage tanks, based on a simple mechanical model (combination of mass-spring systems with different characteristics) that represents the fluid. The computation of the physical constants in this procedure is based on the separation of the hydrodynamic behavior into two components: (1) the impulsive component that is related to the mass that

moves together with the structure; and (2) the convective component that takes into account the free surface oscillations (Housner 1957; Housner 1963). This is a broadly adopted model in civil engineering since it provides closed form solutions for the transmitted force due to the liquid sloshing, and represents the basis of many design codes, i.e. API 650 (American Petroleum Institute (API) 2003), AWWA D100 (American Water Works Association (AWWA) 2005) and the New Zealand recommendation guidelines NZSEE (Priestley et al. 1986), that establish procedures for the seismic response analysis of liquid tanks based on the linear model proposed by Housner. At the same time, it is an approximation that is based on the assumption that simplified flows can represent the actual fluid movement, restricting its use to tanks with simple geometries (such as rectangular or circular tanks).

To obtain higher accuracy solutions, various high-fidelity procedures have been also established, applicable to arbitrary tank geometries, using the Finite Element Method (FEM) to model the fluid utilizing (depending on the numerical scheme) displacement, pressure or potential variables to characterize the fluid motion. For fluid-structure interaction applications, as the equations of the structure are expressed in terms of displacements it is convenient to also express the fluid equations through displacement variables. With respect to the fluid motion modeling, such a FEM approach, based on a displacement formulation, leads to a symmetric eigenvalue problem but it produces non-zero spurious frequencies that are difficult to identify (Bermudez et al. 1997; Kiefling and Feng 1976) and suppress (Chen and Taylor 1990;

Bermudez and Rodriguez 1994). Additionally, this approach requires discretizing a vector field (displacement) instead of a scalar field (pressure or potential variables), increasing the number of degrees of freedom. In contrast, a FEM approach based on pressure or potential variables involves less unknowns, increasing the computational efficiency and avoiding physical inconsistencies (Mellado and Rodriguez 2001). In this case, the fluid-structure system leads to a non-symmetric eigenvalue problem, though it is possible to keep the symmetry if the fluid is described in a redundant way using both pressure and potential variables (Olson and Bathe 1985; Morand and Ohayon 1979; Bermudez et al. 1998). In particular, Olson and Bathe presented such a linear formulation based on velocity potentials and pressures (Olson and Bathe 1985), expanded later to take into account also gravity loads (Kock and Olson 1991). An important aspect of this formulation is its suitability for both time-history and frequency analysis of fluids with free surface. More recently, an increased number of even more complex procedures have been proposed, for example taking into account non-linear sloshing due to large free surface motions (Hernandez-Barrios et al. 2007; Frandsen and Borthwick 2003; Ali Goudarzi and Reza Sabbagh-Yazdi 2012; Ikeda et al. 2012) and including identification of damping effects introduced at the tank walls due to viscosity effects in the thin interface layer (Wang et al. 2006). However, implementation of these procedures is almost exclusively relegated to scientific and research professionals due to the complexity of the formulations and the high level of expertise required for their implementation.

Despite such high-fidelity modeling developments and advances in computer and computational science, the philosophy of the analysis methods of design codes is still based on analytical expressions and equivalent mechanical models. Though undoubtedly some practitioners are utilizing commercial software to solve multi-physic problems under seismic loads, avoiding the use of simplified models proposed by the design codes or even the complex implementation of the procedures described above, such approaches are still not widely used (presumably because a significant background is required not only in the software know-how but also in the theoretical knowledge about the involved physics). Furthermore, many traditional software packages used for seismic and structural analysis lack fluid-structure interaction modules, enforcing engineers to work with alternative packages that were not designed to perform seismic analysis. There is a gap for a methodology that is more simple and attractive than the commercial packages but still maintains the accuracy of the advanced methods presented in the literature.

The present chapter aims to develop a simplified, computationally efficient approach, utilizing a FEM modeling based on potential variables, for describing the dynamic behavior of arbitrary geometry liquid tanks. The approach takes advantage of the concept introduced recently in (Cerda 2006; Bertoglio 2007; Almazan et al. 2007) for static condensation in order to express equation of motion with respect to the free surface elevation of the liquid. It establishes, though, further simplifications in the problem (leveraging the simplified scope of the analysis here) and established a

complete numerical framework. This procedure is useful not only for the TLD-FR implementation considered in this dissertation, but also for general seismic analysis of liquid storage tanks, to bridge the gaps identified in the previous paragraph.

3.2 Development of the Simplified Sloshing Model (SSM)

A schematic diagram for the considered liquid storage tank is presented in Figure 3.1. An inertial system of reference x-z is located at the middle of the non-perturbed free surface and an auxiliary coordinate η is defined to measure the relative displacement between the free surface and the coordinate system. Let Ω represent the volume of liquid, Γ_o the non-perturbed free surface (at $z=0$), Γ_s the free surface at any time t, and Γ_p the walls and bottom surfaces (all these variables are also shown in Figure 3.1).

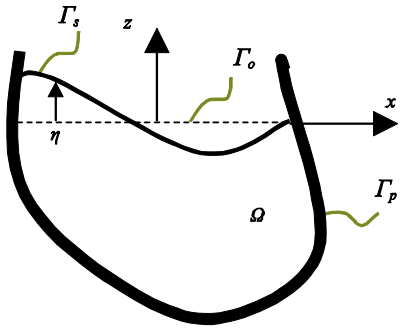

Figure 3.1 Schematic for liquid storage tank with arbitrary geometry. Various boundaries utilized in the SSM also shown.

The liquid motion is modeled using principles of Mass and Momentum Conservation, while the tank walls and bottom are considered to be rigid. The liquid is assumed to be inviscid, incompressible, and irrotational, allowing its motion to be completely defined by a velocity potential function φ. Additionally, body forces are assumed conservative and nonlinear terms are neglected. Thus, Mass and Momentum Conservation Equations take the form of Laplace and Bernoulli Equations, which are given, respectively, by (Reddy 2005):

$$\Delta\varphi = 0 \tag{3.1}$$

$$\frac{\partial \varphi}{\partial t} + \frac{p}{\rho} + \Pi + \ddot{u}_b\, x = 0 \tag{3.2}$$

where p is pressure, ρ is the fluid density, Π is the potential of the conservative forces and $\ddot{u}_b$ is the horizontal acceleration of the tank (at its base). The term $\ddot{u}_b x$ must be introduced because the motion of the liquid is expressed with respect to a coordinate system (x-z) that moves along with the tank, whereas the horizontal acceleration $\ddot{u}_b$ is expressed with respect to a fixed coordinate system [full details can be found in (Ibrahim 2005)]. It is important to notice that $\Delta\varphi$ defines the velocity of any particle of the liquid. Therefore, $\nabla\varphi \cdot \mathbf{n}$ corresponds to the velocity of the liquid projected over the normal vector $\mathbf{n}$. Two normal vectors are defined: $\mathbf{n}_o$, perpendicular to the free surface Γ_o, and $\mathbf{n}_p$, perpendicular to the tank walls and bottom. Small displacements at the free surface are assumed, in order to simplify the problem. Thus, the linearized boundary condition at the free surface is given by (Komatsu 1987):

$$\nabla\varphi \cdot \mathbf{n}_o = \frac{\partial \varphi}{\partial z} = \dot{\eta} \qquad \text{at} \qquad \Gamma_o \tag{3.3}$$

In turn, the normal velocity of the liquid at Γ_p is zero due to the rigid condition of the tank walls and bottom, and the boundary condition at Γ_p is given by (Komatsu 1987):

$$\nabla\varphi \cdot \mathbf{n}_p = 0 \qquad \text{at} \qquad \Gamma_p \tag{3.4}$$

A specific manipulation of the Laplace and Bernoulli Equations is required to combine both equations such that the sloshing dynamics could be expressed only by the elevation of the free surface. Section 3.2.1 shows the procedure based on the FEM to handle the Laplace Equation. It is important to note that Laplace Equation defines only the spatial solution, in other words, the solution for the velocity of any particle of the fluid (as a function of the walls and free surface velocities) but does not give information about how the velocities change over time. Section 3.2.2 shows how to manipulate the Bernoulli Equation to make it compatible with the Laplace Equation. The combination of these equations addresses the temporal variation, allowing for the modeling of the time-history evolution of the liquid motion. Section 3.2.3 then discusses how the shear forces transmitted by the tank to the supporting ground can be estimated. Such a connection, ultimately between the free surface elevation and the transmitted forces to the ground, allows the analysis of liquid storage tanks supported by elastic structures (which for example facilitate the analysis of TLDs). The numerical details of all these components are summarized in Section 3.2.4.

3.2.1 Laplace Equation Modification

Galerkin's Weighted Residual Method is applied to solve the Laplace Equation. In particular, Equation (3.1) is expressed in a weak formulation using ψ as a weighting function, leading to (Reddy 2005):

$$\int_{\Omega} \psi \, \Delta\varphi \, \mathrm{d}\Omega = 0 \tag{3.5}$$

Then, Green's First Identity is applied to Equation (3.5) separating this equation in two integrals, one that operates over the entire domain Ω while the other over the boundary Γ_o and Γ_p:

$$\int_{\Gamma_o} \psi \left(\nabla\varphi \cdot \mathbf{n_o} \right) \mathrm{d}\Gamma_o + \int_{\Gamma_p} \psi \left(\nabla\varphi \cdot \mathbf{n_p} \right) \mathrm{d}\Gamma_p - \int_{\Omega} \left(\nabla\psi \cdot \nabla\varphi \right) \mathrm{d}\Omega = 0 \tag{3.6}$$

Here, Equation (3.6) facilitates the introduction of the boundary conditions defined in Equations (3.3) and (3.4), leading to:

$$\int_{\Gamma_o} \psi \dot{\eta} \, \mathrm{d}\Gamma_o - \int_{\Omega} \nabla\psi^T \nabla\varphi \, \mathrm{d}\Omega = 0 \tag{3.7}$$

A typical FEM discretization (more details on this later) is then applied to the velocity potential φ, the auxiliary coordinate η and the weighting function ψ, such that:

$$\varphi(x,z,t) = \mathbf{N}\left(x,z\right)\boldsymbol{\varphi}(t) \tag{3.8}$$

$$\eta(x,t) = \mathbf{N}_{\eta}\left(x\right)\boldsymbol{\eta}_{\mathrm{s}}(t) \tag{3.9}$$

$$\psi(x,z,t) = \mathbf{N}\left(x,z\right)\boldsymbol{\psi}(t) \tag{3.10}$$

It is important to mention that $\boldsymbol{\varphi}$ is a vector built with the values of the nodal velocity potential in the volume Ω, and that $\boldsymbol{\eta}_s$ is a vector that contains the values of the nodal displacements of the free surface (here, the Greek letters in bold are used to distinguish vectors and functions, indicating vector variables when bold letters are used and scalar function when are not used). Also, $\mathbf{N}$ is the vector of interpolation functions for the velocity potential φ, while $\mathbf{N}_\eta$ is the vector of interpolation functions for the auxiliary coordinate η within the FEM scheme. In this study linear functions are adopted for both $\mathbf{N}$ and $\mathbf{N}_\eta$. By partitioning $\boldsymbol{\varphi}$ into components associated and non-associated with the free surface ($\boldsymbol{\varphi}_s$ and $\boldsymbol{\varphi}_r$, respectively), Equation (3.7) is transformed into a linear system of ordinary differential equations given by:

$$\begin{bmatrix} \mathbf{G} & \mathbf{0} \\ \mathbf{0} & \mathbf{0} \end{bmatrix} \begin{bmatrix} \dot{\boldsymbol{\eta}}_s \\ \dot{\boldsymbol{\eta}}_r \end{bmatrix} - \begin{bmatrix} \mathbf{D}_{ss} & \mathbf{D}_{sr} \\ \mathbf{D}_{rs} & \mathbf{D}_{rr} \end{bmatrix} \begin{bmatrix} \boldsymbol{\varphi}_s \\ \boldsymbol{\varphi}_r \end{bmatrix} = \mathbf{0} \tag{3.11}$$

with:

$$\mathbf{G} = \int_{\Gamma_s} \mathbf{N}_\eta{}^{\mathrm{T}} \, \mathbf{N}_\eta \, \mathrm{d}\Gamma_s \tag{3.12}$$

$$\mathbf{D} = \begin{bmatrix} \mathbf{D}_{ss} & \mathbf{D}_{sr} \\ \mathbf{D}_{rs} & \mathbf{D}_{rr} \end{bmatrix} = \int_{\Omega} \nabla \mathbf{N}^{\mathrm{T}} \nabla \mathbf{N} \, \mathrm{d}\Omega \tag{3.13}$$

The vector $\boldsymbol{\eta}_r$ is included only to complete the second block of equations, allowing to express Equation (3.11) in a matrix form. A static condensation is finally performed (Cerda 2006; Bertoglio 2007) in order to express Equation (3.11) only in terms of the surface variables, such that the condensation is defined by:

$$\mathbf{J} = \mathbf{D}_{ss} - \mathbf{D}_{sr}\mathbf{D}_{rr}^{-1}\mathbf{D}_{rs} \tag{3.14}$$

and then Equation (3.11) becomes:

$$\mathbf{G}\,\dot{\boldsymbol{\eta}}_s - \mathbf{J}\,\boldsymbol{\varphi}_s = \mathbf{0} \tag{3.15}$$

which is the final expression of the Laplace Equation, where the free elevation velocity and velocity potential of the free surface are related such that the coupling with the Bernoulli Equation is possible. It is important to notice that the static condensation introduced here [shown in Equation (3.14)] is key in this procedure because: (a) it will make possible in the next section to express the equations of motion in terms of variables whose physical meaning can be readily appreciated (vertical displacements of the liquid surface); and (b) it makes the method computationally efficient as it considerably reduces the number of variables involved.

3.2.2 Bernoulli Equation Modification

In order to solve the Bernoulli Equation, it is necessary to define the potential Π. Under this setup, the potential of volume forces is defined as $\Pi = g\,z$, where g is the gravity acceleration. The Bernoulli Equation is evaluated at the free surface, imposing $z = \eta$, $p\big|_{z=\eta} = 0$ and $\dot{\varphi}\big|_{z=\eta} \approx \dot{\varphi}\big|_{z=0}$. Then Equation (3.2) is simplified to:

$$\dot{\varphi} + g\,\eta + \ddot{u}_b\,x = 0 \quad \text{at} \quad \Gamma_s \tag{3.16}$$

Furthermore, Equation (3.16) is particularized for each node located at the free surface using the previous FEM discretization, leading to:

$$\dot{\boldsymbol{\varphi}}_s + (g\mathbb{I})\boldsymbol{\eta}_s + (\mathbb{I}\,\mathbf{X}_s)\ddot{u}_b = \mathbf{0} \tag{3.17}$$

where $\mathbb{I}$ is the identity matrix and $\mathbf{X}_s$ is a vector containing the x coordinate of each node located at the free surface. Then Equation (3.15) is introduced in Equation (3.17), leading to:

$$\mathbf{M_s}\,\ddot{\boldsymbol{\eta}}_s + \mathbf{K}_s\,\boldsymbol{\eta}_s = -\mathbf{R}_s\,\ddot{u}_b \tag{3.18}$$

with:

$$\mathbf{M}_s = \mathbf{J}^{-1}\mathbf{G}; \qquad \mathbf{K}_s = g\,\mathbb{I}; \qquad \mathbf{R}_s = \mathbb{I}\,\mathbf{X}_s \tag{3.19}$$

This numerical procedure allows expressing the dynamic behavior of liquid tanks as a second order lineal system of equations, such that the sloshing problem could be interpreted as a mass-spring system as the resultant equation of motion involves equivalent mass and stiffness characteristics. Moreover, Equation (3.18) is expressed in physical variables since it uses the base acceleration as input and the free surface elevation as the dependent variable. This ultimately allows the solution of the sloshing problem to be computed with respect to the same physical variables (displacement and acceleration) as typically used in structural modeling, circumventing the velocity potential variables. Note that the obtained solution completely characterizes the temporal variation, facilitating ultimately both time-history or (if preferred) frequency analysis.

3.2.3 Pressure on the tank walls

The methodology described previously only estimates the free surface elevation when the tank is subjected to a specific motion at its base, but does not give information about the force transmitted to the base (or the supporting structure in general). The coupling between the fluid storage tank and the support structure may be then described by the reaction force between them. This requires a proper estimation of the dynamical pressure on the walls due to the sloshing effect. For this purpose Equation (3.2) is evaluated at the tank wall and bottom in order to obtain the dynamic pressure over surface Γ_p:

$$\mathbf{P}_p = -\rho \dot{\boldsymbol{\varphi}}_p - \rho \mathbf{X}_p \ddot{u}_b \tag{3.20}$$

where $\mathbf{P}_p$, $\boldsymbol{\varphi}_p$ and $\mathbf{X}_p$ are vectors with the pressures, velocity potentials and x coordinates of the nodes located at the surface Γ_p, respectively. Then, $\mathbf{Q}$ is defined as a transformation matrix, in order to express $\boldsymbol{\varphi}_p$ as function of $\boldsymbol{\varphi}_s$, such that $\boldsymbol{\varphi}_p = \mathbf{Q}\boldsymbol{\varphi}_s$. The pressure at Γ_p is finally expressed as a function of $\ddot{u}_b$ and $\ddot{\boldsymbol{\eta}}_s$ by the combination of Equations (3.20) and (3.15):

$$\mathbf{P_p} = -\left(\rho \mathbf{Q}\ \mathbf{J}^{-1}\mathbf{G}\right)\underline{\ddot{\boldsymbol{\eta}}}_{\mathbf{s}} - \left(\rho \mathbf{X_p}\right)\ddot{u}_b \tag{3.21}$$

Nodal forces at the nodes located at Γ_p are calculated by integrating the pressure along the edge of the corresponding element (only the edge that coincides with Γ_p). The vector of the horizontal components of these nodal forces at the nodes of the i-th element is given by:

$$\mathbf{F}_p^{(i)} = \sin(\alpha_o{}^{(i)}) \int_{\Gamma_p^{(i)}} \mathbf{N}_\eta^{(i)\mathrm{T}} \mathbf{N}_\eta^{(i)} \, \mathrm{d}\Gamma_p^{(\mathrm{i})} \, \mathbf{P}_p^{(i)} \tag{3.22}$$

where $\alpha_o{}^{(i)}$ is the angle between the surface $\Gamma_p^{(i)}$ and the *x*-*y* plane. Recall that Equation (3.22) is computed considering only those elements where one of the edges coincides with Γ_p. After computing all nodal forces, the system is expressed by:

$$\mathbf{F}_p = \mathbf{R}_p \mathbf{P}_p \tag{3.23}$$

If *"m"* is the number of nodes on Γ_p the dimension of $\mathbf{R}_p$ is *"m x m"* and the dimension of $\mathbf{P}_p$ is *"m x* 1*"*. Note that an easy way to obtain the total horizontal force transmitted to the base is by multiplying $\mathbf{F}_p$ by a *"*1 *x m"* vector of ones, denoted $\mathbf{S}$ herein:

$$F_o = \begin{bmatrix} 1 & 1 & \cdots \end{bmatrix} \mathbf{F}_p = \mathbf{S}\mathbf{F}_p \tag{3.24}$$

Here, F_o represents the force transmitted to the base of the tank per unit of width (transmitted force assuming that the tank width is the 1m). Finally, the total force transmitted to the base is expressed as:

$$F_o = -\left(\rho \mathbf{S}\mathbf{R}_p \mathbf{Q}\ \mathbf{J}^{-1}\mathbf{G}\right)\ddot{\boldsymbol{\eta}}_s - \left(\rho \mathbf{S}\mathbf{R}_p \mathbf{X}_p\right)\ddot{u}_b = -\rho \mathbf{A}\,\ddot{\boldsymbol{\eta}}_s - \rho B \ddot{u}_b \tag{3.25}$$

This expression ultimately addresses the shear force between the tank and the surface on which the tank rests and can be used to provide the coupling to the supporting structure. For this coupling this force needs to be multiplied by the width of the tank *d* to convert force per unit width to actual force.

3.2.4 Summary of the Numerical Approach

This section summarizes the numerical approach for analyzing the sloshing of a liquid storage tank either on its own or when it is supported by an elastic structure (leading to a fluid structure interaction problem). An overview is presented in Figure 3.2 where the liquid storage tank is analyzed by the proposed here SSM and the support structure by a traditional analysis approach (such as FEM).

Simplified Sloshing Model (SSM): First, is necessary to define the geometry of the tank and the physical characteristics of the fluid. Then, the fluid is discretized (meshed) with respect to the equilibrium position, remarking that is not necessary to re-mesh at any step of the time integration (size of mesh is discussed later). Though any approach can be implemented for this discretization, in all applications within this Thesis the Delaunay Triangulation Algorithm (Lee and Schachter 1980) is used. Second, the FEM is applied to the fluid by computing Equations (3.12) and (3.13) to find $\mathbf{G}$ and $\mathbf{D}$. Next, the matrix $\mathbf{J}$ in Equation (3.14) is computed to condensate the equations at the free surface. Third, the equivalent model is generated by the identification of $\mathbf{M}_s$, $\mathbf{K}_s$ and $\mathbf{R}_s$ in Equation (3.18) and the eigenvalue problem (using $\mathbf{M}_s$ and $\mathbf{K}_s$) is solved to identify the natural sloshing frequencies ω_i. Note that these frequencies (as well as corresponding eigenvectors) are all real numbers which is a result of having a symmetric eigenvalue problem –proof is offered in Appendix A. The accuracy of these frequencies may be used as a criterion to select the mesh size. The original mesh should be iteratively refined and the eigenvalue problem revisited until small variations of the sloshing

frequencies of interest (typically the first few frequencies) is obtained within subsequent iterations. In general, the relative difference between the sloshing frequencies decreases exponentially when the number of elements on the mesh is increased and convergence is quickly established. After the final mesh of the fluid has been determined, damping effects can be incorporated in the formulation by selecting matrix $\mathbf{C}_s$ through any standard approach, for example by establishing a pre-specified modal damping (Clough and Penzien 1993). Finally, the resultant equation of motion [Equation (3.18)] for the liquid sloshing can be integrated in time by any conventional technique, for example through Runge-Kutta family solvers like the Dormand-Prince Method (Dormand and Prince 1980). The parameters $\mathbf{A}$ and B to estimate the transmitted force on the supporting structure can be also calculated using Equation (3.25). These parameters will be needed if the ultimate goal is to address a fluid structure interaction problem as discussed next.

Fluid-Structure Model: The coupling with the structure follows the same process as discussed in Section 2.1 for general mass dampers. In this case a model for the structure that supports the storage tank needs to be first adopted (for example through a FEM approach). This ultimately leads to evaluation of the mass $\mathbf{M}$, damping $\mathbf{C}$ and stiffness $\mathbf{K}$ matrices and of the influence vector $\mathbf{D}_o$ if we are interested in seismic excitation. The SSM and the structural model are then coupled by the dynamic pressure on the tank walls. The resultant coupling equation is a second order system of equations, which can be similarly integrated through any standard approach (as for the

equation of sloshing motion). Similarly to the application for mass dampers discussed in Section 2.1 since the input of the SSM corresponds to its base acceleration $\ddot{u}_b$, for a problem with a multi-story structure a new vector is required ($\mathbf{L_s}$) defining the location (floor) of the tank within the structure as the tank base acceleration ultimately is defined by the acceleration of that floor (further details are offered in Section 3.3.2 through an illustrative example).

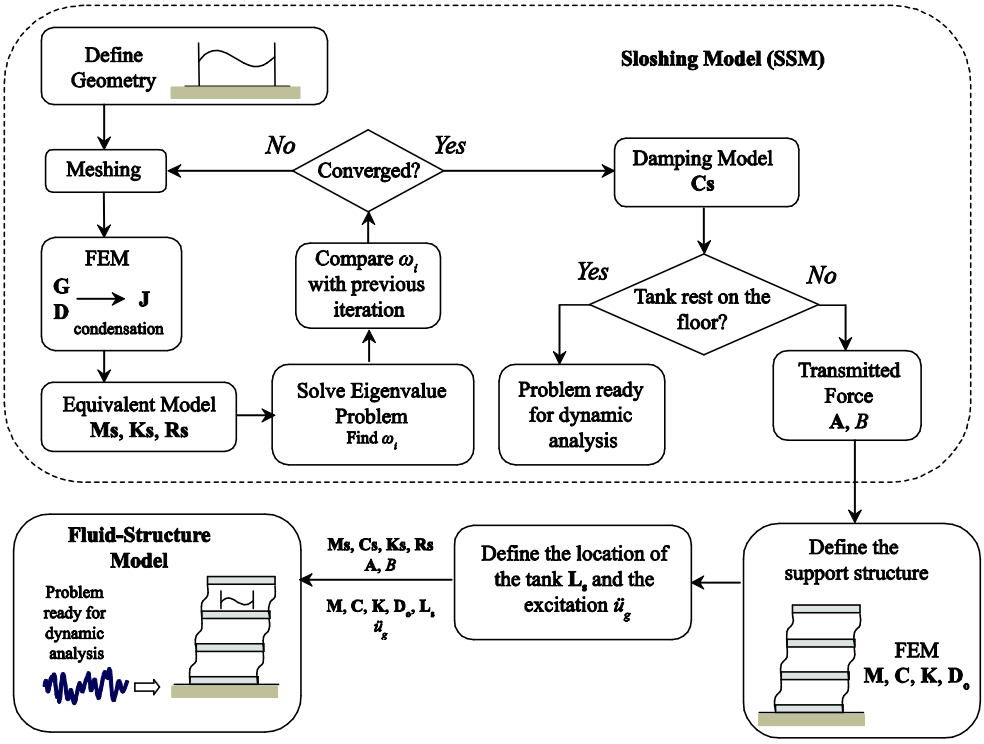

Figure 3.2 Procedure for SSM (top) and its use in fluid-structure interaction problems (bottom).Illustrative excitation in the latter case for structure corresponds to acceleration at its base.

3.3 Validation/Implementation of the Model

The validation of the SSM is considered here in a variety of two dimensional applications. The fluid inside the tank is meshed by a Delaunay Triangulation Algorithm (Lee and Schachter 1980) with the size of the triangles controlled by imposing a maximum admissible value for its side length. The equivalent model generated by the SSM ($\mathbf{M}_s$, $\mathbf{K}_s$, $\mathbf{R}_s$, $\mathbf{A}$ and B) is evidently affected by the quality of the mesh, and the refinement procedure described in Section 3.2.4 is implemented to adaptively choose the mesh size. Convergence is defined when the variation in the first sloshing frequency is smaller than 1% (this applies to all cases studied).

3.3.1 Tanks Resting on the Ground

In this section, harmonic and earthquake excitations are imposed to different tank geometries. The characteristics of these geometries have been already presented in Section 2.3. The fluid response obtained by the SSM, the Housner Model and a full FEM implementation through the commercial software ANSYS (ANSYS 2007) are compared in terms of accuracy and computational efficiency. The tank walls and bottom are considered rigid and the liquid used is water. Before moving forward, a brief review of the Housner Model and ANSYS implementation is given.

Housner Model: as described earlier this approximate model is typically used for describing the sloshing in tanks with simple geometries (primarily cylindrical and rectangular tanks that lead to closed form solutions for all quantities of interest).

Sloshing is modeled by a linear system formed by a group of masses that are attached to the walls. The first mass (named impulsive mass) is attached rigidly to the tank walls and moves along with the base. The additional masses (named convective masses) are attached to the walls by linear springs. When only one such mass is added, it approximates explicitly the effect of the fundamental sloshing mode. The transmitted force to the ground is calculated as the sum of the force generated by the impulsive mass and the force that the springs transmit to the wall due to the movement of the convective masses. The most common implementation (and the one that is used in the present work) of this procedure only takes into account one impulsive and one convective mass, such that the effect of the higher modes are neglected and the equivalent system is defined only with a single degree of freedom. The linear spring stiffness, the impulsive and convective mass values are then given in a closed form as described in (Housner 1963), which is the reason why this model is primarily used to approximate the fundamental sloshing mode of simple tank geometries.

ANSYS implementation: the element FLUID79 is used in the analysis, which consists of a modification of a plane element to model solid structures. It uses 4 nodes with 2 degree of freedom on each node, where the degrees of freedom are the horizontal and vertical displacements of the node (ANSYS 2007). The tank walls and bottom are not discretized since they are considered non-deformable. The mesh is refined in the same way as for the SSM to obtain a variation in the fundamental sloshing frequencies smaller than 1%. To facilitate the transient analysis, a reduced model

approximation is adopted defining the nodes on the walls, bottom and free surface as master nodes. In contrast to the SSM (in which the equations are reduced to use only the free surface nodes), the reduced ANSYS model requires explicitly the use of all border nodes (free surface, walls and bottom nodes) to impose the boundary and initial conditions. This ultimately increases the computational time since ANSYS is enforced to use more degrees of freedom than the SSM. The fluid displacements at the tank walls and bottom are constrained such that the fluid movement is parallel to the surface.

Case Study: Rectangular Tanks

A rectangular tank (Figure 2.3) fixed to the ground is considered first. Table 3.1 presents the fundamental sloshing period of a specific geometry (L=9.144m and R=0.5) calculated via three different methods. The first method is the analytical solution presented in (Chen et al. 1996), which is valid only for rectangular tanks. The second method is the Housner Model (used only for approximating the fundamental mode) and the third method corresponds to the SSM. The three methods predict essentially the same fundamental sloshing period. Table 3.1 also includes higher sloshing periods computed by the analytical solution and by the SSM, which are also very similar to each other (differences are in all cases less than 1%). The ANSYS estimation is not included here since the availability of an analytical solution is considered more appropriate to compare the sloshing frequencies obtained by the SSM (the ANSYS model will be used later only in the time-history analysis comparison).

In order to investigate the behavior of the sloshing periods for different rectangular tank dimensions, iso-period curves are plotted in Figure 3.3, Figure 3.4 and Figure 3.5 calculated by all three aforementioned approaches (Housner model used only for fundamental period). The value of the tank length L varies between 1m and 6m while the aspect ratio R varies between 0.2 and 2.0. For the tank dimensions studied, the fundamental sloshing period depends only on L if the aspect ratio is greater than 0.8 (Figure 3.3). The second and third sloshing periods are, though, practically independent of the aspect ratio as shown in Figure 3.4 and Figure 3.5, respectively. In other words, the sloshing periods of a rectangular tank is independent of the water depth unless R<0.8. For all cases presented, the maximum error found is less than 1.1% when the sloshing periods of the analytical and the SSM solutions are compared.

Table 3.1 Sloshing periods for a rectangular tank with L=9.144m and R=0.5

	Analytic Solution (Chen et al. 1996)	Housner Model	SSM
Fundamental Period [s]	3.5755	3.5834	3.5734
Second Sloshing Period [s]	1.9771	-	1.9698
Third Sloshing Period [s]	1.5314	-	1.5158

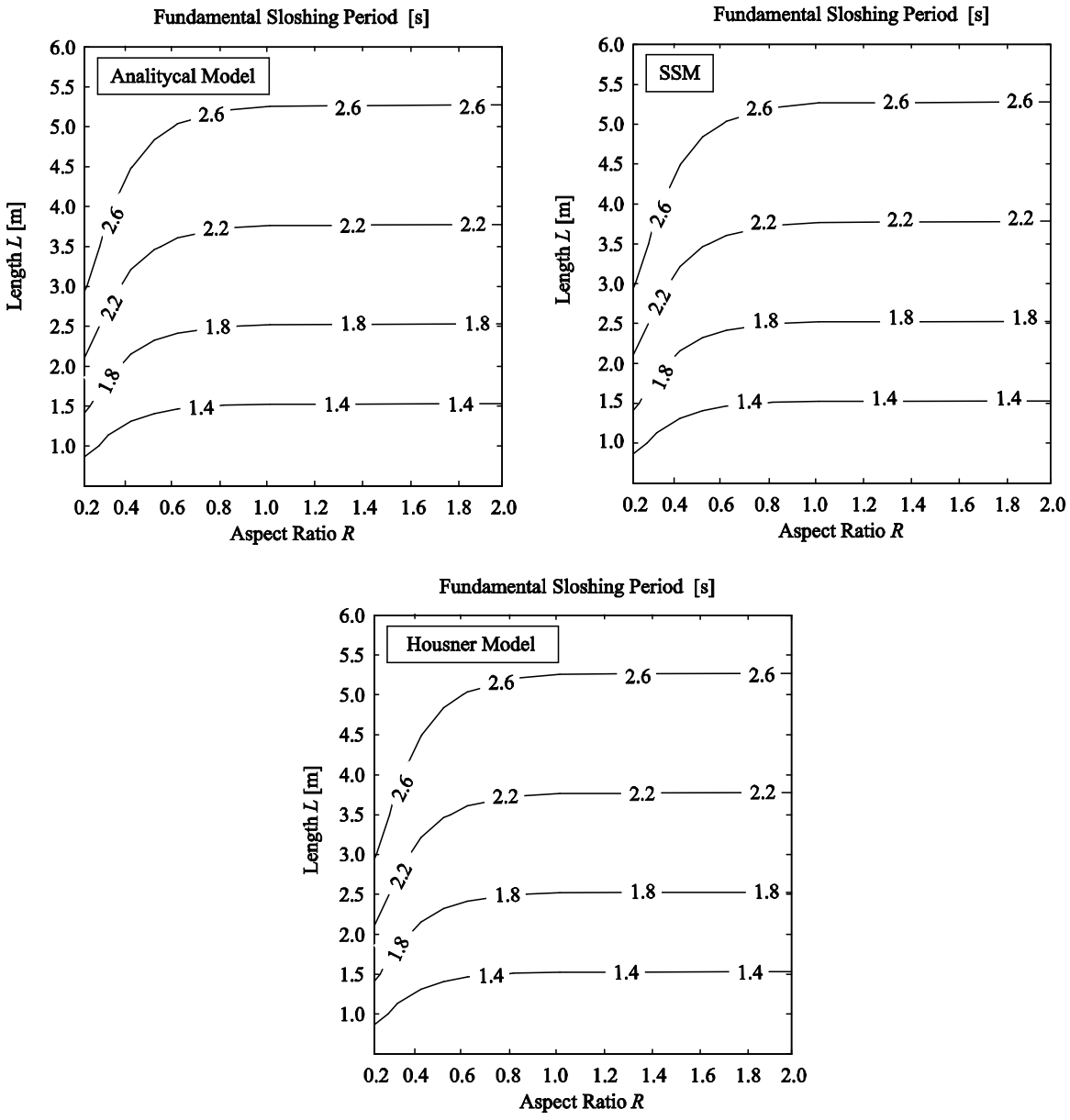

Figure 3.3 Fundamental sloshing period of rectangular tanks as a function of length L and aspect ratio R. Comparison between the SSM, Housner model and analytic solution of (Chen et al. 1996) is shown.

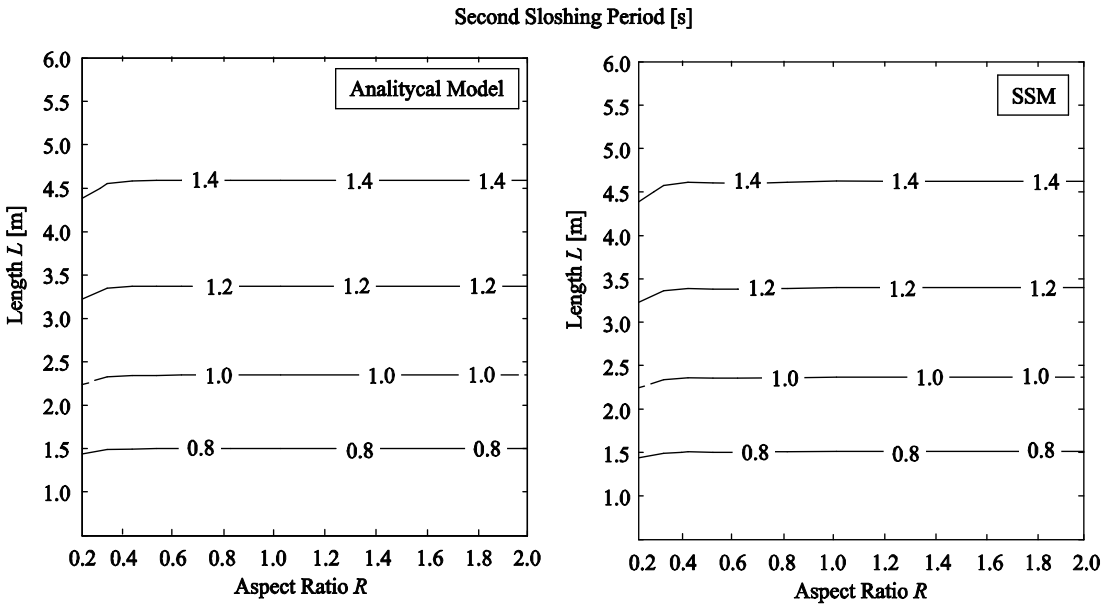

Figure 3.4 Second sloshing period of rectangular tanks as a function of length L and aspect ratio R. Comparison between the SSM and analytic solution of (Chen et al. 1996) is shown.

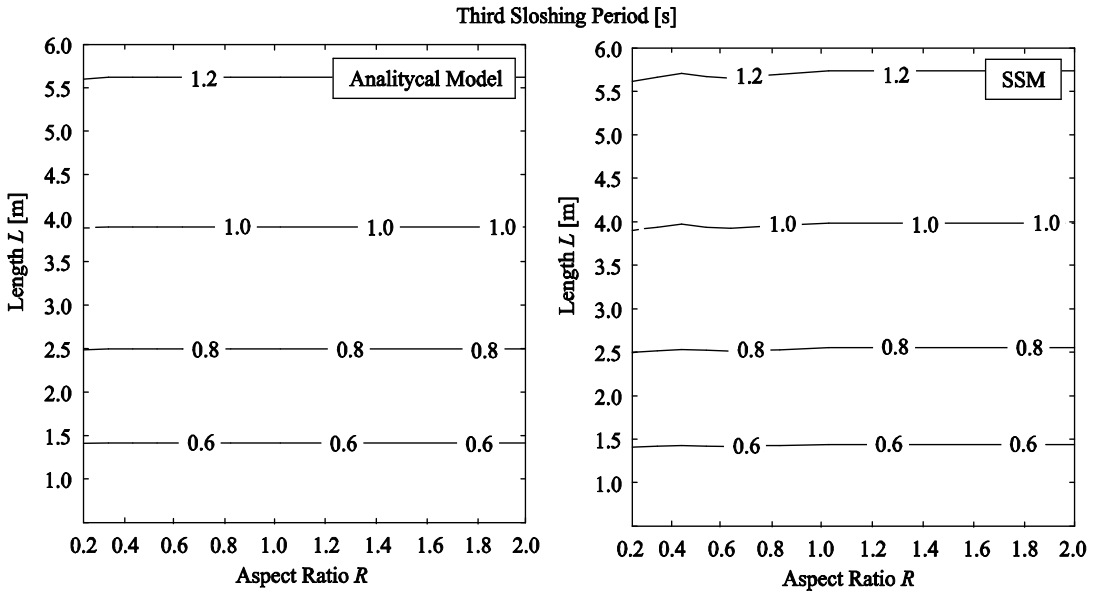

Figure 3.5 Third sloshing period of rectangular tanks as a function of length L and aspect ratio R. Comparison between the SSM and analytic solution of (Chen et al. 1996) is shown.

The harmonic response is then studied by imposing harmonic accelerations at the base of the tank. Here, the Normalized Transmitted Force and the Period Ratio are utilized to examine the results, defined, respectively, as:

$$F_n = \frac{\left|F(t)\right|_{max}}{m_{liq}\left|\ddot{u}_g(t)\right|_{max}} \tag{3.26}$$

$$r_{sp} = \frac{T_{exc}}{T_{slo}} \tag{3.27}$$

where m_{liq} is the total mass of liquid, T_{exc} is the excitation period and T_{slo} is the fundamental sloshing period. The Normalized Transmitted Force is an indicator of the force amplification due to the sloshing effects. In a sloshing tank, part of the liquid mass moves together with the walls (impulsive component) and part moves together with the free surface (convective component). Notice that F_n=1 corresponds to a system for which the sloshing effect is non-important since all the liquid mass moves together with the walls. In these systems, the liquid could be modeled by a rigid solid of mass m_{liq}. If F_n is higher than 1 then the sloshing increase the total force transmitted to the base, and if F_n is lower than 1 then the opposite behavior occurs.

The numerical analysis is conducted with a tank of length L=9.144m and results are presented for three different aspect ratios, R=0.3, R=0.5 and R=1. The liquid is assumed to have 0.5% modal damping while the excitation period varies between 0.1 and 2.0 times the fundamental sloshing period. It is observed that for r_{sp}>>1, the normalized transmitted force is close to 1 so the convective component is not

important. The maximum value of F_n is reached when the excitation and the fundamental sloshing periods are close ($r_{sp} \approx 1$) which is expected since this condition corresponds to resonance for the liquid. On other hand, the minimum value of F_n is reached when $r_{sp}<1$. In this case, the impulsive mass moves at the same phase as the excitation but the convective mass moves with a 180 degrees phase difference with respect to the excitation. Then, the forces related to the impulsive and convective masses counteract each other leading to a reduced force transmitted to the ground, Figure 3.6.

The SSM and the Housner Model predict similar values of F_n when the period ratio is close to 1. The SSM additionally provides local maxima of F_n located at the second and third sloshing periods. The Housner Model is of course not capable of estimating these local maxima since it only takes into account one degree of freedom. It is also evident that the differences between the models depend not only on the period ratio r_{sp} but also on the aspect ratio R. The biggest differences occur when the aspect ratio R is small and the excitation period is close to the second and third sloshing periods, that is, in Figure 3.6, the difference between the model responses is much more dramatic when R=0.3 and $r_{sp}<1$ (Figure 3.6a), while the differences decrease when the aspect ratio R increases (Figure 3.6b and Figure 3.6c).

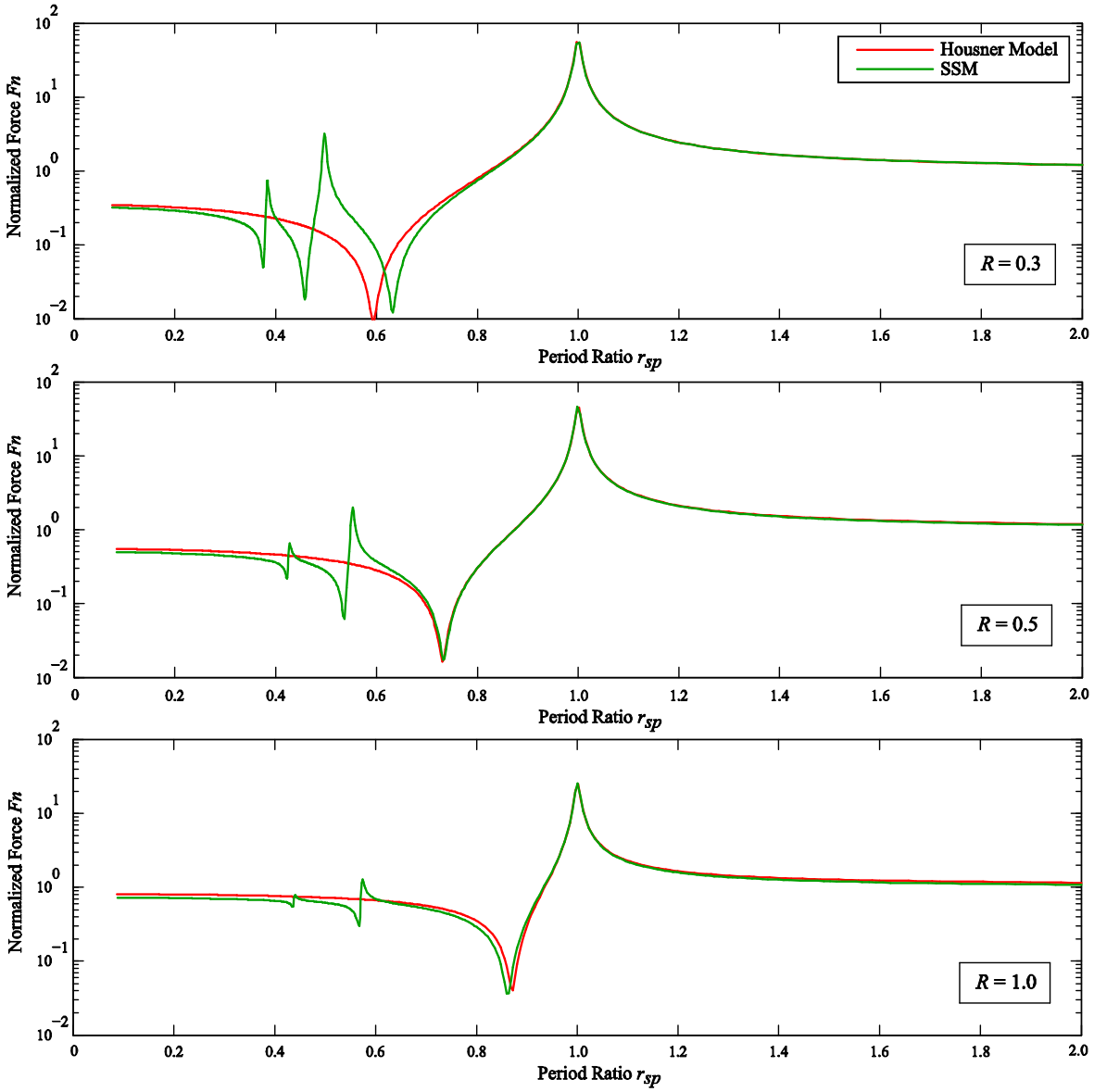

Figure 3.6 Normalized transmitted force to the walls of a rectangular tank, with L=9.144m for different values of R under harmonic response for different period ratios r_{sp} (excitation period to fundamental sloshing period)

The seismic response of the liquid tank is finally studied by imposing two different ground motions: the 1940 El Centro earthquake (Component S90W) and the 1985 Mexico City SCT1 record (Component N90W). These seismic excitations are chosen to directly compare the SSM with the model implemented by (Chen et al. 1996), in which a finite difference scheme is applied to resolve the non-linear and linear sloshing problem, where the non-linearities are primarily related to the second order differential terms that appear in the Bernoulli Equation and the border conditions at the free surface due to large sloshing amplitudes. In (Chen et al. 1996) modal damping of 5% was assumed for the analysis, and the same value is adopted here for the Housner and SSM models and for the ANSYS implementation. An interesting result mentioned by (Chen et al. 1996) is that the linear theory predicts the transmitted force relative well compared to the non-linear model. Results are provided in

Table 3.2: the SSM provides good agreements with the Linear Model and the FEM through ANSYS while the accuracy of the Housner Model shows a significant excitation dependency. The average computational time required to conduct the time-history analysis on a PC with a 3.3 GHz Xeon quad processor and 8GB RAM is 0.5s, 6.8s and 738s for the Housner Model, the SSM and ANSYS simulation, respectively. This shows that the proposed SSM offers high accuracy results with a remarkable computational efficiency.

Table 3.2 Comparison of transmitted force to the ground obtained by different methods for the considered rectangular tanks under different earthquake excitations

Maximum Transmitted Force to the Ground [kN]					
Earthquake Record	Non-linear Model (Chen et al. 1996)	Linear Model (Chen et al. 1996)	Housner Model	SSM	ANSYS
El Centro	52.32	51.40	53.92	50.21	51.72
Mexico City	48.70	47.52	36.20	47.19	47.93

Case Study: Non-Rectangular Tanks

Extending now the comparison to non-rectangular tanks, three different types of tanks are chosen to compare the fundamental sloshing period obtained by the SSM with experimental results found on previously published studies (Idir et al. 2009; Gardarsson 1997). The tank geometries used here correspond to W-Type, U-Type and V-Type described earlier in Figure 2.4.Five different tank configurations are used in the analysis, with each tank identified by a letter and geometry specification as presented in Table 3.3. The geometry of tanks A and B were obtained from (Idir et al. 2009) while the geometry of tanks C, D and E were obtained from (Gardarsson 1997).

Table 3.3 Details of the tank geometries selected from (Idir et al. 2009) and (Gardarsson 1997) and used here

Tank ID	Tank Type	L[mm]	H[mm]	a[mm]	h[mm]	Total water mass [kg]
A	W-type	380	76	52.62	50	0.594
B	U-type	380	76	137.38	50	0.594
C	V-type	590	40	250	144.34	2.134
D	V-type	590	70	250	144.34	4.954
E	V-type	590	100	250	144.34	8.817

Table 3.4 Fundamental sloshing period [in s] for the considered non-rectangular tanks

Tank ID	SSM	ANSYS	Experimental
A	1.226	1.183	1.024[1]
B	0.953	0.984	0.970[1]
C	0.779	0.832	0.7805[2]
D	0.904	0.976	0.9412[2]
E	1.022	1.115	1.0667[2]

[1] Obtained from (Idir et al. 2009)

[2] Obtained from (Gardarsson 1997)Table 3.4 presents the comparison between the fundamental sloshing period obtained by the SSM, ANSYS and the experiments conducted in the aforementioned two studies. The period obtained by the SSM and the experimental tests are in good agreement for all geometries with the maximum

difference being close to 4%, except for tank A for which the difference is higher. The study (Idir et al. 2009) also reported significant differences between the experimental and numerical value of the fundamental sloshing period for this tank. A reason of this difference is a potential inaccuracy in the experimental details provided. With respect to the computational time required to calculate the sloshing periods presented in Table 3.4, the slowest calculation time (this corresponds to Tank A) is 5.2sec using the SSM and 78sec using ANSYS. Note that these calculation times do not take into account the time used to remesh the domain in the convergence process. This further validates the previous claims for the computational efficiency of the SSM.

As discussed in Section 3.1 the computational efficiency/simplicity of the SSM can be exploited to further perform sensitivity studies of such non-rectangular tanks, which is one of the motivations for establishing this new approach. An interesting related question is to identify how variations of critical characteristics affect the fundamental sloshing period. In particular, the change of the fundamental sloshing period due to variations in $\bar{a}$ and $\bar{h}$ for a W- and U-Type Tank (both with L=380mm and H=76mm) is presented in Figure 3.7. Results show that the sloshing period of the W-Type tank exhibits greater variations in comparison to the U-Type Tank. Also, a variation of $\bar{h}$ has greater effect on the sloshing period than a variation of $\bar{a}$. This discussion shows the utility of the established methodology in examining the behavior of tanks with different geometric characteristics.

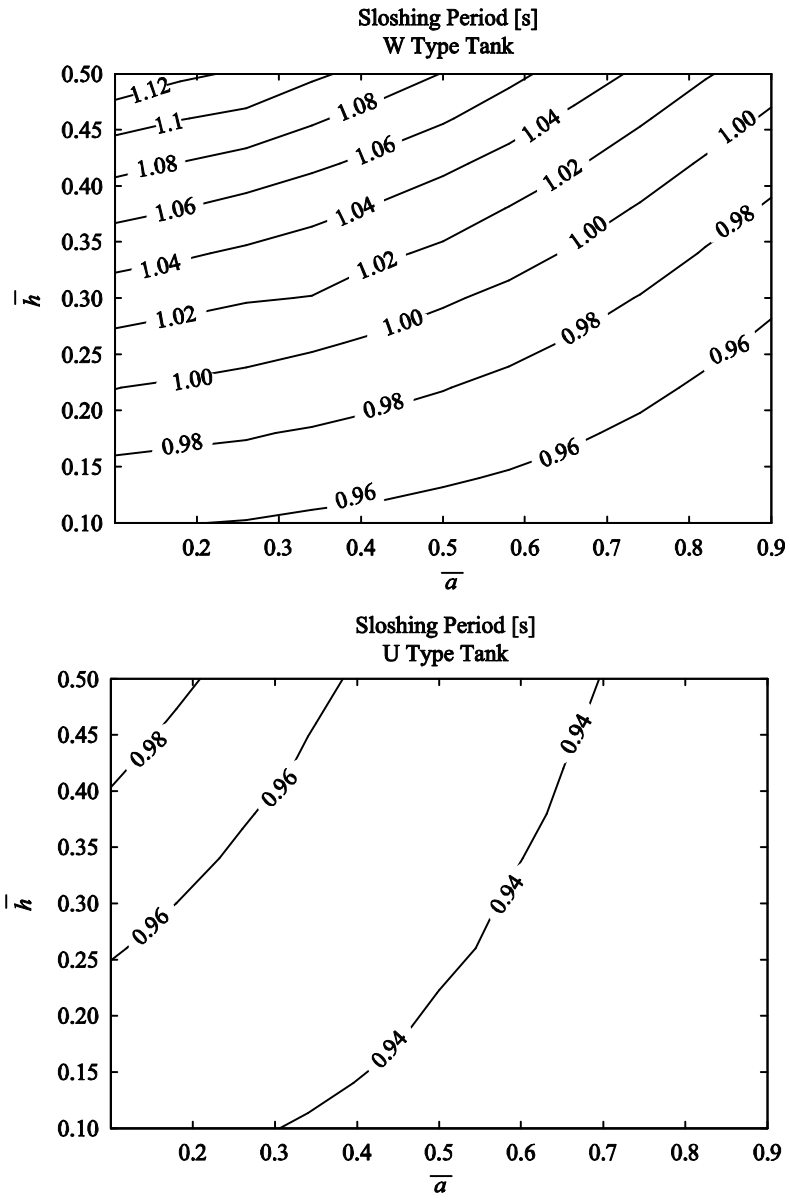

Figure 3.7 Sloshing period as a function of $\overline{a}$ and $\overline{h}$ for W- and U-type tanks. Cases correspond to L=380mm and H=76mm

The final step for the validation of the SSM for non-rectangular tanks is to evaluate its accuracy for time-history analysis. For this reason, the seismic response of tanks A and B is finally examined for the same ground motions considered previously for

rectangular tanks. Again, it is assumed that the modal damping of the liquid is 0.5%.In particular, the time-history of the transmitted force obtained by the SSM and ANSYS are compared in Figure 3.8. The maximum transmitted force predicted by both methods is practically the same for the cases studied (but with a computational time required by ANSYS greater by a factor of 300 compared to the SSM), further validating the accuracy of the new model. It is interesting to note that even though both tanks (A and B) have the same volume of water and the same external dimensions (H and L), meaning same space requirements, tank A exhibits lower sloshing amplitudes that lead ultimately to smaller forces acting on the walls. The difference in the transmitted force is related to the amount of water that moves (convective mass) and does not move (impulsive mass) inside the tank, features that ultimately depend on the tank geometry. For maximizing (or minimizing, depending on the application of interest) this force an optimization problem can be further formulated by changing the tank geometry, something that can be easily facilitated through the computational efficiency of the SSM.

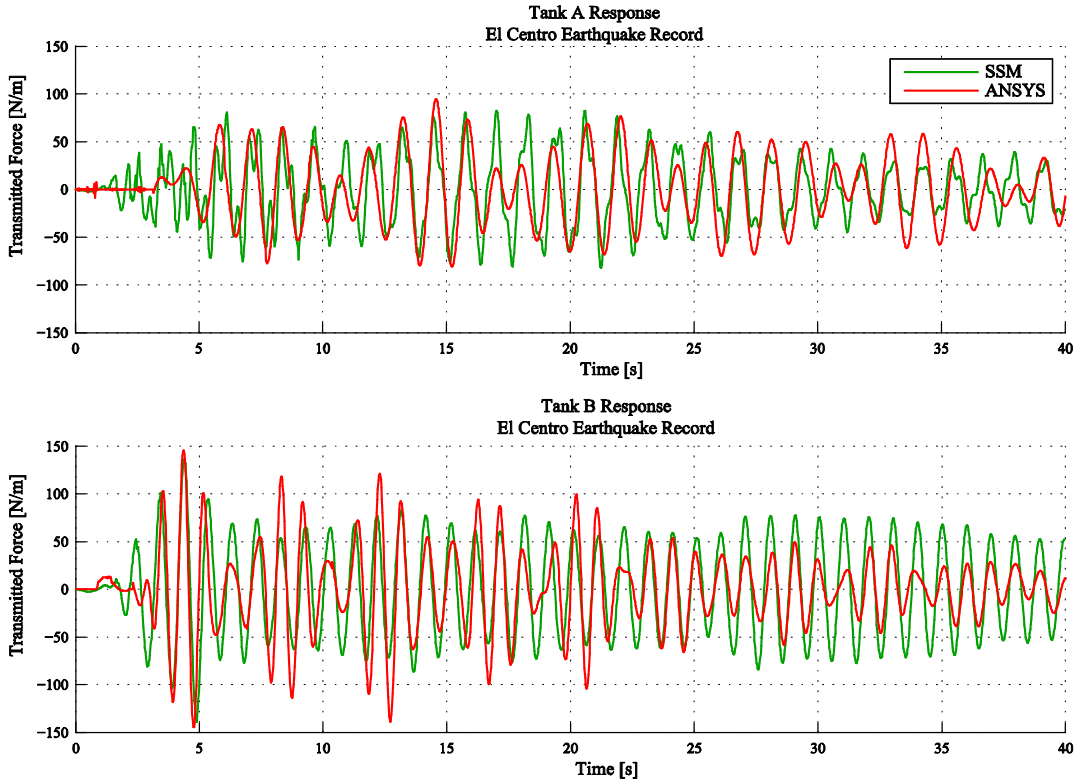

Figure 3.8 Seismic response histories (expressed through the transmitted force to the base) of non-rectangular tanks A and B under El Centro excitation

3.3.2 Tank Supported by a Linear Structure

The SSM can be readily implemented to evaluate the behavior of Tuned Liquid Dampers (TLD) which is the ultimate goal within this dissertation. This implementation, corresponding ultimately to a liquid tank located on an elastic structure, is examined here. In this case the numerical model needs to capture the fluid-structure interaction with a high level of accuracy. An elastic structure with a TLD on top is thus studied to determine the effectiveness of SSM to simulate the response of these type of systems.

The numerical scheme for this evaluation was presented earlier in Figure 3.2. Each TLD is assumed to be tuned to the fundamental period of the structure.

The chosen structure corresponds to the linear 9-story benchmark building presented by (Ohtori et al. 2004). This building was first modeled in a commercial software and then the mass and stiffness matrix were condensed at the lateral floor displacements producing a planar model with 9 translational degrees of freedom. The first four natural periods were calculated to correspond to 2.10s, 0.80s, 0.47s and 0.32s. Also a 2% of modal damping is assumed for the structure for all modes of vibration. The equation of motion for the coupled TLD-structure system is obtained following the procedure described in Section 3.2.4 [that is, Equation (2.8)], simply substituting the force from the mass damper initially described by Equation (2.6) with the product of the tank width d with the force per width transferred by the tank given by Equation (3.25), and results ultimately to:

$$\begin{bmatrix} \mathbf{M}+\mathbf{L}_s^{\mathrm{T}}\,dB\,\mathbf{L}_s & \mathbf{L}_s^{\mathrm{T}}\,d\mathbf{A} \\ \mathbf{R}_s\,\mathbf{L}_s & \mathbf{M}_s \end{bmatrix} \begin{bmatrix} \ddot{\mathbf{u}} \\ \ddot{\underline{\boldsymbol{\eta}}}_s \end{bmatrix} + \begin{bmatrix} \mathbf{C} & 0 \\ 0 & \mathbf{C}_s \end{bmatrix} \begin{bmatrix} \dot{\mathbf{u}} \\ \dot{\underline{\boldsymbol{\eta}}}_s \end{bmatrix} + \begin{bmatrix} \mathbf{K} & 0 \\ 0 & \mathbf{K}_s \end{bmatrix} \begin{bmatrix} \mathbf{u} \\ \underline{\boldsymbol{\eta}}_s \end{bmatrix} = -\begin{bmatrix} \left(\mathbf{M}+\mathbf{L}_s^{\mathrm{T}}\,dB\,\mathbf{L}_s\right)\mathbf{D}_o \\ \mathbf{R}_s \end{bmatrix} \ddot{u}_g \tag{3.28}$$

where the mass $\mathbf{M}$, damping $\mathbf{C}$ and stiffness matrix $\mathbf{K}$ of the structure, the displacement of each story relative to the ground $\mathbf{u}$, the influence coefficient vector $\mathbf{D}_o$, in this case corresponding to a nine-dimensional vector (number of degrees of freedom of the planar structural system) of ones, and the location vector $\mathbf{L}_s$ are defined in the same

way as in Section 2.1, specifically Equation (2.8). The TLD is assumed to be at the top of the building leading to $\mathbf{L}_s$ as a vector of zeros with the 9th element being equal to 1 so that $\mathbf{L}_s\mathbf{u}=u_9$, where u_9 represents the lateral displacement of the top floor (which is the floor that contains the TLD in this case).

A Rectangular Tank and U-Type Tank are used as TLDs. The fundamental sloshing period of both tanks is tuned to the fundamental period of the structure, while the total mass of water (defining the width of the tank) is fixed as 2% of the total mass of the structure. Additionally, the damping matrix $\mathbf{C}_s$ is defined so that a 0.5% of modal damping is obtained for the fluid.

The SSM is utilized here to predict the response of the structure and is compared against the predictions provided by ANSYS or the Housner model. Before describing the comparisons the coupling of the latter two models with the structural model is briefly discussed. The coupling of the Housner Model with the structure is realized by equation (3.28) but taking into account the following modifications: i) the impulsive mass is added to the mass matrix element $\mathbf{M}_{9,9}$ due to the 9th floor which contains the TLD; ii) B, $\mathbf{A}$ and $\mathbf{R}_s$ are now scalars and all equal to the convective mass, iii) $\boldsymbol{\eta}_s$, $\mathbf{K}_s$ and $\mathbf{C}_s$ are also scalars, $\boldsymbol{\eta}_s$ represents only the movement of the convective mass (not the elevation of the free surface), $\mathbf{K}_s$ is defined by the spring proposed by Housner whereas $\mathbf{C}_s$ is similarly defined to correspond to 0.5% of modal damping. For ANSYS, the characteristics of the analysis are similar to those described in Section 3.3.1, the only

difference being that the TLD is now supported by a frame structure which is modeled using the elements BEAM3 and PLANE42. Spurious frequencies are expected in this case since the formulation is based on displacement variables (Bermudez et al. 1997; Kiefling and Feng 1976) as indicated in (ANSYS 2007). Many spurious frequencies were indeed observed between the first three sloshing frequencies, with the problem ultimately resolved by adopting a modal reduction (Ray Clough and Penzien 1993) to reduce the computational burden (i.e., the time needed by ANSYS to integrate the equations of motion).

Case study: Rectangular Tuned Liquid Damper

As illustrated in Figure 3.3 earlier, it is possible to find many different combinations of R and L that result in the same fundamental sloshing period. For this illustrative application the dimensions of the tank are chosen as R=0.6 and L=3.29m, satisfying the tuning requirements to the fundamental structural period. The building is subjected to the El Centro ground motion and results are presented for the response of floors 3, 6 and 9 of the structure. The floor displacements and absolute accelerations are presented in Figure 3.9 and Figure 3.10, respectively, where the blue line is obtained by solving Equation (3.28) and the red line is obtained by using ANSYS. The results show that the TLD modeled by the SSM or ANSYS generate similar responses. Table 3.5 then presents the floor peak response values (accelerations and displacements) obtained by the different methods examined. All approaches yield similar results, verifying their

accuracy, whereas in general good efficiency is obtained by incorporation of the TLD in reducing the structural response (compare the results with and without the TLD). It should be stressed that the differences observed between the ANSYS and the SSM may be attributed to the contribution of higher sloshing modes that cannot be taken into account in the ANSYS model due to the modal reduction implemented.

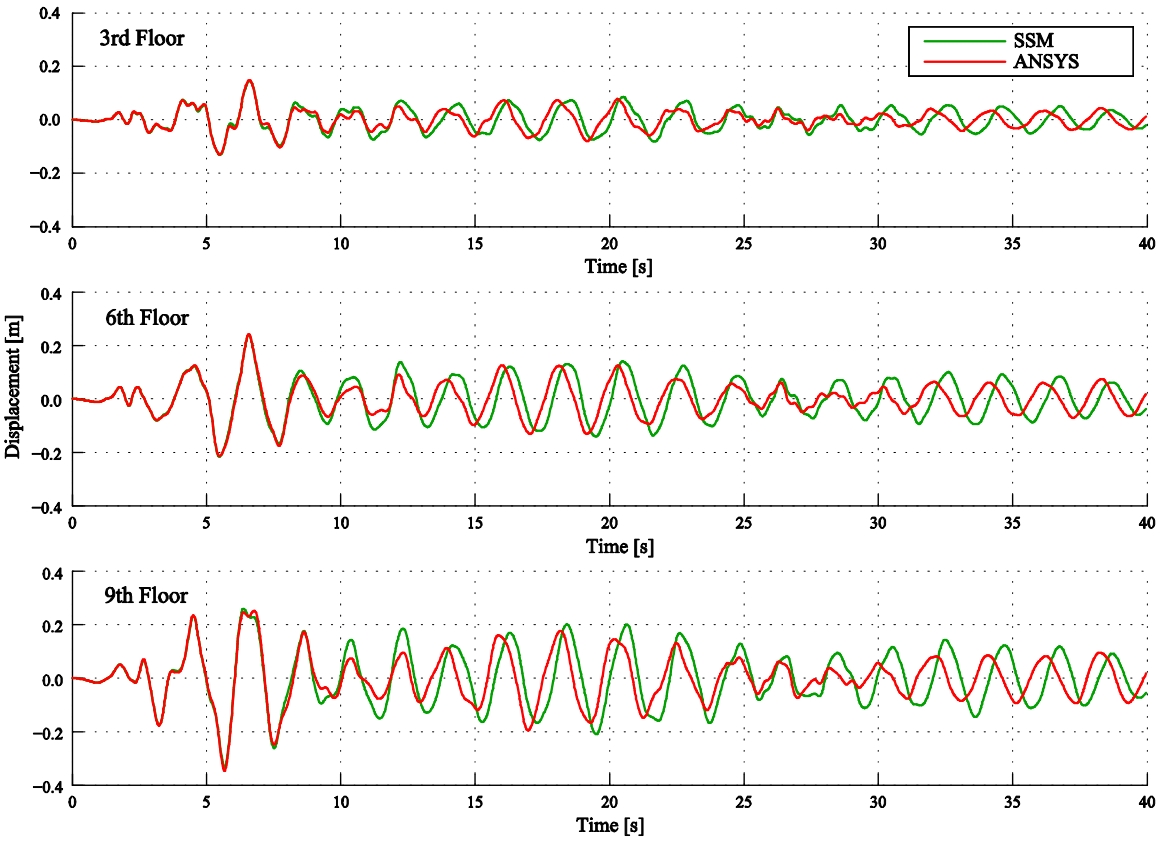

Figure 3.9 Displacement response of the 9-floor building with a rectangular TLD under seismic excitation

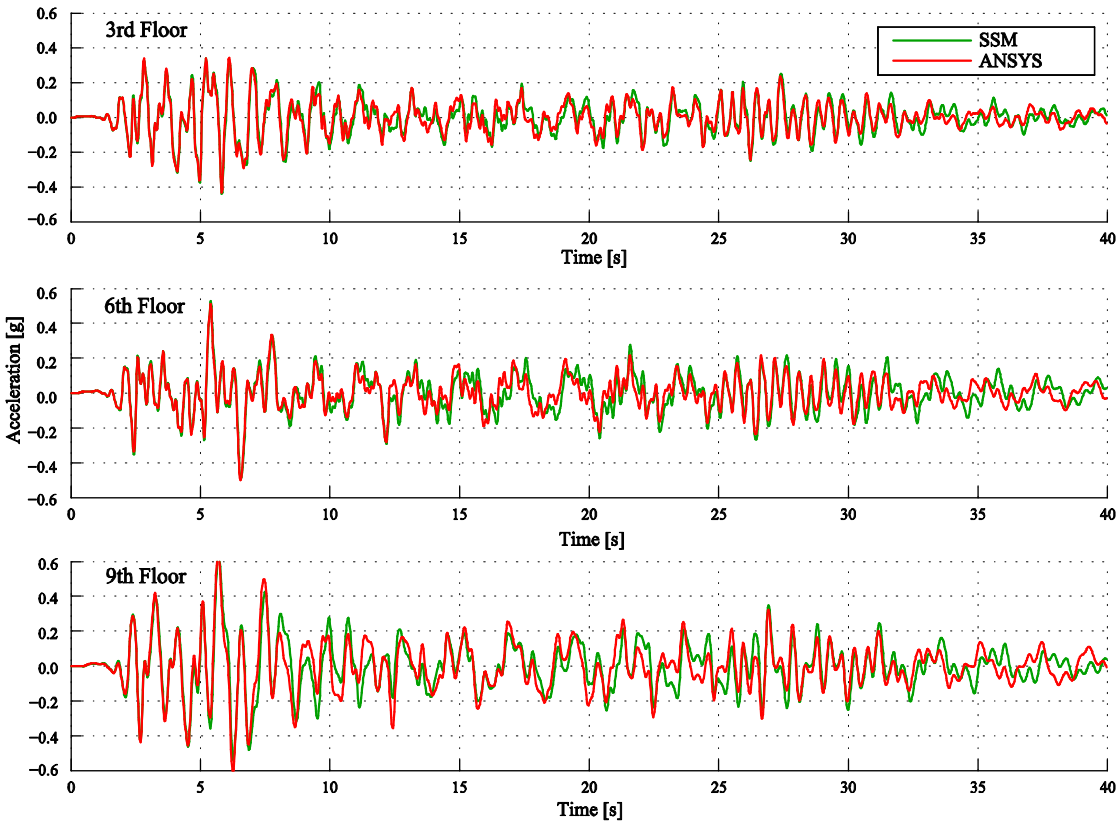

Figure 3.10 Acceleration response of the 9-floor building with a rectangular TLD under seismic excitation

Table 3.5 Peak response values of the 9-floor structure with a rectangular TLD under seismic excitation

	Peak Displacement [m]				Peak Absolute Acceleration [g]			
	Without TLD	Housner	SSM	ANSYS	Without TLD	Housner	SSM	ANSYS
3rd floor	0.1664	0.1470	0.1452	0.1475	0.4087	0.4351	0.4399	0.4316
6th floor	0.2745	0.2401	0.2394	0.2412	0.5400	0.5198	0.5277	0.5108
9th floor	0.3723	0.3350	0.3321	0.3381	0.7041	0.6510	0.6481	0.6550

Case study: Non-rectangular Tuned Liquid Damper

The same analysis is implemented for the structure equipped with a U-Type TLD with dimensions of R=0.625, L=3.29, $\overline{a}$ =0.5, $\overline{h}$ =0.3. The time history is only compared with the results obtained by ANSYS in Figure 3.11 and Figure 3.12 (since the Housner Model is not applicable for such tank geometries). Results are also reported in Table 3.6 which shows good agreement between the SSM and ANSYS. Moreover, the behavior estimation of the building with a rectangular TLD and non-rectangular TLD are similar since the geometries are not significantly different. For both TLD geometries, the SSM estimates 10% on peak displacement reduction and 8.0% on peak acceleration reduction when the time-histories of the building with and without TLD are compared. For this case, comparative analysis in terms of computational time are not presented since the fluid-interaction using the SSM and ANSYS operate under different conditions: while ANSYS applied the FEM to the whole problem (TLD and building together), the fluid-structure analysis using the SSM requires to have the structure already modeled (on the implementation, the structural model of the building is taken as an input and not as part of the calculation).

Overall the discussion shows the computational efficiency of the proposed method for evaluating the behavior of structures equipped with TLDs.

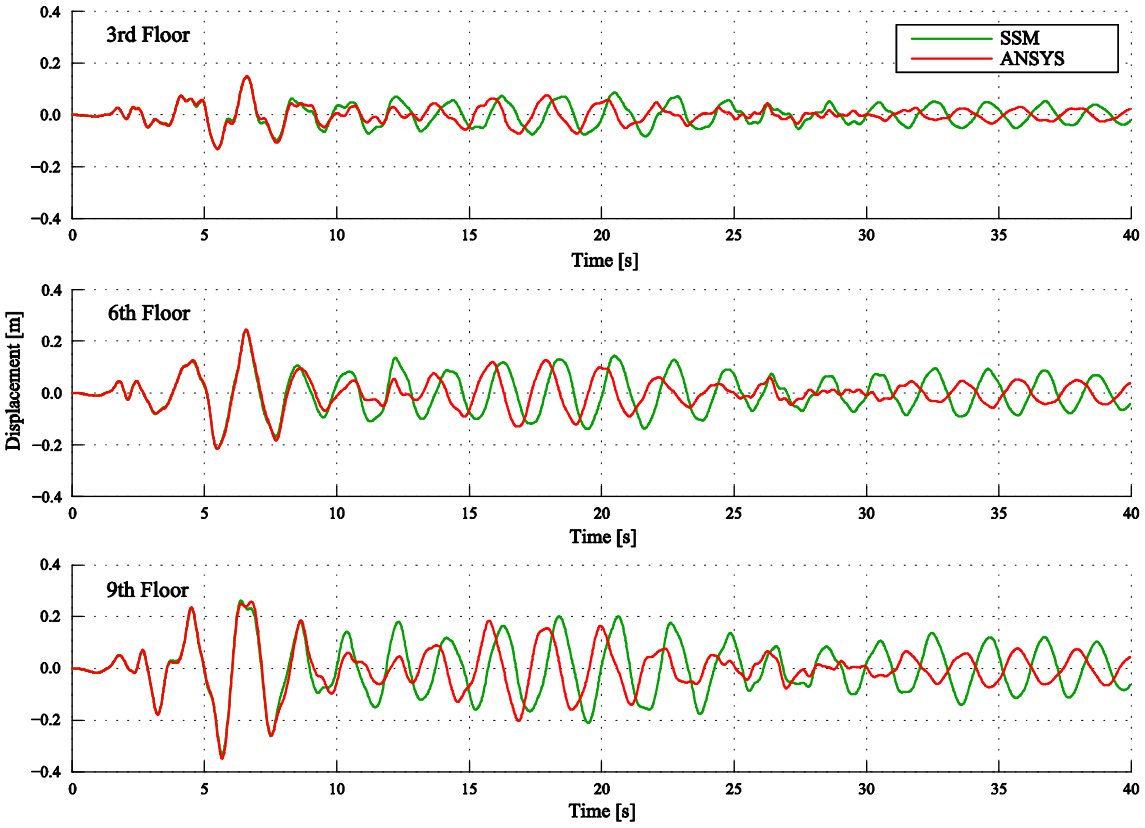

Figure 3.11 Displacement response of the 9-floor building with a U-type TLD under seismic excitation

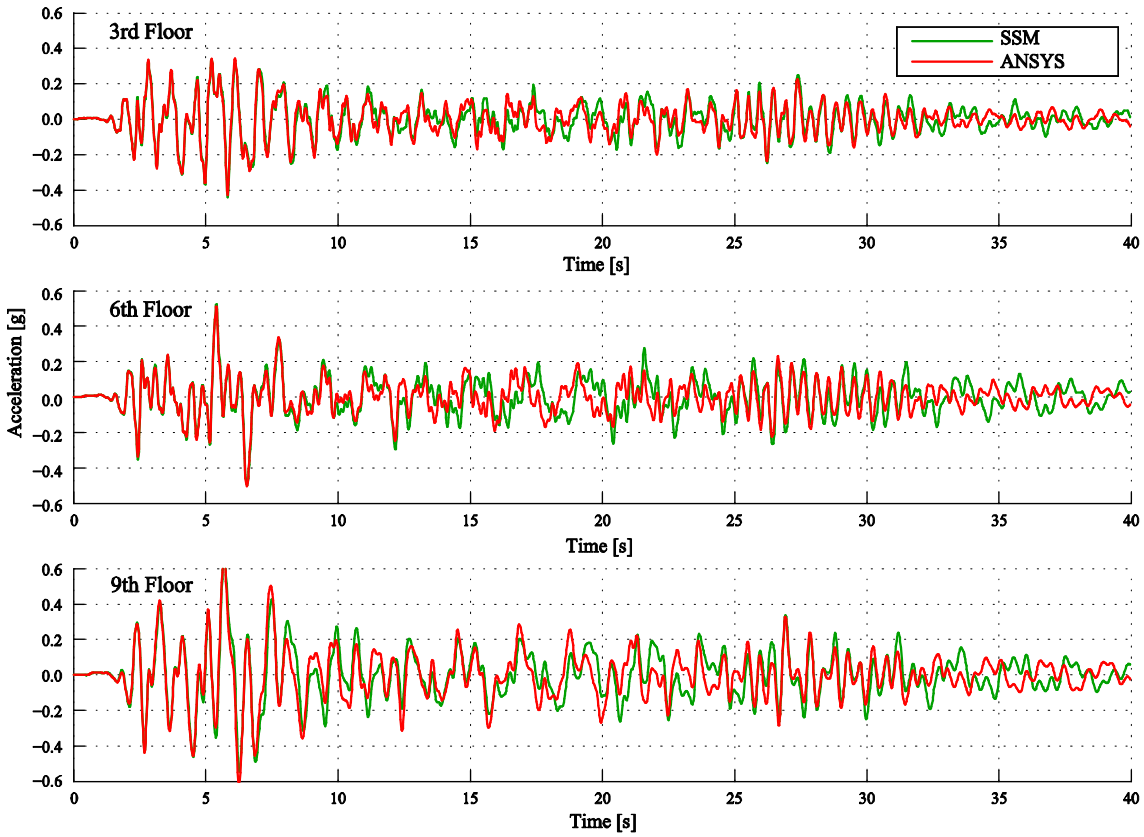

Figure 3.12 Acceleration response of the 9-floor building with a U-type TLD under seismic excitation

Table 3.6 Peak response values of values of the 9-floor structure with a U-type TLD under seismic excitation

	Peak Displacement [m]			Peak Acceleration [g]		
	Without TLD	SSM	ANSYS	Without TLD	SSM	ANSYS
3rd floor	0.1664	0.1458	0.1495	0.4087	0.4395	0.4292
6th floor	0.2745	0.2408	0.2447	0.5400	0.5254	0.5108
9th floor	0.3723	0.3327	0.3483	0.7041	0.6503	0.6571

3.4 Summary

In this Chapter, a numerical procedure (SSM) to represent the linear sloshing of liquid tanks was described and validated. The proposed model is based on the potential flow theory, where the continuity equation is resolved by a FEM scheme and then combined with the equilibrium equation generating a second order linear system of equations. The implementation of the new approach requires simply the computation of the equivalent fluid mass, damping and stiffness matrices, in addition to the computation of the terms related to the transmitted force that finally allows the numerical coupling with the support structure.

Contrary to the Housner model, that represents the sloshing only through a single degree of freedom, the SSM approximates it as a full system of n degrees of freedom facilitating a more accurate description (higher modes of vibration can be accounted for). For a rectangular tank sloshing periods obtained by the SSM, Housner model and analytical approximation had a maximum difference of 1.0% (for different tank geometries). When looking at the response under harmonic excitations the Housner and SSM were similar only if the excitation period was higher than 0.8 times the fundamental sloshing period. This should be attributed to the inability of the Housner model to represents higher modes of vibration. Under seismic excitations the examined methods (including a full FEM implementation through ANSYS) were found to yield comparable results, whereas similar trends were also found for non-rectangular tanks. In addition, the utility of the proposed model to evaluate the performance of

rectangular and non-rectangular Tuned Liquid Dampers (TLDs) was examined. For this purpose the seismic response of a 9-story building equipped with a TLD was simulated through ANSYS and SSM, with results showing good agreements since the maximum differences were lower than 3%.

The SSM offers a more accurate representation of the sloshing dynamic than the Housner Model but also a faster model and free of inconsistencies (that is, presence of spurious frequencies) than the ANSYS simulation. Ultimately, the SSM establishes a simple, (second order lineal system of equations that can be interpreted as a mass-spring system), generalized (any tank geometry) mathematical modeling of the liquid sloshing based on variables that have physical meaning (free surface elevation and base acceleration), and facilitates an easy coupling between rigid tanks and elastic structures that support them. Furthermore, its high computational efficiency and accuracy make it a valuable tool that could be used by designers to conduct parametric studies, preliminary dimensioning of storage tanks, seismic performance identification, or as it will be utilized within this dissertation, design and dimensioning of tuned liquid dampers.

I

INTRODUCTION OF TUNED LIQUID DAMPER WITH FLOATING ROOF; NUMERICAL MODEL FORMULATION, EXPERIMENTAL VALIDATION AND FUNDAMENTAL VIBRATION BEHAVIOR EXPLORATION

This Chapter introduces the Tuned Liquid Damper with Floating Roof (TLD-FR), putting special attention on the adaptation of the Simplified Sloshing Model (SSM) developed in Chapter 2 to describe the dynamic behavior of the new device. The accuracy of this model is then evaluated through comparisons to the experimental behavior of a scaled TLD-FR under different base excitations.

4.1 Introduction of the TLD-FR

As it was mentioned briefly in Chapter 1, TLD-FR consists of a traditional TLD with addition of a floating roof, constructed with a lightweight material with small density (reduce self-weight and facilitate the floating over the liquid). The idea behind this modification it that since the roof is much stiffer than water, it will prevent wave breaking, hence making the response linear even at large amplitudes. The roof also makes possible the addition of supplemental devices (either passive, semi-active or active) with which the level of damping can be substantially augmented. A scheme of

TLD-FR is presented in Figure 4.1, where is possible to identify three main parts: the liquid container, the floating roof and the external source of damping (different options could be explored such frictional, viscous, magneto-rheological dampers, etc). This device can be categorized somewhere between a TLD and a TLCD, since it is expected that TLD-FRs share the desire characteristics of both systems. It will be shown that it maintains practical TLCD attributes such as: (1) its dynamics can be ultimately characterized by considering just one degree of freedom; (2) incorporation of control strategies is straightforward; and (3) the mathematical model (presented later in this chapter) is relative easy to implement and understand. In parallel, the TLD-FR maintains desired characteristic of TLDs such as: (1) it has the same, familiar to practitioners, tank geometry; (2) the modification of the natural frequency (to facilitate tuning effects) is similarly versatile; and (3) it can be independently tuned and operated in two directions. Furthermore, it will be shown that it exhibits a lower dependency on the excitation amplitude than TLDs and TLCDs (its behavior is practically completely linear).

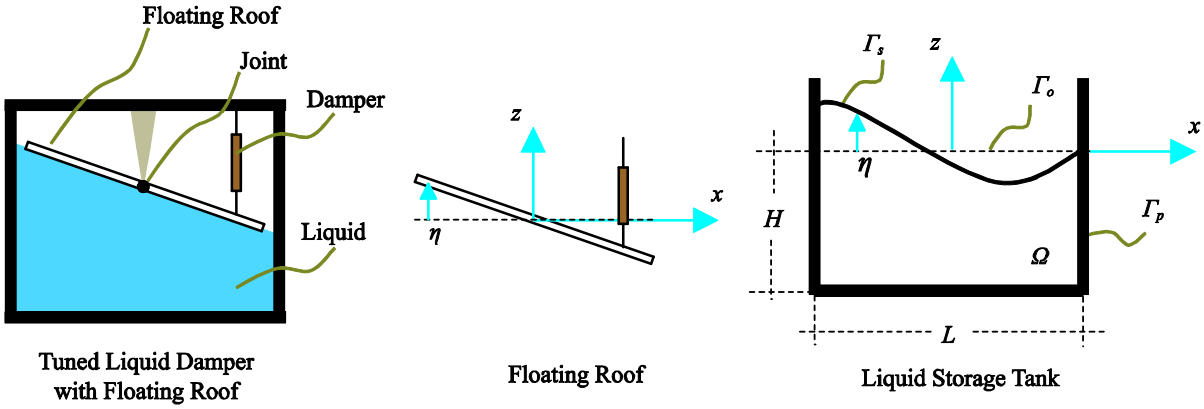

Figure 4.1 Schematic for a rectangular TLD-FR

Within this dissertation the focus is placed on one-dimensional application of the TLD-FR. Extension to bi-directional control requires proper concurrent design of the dimensions of the liquid tank in both directions. Note that for non-rectangular tanks this might be challenging as the non-rectangular cross-section in one direction creates a non-uniform cross section in the other direction. Through the numerical tools discussed here are applicable to this case as well, it should be stressed that they have not been validated for such applications. The overall modeling and design framework discussed though is readily extendable.

4.2 Mathematical Modeling

To develop the numerical model for the TLD-FR, the liquid and the floating-roof are modeled separately and then combined by the internal pressures generated at the liquid-roof interface. The liquid is modeled by the SSM described in Chapter 3 through Equations (3.18) and (3.25), which represent the sloshing dynamic and the transmitted force to the base of the tank respectively. It is important to note that Equation (3.18) was obtained considering that the pressure at the free surface is zero, which it is not the case in TLD-FR since the presence of the floating roof generates a non-zero pressure condition at the free surface. Therefore, Equation (3.18) is modified to introduce the pressure in the liquid/floating-roof interface:

$$\mathbf{M}_s \ddot{\boldsymbol{\eta}}_s + \mathbf{K}_s \boldsymbol{\eta}_s = -\mathbf{R}_s \ddot{u}_b - \frac{1}{\rho}\mathbf{P}_s \tag{4.1}$$

where $\mathbf{P}_s$ contains the nodal pressure at the free surface. Also, it is important to mention that Equation (3.25) quantifies the transmitted force to the base of the tank per unit of tank width d, such that $F = F_o\, d$, with F corresponding to the total force transmitted to the base, expressed as:

$$F = -\rho d \mathbf{A}\, \ddot{\boldsymbol{\eta}}_s - \rho d B \ddot{u}_b \tag{4.2}$$

4.2.1 Inclusion of the floating roof

The floating-roof is modeled as a flexible Euler-Bernoulli-beam through a FEM approach employing 2D elements composed by 2-nodes and 4-degree-of-freedom (one deflection and rotation per node). Under this scheme, the elemental stiffness matrix of the beam is proportional to EI/l^3; with E, I and l corresponding to the elasticity module, moment of inertia and length of the element, respectively. On the other hand, the elemental mass matrix is computed employing a lumped-mass approach. A coincident mesh between liquid and floating-roof is recommended to simplify the coupling between the two individual numerical models of the liquid and the floating roof. Figure 4.2 demonstrates this discretization where the nodes at Γ_s are shared between liquid and floating roof. The mass and stiffness matrices are then manipulated by a condensation process in order to express the dynamics of the floating roof only in terms of the vertical displacements $\boldsymbol{\eta}_s$ while additionally utilizing the pressure vector $\mathbf{P}_s$. The damping of potential external devices is incorporated by adding damping forces at the

proper nodes. Assuming linear viscous dampers this process leads to the following equation of motion of the floating roof:

$$\mathbf{M}_f \ddot{\boldsymbol{\eta}}_s + \mathbf{C}_f \dot{\boldsymbol{\eta}}_s + \mathbf{K}_f \boldsymbol{\eta}_s = \mathbf{F}_s \tag{4.3}$$

where $\mathbf{M}_f$ and $\mathbf{K}_f$ are the condensed mass and stiffness matrices of the floating roof. Ultimately, the mass matrix $\mathbf{M}_f$ depends on geometry (cross section) and the material density of the floating roof while the stiffness matrix $\mathbf{K}_f$ increases linearly with the product EI and decreases proportional to the cubic length of the floating roof. The elastic module and the moment of inertia can be chosen independently since E depends on the material and I on the transversal section.

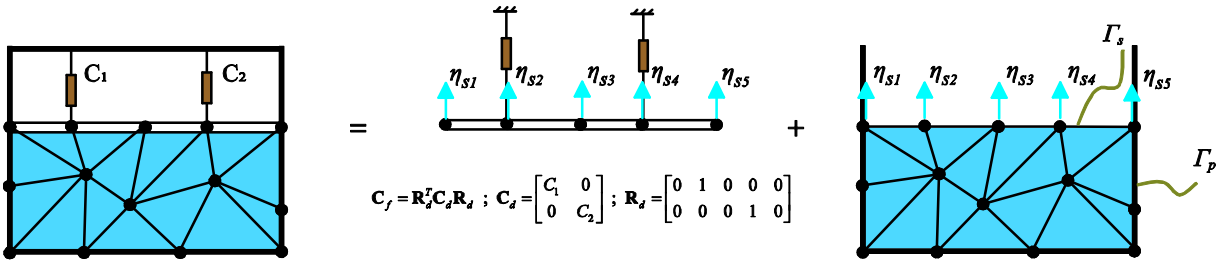

Figure 4.2 Scheme of the coincident mesh between liquid and floating roof and illustration example for derivation of damping matrix

Finally, the damping matrix $\mathbf{C}_f$ can be determined considering the external dampers connected to the roof. If $C_{damper,i}$ is the damping coefficient of the i^{th} damper and $\mathbf{R}_d$ is the collocation matrix with the i^{th} column relating the degree of freedom of the i^{th} damper to vector $\boldsymbol{\eta}_s$, matrix $\mathbf{C}_f$ is obtained as:

$$\mathbf{C}_f = \mathbf{R}_d^T \mathbf{C}_d \mathbf{R}_d = \mathbf{R}_d^T \begin{bmatrix} C_{damper1} & & 0 \\ & \ddots & \\ 0 & & C_{damper\,N} \end{bmatrix} \mathbf{R}_d \tag{4.4}$$

where $\mathbf{C}_d$ is the diagonal matrix composed of the damping coefficients of each damper. Figure 4.2 illustrates this process for a particular case in which two external dampers are used in a tank that is discretized with 5 nodes on its free surface.

For a complete description of the dynamics of the floating roof, the vector $\mathbf{F}_s$ that contains the external nodal forces is further defined, related to the vector of superficial pressures $\mathbf{P}_s$ through:

$$\mathbf{F}_s = \mathbf{G}\,\mathbf{P}_s \quad \text{with} \quad \mathbf{G} = \int_{\Gamma_s} \mathbf{N}_\eta{}^{\mathrm{T}}\, \mathbf{N}_\eta \, \mathrm{d}\Gamma_s \tag{4.5}$$

The interpolation function $\mathbf{N}_\eta$ used here corresponds to the same functions used in Chapter 3 to interpolate the elevation η at the free surface Γ_s [Equation (3.9)]. In other words, the spatial variation of the elevation and the pressure between nodes at the free surface are assumed linear. Note that the only physical connection between liquid and floating-roof is through the pressure in the interface liquid/floating-roof.

4.2.2 TLD-FR Numerical Model

The two models for the fluid and the floating roof can be finally combined through the nodal pressures to yield the differential equation of motion:

$$\mathbf{M}_a\, \ddot{\boldsymbol{\eta}}_s + \mathbf{C}_a\, \dot{\boldsymbol{\eta}}_s + \mathbf{K}_a\, \boldsymbol{\eta}_s = -\mathbf{R}_a\, \ddot{u}_b \tag{4.6}$$

where the augmented matrices involved are defined as:

$$\mathbf{M}_a = \left[\rho\left(\mathbf{M}_s\right) + \mathbf{G}^{-1}\mathbf{M}_f \right]$$
$$\mathbf{C}_a = \left[\mathbf{G}^{-1}\mathbf{C}_f \right];\ \mathbf{K}_a = \left[\rho\left(\mathbf{K}_s\right) + \mathbf{G}^{-1}\mathbf{K}_f \right];\ \mathbf{R}_a = \rho\left(\mathbf{R}_s\right) \tag{4.7}$$

This is a second order linear system of differential equations (can be considered as a mass-spring-dashpot system excited as its base) where the dependent variable is the vertical displacement of the floating roof and the input corresponds to the acceleration imposed at the base of the TLD-FR.

Another important characteristic of the TLD-FR is the force transmitted to its base, which is given by Equation (4.2), and only depends on the tank geometry, the sloshing amplitude and the horizontal acceleration of the tank (not directly influenced by the floating roof). The sloshing amplitude is computed by Equation (4.1) if the floating roof is not installed (traditional TLD) or by Equation (4.6) if the configuration corresponds to a TLD-FR. The behavior of a structure equipped with a TLD-FR can be then characterized by combining its equation of motion with Equation (4.6), with $\ddot{u}_b$ corresponding to the absolute acceleration of the floor in which the damper is installed and utilizing Equation (4.2) to estimate the force transmitted by the TLD-FR to the structure.

Therefore, the dynamic behavior of a traditional TLD can be ultimately described by Equations (4.1) and (4.2) (which corresponds to the SSM procedure) while the dynamic of the TLD-FR is defined by Equations (4.6) and (4.2), denoted herein as Simplified Sloshing Model with Floating Roof (SSM-FR).

4.3 Experimental Validation

For validating the numerical model of the TLD-FR an experimental study is performed utilizing a shaking table at the Structural Dynamics Laboratory of the Pontificia Universidad Catolica de Chile.

4.3.1 Experimental Setup

Figure 4.3 illustrates the experimental setup. The scaled TLD-FR was constructed using a rectangular-base glass tank, which is reinforced by an ad hoc chassis built around it. The plan dimensions of the tank are 0.8 m in the direction of the excitation (length L) and 0.4 m in the perpendicular direction (width d), while the total height is 0.6 m. The floating roof consists of a 1.5 in thick expanded polystyrene foam board (with elastic module E=3GPa and associated EI=5530Nm^2), and is attached to the chassis by two spherical joints located at mid-span. The location of the joints is such that rotational movement of the floating roof is enforced, and contact between the floating roof and the walls is prevented. Two air dampers are installed between the chassis and the floating roof. The damping coefficient of the dampers is adjustable, and the range of possible values is 0 - 0.35 N/mm/s. The dampers act in both directions (pushing-pulling) and have a total stroke of 76.2 mm (3 in). They are located at 0.2m from mid-span, allowing a maximum rotation angle of the floating-roof close to 11 degrees. The liquid used is blue-colored water. The damper-chassis and joint-chassis connections are built in such a way that different water depths H can be established. It is important to

mention that although the height of the tank is 0.6 m, the water depth H is only a fraction of it in order to have enough space to place the dampers. The tank is mounted on the shaking table by three rollers, and the horizontal motion of the tank relative to the shaking table is constrained by two load cells. In that sense, the rollers support only the vertical load while the load cells take the total horizontal force generated in the system. The tank, chassis, floating-roof and dampers assembly have a total dry weight of 55 kg. The model is instrumented with two accelerometers to measure the absolute acceleration of the shaking table and the tank. Two LVDT (Linear Voltage Displacement Transducers) sensors are provided to measure the vertical displacement of the floating roof. The LVDTs are located next to the dampers (0.2 m from the mid-span). The rotation of the floating-roof is obtained through these measurements and by further assuming that the floating-roof is rigid. The load cells are S-type cells utilizing strain-gauges to measure tensile and compressive forces in static or dynamic conditions.

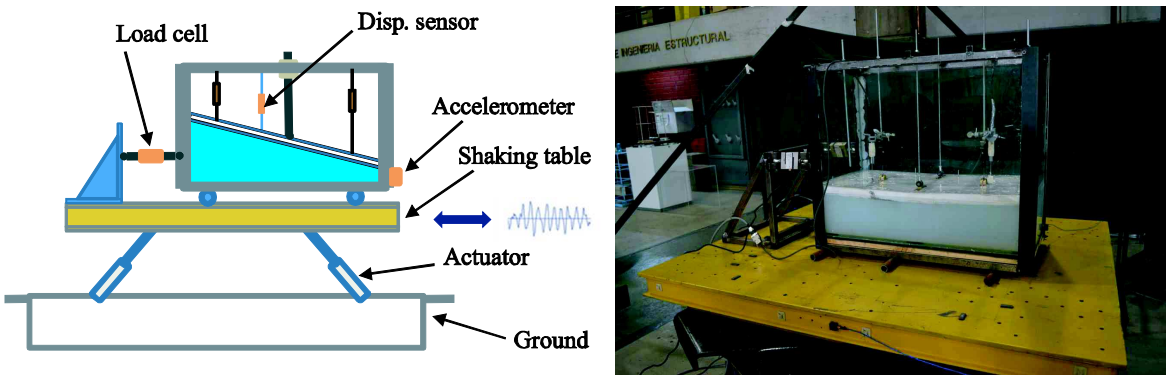

Figure 4.3 Scheme for experimental setup for validation of the TLD-FR

All instruments are connected to a universal data acquisition system, which allows to simultaneously acquire and record the signals from the different sensors. The shaking table used has 6 degrees of freedom and a maximum support load of approximately 15 kN, but in this study only one-directional translational excitations are used. These excitations represent the input to the TLD-FR. The focus is placed here on validating the SSM-FR by comparing analytical results with experimental measurements. Six different TLD-FR configurations having different water depths and different levels of external damping are examined (Table 4.1). The characterization and validation is established considering different dynamic tests: free vibration, response to harmonic excitations, and response to earthquake excitations.

Table 4.1 Details of the TLD-FR configurations considered in the experimental study

Tank ID	Width (d)	Length (L)	Water Height (H)	External Damping
A	0.4 m	0.8 m	0.2 L	No
B	0.4 m	0.8 m	0.2 L	Yes
C	0.4 m	0.8 m	0.3 L	No
D	0.4 m	0.8 m	0.3 L	Yes
E	0.4 m	0.8 m	0.4 L	No
F	0.4 m	0.8 m	0.4 L	Yes

4.3.2 Free Vibration

The free vibration of the TLD-FR is first considered by providing a pulse-like instantaneous excitation. The response (which is presented in Figure B.1, Figure B.2 and Figure B.3 in Appendix B) allows for identification of the fundamental period under free vibration conditions. This period of the TLD-FR and of the corresponding traditional TLD (without the roof) are additionally obtained through eigenvalue analysis using Equations (4.6) and (4.1), respectively, and are found to be very similar to one another (this matching is further explored later in this Chapter). Finally for comparison purposes these periods are also obtained by the analytical closed-form expressions derived by (Chen et al. 1996) and by (Housner 1963) for liquid dampers with rectangular geometries; which correspond to the same methods used previously in Chapter 3 to estimate periods of different liquid tanks. All of the estimates of the fundamental sloshing period turned out to be very close to each other (Table 4.2), with the maximum differences of the order of 2%.

Through the free vibration tests, the damping ratio is also experimentally identified by applying the decrement logarithm method to the rotation response of the floating-roof. In particular it is observed in cases A, C and E (configurations without external damping) that the TLD-FR has a significant level of inherent damping (≈ 3-4%), possibly due to the presence of drag or friction forces acting at the thin layer of liquid located between the floating roof and the tank walls.

Table 4.2 Undamped sloshing periods of the TLD-FR configurations considered in the experimental study

	TLD Natural Period [sec]			TLD-FR Natural Period [sec]	
Tank ID	SSM	Analytic	Housner	SSM-FR	Experimental
A	1.3542	1.3572	1.3539	1.3496	1.36
C	1.1835	1.1803	1.1795	1.1734	1.16
E	1.0950	1.0985	1.0995	1.0925	1.08

Table 4.3 Experimental damping ratios for the different TLD-FR configurations

Tank ID	Total Damping Ratio (ξ_m)	Inherent Damping Ratio (ξ_{int})	External Damping Ratio (ξ_{ext})
A	3.6%	3.6%	-
B	7.7%	3.6%	4.1%
C	3.7%	3.7%	-
D	8.4%	3.7%	4.7%
E	3.5%	3.5%	-
F	8.3%	3.5%	4.8%

The experimental damping ratios of all configurations are presented in Table 3, using the responses presented in Figure B.1, Figure B.2 and Figure B.3. Note that for configurations A, C and E the total (ξ_m) and inherent (ξ_{int}) damping ratios coincide since no external dampers are considered. On the other hand, for configurations B, D and F the external damping ratio (ξ_{ext}) is obtained by the difference between the total (ξ_m) and the inherent (ξ_{int}) damping ratios, where the last one is assumed to be independent of the external damping, meaning that is assumed equal between the TLD and TLD-FR cases (Tanks A and B, Tanks C and D and Tanks E and F are assumed to have the same inherent damping values).

4.3.3 Harmonic Response

Next, the response under harmonic excitations of different amplitudes is examined. The Normalized Transmitted Force F_n and the Amplitude Ratio AR are used to characterize the response given, respectively, by:

$$F_n = \frac{\left|F(t)\right|_{\max}}{m_{TLD-FR}\left|\ddot{u}_b(t)\right|_{\max}} \quad \text{and} \quad AR = \frac{\left|\eta(t)\right|_{\max} x\ 100}{H} \tag{4.8}$$

Where $F(t)$ is the time variation of the transmitted force, $m_{TLD\text{-}FR}$ is the total mass of the TLD-FR, $\ddot{u}_b(t)$is the acceleration history of the shaking table, $\eta(t)$ is the time variation of the oscillation of the floating roof and H corresponds to the water depth. Note that expressions for the transmitted force presented in Equations (4.8) and (3.26) are equivalent; the only difference is that Equation (4.8) takes into account not only the

mass of the liquid m_{liq} but also the mass of the floating-roof, chassis, dampers and tank since all of these elements contributes to the transmitted force registered by the load cell. The Normalized Transmitted Force F_n is ultimately an indicator of the force amplification due to sloshing effects, and the Amplitude Ratio AR relates the maximum amplitude of the oscillation of the floating-roof to the water depth. Eight different excitation periods and different excitation amplitudes are considered. In particular, two conditions are studied in terms of the shake table motion: (i) excitations with specific displacement amplitude (ranged between 5-20mm) and (i) excitations with specific acceleration amplitude (ranged between 0.01-0.02g). It is important to mention that since the normalized force F_n is an amplification factor of the transmitted force, it is affected by the excitation period but not by the excitation amplitude. For the amplitude ratio AR the results are normalized by the excitation amplitude $\left|\ddot{u}_b\left(t\right)\right|_{\max} / g$ to similarly avoid an excitation amplitude dependency.

The numerical and experimental results corresponding to the configurations without external damping are presented in Figure 4.4 and Figure 4.5, while the response of TLD-FRs with external damping is shown in Figure 4.6 and Figure 4.7. The first three sloshing frequencies of the corresponding traditional TLD without the floating roof are also shown in the figures with vertical black dashed lines.

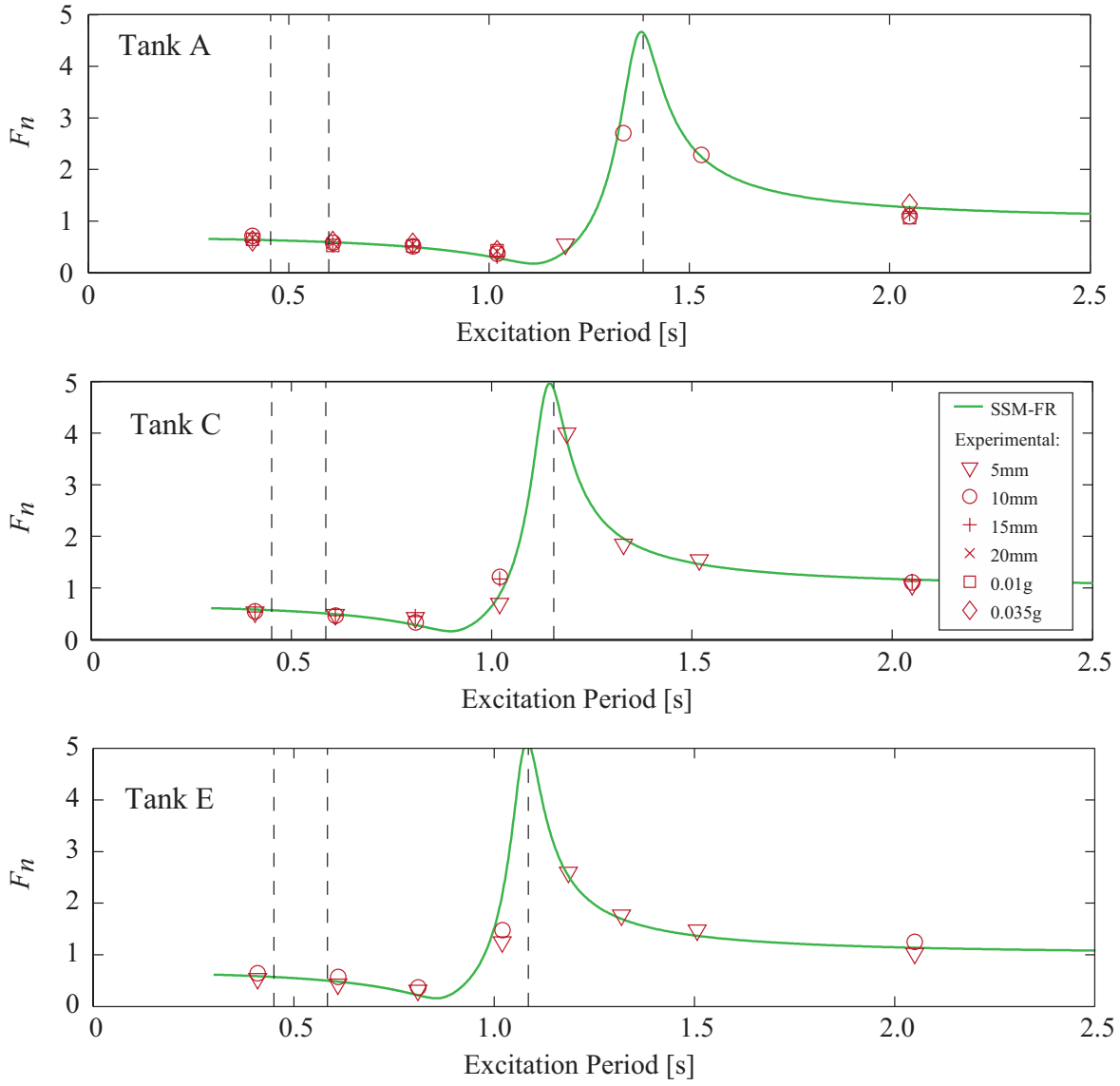

Figure 4.4 Normalized transmitted force (non-dimensional) for experimental configurations without external damping under harmonic excitation for different excitation periods. (i) Numerical and (ii) experimental results under different excitation amplitudes are compared

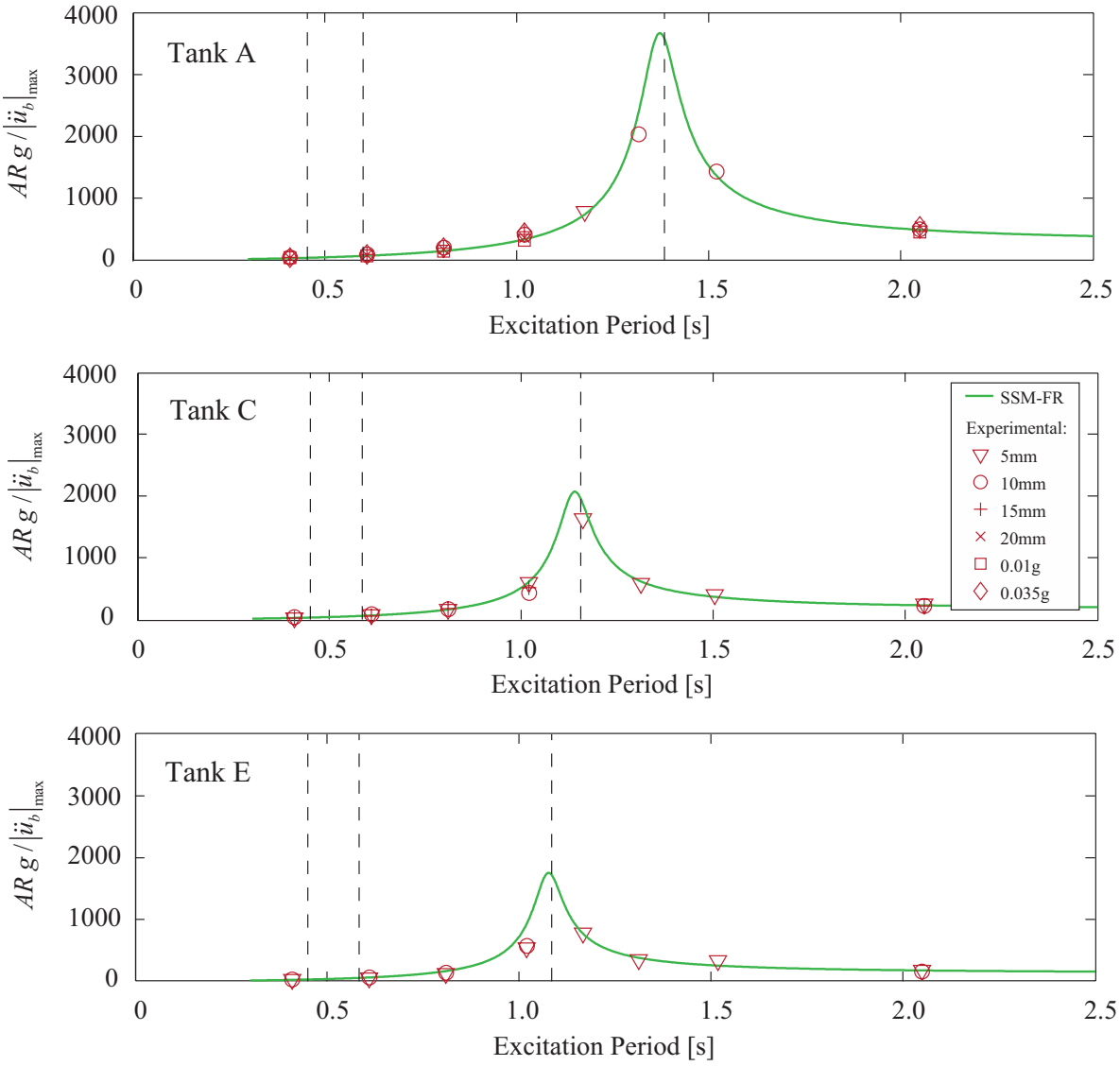

Figure 4.5 Floating roof amplitude (normalized by excitation amplitude) for experimental configurations without external damping under harmonic excitation for different excitation periods. (i) Numerical and (ii) experimental results under different excitation amplitudes are compared

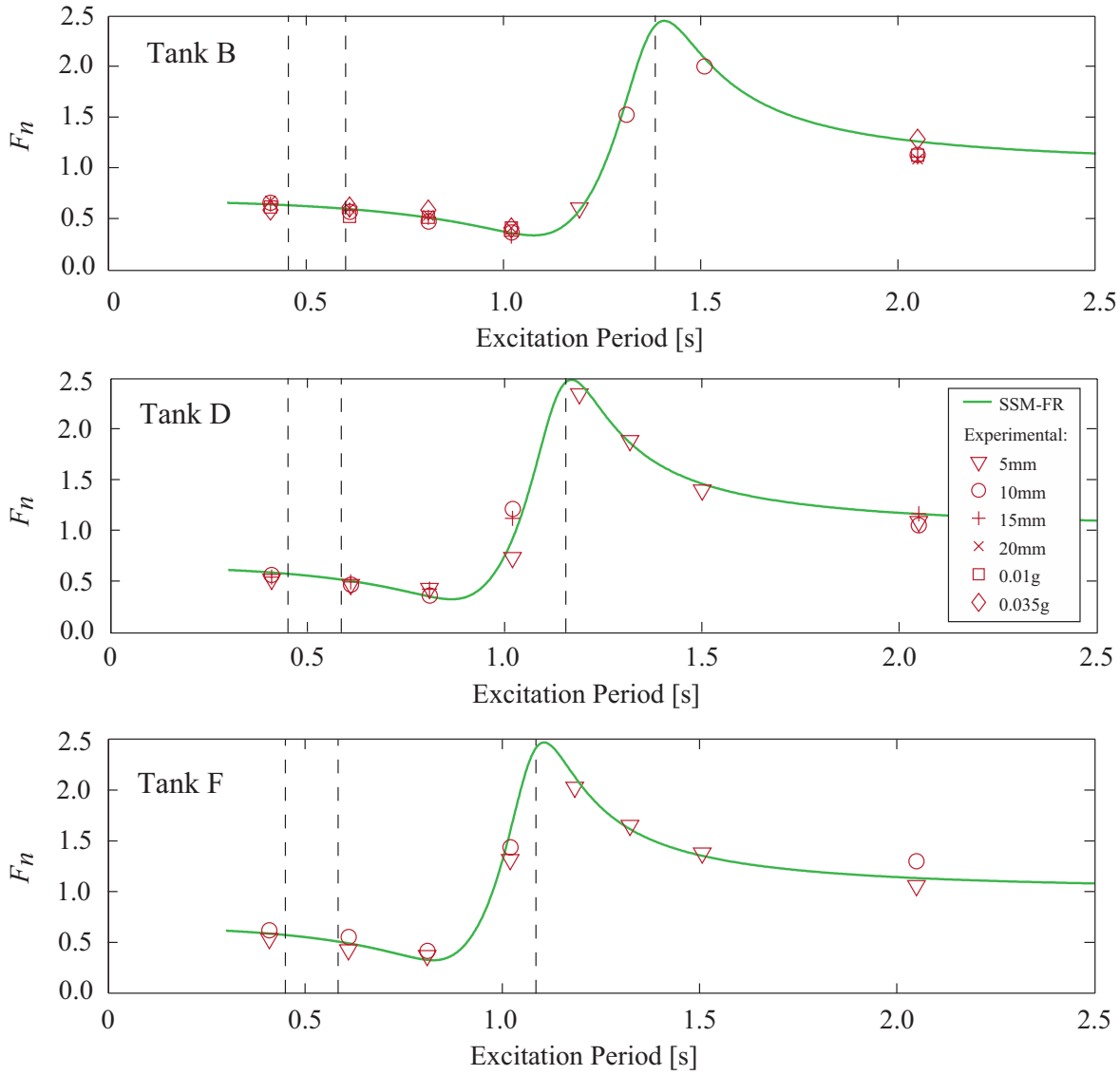

Figure 4.6 Normalized transmitted force (non-dimensional) for experimental configurations with external damping under harmonic excitation for different excitation periods. (i) Numerical and (ii) experimental results under different excitation amplitudes are compared

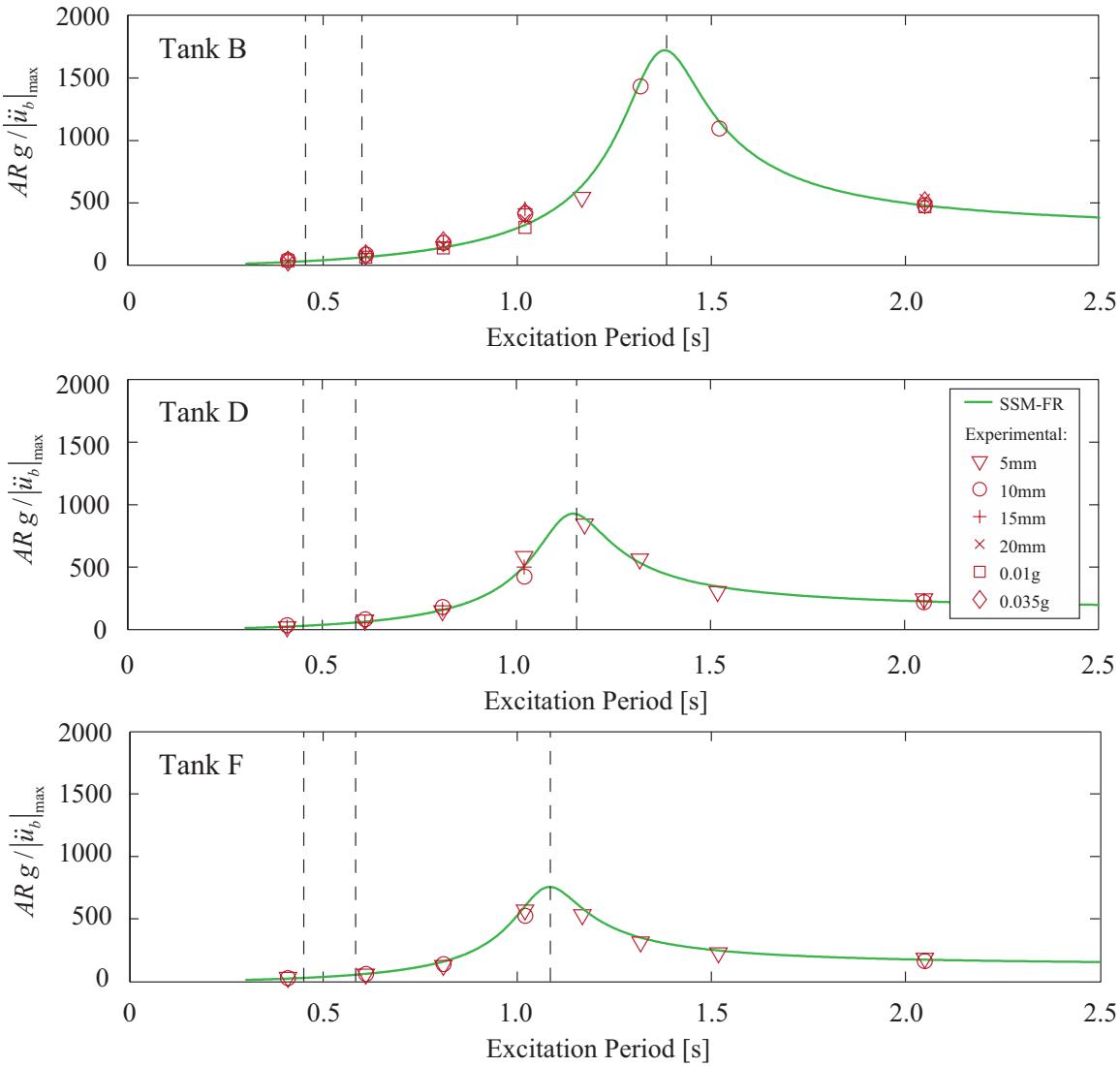

Figure 4.7 Floating roof amplitude (normalized by excitation amplitude) for experimental configurations with external damping under harmonic excitation for different excitation periods. (i) Numerical and (ii) experimental results under different excitation amplitudes are compared

The first observation from these results it that there is a good agreement between theoretical and experimental results, offering a further validation of the numerical model. Additionally, the absence of maxima at the second and third natural

frequencies (dashed-lines) indicates that the TLD-FR does behave essentially as a single degree-of-freedom system and that the assumptions presented in Section 4.1 are indeed valid. In all cases studied, it is observed that different excitation amplitudes do not significantly affect neither the Normalized Transmitted Force F_n nor the ratio$AR/\left|\ddot{u}_b(t)\right|_{\max}$, which means that the dynamic behavior of the TLD-FR can indeed be considered essentially linear (no amplitude dependence).

Additionally, some general characteristic can be observed. The maximum value of the normalized transmitted force is affected by the damping (F_n decreases when the damping increases) but not by the water depth (maximum F_n does not change for tanks A, C, E nor for B, D, F), these trends are shown in Figure 4.4 and Figure 4.6. On the other hand, the maximum value of the ratio $AR/\left|\ddot{u}_b(t)\right|_{\max}$ decreases with increasing damping, and also decreases with increasing water depth (Figure 4.5 and Figure 4.7). Results (both analytical and experimental) also indicate that F_n is close to unity when the excitation period is much greater than the natural period, indicating that, as expected, all the mass of water moves with the tank. Results also show a local minimum of F_n, which is related to in- and out-of-phase movements of the impulsive and convective masses of water with respect to the excitation. Finally, it is important to point out that at near-resonance conditions it was not possible to impose harmonic excitations of displacement amplitudes greater than 10 mm (greater amplitudes could lead to unsafe oscillations of the floating roof).

4.3.4 Seismic Response

Finally the response to earthquake excitations is examined using different ground motions. The response of TLD-FRs subjected to the ground acceleration history recorded at the Melipilla station during the 1985 Chile earthquake is discussed here in detail. Figure 4.8 shows the excitation whereas Figure 4.9 and Figure 4.10 show the TLD-FR response in terms of transmitted force to the base and floating roof amplitude, respectively.

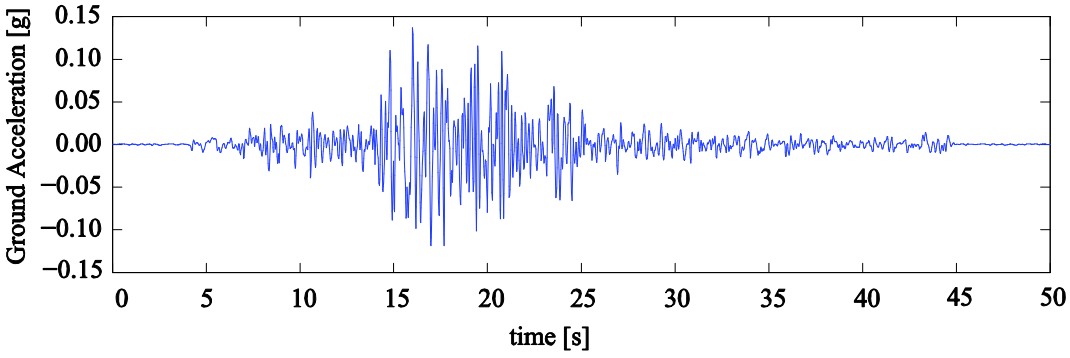

Figure 4.8 Ground motion imposed as excitation, corresponding to the ground motion recorded at Melipilla station during the 1985 Chile earthquake

The numerical results are in very good agreement with the experimental data (Figure 4.9 and Figure 4.10) with differences between peak responses being less than 6%. Some differences between the response histories are observed after t = 25 sec. In the case of Tank A (a TLD-FR without external dampers), the differences might be due to the fact that the inherent damping of the TLD-FR (drag and/or friction) is possibly

nonlinear. In the case of Tank B (a TLD-FR with external dampers), the differences are probably due to the fact that the external dampers are most likely not perfectly linear, but were assumed linear in the numerical procedure.

Since in earthquake engineering the response characteristics of interest are typically peak values, the close agreement between experimental and analytical peak values (as opposed to the behavior at the tails of the response) provides a degree of confidence for the established numerical models. Although only results for tanks A and B are presented in this chapter, it is important to mention that tests on other configurations exhibited similar trends (results are included in Appendix B).

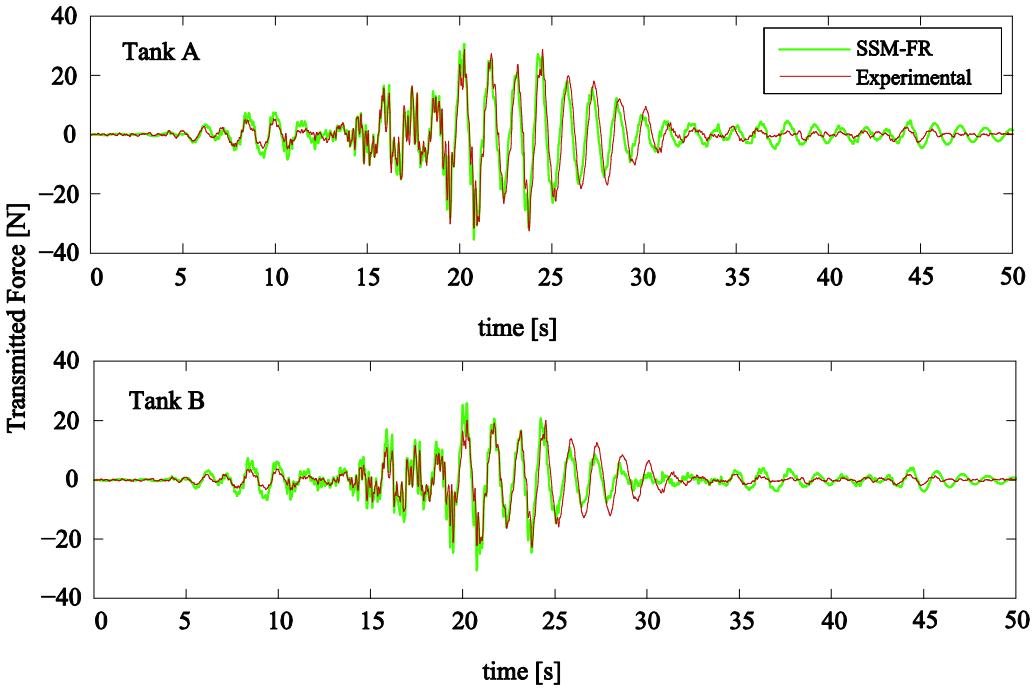

Figure 4.9 Transmitted force for tanks A and B under seismic excitation. Comparison between numerical and experimental results shown.

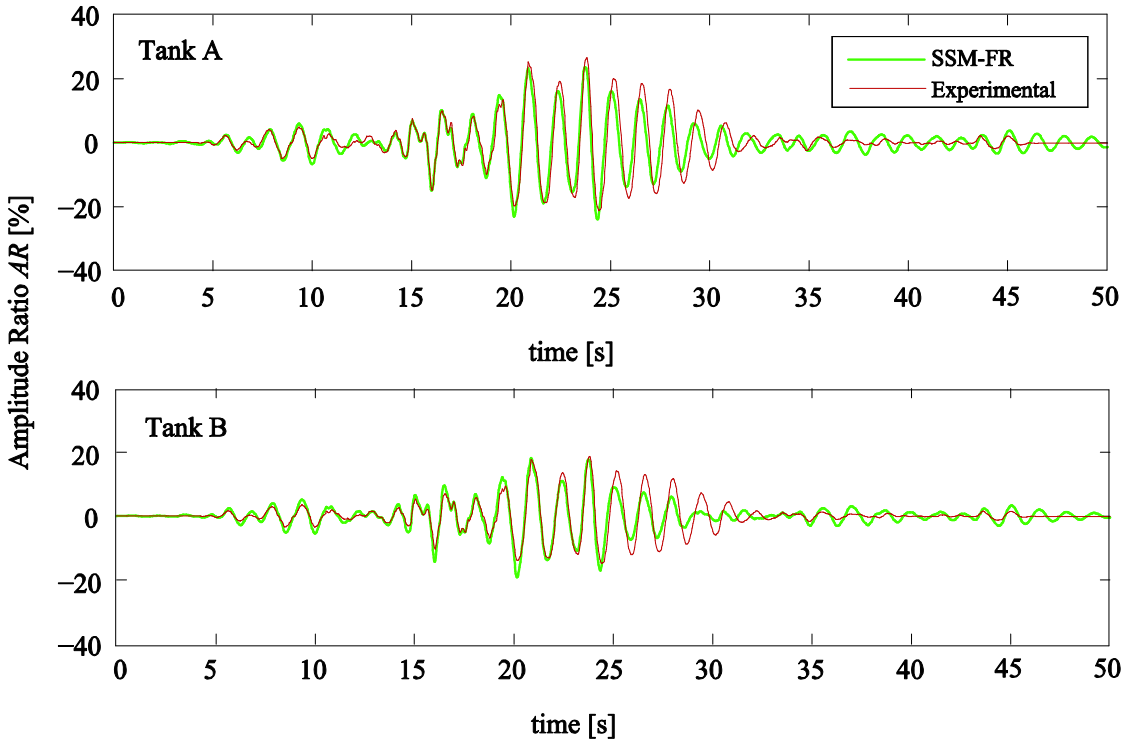

Figure 4.10 Floating roof amplitude for tanks A and B under seismic excitation. Comparison between numerical and experimental results shown.

A sequence of photos was taken when the ground motion was applied to the TLD-FR. Figure 4.11 shows the instants of maximum displacement response in a window from 20 to 24 seconds. The system without floating roof is also presented, for the same excitation and time window. The first row of photographs corresponds to the TLD-FR (configuration A) while the second row corresponds to a traditional TLD. The only difference between them is that one has the floating roof and the other does not. It is evident from this sequence that the TLD-FR exhibits a linear behavior, offering a further validation of our assumptions, in this case for arbitrary excitation conditions. The wave breaking and nonlinear behavior of TLD is also evident in the photos.

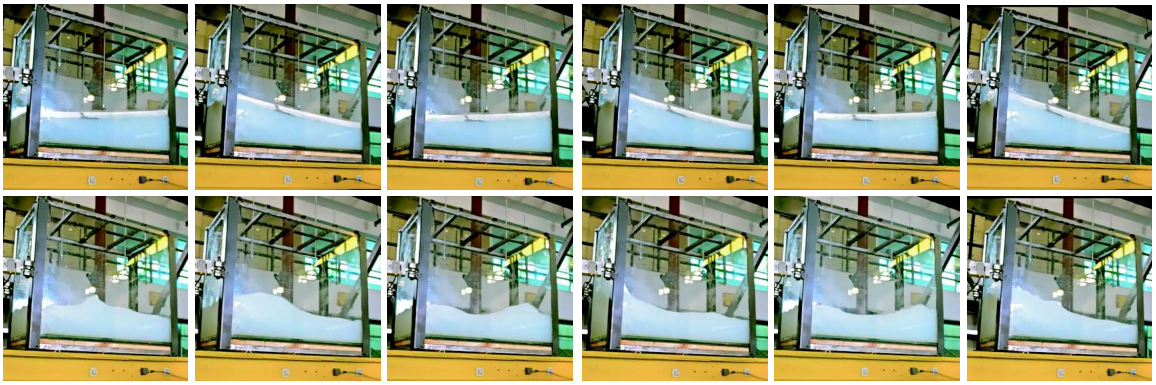

Figure 4.11 Photograph sequence of a TLD-FR (upper row) and TLD (lower row) under seismic excitation. Same tank geometry used in the two cases. Wave breaking and nonlinear behavior is evident in the latter but the presence of the floating roof keeps former practically linear.

Overall the experimental analysis shows that the TLD-FR exhibit a behavior that can be adequately approximated by a single degree of freedom system, and that its dynamics can be accurately represented through the proposed SSM-FR numerical procedure.

4.4 Fundamental Vibration Behavior of TLD-FR and Impact of Floating Roof

The experimental validation performed in the last section has demonstrated the accuracy of both the SSM-FR and SSM numerical models. An immediate question one can now explore is a more in-depth understanding of the impact of the floating roof on the liquid vibration (and therefore the liquid damper behavior). For this purpose Figure 4.12, Figure 4.13 and Figure 4.14 report the modal shapes and transfer functions over the first three modes for a TLD and a TLD-FR for three different tank geometries: (i) one

with a larger TLD fundamental period (length = 8m and water depth = 4m), (ii) one with a median period (length = 4m and water depth = 2m) and (iii) one with a lower TLD fundamental period (length = 1.5m and water depth = 0.75m). The transfer functions for TLD and TLD-FR are defined, respectively, as

$$\left|H_{TLD}(i\omega)\right| = \left|\left(-\omega^2\mathbf{M}_s + i\omega\mathbf{C}_s + \mathbf{K}_s\right)^{-1}\mathbf{R}_s\right| \tag{4.9}$$

$$\left|H_{TLD-FR}(i\omega)\right| = \left|\left(-\omega^2\mathbf{M}_a + i\omega\mathbf{C}_a + \mathbf{K}_a\right)^{-1}\mathbf{R}_a\right| \tag{4.10}$$

For all cases the tank width is taken as 1m while a 0.5% of damping ratio (inherent damping) is assumed for all modes. The stiffness of the floating roof is modeled by an elastic beam with a moment of inertia (I) and modulus of elasticity (E) defined as: EI=1400Nm^2 and EI=1400000Nm^2 for Figure 4.13 and Figure 4.14 respectively. To put these values into better perspective, if, for example, the material for the floating roof was polystyrene with E=3x10^{9}GPa and rectangular cross section then the thickness of the floating roof should be 2cm and 18cm to match the specified values EI=1400Nm^2 and EI=1400000Nm^2, respectively. The first two modal shapes for the tank with R=0.5, L=8m and EI=1400Nm^2 are presented in Figure 4.12. The modal shapes for the rest of the tanks configurations are not presented since they are practically the same.

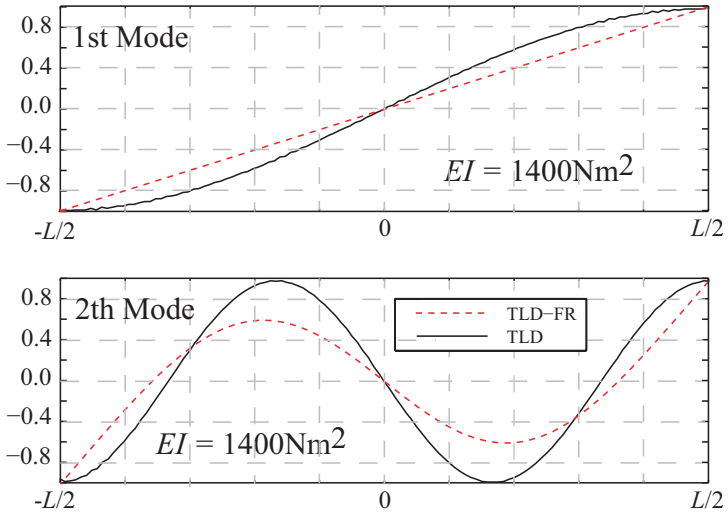

Figure 4.12 Modal shapes for a tank with R=0.5, L=8m. For TLD-FR the beam stiffness is set to EI=1400Nm^2

It is observed that the behavior around the first sloshing period and the first modal shape are practically same for both the TLD and TLD-FR whereas the floating roof moves higher sloshing modes to higher frequencies (lower periods), allowing a larger separation between these modes. Additionally, higher modes are suppressed (amplitude reduced), whereas for floating roofs with higher stiffness no higher modes are observed. This behavior is easy to explain, especially when coupled with the information in Figure 4.12 about the mode shapes of different modes for the TLD; for the fundamental mode the roof is allowed to participate as a rigid body so has limited impact on the vibratory characteristics. Coupling within higher modes requires the roof to vibrate according to the coupled dynamics, which is difficult due to the higher rigidity of it (note this is the case even for the smaller EI considered). This ultimately leads to

the observed suppression of the higher modes. This further supports the intended tuning of the TLD-FR to only a specific mode (discussed at the beginning of this section), since its own modes are better separated (compared to the TLD) with higher modes significantly suppressed.

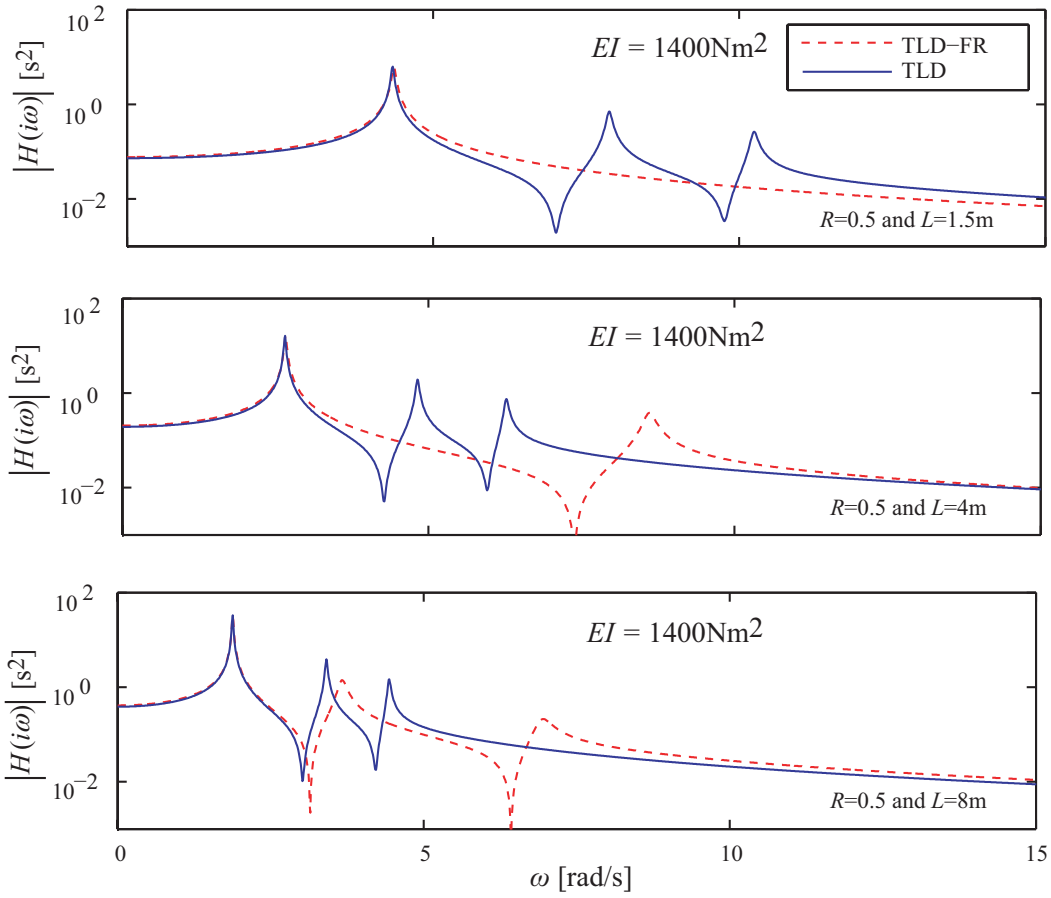

Figure 4.13 Transfer function for TLD and TLD-FR employing a floating roof with a EI=1400Nm^2. Different tank geometries examined.

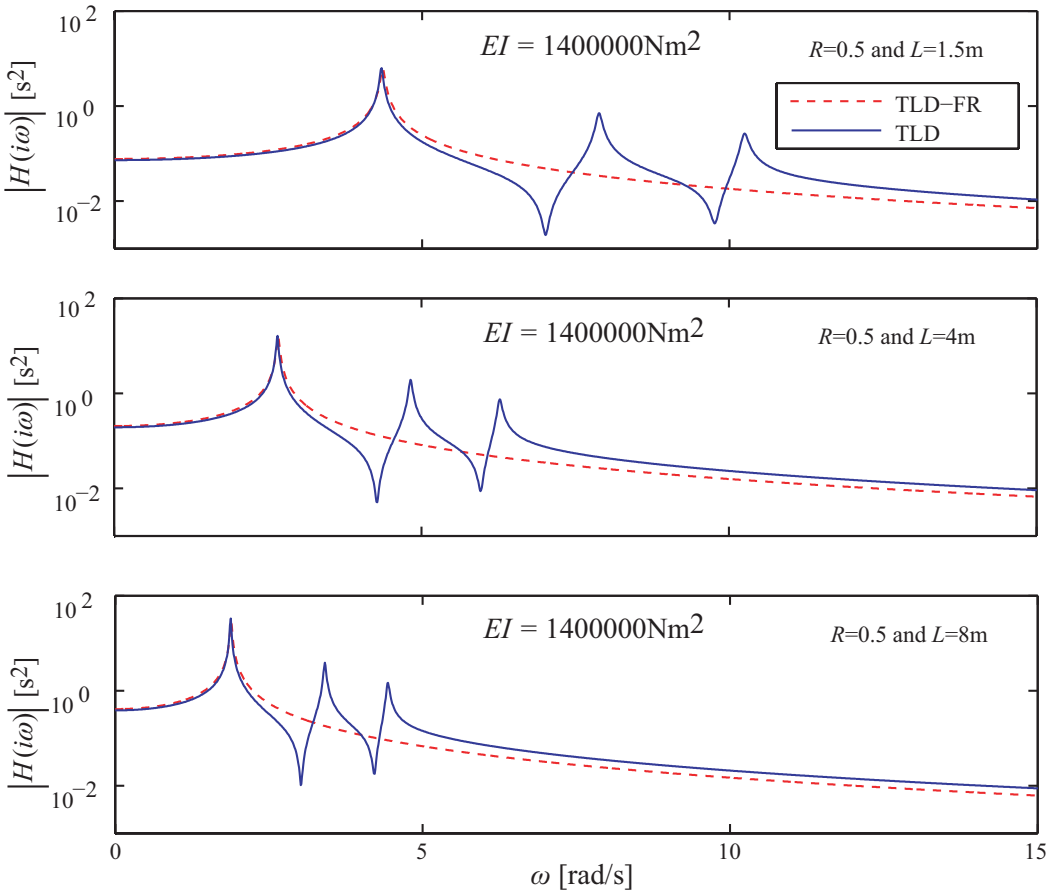

Figure 4.14 Transfer function for TLD and TLD-FR employing a floating roof with a EI=1400000Nm^2. Different tank geometries examined.

Similar results are observed in Figure 4.15, corresponding this case with a liquid damper employing a non-symmetric tank. The geometry, mode shapes for the first two modes as well as frequency response are all shown in this figure. It is again evident that the floating roof suppresses higher modes. In this case, since the mode shape in the fundamental mode is not completely symmetric the inclusion of the floating roof has a minor impact on it as well. This should be attributed to the fact that the floating roof is allowed to vibrate as a rigid body.

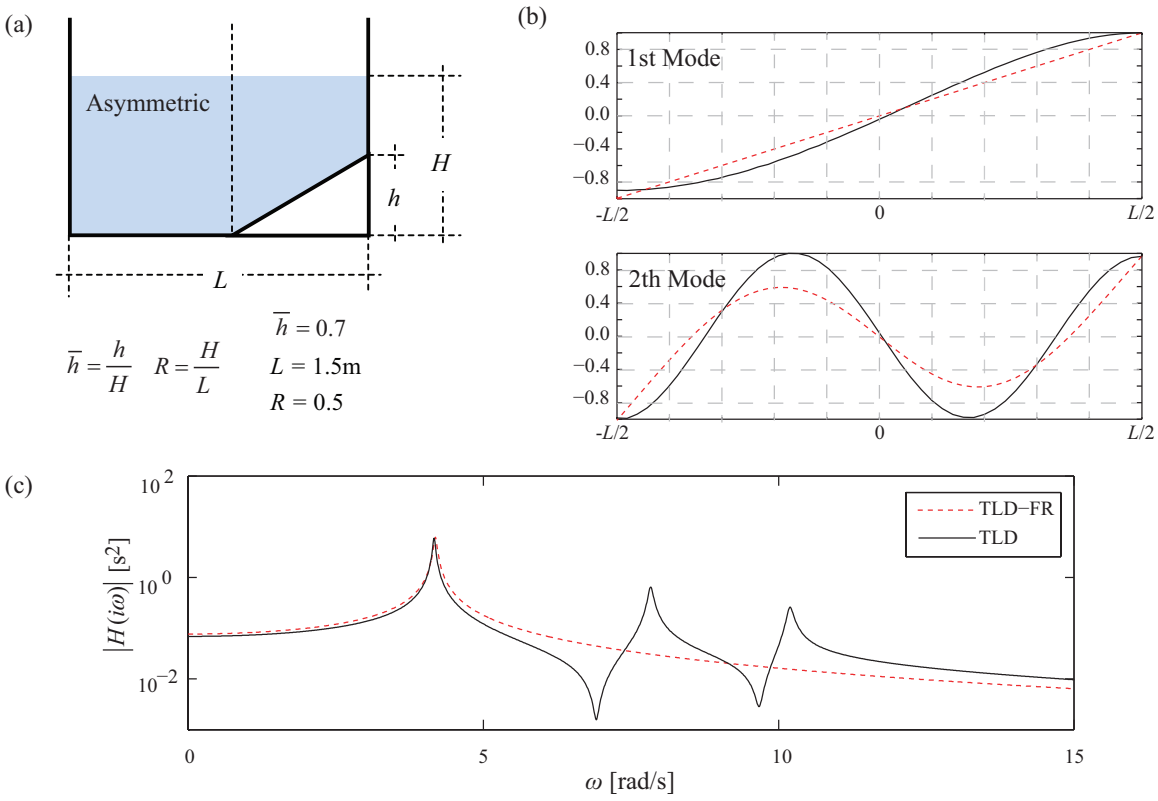

Figure 4.15 Results for non-symmetric tank for TLD and TLD-FR (a) Schematic of a tank and its geometric details, (b) mode shapes for first and second mode and (c) frequency response function. Value of EI is 1400000Nm^2 for the TLD-FR.

4.5 Summary and General Considerations

The Tuned Liquid Damper with Floating Roof (TLD-FR) was introduced in this Chapter. This mass damper is a variation of the traditional Tuned Liquid Damper, established through the introduction of a floating roof that imposes a kinematic constraint on the surface of the liquid while also facilitating the incorporation of external dampers to achieve the desired optimal damping ratio. A numerical model was developed for the TLD-FR, combining the SSM model discussed in the previous Chapter

with a Finite Element Model for the floating roof and coupling them through the pressure at the roof-liquid interface. Additionally an extensive experimental validation was undertaken considering a variety of dynamic excitations (shake table experiments) and rectangular tank geometries for the TLD/TLD-FR. The results indicate that, contrary to the behavior of TLDs, the response of the TLD-FR is practically linear and does not exhibit a significant amplitude dependency. The TLD-FR behaves essentially as a single-degree-of-freedom system, which is a consequence of the floating roof preventing wave breaking(this was particularly evident when looking at the time-history of the response –through sequence of snapshots- in the experimental investigation) and suppressing higher modes of vibrations. Experimental results also demonstrate that the TLD-FR possesses an important level of inherent damping, possibly related to friction and/or drag forces in the gap between the walls and the roof. This is an important consideration for design purposes since it means that external dampers should be selected to provide only a portion of the total optimal damping for the TLD-FR (the remaining portion contributed by the inherent damping).The experimental response of the TLD-FR to both harmonic and seismic excitations was shown to be in very good agreement with the response predicted by the numerical model, validating the latter.

[redacted]

PARAMETRIC FORMULATION FOR TLD-FR VIBRATION AND DESIGN PROCEDURE

It was demonstrated in the previous section that the TLD-FR presents same behavior as other type of linear mass dampers with vibratory characteristics dominated by a single mode, especially for rigid floating roofs. This ultimately means that its dynamics can be represented by a second order linear oscillator with the coupling to the primary structure established, like in other type of mass dampers, through the force transmitted by the TLD-FR to its walls/base. The question that is investigated in this section is how can this representation be established, especially how can the behavior of the TLD-FR, dependent on specific characteristics of the tank geometry, be simplified so that it is represented by similar parameters as other mass dampers (such as tuning ratio, efficiency index and mass ratio). A parametric formulation is introduced in this chapter to support this goal. This formulation has two components (a) simplification of equations of motion through only four variables and (b) derivation of simplified relationships to relate these variables to the tank geometry and the external dampers, to support the design of the TLD-FR. These two components are independently discussed next. Additionally, insight is provided on the effect of the transverse tank

geometry on the TLD-FR fundamental vibratory characteristics. Finally an illustrative example is presented to demonstrate these concepts considering the design of TLD-FR under stationary excitation.

5.1 Simplification of Equations of Motion through Parametric Formulation

The parametric formulation is based on a modal reduction retaining only the first mode of the TLD-FR which has been shown in the previous Chapter to be the dominant one. Let $\mathbf{\Phi}$ represent the eigenvector for the first sloshing mode and y the corresponding modal coordinate, so that $\boldsymbol{\eta}_s = \mathbf{\Phi}\, y$ .The modeshape $\mathbf{\Phi}$ is normalized so that the modal value at the wall (which is expected to be the maximum for the fundamental mode) is equal to one. This is chosen so that the modal displacement corresponds to the displacement of the floating roof at the wall. Both these terminologies, modal displacement or floating roof displacement, will be used herein to describe y. The proposed modal reduction leads then to the scalar differential equation:

$$m_m\, \ddot{y} + c_m\, \dot{y} + k_m\, y = -R_m\, \ddot{u}_b \tag{5.1}$$

where the modal characteristics are

$$\begin{aligned} m_m &= \mathbf{\Phi}^T \mathbf{M}_a \mathbf{\Phi} \\ c_m &= \mathbf{\Phi}^T \mathbf{C}_a \mathbf{\Phi} \\ k_m &= \mathbf{\Phi}^T \mathbf{K}_a \mathbf{\Phi} \\ R_m &= \mathbf{\Phi}^T \mathbf{R}_a \end{aligned} \tag{5.2}$$

Further introduction of the natural frequency and the damping ratio, given, respectively, by:

$$\omega_m = \sqrt{\frac{k_m}{m_m}}$$
$$\xi_m = \frac{c_m}{2\, m_m\, \omega_m} \tag{5.3}$$

and of the normalized modal displacement:

$$y_n = y\, m_m / R_m \tag{5.4}$$

leads to:

$$\ddot{y}_n + 2\xi_m\, \omega_m\, \dot{y}_n + \omega_m^2\, y_n = -\ddot{u}_b \tag{5.5}$$

which is the standard equation for mass dampers [note that this equation is equivalent to Equation (2.5) presented earlier] describing the behavior of any linear mass damper. As illustrated in Chapter 2 for liquid column dampers derivation of this equation requires definition of a similar normalized damper displacement.

The transmitted force can be expressed using the previous transformations as:

$$F = -\rho\, d \left[\mathbf{A\Phi} \frac{R_m}{m_m} \right] \ddot{y}_n - \rho\, d\, B\ddot{u}_b \tag{5.6}$$

The first term in this equation is related to the liquid sloshing and the second to the acceleration imposed at the base of the tank. When the floating roof has small accelerations (this situation can occur when $\ddot{u}_b$ has a frequency contain far away from the first sloshing frequency) the first component can be neglected and the total transmitted force to the base corresponds to the total mass of liquid multiplied by the

acceleration of the tank-base (fluid-tank behaves as a rigid body). This shows that term ρdB may be considered to correspond to the liquid mass, denoted from now on as m_{liq}, while B may be interpreted as the transversal area of the tank.

Of course for general excitation conditions the effect of the sloshing on the transmitted force needs to be taken into account and for better characterizing this effect the following efficiency index is defined, dependent upon only the tank geometry:

$$\gamma = \mathbf{A\Phi}\left(\frac{R_m}{B m_m}\right) \tag{5.7}$$

The introduction of the efficiency index allows to rewrite Equation (5.6) as:

$$\begin{aligned} F &= -m_{liq}\left[\gamma\right]\ddot{y}_n - m_{liq}\ddot{u}_b \\ &= m_{liq}\left[\gamma 2\xi_m \omega_m\right]\dot{y}_n + m_{liq}\left[\gamma \omega_m^2\right] y_n - m_{liq}[1-\gamma]\ddot{u}_b \end{aligned} \tag{5.8}$$

where for deriving the second equality Equation (5.5) was utilized. The efficiency index represents the amount of liquid that participates in the sloshing; an efficiency index equal to zero indicates a non-sloshing condition (case described previously) in which the liquid acts like a rigid body. On the other extreme, an efficiency index equal to 1 indicates that the whole liquid mass is participating in the sloshing and contributing dynamically in the transmitted force, condition which corresponds to a traditional TMD. In general, only part of the liquid is expected to contribute dynamically in TLDs (Sun et al., 1995), which indicates that the values of the efficiency index range between zero and one.

This efficiency index discussed here is equivalent to the similar parameter introduced in (Taflanidis et al. 2007) to describe the behavior of liquid column dampers (TLCDs/LCVAs) as discussed in Chapter 2 (Section 2.1). For liquid column dampers the efficiency index is related to the percentage of the total mass that participates in the horizontal liquid vibration and as discussed in Section 2.1 its calculation is straightforward as explicit relationships for it exist (relating it to the geometry of the liquid columns). For the TLD-FR it needs to be ultimately calculated through the FEM approach discussed in the previous Section. It leads, though, to an identical representation of the transmitted force to the supporting structure as for general mass dampers, with only one part of the total liquid mass contributing through inertia effect on that force, represented by term $m_{liq}[\gamma]\ddot{y}_n$ in Equation (5.8). This equation is identical to Equation (2.6) that holds for general mass dampers considering the equivalence of mass, frequency and damping properties in the two cases, $m_d = m_{liq}$, $\omega_d = \omega_m$ and $\xi_d = \xi_m$, and the differences in the notation for the damper and base displacements $y_{n_o} = y_n$ and $u_o = u_b$. This is the reason that the parameter in Equation (5.7) has been chosen to be termed as efficiency index, though it does not seem similar to the same parameter used for liquid column dampers. It ends up describing exactly the same behavior, that is, the fact that only one part of the total liquid mass contributes in the considered vibratory behavior (for different reasons for each of these

two type of liquid dampers), and leads to an identical formulation of the equations of motion.

Should be also pointed out that alternative definitions of the efficiency index have been proposed for mass dampers [for example the one in (Chang 1999) combining the efficiency index as it is defined here with the mass ratio for the damper], but the definition adopted here is preferable since it gives direct information about the amount of liquid that participates in the vibration mode.

Finally the parametric formulation leads to description of a TLD-FR operating in its fundamental model through only 4 variables when considering response in terms of normalized modal displacements, its mass m_{liq}, its efficiency index γ, its natural frequency ω_m, and its damping ratio ξ_m. The first three variables are related to the tank geometry, with the latter two completely dependent upon the tank transversal area and the first one independently defined through proper selection of the tank width, whereas the fourth variable is ultimately related to the external dampers and (as will be discussed later) any internal (inherent) damping existent in the vibration of the liquid. If the modal displacement is required then knowledge of ratio m_m / R_m is also needed to invert the relationship of Equation (5.4). But if the response of the primary structure is only of interest (i.e. the efficiency of the TLD-FR implementation) then the latter is not required. This formulation also directly relates the behavior of TLD-FR to the behavior of liquid column dampers and TMDs (with the later corresponding to γ=1). Therefore

results from the analysis of liquid column dampers (Chang 1999; Taflanidis et al. 2007) discussed in Section 2.2 directly extrapolate to the TLD-FR: higher values for γ or of m_{liq} lead to better efficiency (greater suppression of the vibration of the primary structure) whereas they also effect the optimal tuning values for ω_m and ξ_m. In particular, the optimal values for both ω_m and ξ_m of the TLD-FR decrease if m_{liq} or γ increase whereas the efficiency (suppression of primary structure vibration) is very sensitive to the frequency of the TLD-FR and to damping ratios lower than the optimal damping (Chang 1999; Taflanidis et al. 2007).

The question then arises how does the transversal area affect the efficiency index and the sloshing frequency? This question is examined next by investigating the sensitivity of these two properties to the tank geometry characteristics.

5.2 Relationship of Transversal Geometry of the Tank to Vibratory Characteristics

The values of the efficiency index γ and sloshing period T_m (defined as $2\pi/\omega_m$) for different geometries of TLD-FR are presented here. In all instances the identification of γ and T_s are obtained through the SSM-FR described in section 4.2. The beam characteristics are chosen such that higher modes of the TLD-FR are not excited, i.e. the amplification factor presents only one peak at the fundamental frequency, similar to the cases presented in Figure 4.14.

5.2.1 Case 1: Rectangular Tanks

The simplest configuration is the rectangular tank, completely defined by the length L and the water depth H (Figure 2.3) or the aspect ratio R=H/L. Results for this case are presented in Figure 5.1. It is observed that for aspects ratios greater than certain value (approximately R>0.8) the sloshing period only depends on L. The easiest way for TLD to change its sloshing period, which is an important characteristic for establishing tuning of its properties, is by altering the water depth while the length of the tank is kept constant, situation that corresponds to the use of the same tank while the amount of liquid inside the tank is altered (same L but allowing changes in H). In that sense and observing the results presented in Figure 5.1, it is clear that TLD-FRs with aspects ratios greater than 0.8 (shaded area) should be avoided since the sloshing period is not sensitive to changes of H for these configurations.

On the other hand the efficiency index is independent of L and is completely defined by the shape of the tank (R). This validates the preference for using R for describing the tank geometry since it leads uniquely to definition of R. Tanks with lower aspect ratios present higher efficiency indexes. Therefore, geometries with higher aspects ratios are also non-desired (shaded area in Figure 5.1 below) since efficiency of vibration suppression is larger for larger values of γ.

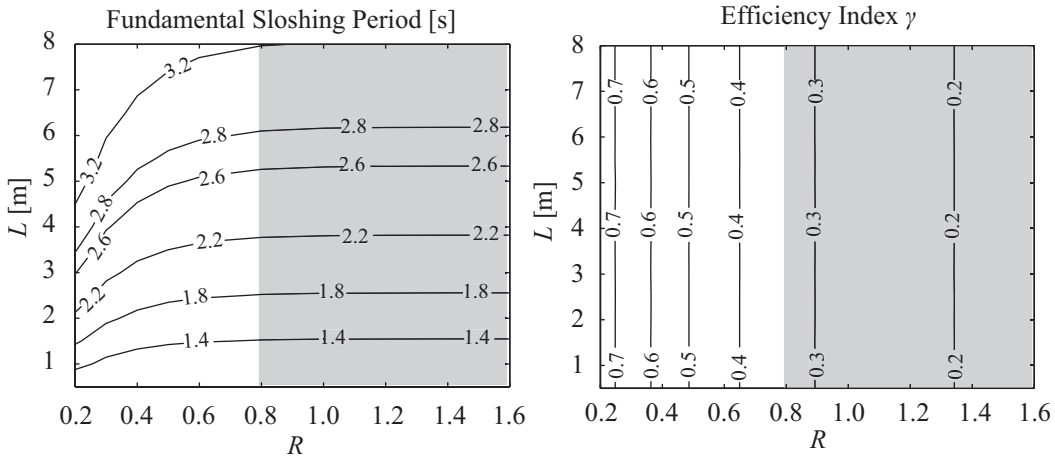

Figure 5.1 Fundamental periods and efficiency indexes for different TLD-FR for rectangular tanks

Additionally, it is possible to compare the efficiency indexes of TLDs-FR with linear TLDs, as demonstrated in Figure 5.2. Although the TLD-FR presents higher efficiency indexes the difference is small (around 2% more of liquid acts in the TLD-FR), something that should be attributed to the fact that both dampers have similar but not identical modal shapes (as discussed previously in Section 4.4). Therefore the presence of the floating roof also contributes, though only at a small fraction, on the amount of liquid that participates in the fundamental mode of vibration for the TLD.

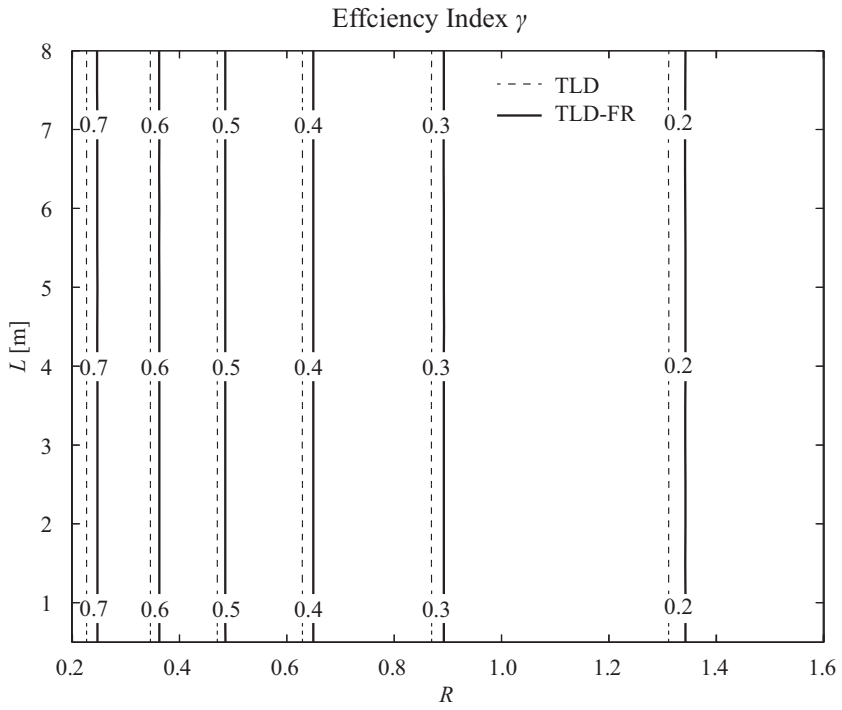

Figure 5.2 Comparison of efficiency indexes for different TLDs-FR and TLDs for different rectangular tanks

5.2.2 Case 2: Non-Rectangular Tanks

Further manipulation of the efficiency index and sloshing period can be established by considering more complicated, non-rectangular tanks. Here two different tank geometries are examined corresponding to U-Tank and T-Tank presented in Figure 2.4. The sensitivity of the efficiency index and sloshing period to changes in the geometry of U-Tanks is studied first and the results are presented in Figure 5.3. Set of iso-curves for sloshing period and efficiency index are shown for three different configurations: (a) R=0.2 and L=4m, (b) R=0.2 and L=6m and (c) R=0.4 and L=4m. In that sense, the configurations (a) and (b) correspond to tanks with the same shape but

different sizes, while the configurations (a) and (c) correspond to tanks with the same length L but different shapes.

The first interesting result is that the sensitivity of the sloshing period increases for lower values of $\bar{a}$ and higher values of $\bar{h}$, configuration that corresponds to tanks with a transversal sections close to conical. Moreover, those configurations present also a higher efficiency index indicating that the largest part of the liquid, more than 88% for configuration (a) and (b), contributes in the sloshing. It is also observed that configuration (a) and (b) present the same efficiency index, indicating that it is sensitive only to the shape and not to the size of the tank. On the other hand, comparing configuration (a) with (c), it is evident that for higher values of R the efficiency index presents an important reduction. These trends follow the ones for rectangular tanks but demonstrate a significant sensitivity to the other transversal area characteristics.

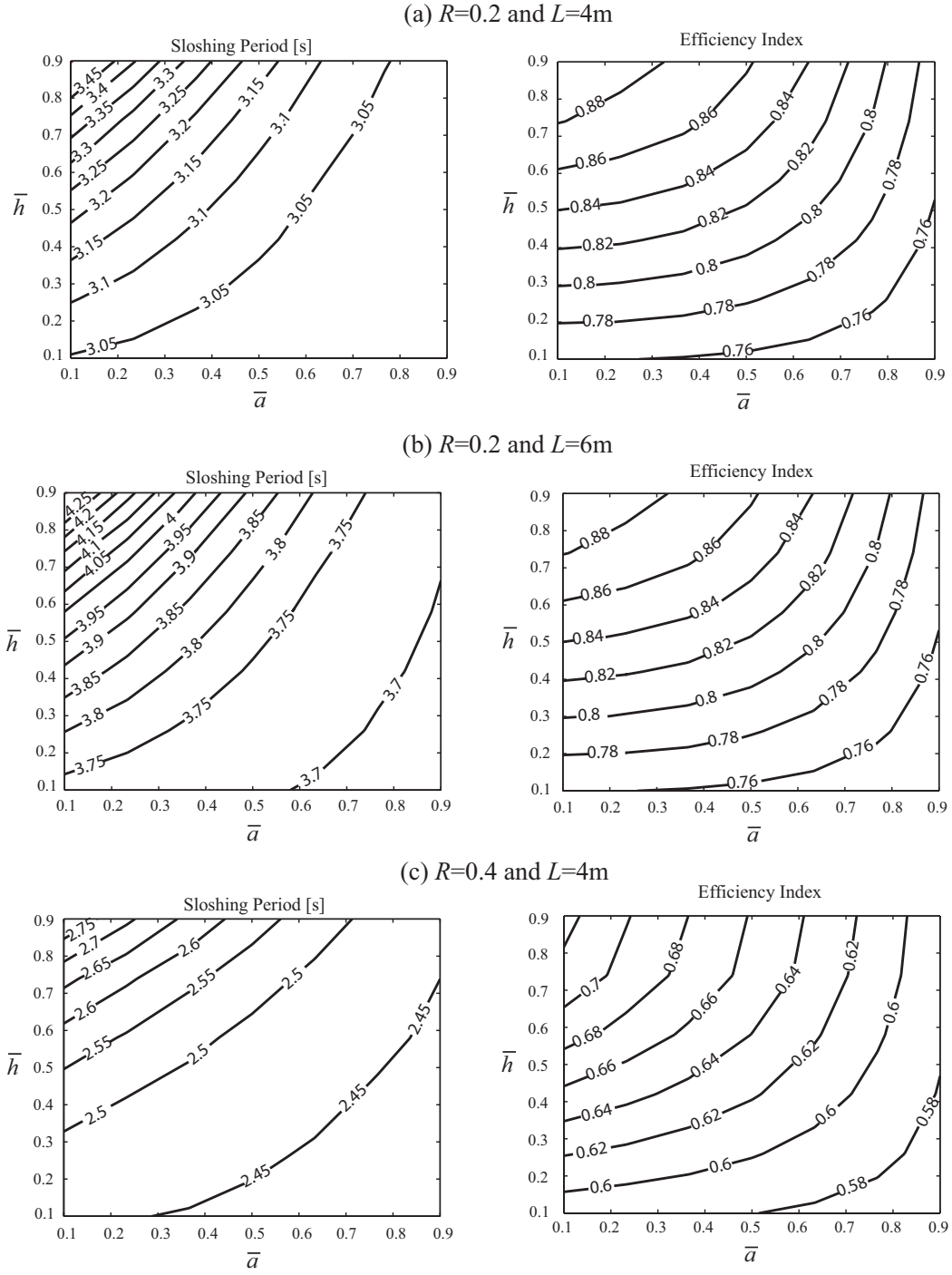

Figure 5.3 Iso-curves for fundamental periods and efficiency indexes of a TLD-FR employing a U-tank. Upper row corresponds to: (a) R=0.2 and L=4m, center row to (b) R=0.2 and L=6m and lower row to (c) R=0.4 and L=4m

(a) R=0.2 and L=4m

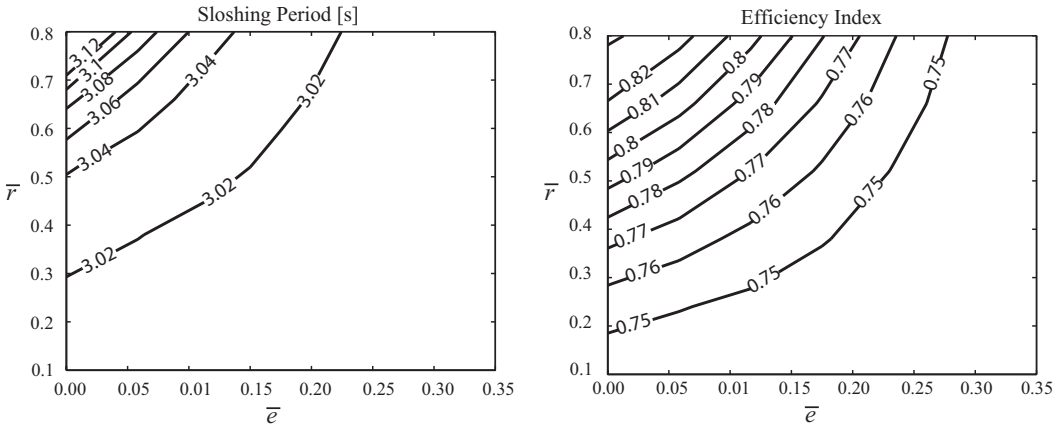

(b) R=0.2 and L=6m

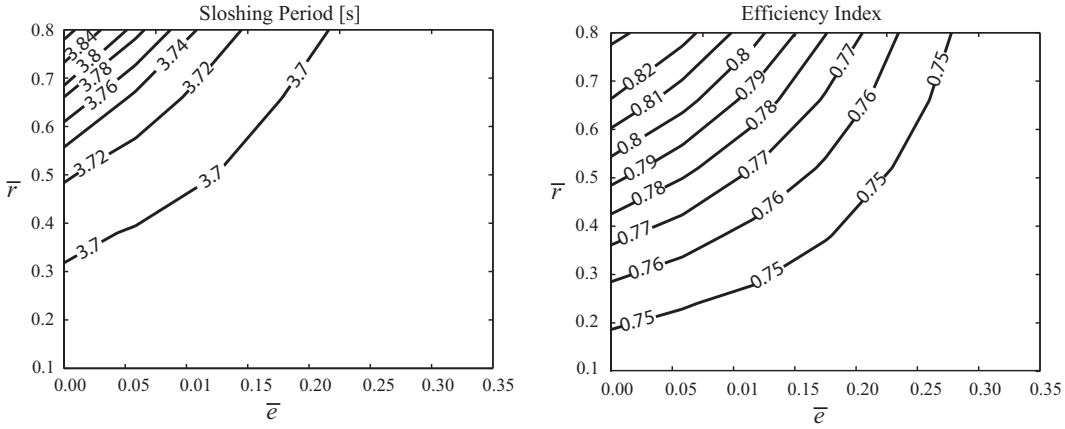

(c) R=0.4 and L=4m

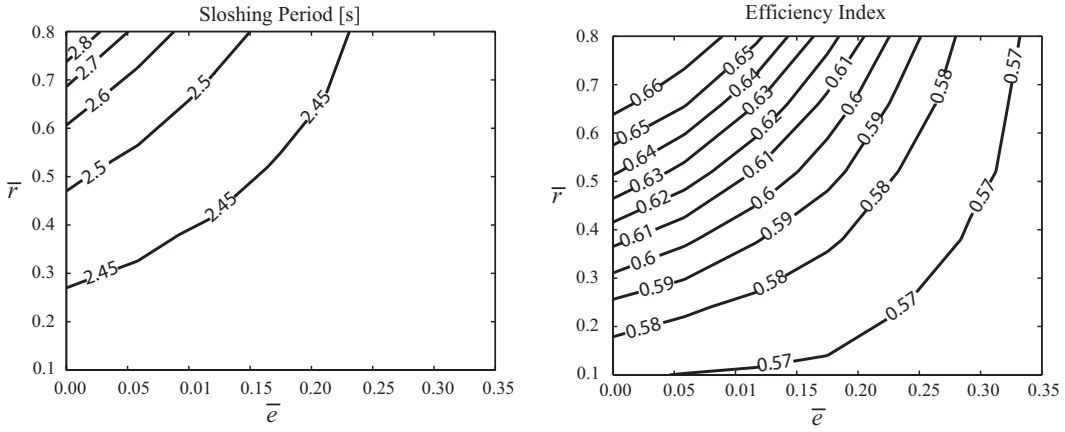

Figure 5.4 Iso-curves for fundamental periods and efficiency indexes of a TLD-FR employing a T-tank. Upper row corresponds to: (a) R=0.2 and L=4m, center row to (b) R=0.2 and L=6m and lower row to (c) R=0.4 and L=4m

A similar analysis is performed with the T-Tank examining the same combination for R and L. Results are shown in Figure 5.4. Large sensitivity of the sloshing period for lower eccentricities $\overline{e}$ and higher radius $\overline{r}$ is again reported whereas the efficiency index in sensitive to the shape and not to the scale of the tank with lower aspect ratios contributing to larger efficiency indexes.

The overall discussion shows the following trends (i) tanks with lower aspect ratios present higher efficiency indexes (it is easier for shallow tanks to incorporate greater amount of liquid in the sloshing vibration), (ii) the efficiency index depends entirely on the shape and not on the size of the tank (tanks can be scaled without affecting the efficiency index), (iii) the sloshing period sensitivity due to changes in the geometry is higher for configuration with higher efficiency indexes.

Another important, final, remark it that higher values of the efficiency index (say higher than 0.5) are straightforward to obtain for all the different tank geometries examined here for the TLD-FR. The same is not true for liquid column mass dampers. For example, based on the discussion in Section 2.1, for a TLCD a value of the efficiency index equal to 0.5 means that 70% of the total liquid mass is within the horizontal part of the tube. This allows for only 15% of the total liquid-column length within each of the two columns of the tube, which reduces significantly the allowable liquid displacement (to 15% of the total liquid-column length) making the configuration impractical. Of

course, behavior of the TLD-FR approaching the one of TMDs (efficiency index equal to 1) is challenging to achieve.

5.3 Design of TLD-FR and Relationships between Parametric Description and Tank Configuration

It was illustrated in the previous two sections that the behavior of the TLD-FR can be described through only four variables, representing characteristics of the fundamental sloshing mode, whereas the tank geometry has a big impact on these variables. When represented in terms of these four variables the TLD-FR can be considered equivalent to linearized liquid column dampers with the efficiency index definition facilitating this equivalence. All results from liquid column dampers can be then directly extrapolated to the TLD-FR. For efficiency index equal to one the TLD-FR is identical to a TMD.

Design of the TLD-FR requires, therefore, first an optimal selection of these four variables based on any appropriately defined criteria as discussed in Chapter 1 and then selection of the damper configuration and tank geometries based on these four variables. This two-stage approach is preferable over the alternative, i.e. the optimization directly for the tank/damper configurations since the latter (i) is a highly non-convex problem since it is evident from the discussion in the previous section that multiple geometries lead to exactly same vibratory characteristics, (ii) has a large

associated cost since it requires implementation of the SSM-FR at each iteration of the optimization to derive the equations of motion for the TLD-FR.

Of course the match of the parametric formulation to the physical characteristics of the TLF-FR is still required. For the m_{liq} this is easily established by selecting the transverse width d that has no effect on any other vibratory characteristics. If architectural constraints do not allow for use of such a large d then multiple TLD-FR can be considered with sum of widths equal to the targeted width. The tank geometry can be then chosen to match the intended efficiency index and frequency while also considering the displacement of the roof whereas the dampers can be chosen to match the damping ratio. These two are separately discussed next, with greater emphasis placed on the first topic.

5.3.1 Selection of Tank Geometry Based on Efficiency Index and Frequency

The tank geometry can be chosen based on the targeted efficiency index and frequency. For rectangular tanks this is a unique relationship and the two vibratory characteristics lead to a unique definition of the two tank dimensions (H-L). Note that in this case, as shown in Figure 5.3 earlier, a one-to-one relationship holds between the efficiency index and $R=H/L$ whereas any sloshing period can be established independently of the efficiency index. The unique relationship between the vibratory characteristics and the dimensions of the tank does not extend to more complex tank geometries that are characterized by a larger number of geometrical parameters

(defining the transverse tank area), such as the U and T tanks discussed in the previous Section, with characteristics also shown in Figure 2.4. In this case different tank geometries can lead to the same characteristics of vibration.

An additional challenge is the fact that this mapping does not have an analytic closed-form solution, relying on FEM analysis based on the SSM-FR approach. To circumvent the computational burden of repeating the FEM analysis for every geometrical configuration examined, derivation of an approximate relationship based on kriging metamodeling is adopted here. Kriging (Lophaven et al. 2002) in this case offers a surrogate model between the input parameters (tank geometrical characteristics) and the output of interest (vibratory characteristics used to provide the simplified parametric formulation) and is built using an extensive base of high-fidelity (established through the FEM analysis) evaluations of the input-output pair (also known as support points). After generated, the metamodel can be then used to represent the input output mapping and find all configurations that lead to the targeted vibration properties, for example through an exhaustive blind search (Coello et al. 2007). Kriging is chosen here for this purpose (over other available metamodel) because it has been proven accurate in approximating complex functions and it is highly efficient in blind search setting since it can be easily parallelized as it relies simply on matrix manipulations (Jia and Taflanidis 2013). A review of the equations for the kriging metamodel is provided in Appendix C.

The intended selection of tank geometries is established finally through the following process. First a kriging metamodel is developed to approximate the system output of interest $\mathbf{z}$, corresponding to natural frequency (period T_m is used here), efficiency index γ and parameters needed to describe the actual liquid modal displacement (ratio R_m/m_m) so that $\mathbf{z}=[T_m \quad \gamma \quad m_m / R_m]^T$, as a function of the tank geometry, corresponding to the system input $\mathbf{x}$. The latter depends on the tank characteristics, for example for V-Tanks the input is defined by $\mathbf{x}=[L \quad R \quad \bar{a} \quad \bar{h}]^T$. For developing this metamodel an initial database of n_{sup} (=8000 in the case study discussed later) support points is established based on the FEM approach and some choice for the EI value (this selection will ultimately not affect the dynamic of the system as demonstrated earlier in Chapter 4.4) and using Latin Hypercube Sampling to decide on the support points based on the range X that the input $\mathbf{x}$ is expected to take values is. Note that this is independent of the structure and application of interest, i.e the metamodel is developed once and used then as needed. Based on the targeted values for T_m and γ the input parameters $\mathbf{x}$ (that lead to the corresponding output) are subsequently identified. This can be established in a blind-search approach, especially for complex geometries for which a manifold is expected to exist in the $\mathbf{x}$ space that provide same $\mathbf{z}$ (more on this in the case study discussed later). Such manifolds cannot be identified through algorithms identifying only countable solutions (or even yielding a unique solution). This blind-search entails a derivation of another, very extensive in this

case database (10.000.000 components in the case study discussed later), this time established by utilizing the surrogate model. Note that this latter database is also independent of the application considered and can be used multiple times. Finally the value m_m/R_m can be used to examine the implications of the liquid vibration, i.e. whether the floating roof might encounter obstacles in its vibration and hits side walls or bottom of the tank. This can be accommodated by calculating the free space available as will be illustrated in the example considered later.

5.3.2 Damper Configuration

The relationship between the damping ratio and the external dampers can be established by utilizing Equations (4.7) and (5.2) and the definition of ξ_m, to lead to

$$\mathbf{\Phi}^T \mathbf{G}^{-1} \mathbf{R}_d^T \begin{bmatrix} C_{damper\,1} & & 0 \\ & \ddots & \\ 0 & & C_{damper\,N} \end{bmatrix} \mathbf{R}_d \mathbf{\Phi} = 2\,\xi_m\,\omega_m\,M_m \qquad (5.9)$$

Based on known ξ_m (and ω_m) the damper coefficients can be then chosen so that the above equality is satisfied. Using the same coefficients for all dampers will lead to a unique solution, though the approach allows the adoption of dampers with different coefficients. It was, though, experimentally demonstrated in section 4.3.2 that TLD-FRs present some level of inherent damping (i.e., damping that is not associated with the external dampers), related to drag between liquid and floating roof, which contributes to the total damping ratio ξ_m. This can be taken into account as discussed earlier by expressing the total damping ratio as the sum of the inherent (ξ_{inh}) and the external (ξ_{ext})

damping ratios, such that $\xi_m=\xi_{inh}+\xi_{ext}$. The external dampers are then designed based on the ξ_{ext}, i.e. ξ_{ext} is used in Equation (5.9) instead of ξ_m. Since a complete understanding (ability to predict it reliably) is not yet available for ξ_{inh} a conservative approach is to use a small value for ξ_{inh}; as discussed earlier high sensitivity is expected for values of ξ_m less than the optimal one (common characteristic of linear mass dampers as demonstrated in Figure 2.2), yielding to significant deterioration of the level of protection offered by the TLD-FR. Therefore a conservative approach is to assume a small value for ξ_{inh} so that to guarantee a damping factor equal or greater than the optimal damping ratio.

5.4 Case Study for Design of TLD-FR

The TLD-FR design procedure discussed above is demonstrated in this section. The focus is here on the selection of the characteristics of the TLD-FR so a relative simple, but very popular for mass dampers, performance quantification is adopted, considering the variance reduction under stationary earthquake excitation for a single-degree of freedom (SDOF) oscillator. This SDOF ultimately represents the fundamental mode for the structure that is controlled through the introduction of the mass damper. Though design procedures for mass dampers mainly focus on the suppression of the vibration of the primary structure, as discussed in the introduction the displacement of the secondary mass is also of concern (Kim and Kang, 2012)(Chakraborty et al., 2012). This is particular important for TLD-FR or even for TLCD and LCVA applications, so that undesired behaviors that compromise its effectiveness can be avoided, e.g., collision of

the floating roof at the bottom part of the tank for the case of TLD-FR or displacement of parts of the liquid outside of a column in TLCD or LCVA. For TLD-FR applications with complex geometries such concerns can be indirectly incorporated in the analysis by selecting a proper configuration (that allows greater movement of the floating roof) among the manifold of solutions yielding the same vibratory characteristics.

5.4.1 Equation of Motion and Response under Stationary Excitation

The equations of motion of a structure with TLD-FR are established through the parametric formulation by utilizing Equation (5.8) to describe the transmitted force and Equation (5.5) to characterize the TLD-FR vibration. As discussed in Section 2.2. for general mass dampers, the mass ratio, r, defined as the ratio of the liquid mass m_{liq} to the total mass of the structure m_s (i.e. $m_{liq}=rm_s$), and the tuning ratio α, defined as the ratio of the fundamental sloshing frequency ω_m to the SDOF frequency ω_s (i.e. $\omega_m=\alpha\omega_s$), can be further used to simplify parametric description. Therefore, the dynamic behavior of the coupled system is described by four non-dimensional parameters: the mass ratio r, the damping ratio ξ_m, the tuning ratio α and the efficiency index γ. Denoting as in Section 2.1 by ω_s, ξ_s and m_s the natural frequency, damping ratio and mass of the SDOF, u_o its displacement relative to the ground and $\ddot{u}_g$ the base acceleration, then the coupled system of equations of motion is:

$$\begin{bmatrix} 1+r & \gamma r \\ 1 & 1 \end{bmatrix}\begin{bmatrix} \ddot{u}_o \\ \ddot{y}_n \end{bmatrix}+\omega_s\begin{bmatrix} 2\xi_s & 0 \\ 0 & 2\xi_m\alpha \end{bmatrix}\begin{bmatrix} \dot{u}_o \\ \dot{y}_n \end{bmatrix}+\omega_s^2\begin{bmatrix} 1 & 0 \\ 0 & \alpha^2 \end{bmatrix}\begin{bmatrix} u_o \\ y_n \end{bmatrix}=-\begin{bmatrix} 1+r \\ 1 \end{bmatrix}\ddot{u}_g \qquad (5.10)$$

This formulation further verifies the aforementioned equivalence to other type of mass dampers as Equation (5.10) is identical to Equation (2.10).

For calculating the response to stationary excitation a state space approach is adopted here (Lutes and Sarkani 1997; Taflanidis and Scruggs 2010). For this purpose Equation (5.10) is re-arranged in state space format as:

$$\begin{aligned}
&\dot{\mathbf{x}}_o = \mathbf{A}_o\,\mathbf{x}_o + \mathbf{B}_o\,\ddot{u}_g \\
&\mathbf{y}_o = \mathbf{C}_o\mathbf{x}_o \\
&\mathbf{A}_o = \begin{bmatrix} \mathbf{0}_{2x2} & \mathbb{I}_2 \\ \omega_s^2\begin{bmatrix} 1+r & \gamma r \\ 1 & 1 \end{bmatrix}^{-1}\begin{bmatrix} 1 & 0 \\ 0 & a^2 \end{bmatrix} & \omega_s\begin{bmatrix} 1+r & \gamma r \\ 1 & 1 \end{bmatrix}^{-1}\begin{bmatrix} 2\xi_s & 0 \\ 0 & 2\xi_m\, a \end{bmatrix} \end{bmatrix} \\
&\mathbf{B}_o = \begin{bmatrix} \mathbf{0}_{2x1} \\ -\begin{bmatrix} 1+r & \gamma r \\ 1 & 1 \end{bmatrix}^{-1}\begin{bmatrix} 1+r \\ 1 \end{bmatrix} \end{bmatrix} \quad \mathbf{C}_o = \begin{bmatrix} 1 & 0 & 0 & 0 \\ 0 & 1 & 0 & 0 \end{bmatrix}
\end{aligned} \tag{5.11}$$

where the state vector is defined as $\mathbf{x}_o = [u_o \quad y_n \quad \dot{u}_o \quad \dot{y}_n]^T$, the output vector is composed of displacements for the SDOF and TLD-FR $\mathbf{y}_o = [u \quad y_n]^T$, $\mathbf{0}_{jxk}$ is a matrix of zeros with dimension of *jxk* and $\mathbb{I}_j$ is the identify matrix of dimension *j*. The earthquake excitation is modeled as a stationary stochastic process using the well known Kanai-Tajimi filter (Ray Clough and Penzien 1993), expressed in a state-space form as:

$$\begin{aligned}
&\dot{\mathbf{x}}_g = \mathbf{A}_g\,\mathbf{x}_g + \mathbf{B}_g w \\
&\ddot{u}_g = \mathbf{C}_g\mathbf{x}_g \\
&\mathbf{A}_g = \begin{bmatrix} 0 & 1 \\ -\omega_g^2 & -2\xi_g\omega_g \end{bmatrix} \;;\; \mathbf{B}_g = \begin{bmatrix} 0 \\ 1 \end{bmatrix} \\
&\mathbf{C}_g = \sqrt{2\pi\, s_o}\begin{bmatrix} \omega_g^2 & 2\xi_g\omega_g \end{bmatrix} \;;\; s_o = \frac{2\xi_g\,\sigma_g}{\pi\omega_g\left(4\xi_g^2+1\right)}
\end{aligned} \tag{5.12}$$

where the input *w* represents zero mean Gaussian white noise, ω_g corresponds to the dominant frequency of the ground motion, ξ_g controls its bandwidth while σ_g defines the RMS value of the acceleration $\ddot{u}_g$.

Augmentation of the two previous state space representations ultimately leads to the final desired state-space formulation:

$$\begin{aligned} \dot{\mathbf{x}}_s &= \mathbf{A}_s\,\mathbf{x}_s + \mathbf{B}_s w \\ \mathbf{y}_o &= \mathbf{C}_s \mathbf{x}_s \\ \mathbf{x}_s &= \begin{bmatrix} \mathbf{x}_o^T & \mathbf{x}_g^T \end{bmatrix}^T ;\ \mathbf{A}_s = \begin{bmatrix} \mathbf{A}_o & \mathbf{B}_o\mathbf{C}_g \\ \mathbf{0} & \mathbf{A}_g \end{bmatrix} ;\ \mathbf{B}_s = \begin{bmatrix} \mathbf{0} \\ \mathbf{B}_g \end{bmatrix} ;\ \mathbf{C}_s = \begin{bmatrix} \mathbf{C}_o & \mathbf{0} \end{bmatrix} \end{aligned} \tag{5.13}$$

that has as input the white noise *w* and provides output $\mathbf{y}_o$ composed of the displacements for the SDOF and the floating roof.

Under these assumptions (white noise), the output has zero mean and a covariance matrix defined by:

$$\mathbf{K}_{\mathbf{y}_o\mathbf{y}_o} = \mathbf{C}_s \mathbf{P} \mathbf{C}_s^T \tag{5.14}$$

where the state covariance matrix $\mathbf{P}$ is determined by the solution of the Lyapunov equation (Lutes and Sarkani 1997):

$$\mathbf{A}_s\mathbf{P} + \mathbf{P}\mathbf{A}_s^T + \mathbf{B}_s^T\mathbf{B}_s = 0 \tag{5.15}$$

The structure response variance $\sigma_{u_o}^2$ corresponds to the first diagonal element of the covariance matrix $\mathbf{K}_{\mathbf{y}_o\mathbf{y}_o}$ and the modal floating roof response variance $\sigma_{y_n}^2$ to the second diagonal element.

5.4.2 Design Procedure

The optimal design is finally formulated by identifying the characteristic of the TLD-FR that minimize $\sigma_{u_o}^2$:

$$\mathbf{q} = \arg\min_{\mathbf{q}\in Q} \left(\sigma_{u_o}^2 (\mathbf{q}) \right) \tag{5.16}$$

where the vector $\mathbf{q}$ contains the TLD-FR variables that are going to be optimized and Q represents the admissible design space Q. The optimization for stationary response is conducted assuming specific valued for the efficiency index and the mass ratio (since larger values for either of them leads to higher efficiency in terms of reduction of the displacement of the primary structure), meaning that $\mathbf{q}$ corresponds here to the damping ratio ξ_m and the frequency ratio α. Therefore, the optimization of Equation (5.16) represents tuning of the parameters of the TLD-FR.

This process will lead to a desired configuration in the parametric space, characterized by r_{opt} [or equivalently $m_{liq,opt}= r_{opt}m_s$], γ_{opt}, α_{opt} [or equivalently $T_{opt}=2\pi/(\omega_s\alpha_{opt})$] and ξ_{opt}. It is necessary then to select the tank geometry and the external damper characteristics that lead to this configuration, following the blind-search process discussed in the previous Section and exploiting the established surrogate model. An additional preference can be then incorporated in the final selection considering the amplitude of vibration for the floating roof among the configurations leading to the same efficiency. This is established through the following approach: a maximum admissible amplitude is adopted y_{adm} as a percentage of the

water depth H, leading to a constraint for the standard deviation of the response, i.e. desire that the actual response of the floating roof be bounded by y_{adm}. This entails multiplication of σ_{y_n} by ratio R_m / m_m so that the standard deviation for modal displacement is converted to standard deviation for maximum displacement of the roof by the wall. Therefore the identification of the transversal geometry of the tank is established so that T_m is equal to $2\pi/(\omega_s \alpha_{opt})$, γ is equal to γ_{opt} and $\sigma_{y_n} R_m / m_m$ is less than a fraction (say 1/3 or 1/4) of y_{adm}. The latter fraction is utilized to convert statistical quantities to expected maximum displacements; in the example in the parenthesis above the max displacement is considered, respectively, 3-5 standard deviations away from the mean –this might seem like optimistic values but since stationary excitation is being considered they are rather conservative. An alternative approach would have been to consider the first-passage problem to identify the probability that the displacement of the roof exceeds the acceptable threshold (Taflanidis et al. 2007).

5.4.3 Illustrative Implementation

For the illustrative implementation the structure is considered to have natural frequency of $\omega_s = \pi$ rad/sec (corresponding to 2sec of natural period) and damping ratio ξ_s = 2% while the TLD-FR corresponds to a U-Tank (reference is shown in Figure 2.4). For the excitation common recommendation for the Kanai-Tajimi filter are adopted: $\omega_g = 2\pi = 4\omega_s$, ξ_g= 50% and σ_g = 0.11g. Note that the values for ω_s and σ_g do not affect the

optimization on the parametric space. They only impact the selection of the TLD-FR geometry because they influence the constraint for the response of the floating roof.

For the proposed blind-search identification a kriging metamodel is established. The input for this metamodel is the characteristics of the U-Tank geometry $\mathbf{x} = [L \quad R \quad \bar{a} \quad \bar{h}]^T$ whereas the output as discussed previously is $\mathbf{z} = [T_m \quad \gamma \quad m_m / R_m]^T$. The number of support points is selected as 8000 utilizing Latin-hypercube sampling within the following domain for $\mathbf{x}$: $L \in [2m, 4m]$; $\mathrm{R} \in [0.2, 0.8]$; $\bar{a} \in [0.05, 0.95]$; $\bar{h} \in [0.05, 0.95]$. The accuracy is evaluated though a cross-validation approach and the maximum error reported is lower than 2%, representing a very high accuracy for the kriging metamodel. For the blind-search 10.000.000 different tank configurations are generated, again within the aforementioned domain.

The optimization of Equation (5.16) is then performed for different combination of mass ratios *r* and efficiency indexes γ. The optimal damping and frequency ratios are reported in Figure 5.5 whereas Figure 5.6 shows the variation as function of *r* and γ of the percentage reduction of the response (standard deviation) though the introduction of the liquid damper, and of the standard deviation of the normalized amplitude of the floating roof σ_{y_n}. The results follow anticipated trends: higher values of *r* and γ lead to higher values of the optimal damping ratio and lower values of the optimal frequency and to higher efficiency (higher reduction of the response). Simultaneously they lead to lower values for the normalized roof displacement.

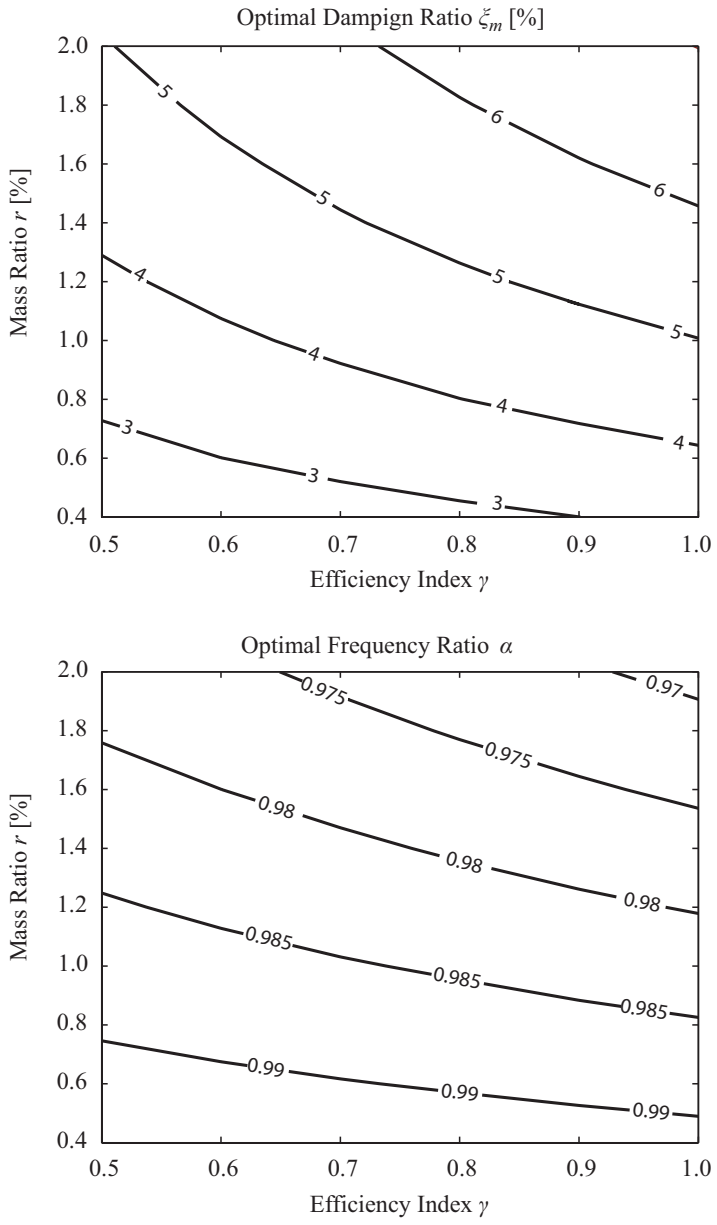

Figure 5.5 Optimal frequency and damping ratio for different efficiency indexes and mass ratios for a TLD-FR attached to a SDOF under stationary seismic excitation. Stationary variance is utilized as objective function.

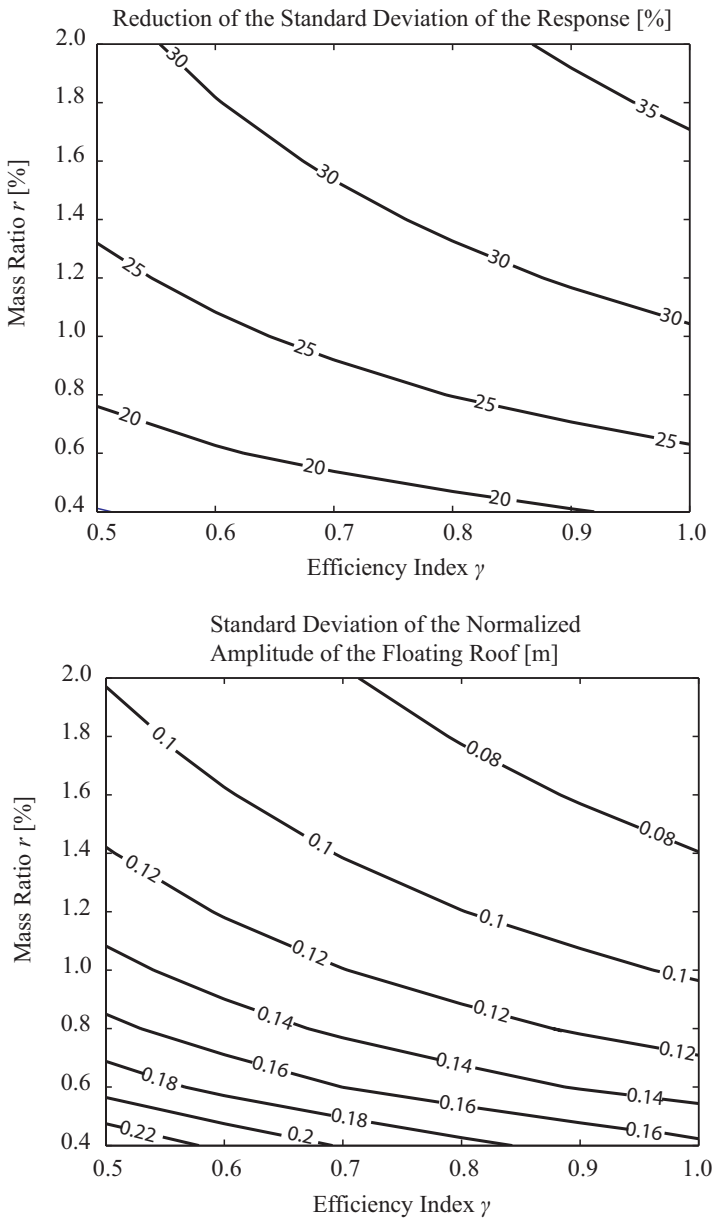

Figure 5.6 Responses of the structure (as percentage reduction over the uncontrolled response) and of the floating roof under optimal design for a TLD-FR attached to a SDOF under stationary seismic excitation. Stationary variance is utilized as objective function for calculating the optimal damper design configuration.

Ultimately, the designer has to decide the value of the mass ratio and the efficiency depending of particular constrains of each implementation. In this example,

1% of mass ratio [typical value for TMDs (Soong and Dargush 1997)] and an efficiency index equal to 0.5 [typical value for Tuned Liquid Column Dampers (Taflanidis et al. 2007)] are adopted. Using these values and the results presented in Figure 5.5 is possible to determine that the optimal parameters of the TLD-FR correspond to: γ= 0.5, *r* = 1%, α_{opt} = 0.9875 and $\xi_{m,opt}$ = 3.53 %. The use of a TLD-FR with these characteristics leads to a reduction of 22.47% and a normalized floating roof displacement of $\sigma_{y_n} = 0.15$ m.

Then, it is possible to perform a blind-search in the database to identify which geometries match with γ= 0.5, $T_{m,opt}$ = 2.03s (=T_s/α_{opt}) and $\sigma_{y_n} R_m / m_m \leq f_o \, y_{adm}$. In the latter condition three different fractions f_o of y_{adm} are used, taking the following values f_o = 1/3, 1/4 and 1/5 whereas the y_{adm} is defined as H-h (total available space for roof).

The respective geometries that match with those characteristics are presented in the Figure 5.7. The different symbols categorize the standard deviation of the amplitude of the floating roof in three groups: (1) amplitudes lower than 1/5 of the available space [identified with black squares], (2) amplitudes between 1/5 and 1/4 of the available space [identified with blue plus signs] and (3) amplitudes between 1/4 and 1/3 of the available space [identified with red circles]. An immediate observation is the fact that a large number of geometries exist that satisfy the desired vibratory characteristics, while having different associated amplitudes for the floating roof. The ability to identify all these configurations demonstrates the efficiency of the proposed blind-search

approach. Instead of finding a single configuration (if a traditional optimization approach was adopted) all these different configurations are successfully identified.

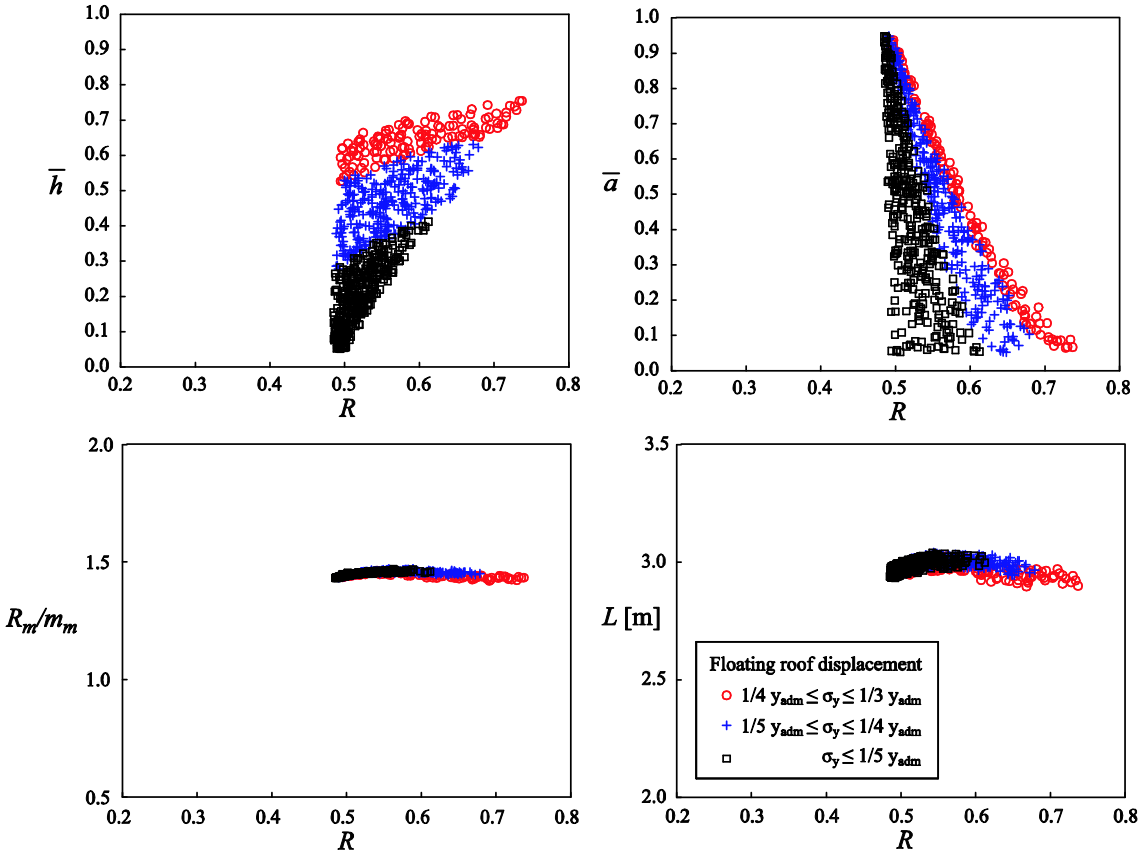

Figure 5.7 Characteristics for the different tank geometries that match with the optimal values of the TLD-FR and satisfy the various chosen constraints for the roof displacement. The value R_m/m_m is also shown. Value of R is used as reference for the comparisons and is included in all the subplots. With respect to the constraints for the floating roof, the configurations are separated into three different groups satisfying the different constraints (denoted with different symbols)

Remember that the interest in the floating roof amplitude is the avoidance of potential impacts with the bottom part of the tank. In that sense, geometries identified with black squares correspond to the most conservative case. For this case, lower values

of $\bar{h}$ are obtained, which is expected since lower $\bar{h}$ is associated with larger space in the vertical section of the wall. On the other hand, practically any $\bar{a}$ can be chosen for the three cases presented, indicating that its impacts on the displacement of the floating roof is not as relevant as $\bar{h}$. Additionally, the amplitude of the floating roof presents a low sensitivity respect to the length L and to the ratio R_m / m_m while it has an important sensitivity respect R when $\bar{h}$ and $\bar{a}$ have higher and lower values respectively. The latter condition can be explained if one considers that lower values of $\bar{h}$ and higher values of $\bar{a}$ represents configurations close to a rectangular tank for which, as explained earlier, the mapping between the vibratory characteristic and the geometry is one-to-one. Therefore only few aspect ratios R match the desired vibratory characteristics (with limiting case a single match).

Recall also that once the transversal area of the floating roof is defined (based on the chosen geometry for the cross-section al area), the identification of d (tank width) is straight forward; it is simply chosen to match the desired mass (1% of the mass of the primary system). If that width is excessive for a single tank (architectural/space constraints) then multiple, identical tanks can be used to provide the total required width. If the TLD-FR is intended to operate in bi-directional mode, then appropriate concurrent design in both directions is required, as discussed in Section 4.1.

Finally, equipped with the information in the Figure 5.7 as well as information about the necessary width, the designer can make a final choice as to which of these

geometries represents the best choice for a particular application taking into account the overall space constraints. As a last step, the characteristics of the external dampers can be obtained directly by the solution of the Equation (5.9), assuming a known inherent damping ξ_{inh} and defining the external damping ratio as $\xi_{ext} = \xi_{opt} - \xi_{inh}$. Since damping ratios lower than optimal deteriorates the protection offered by the TLD-FR (as discussed in Section 5.3.2), then a conservative scenario is to assume small values of inherent damping.

5.5 Summary

In this Chapter the fact that the TLD-FR behaves linearly and in a predominant mode was further exploited to establish a simplification for its equation of motion and to facilitate a simpler comparison to other type of mass dampers. Though modal analysis and truncation (retaining only the predominant mode) its equation of motion was simplified to a single-degree of freedom oscillator. Furthermore through a proper parameterization and normalization and, in particular, through the introduction of a parameter, termed efficiency index, that for TLD-FR represents the portion of the liquid mass contributing in the sloshing vibration in its fundamental mode, complete equivalence to the behavior of liquid column mass dampers was established. In parameterized format the behavior of any structure with a TLD-FR can be described by only four parameters that are common with the parameters used for other type of mass dampers: the mass, frequency and damping ratio and the efficiency index. Due to this

established equivalence all results for liquid column mass dampers and TMDs (representing the limiting case of efficiency index equal to 1) are directly extendable to the behavior of TLD-FR. Additionally, it was shown through parametric investigation for different tank geometries that higher values of the efficiency index are easy to obtain for the TLD-FR something that provides a distinct advantage over liquid column mass dampers. Though this investigation it was also shown that the efficiency index is related to the transversal geometry of the tank while the frequency is sensitive to its size and shape, i.e. tanks with the same shape present the same efficiency index but different fundamental frequencies.

For complex cross-sectional geometries (i.e. not rectangular tanks), different tank geometries can lead to the same efficiency index or fundamental frequency, creating a mapping that is not one-to-one. Motivated by this realization a design procedure was established to relate the four aforementioned parameters to geometrical properties of the TLD-FR. The targeted mass ratio (or more generally mass) can be established through proper selection of the tank width whereas the optimal damping ratio through proper dimensioning of the external dampers. In the latter case a conservative estimate of the inherent damping can be used to avoid damping values lower than the optimum one (feature that leads to significant deterioration of performance). The efficiency index and optimal frequency can be then chosen based on the cross-sectional tank geometry through a blind-search approach, so that all possible solutions can be identified. These solutions correspond, though, to different

displacements for the liquid, so considerations for the maximum allowable displacement to avoid collisions of the floating roof to the walls or bottom of the tank can provide an additional preference between these solutions. To support the blind-search a surrogate modeling approach was adopted; a highly efficient kriging metamodel was first developed to approximate the relationship between tank geometry and vibratory characteristics and this metamodel was then utilized for all evaluations required within the blind-search. This procedure was demonstrated for the design of a TLD-FR considering stationary earthquake excitation.

LIFE-CYCLE BASED DESIGN OF TLD-FR ADOPTING A SEISMIC RISK CHARACTERIZATION APPROPRIATE FOR CHILE

In the last decades significant advances have been established in seismic-risk decision management through development of assessment and design methodologies based on detailed socio-economic metrics quantifying life-cycle-performance/seismic-risk, such as casualties, repair costs and downtime (Goulet et al. 2007). A powerful framework, widely acknowledged to provide the basis for these advances, has been Performance Based Earthquake Engineering (PBEE) (Augusti and Ciampoli 2008; Zareian and Krawinkler 2012; Bozorgnia 2004). Within this context, the life-cycle cost analysis of structures has been becoming increasingly popular. This analysis considers in the decision making the contributions from the initial (upfront) cost as well as the maintenance cost and more importantly the expected direct and indirect losses due to future seismic events, and has motivated researchers to look into the life-cycle cost based assessment/design of structures (Ang and Lee 2001; Liu et al. 2003; Fragiadakis et al. 2006), especially in the context of retrofitting strategies or design of supplemental protective devices (Taflanidis and Beck 2009; Park et al. 2004; Shin and Singh 2014;

Tubaldi et al. 2014). For performing such an analysis, especially for estimating in detail losses and repair costs due to future seismic events, a probabilistic treatment of the problem is necessary for addressing the uncertainty in the seismic hazard description as well as uncertainties related to any other components of the assumed models (such as uncertainties associated with structural properties). Furthermore, recent studies have stressed the importance of the adoption of advanced criteria for describing life-cycle performance within such an assessment/design setting, especially criteria that can characterize risk-averse attitudes of the stakeholders (Cha and Ellingwood 2013; Haukaas 2008; Corotis 2009). Such an approach, extending beyond the simple adoption of total life-cycle cost as single performance objective, can support an enhanced seismic-risk decision management, especially if couched within a multi-criteria design formulation (Gidaris et al. 2014).

This Chapter implements these concepts for analysis/design of the TLD-FR to establish a more proper comparison to other type of mass dampers. To better understand the motivation for this comparison one needs to start first considering that like TLDs, TLDs-FR are characterized by a lower installation and maintenance cost than TMDs. The only difference between TLDs and TLDs-FR is the necessity to add the floating roof, which should not significantly increase cost. On the other hand it was demonstrated in Chapter 5 that for the same mass, TMDs offer enhanced vibration suppression, since they are ultimately characterized by a higher efficiency index. Therefore, proper comparison of such devices needs to consider the life-cycle

performance over their entire lifetime, incorporating both (a) the differences in upfront cost and (b) the benefits from the different level of vibration suppression (and thus benefits from reduction of seismic losses) offered by each. To support this goal, a simulation-based, probabilistic framework is developed here to estimate and optimize the life cycle cost of Chilean buildings with TLDs-FR, following the guidelines in (Taflanidis and Beck 2009). The simulation-based character of the framework allows for adoption of complex numerical and probability models to quantify risk and allows for explicitly addressing all important sources of variability within the examined models. Within this setting seismic losses are quantified through an assembly-based vulnerability approach (Porter et al. 2001), structural performance is evaluated through time-history analysis, an approach that agrees with recent recommendations for comprehensive probabilistic risk assessment (Deierlein 2004; Bozorgnia 2004), whereas seismic hazard is described through a stochastic ground motion model calibrated to offer hazard-compatibility for the Chilean region (Vetter et al. 2014; Boroschek and Contreras 2012).

The design is performed in the parametric space, which offers simpler characterization for the TLD-FR as discussed in Chapter 5. This also means that the approach considered here is directly applicable to all different mass dampers that enjoy the same parametric formulation (TMDs, TLCDs/LCVAs). A multi-objective formulation of the design problem is established following the guidelines in (Gidaris et al. 2014). Two different criteria, quantifying seismic risk, are utilized in the design optimization. The first one, representing the direct benefits from the mass damper implementation, is the

life-cycle cost of the system, composed of the upfront TLD-FR cost and the anticipated seismic losses over the lifetime of the structure (estimated through the aforementioned assembly-based vulnerability approach). The upfront cost of the damper is related to its mass and due to lack of information a framework is established, utilizing surrogate modeling and blind search techniques, that allows a straightforward incorporation of different assumptions for this cost-relationship. The second criterion is utilized to incorporate risk-aversion attitudes in the design formulation and corresponds to the consequences (repair cost) with a specific probability of exceedance over the lifetime of the structure. Since this metric is not influenced by the upfront damper cost it represents competing objectives to the life-cycle cost, leading to a multi-objective design setting. Solution of this problem leads to the Pareto-front of dominant solutions offering different compromise between the objectives.

Before formalizing the seismic risk assessment and design framework, the equation of motion for a multistory structure with a TLD-FR is quickly reviewed.

6.1 Equation of Motion for Multistory Buildings Equipped with TLD-FR

Utilizing the parametric formulation for the TLD-FR, specifically Equation (5.5), and its equivalence discussed in Chapter 5 to (linearized) TLCDs/LCVAs the equation of motion for a multi-degree of freedom planar structure equipped with a TLD-FR is given by Equation (2.8) [recall this equation is ultimately obtained by coupling Equations (2.7) and (5.5), using Equation (5.8) for the force transmitted from the tank to the structure

while expressing as $\ddot{u}_b = \mathbf{L}_s\left(\ddot{\mathbf{u}} + \mathbf{D}_o \ddot{u}_g\right)$ the acceleration at the base of the tank]. The resulting equation is

$$\begin{bmatrix} \mathbf{M} + \mathbf{L}_s^{\mathrm{T}} m_{liq} \mathbf{L}_s & \mathbf{L}_s^{\mathrm{T}} \gamma m_{liq} \\ \mathbf{L}_s & 1 \end{bmatrix} \begin{bmatrix} \ddot{\mathbf{u}} \\ \ddot{y}_n \end{bmatrix} + \begin{bmatrix} \mathbf{C} & 0 \\ \mathbf{0} & 2\xi_m \omega_m \end{bmatrix} \begin{bmatrix} \dot{\mathbf{u}} \\ \dot{y}_n \end{bmatrix} + \begin{bmatrix} \mathbf{K} & 0 \\ \mathbf{0} & \omega_m^2 \end{bmatrix} \begin{bmatrix} \mathbf{u} \\ y_n \end{bmatrix} = -\begin{bmatrix} \left(\mathbf{M} + \mathbf{L}_s^{\mathrm{T}} m_{liq} \mathbf{L}_s\right) \mathbf{D}_o \\ 1 \end{bmatrix} \ddot{u}_g \tag{6.1}$$

A dimensional characterization of the damper can be then established by using $m_{liq} = r\, m_t$ and $\omega_m = \alpha\, \omega_1$ where m_t is the total structural mass and ω_1 the fundamental structural frequency. For γ=1 and m_{liq}=m_d this equation describes a TMD. Note that linear structural behavior is assumed here since it has been shown that for the Chilean region modern design/construction practices results in structures that demonstrate practically linear behavior even under strong excitations (EERI Special Earthquake Report 2010). Extension to nonlinear behavior is, though, straightforward in the considered simulation-based setting for risk; it simply entails modification of the restoring force and adoption of a nonlinear description. This numerical model is ultimately formulated and solved in the SIMULINK dynamical system modeling environment of MATLAB.

6.2 Seismic Risk Quantification and Assessment

The quantification and evaluation of the different risk characterizations considered in this dissertation is presented in this Section.

6.2.1 Seismic Risk Quantification

Quantification of the life-cycle performance is established through the framework discussed in (Taflanidis and Beck 2009) by establishing a probabilistic description for the uncertainty in the model parameters used to describe the earthquake excitation and the structural performance. This modeling framework starts by the adoption of appropriate *excitation*, *structural* and *loss/performance evaluation* models, describing, respectively, the exposure, the vulnerability and the consequences within the risk characterization. The first model provides the seismic excitation given seismological parameters that are established through a seismic hazard analysis. The second model provides the structural response given that excitation, whereas the last quantifies the favorability of that response in terms relevant to the system stakeholders.

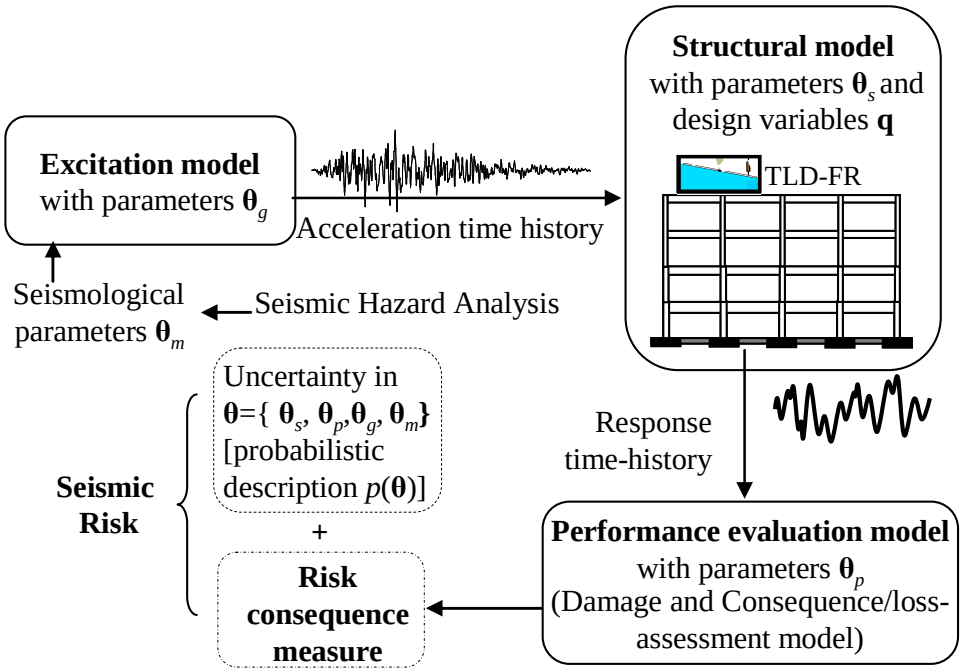

Figure 6.1 Modeling approach for seismic risk quantification

The characteristics of these models are not known with absolute certainty, with potential sources of uncertainty corresponding to (i) the properties of the structural system or to the fragility of its components (uncertainty for structural and performance assessment models), and (ii) to the variability of future seismic events and the characteristics of the resultant excitations (uncertainty for seismic hazard). A probabilistic approach provides a versatile framework for characterizing these uncertainties (Taflanidis and Beck 2009) and explicitly incorporating them into the system description ultimately leading to a rational definition of the seismic risk. Note that this framework (demonstrated in Figure 6.1) is consistent with PEER's approach (Moehle and Deierlein 2004), widely acknowledged to represent one of the most

important advances in seismic life-cycle performance assessment; simply it replaces the conditional probabilities in the PEER approach with the explicit introduction of a probabilistic description for the uncertainties in the various model parameters, and instead of a description of the seismic hazard based on intensity measures utilizes a compatible model-based description, relying on directly addressing the uncertainties on the seismological inputs and the ground motion properties to support the probabilistic characterization of the seismic excitation.

In this context let $\mathbf{q} \in Q$ denote the n_q-dimensional vector of TLD-FR design variables and let $\boldsymbol{\theta} \in \Theta$, denote the n_θ-dimensional augmented vector of model parameters where Θ represents the space of possible model parameter values and Q the admissible design space. Vector $\mathbf{q}$ here includes all parameters required for the TLD-FR characterization (as opposed to the case considered in Section 5.4.3), since a direct optimization for the damper mass is considered. Vector $\boldsymbol{\theta}$ is composed, as illustrated in Figure 6.1, of all the model parameters for the individual structural system $\boldsymbol{\theta}_s$, performance evaluation, $\boldsymbol{\theta}_p$, and excitation, $\boldsymbol{\theta}_g$, models as well as the seismological parameters $\boldsymbol{\theta}_m$. A probability density function (PDF) $p(\boldsymbol{\theta})$, is assigned to $\boldsymbol{\theta}$ based on our available knowledge. For a specific design configuration $\mathbf{q}$ the risk consequence measure, representing the utility of the response from a decision-theoretic point of view, is $h_r(\mathbf{q},\boldsymbol{\theta})$. Multiple risk consequence measures will be examined, each leading to a different risk quantification, with the subscript r utilized herein to denote this

distinction. Each consequence measure is related to (i) the earthquake performance/losses that can be calculated based on the estimated response of the structure (performance given that some seismic event has occurred) as well as to (ii) assumptions made about the rate of occurrence of earthquakes (incorporation of the probability of seismic events occurring). Seismic risk H_r is ultimately described by the expected value the risk-consequence measure under distribution $p(\boldsymbol{\theta})$,

$$H_r(\mathbf{q}) = \int_{\Theta} h_r(\mathbf{q}, \boldsymbol{\theta})\, p(\boldsymbol{\theta}) d\boldsymbol{\theta} \tag{6.2}$$

Through different selection of the risk consequence measure different risk quantifications can be addressed within this framework, supporting the estimation of all necessary life-cycle performance metrics. Specific examples, required in the multi-objective design problem formulation examined here are discussed next.

6.2.2 Total life-cycle Cost

The first life-cycle performance metric examined in the design formulation is the total life-cycle cost $C(\mathbf{q}) = C_i(\mathbf{q}) + C_l(\mathbf{q})$, given by adding the initial cost $C_i(\mathbf{q})$, which is a function of the dimensions of the TLD-FR (or mass damper more generally), and the cost due to earthquake losses over the life-cycle of the structure, $C_l(\mathbf{q})$. The latter is dependent on earthquake losses per seismic event and on assumptions about occurrence rates for such events. For a Poisson assumption for occurrence of earthquakes (i.e., independent occurrence of seismic events), the present value $C_l(\mathbf{q})$ of

expected future seismic losses is given by integral (6.2) with associated risk consequence measure definition (Goulet et al. 2007):

$$h_{rl}(\mathbf{q},\boldsymbol{\theta}) = C_r(\mathbf{q},\boldsymbol{\theta})\nu t_{life}\left[\frac{(1-e^{-r_d t_{life}})}{r_d t_{life}}\right] \tag{6.3}$$

where r_d is the discount rate, t_{life} is the life cycle considered and $C_r(\mathbf{q},\boldsymbol{\theta})$ is the repair cost given the occurrence of an earthquake event. The quantity in the brackets in Equation (6.3) corresponds to the present value factor, used to convert future cost to its present monetary value.

For estimating losses for a specific event an assembly-based vulnerability approach is adopted (Goulet et al. 2007). According to this approach, the components of the structure are grouped into n_{as} damageable assemblies, which consist of components of the system that have common vulnerability and repair cost characteristics (e.g. structural components, wall partitions etc.). For the j^{th} damageable assembly n_{dj} different damage states d_{kj}, $k = 1,\ldots,n_{dj}$ are designated and a fragility function is established for each damage state. These functions quantify the probability $P_e[d_{kj} \mid EDP_j(\mathbf{q},\boldsymbol{\theta})]$ that the component has reached or exceeded its k^{th} damage state, conditional on some Engineering Demand Parameter, $EDP_j(\mathbf{q},\boldsymbol{\theta})$, which is related to the time-history response of the structure under a given excitation (for example, peak transient drift, peak acceleration, etc.). Damage state 0 is used to denote an undamaged condition. A repair cost C_{kj} is then assigned to each damage state, which corresponds

to the cost needed to repair the component back to the undamaged condition. By combining the fragility and the repair cost information the contribution towards the expected cost from the different assemblies is calculated and then summed to obtain the total seismic losses $C_r(\mathbf{q},\boldsymbol{\theta})$ as:

$$\begin{aligned} &C_r(\mathbf{q},\boldsymbol{\theta}) = \sum_{j=1}^{n_{as}} \sum_{k=1}^{n_{d,j}} P[d_{kj} \mid EDP_j(\mathbf{q},\boldsymbol{\theta})] C_{kj} \quad \text{where} \\ &P[d_{kj} \mid EDP_j(\mathbf{q},\boldsymbol{\theta})] = P_e[d_{kj} \mid EDP_j(\mathbf{q},\boldsymbol{\theta})] - P_e[d_{k+1\,j} \mid EDP_j(\mathbf{q},\boldsymbol{\theta})] \\ &P[d_{n_d j} \mid EDP_j(\mathbf{q},\boldsymbol{\theta})] = P_e[d_{n_d j} \mid EDP_j(\mathbf{q},\boldsymbol{\theta})] \end{aligned} \tag{6.4}$$

This approach can be extended to evaluating the cost of injuries and fatalities, though in this case estimating the "unit replacement" cost is less trivial. Also, a similar methodology may be implemented for the downtime cost. In this case the repair time for each damaged state for each assembly needs to be defined and certain assumptions need to be established for how the repairs will progress (for example in parallel or not) to calculate the total downtime. Multiplication of that downtime with the revenue worth provides then the associated cost.

The expected life-cycle losses $C_l(\mathbf{q})$ for a given damper configuration is ultimately given by:

$$C_l(\mathbf{q}) = \int_{\Theta} h_{rl}(\mathbf{q},\boldsymbol{\theta})\, p(\boldsymbol{\theta}) d\boldsymbol{\theta} = v t_{life} \left[\frac{(1 - e^{-r_d t_{life}})}{r_d t_{life}} \right] \int_{\Theta} C_r(\mathbf{q},\boldsymbol{\theta})\, p(\boldsymbol{\theta}) d\boldsymbol{\theta} \tag{6.5}$$

Addition to that of the initial cost $C_i(\mathbf{q})$ yields then the total life-cycle cost $C(\mathbf{q})$.

6.2.3 Repair cost threshold with specific occurrence rate

Consideration of only the life-cycle cost as performance objective facilitates what is commonly referenced as "*risk-neutral*" design, which assumes that preference is assessed only through quantities that can be monetized. In reality, though, engineers and stakeholders have to take into account nontechnical factors such as social risk perceptions that inevitably lead to more conservative designs (*risk aversion*), since *risk-neutral* design does not explicitly address the unlikely but potentially devastating losses that lie on the tail of the losses/consequence distribution (Cha and Ellingwood 2013; Haukaas 2008). Motivated by this realization the incorporation of an additional performance objective corresponding to repair cost with specific probability of exceedance over the life-cycle of the structure was suggested in (Gidaris et al. 2014). Appropriate selection of this probability-level allows consideration of low-likelihood events within the design. This suggestion is adopted also here.

The probability of the repair cost C_r exceeding a threshold $C_{thresh}(\mathbf{q})$ over the considered lifetime based on the Poisson assumption for the occurrence of seismic events, is:

$$P[C_r > C_{thresh}(\mathbf{q}) \mid \mathbf{q}, t_{life}] = 1 - \mathrm{e}^{-t_{life} v \cdot P[C_r > C_{thresh}(\mathbf{q}) \mid \mathbf{q}, E_v]} \tag{6.6}$$

$$P[C_r > C_{thresh}(\mathbf{q}) \mid \mathbf{q}, E_v] = \int_{\Theta} I_C(\mathbf{q}, \boldsymbol{\theta}) p(\boldsymbol{\theta}) d\boldsymbol{\theta} \tag{6.7}$$

where the latter integral is in the generic form of equation (6.2) with risk consequence measure $I_C(\mathbf{q},\boldsymbol{\theta})$ corresponding to the indicator function, which is one if

$C_r(\mathbf{q},\boldsymbol{\theta}) > C_{thresh}(\mathbf{q})$ and zero if not. Equation (6.7) gives the probability of exceeding the acceleration threshold given that a seismic event has occurred, whereas Equation (6.6) transforms that event-probability to probability of exceeding the threshold over the lifetime of the structure.

6.2.4 Simulation-based Risk Assessment

The calculation of the seismic risk quantifications of interest requires calculation of multi-dimensional probabilistic integral of the form of Equation (6.2) for some appropriate definition of the risk consequence measure (this definition was discussed in the previous two sections). To support adoption of probability and numerical models with higher complexity as well as simultaneous calculation of these integrals, stochastic (i.e. Monte Carlo) simulation is adopted here for this purpose (Robert and Casella, 2004). Using a finite number, N, of samples of $\boldsymbol{\theta}$ drawn from proposal density $p_{is}(\boldsymbol{\theta})$, an estimate for the risk integral of interest [expressed through generalized form of Equation (6.2)] and the coefficient of variation for that estimate (quantifying accuracy), δ, are given, respectively, by:

$$\hat{H}_r(\mathbf{q}) = \frac{1}{N}\sum_{j=1}^{N} h_r(\mathbf{q},\boldsymbol{\theta}^j)\frac{p(\boldsymbol{\theta}^j)}{p_{is}(\boldsymbol{\theta}^j)}$$
$$\delta = \frac{1}{\sqrt{N}}\sqrt{\frac{\frac{1}{N}\sum_{j=1}^{N}\left(h_r(\mathbf{q},\boldsymbol{\theta}^j)\frac{p(\boldsymbol{\theta}^j)}{p_{is}(\boldsymbol{\theta}^j)}\right)^2}{\hat{H}_r(\mathbf{q})^2} - 1} \tag{6.8}$$

where $\boldsymbol{\theta}^j$ denotes the sample used in the j^{th} simulation. All samples $\{\boldsymbol{\theta}^j; j=1,...,N\}$ correspond to samples from proposal density $p_{is}(\boldsymbol{\theta})$. This proposal density may be used to improve the efficiency of this estimation [reduce the coefficient of variation], by focusing the computational effort on regions of the Θ space that contribute more to the integrand of the probabilistic integral of Equation (6.2) -this corresponds to the concept of Importance Sampling (IS). For problems with a large number of model parameters, choosing efficient importance sampling densities for all components of $\boldsymbol{\theta}$ is challenging (Taflanidis and Beck 2008) and can lead to convergence problems for the estimator in Equation (6.8); thus it is preferable to formulate importance sampling densities only for the important components of $\boldsymbol{\theta}$, i.e. the ones that have biggest influence on the seismic risk, and use $p_{is}(.)=p(.)$ for the rest (Taflanidis and Beck 2008). For seismic applications the seismological parameters are generally expected to have the strongest impact on the calculated seismic risk, so selection of IS densities may focus only on them (Taflanidis and Beck 2009).

Evaluating, now, the computational efficiency of this simulation-based estimation, the most demanding task is the calculation of the structural model response through time domain analysis. The adopted formulation allows, though, to seamlessly integrate recent advances in high performance computing (parallel/distributed computing) to perform the required N evaluations of the system performance independently, in parallel mode. This significantly reduces the computational barriers that have been

traditionally associated with approaches based on stochastic simulation (Taflanidis 2011). All stochastic simulation evaluations within this dissertation were performed in the Persephone cluster at the University of Notre Dame.

This simulation-based setting allows additionally for a highly efficient assessment of seismic risk for different design scenarios (Gidaris and Taflanidis 2015). These scenarios may be defined to correspond to different assumptions for the components of the model in Figure 6.1 that do not affect the structural response, for example for the seismic hazard uncertainty, or for the characteristics for the earthquake losses. As discussed in (Gidaris and Taflanidis 2015) this is facilitated through the fact that the approach for estimating the structural response for different samples depends only on the proposal densities $p_{is}(\boldsymbol{\theta})$ and not on the exact probability models $p(\boldsymbol{\theta})$. The efficient evaluation for $H_r(\mathbf{x})$ is established, ultimately, by using the same proposal densities for all design scenarios examined. This means that the computational demanding task (simulation of response) needs to be performed only once since it is common for all the design scenarios. Selection of $p(\boldsymbol{\theta})$ and of the characteristics of the loss estimation methodology facilitate afterwards an efficient estimation of seismic risk. For the Chilean region, due to the high variability in seismicity, this can be exploited to assess the efficiency of mass damper implementation under different assumptions for the probability models for the seismological parameters. Further details on the approach are provided in (Gidaris and Taflanidis 2015).

6.3 Seismic Hazard Modeling

Seismic hazard in the proposed framework (Figure 6.1) needs to be described in terms of acceleration time-histories. Though numerous methodologies have been proposed for providing such a description for *probabilistic seismic risk assessment*, the most popular one relies on adoption of intensity measures IMs representing the dominant features of the excitation (such as peak ground acceleration or spectral acceleration for specific periods), and subsequent scaling/selection of ground motion records to different hazard levels [different IM values] (Katsanos et al. 2010; Baker and Cornell 2005; Lin et al. 2013) resulting from a probabilistic seismic hazard analysis. The latter entails a deaggregation (Bazzurro and Cornell 1999; McGuire 1995) of the overall seismic hazard to representative events that then form the basis for the selection/scaling process. Though popular, this approach suffers from concerns regarding the validity for ground motion scaling (Grigoriu 2011; Grigoriu and Radu 2014) and from the fact that it provides biased seismic risk approximations related to high levels of inelastic structural response (i.e. associated with rare/high consequence events) (Jalayer and Beck 2008; Luco and Bazzurro 2007).

An alternative modeling methodology gaining increasing interest within the structural engineering community (Jensen and Kusanovic 2014; Gidaris and Taflanidis 2015), and the one adopted in this dissertation, is the use of stochastic ground motion models (Rezaeian and Kiureghian 2010; Vetter et al. 2014; Boore 2003). These models are based on modulation of a stochastic sequence through functions that address

spectral and temporal characteristics of the ground motion. The parameters of these functions, $\boldsymbol{\theta}_g$ in Figure 6.1, representing characteristics such as the duration of excitation or arias intensity can be related to seismological parameters, $\boldsymbol{\theta}_m$ in Figure 6.1, (such moment magnitude, M , rupture distance, r_{rup}, and shear wave velocity for local soil profile, V_{s30}) by appropriate predictive relationships. Description of the uncertainty (within the context of the seismic risk quantification discussed in Section 6.2.1) in the seismological parameters, through a probabilistic hazard analysis (Kramer 1996; Leyton et al. 2009; Ordaz et al. 2014), and, potentially, additionally in these predictive relationships facilitates then the comprehensive description of the seismic hazard described through time-histories of the ground motion.

The challenge for adopting this approach is that such stochastic ground motion models do not exist for the Chilean region. Similar challenges exist of course for adopting other approaches for ground motion modeling (for example, the popular scaling of ground motions based on IM values described earlier) since extensive probabilistic seismic hazard analysis studies (for example, providing deaggregation information for the seismic hazard) are not available. Even seismic design provisions for Chile have been relying on a deterministic rather than a probabilistic design earthquake definition (NIST 2012). Even though interest in such probabilistic descriptions of the seismic hazard has increased recently (Leyton et al. 2009; Ordaz et al. 2014), partially in response to the increased recent high-intensity seismic activity (EERI Special Earthquake

Report 2010), and hazard maps do exist (defining PGA with 10% probability of exceedance over the next 50 years) as shown in Figure 6.2, complete information for ground motion modeling is not yet available.

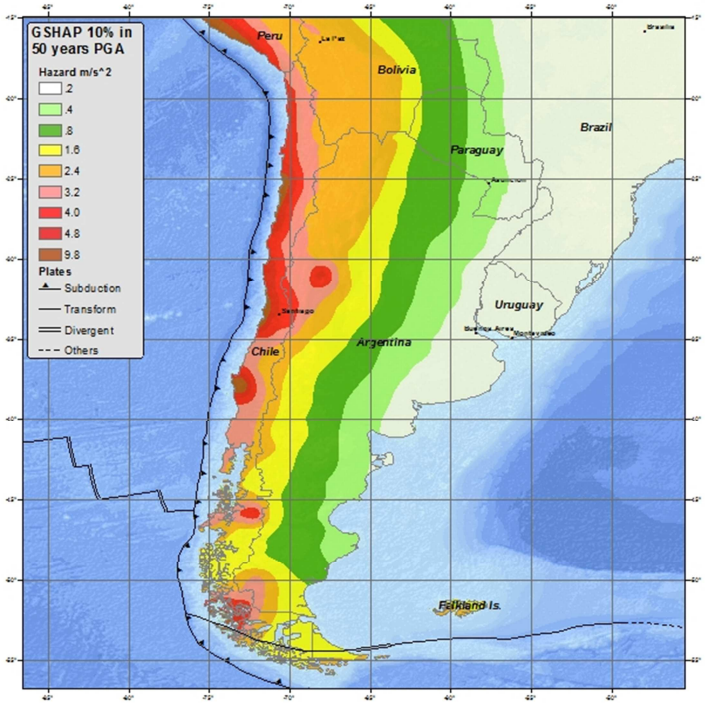

Figure 6.2 Seismic hazard map for Chile from USGS (peak ground acceleration with probability of being exceeded 10% in 50 years) [available at http://earthquake.usgs.gov/earthquakes/world/chile/gshap.php]

This gap is bridged within this dissertation by combining recently published Ground Motion Prediction Equations (GMPEs), also known as attenuation relationships, for Chile (Boroschek and Contreras 2012) with a methodology developed recently (Vetter et al. 2014) to select the predictive relationships in ground motion models so that compatibility of the acceleration time-histories to GMPEs is established. These

GMPEs ultimately provide estimates of the peak ground and spectral acceleration as a function of seismicity and site characteristic and represent the established approach for developing seismic hazard maps (Petersen et al. 2008). Therefore compatibility of the seismic risk provided by ground motion models to such GMPEs is facilitating an accurate and compatible regional hazard description. The goal is then to tune a stochastic ground motion model to match these estimates for a specific structure (defined through the structural periods of interest) and a specific seismicity range (defined by selected values for M and r_{rup}). This ultimately corresponds to an optimization problem for selection of the predictive relationships in the ground motion model, and a highly efficient framework was developed in (Vetter et al. 2014) to support this goal, relying on surrogate modelling concepts. Once the optimization framework for a specific stochastic ground motion model is established, something that requires an initial computational time for developing the underlying surrogate model that supports the optimization, it can easily facilitate tuning to any desired GMPE. Though this approach a ground motion model that is specifically optimized to match the hazard for a specific location (GMPE), structure (period of interest) and seismicity (range for moment magnitude and rupture distance) is established.

Here this framework is exploited to tune the versatile stochastic ground motion model proposed in (Papadimitriou 1990) to the GMPE presented recently for Chile in (Boroschek and Contreras 2012). The model by Papadimitriou (1990) addresses both temporal and spectral non-stationarities. The former is established through a time-

domain modulating envelope function of the exponential type [representing a common selection stochastic ground motion models (Rezaeian and Kiureghian 2010)] while the latter is achieved by filtering a white-noise process by a filter corresponding to multiple cascading SDOF oscillators with time-varying characteristics. A quick review of the model is offered in Appendix D, including the functional form of the predictive relationships adopted as well as the optimized values for the coefficients in these relationships for the hazard compatibility established for the case study examined later. The tuning of the model is established through the optimization approach in (Vetter et al. 2014) through the direct assistance of the first author of that paper.

Indicative results from this hazard compatibility are presented in Figure 6.3 and Figure 6.4 for the case study that is examined in this Chapter. The intended match of the stochastic ground motion predictions to the desired GMPE is established for the peak ground acceleration (PGA) and the peak spectral acceleration S_{pa} for 5% damped elastic SDOFs with period T_{sd} 2 s, chosen close the fundamental period of the structure of interest, and for M and r_{rup} in ranges [5.5 9] and [30 250] km (note that shorter ranges are shown in the figure to better focus the comparative results) which are the ranges anticipated to contribute to the seismic risk in this example.

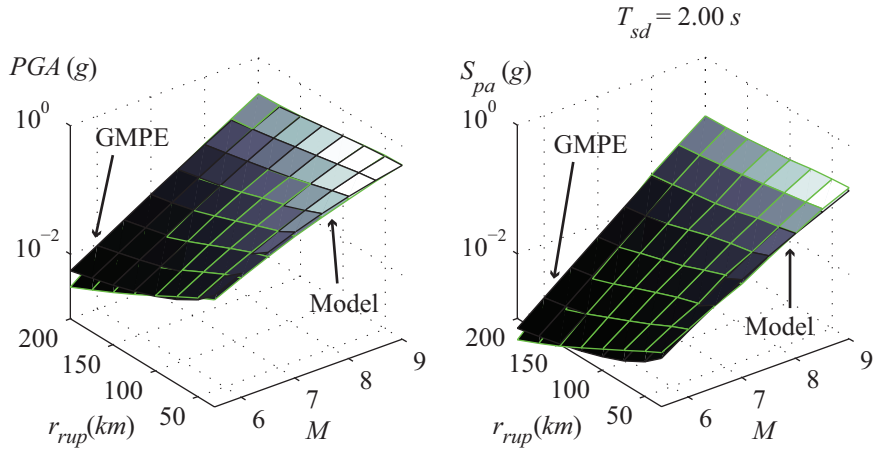

Figure 6.3 Illustration of hazard-compatible ground motion modeling for Chilean GMPEs; comparison of GMPE and model predictions for different $M - r_{rup}$ values for peak ground acceleration (left) and peak spectral acceleration S_{pa} for 5% damped elastic SDOFs with period T_{sd} 2 s (right)

Beyond match to GMPEs, the compatibility of the resultant ground motions to regional excitations characteristics is also important. This compatibility was illustrated in Section 2.4 in Figure 2.5 where same trends were reported under regional for Chile ground motions (set 1 in that figure) and synthetic ground motions generated according to the established stochastic ground motion model (set 3 in that figure). Furthermore it is demonstrated in Figure 6.5 which shows the predictive relationships established through the stochastic ground motion model for the arias intensity I_a and the significant duration $D_{5\text{-}95}$ (representing key ground motion parameters influencing structural behavior and damper efficiency) as well as samples for these two parameters from regional motions from the database (Boroschek et al. 2015). The established relationships lay in between the samples from the real (recorded) motions, showing, again, a compatibility of the proposed ground motion modeling approach.

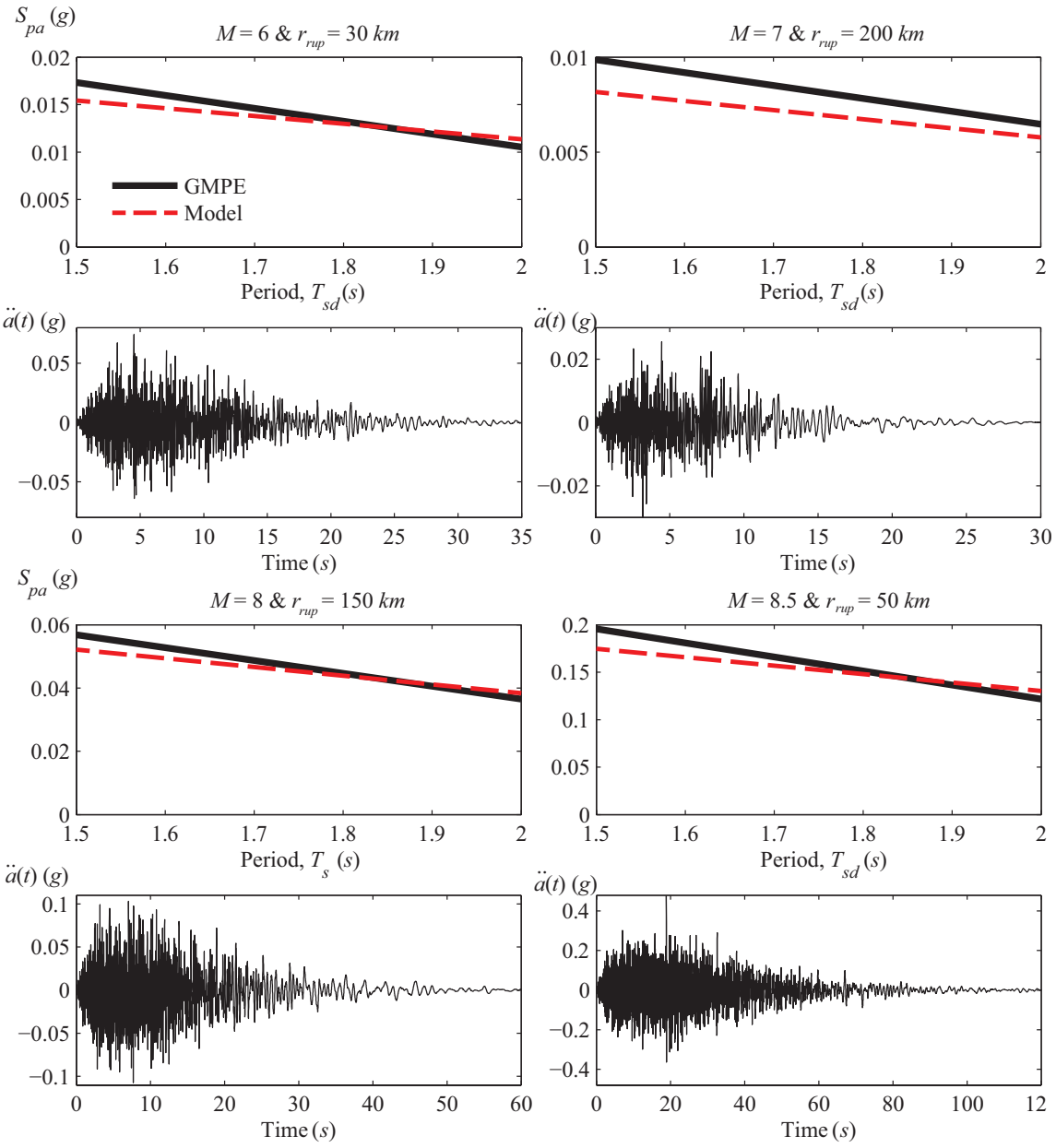

Figure 6.4 Illustration of hazard-compatible ground motion modeling for Chilean GMPEs; for different characteristic $M - r_{rup}$ values spectral plots for peak acceleration of 5% damped elastic SDOFs (comparison between GMPE and model shown) as well as sample ground motions created by the model

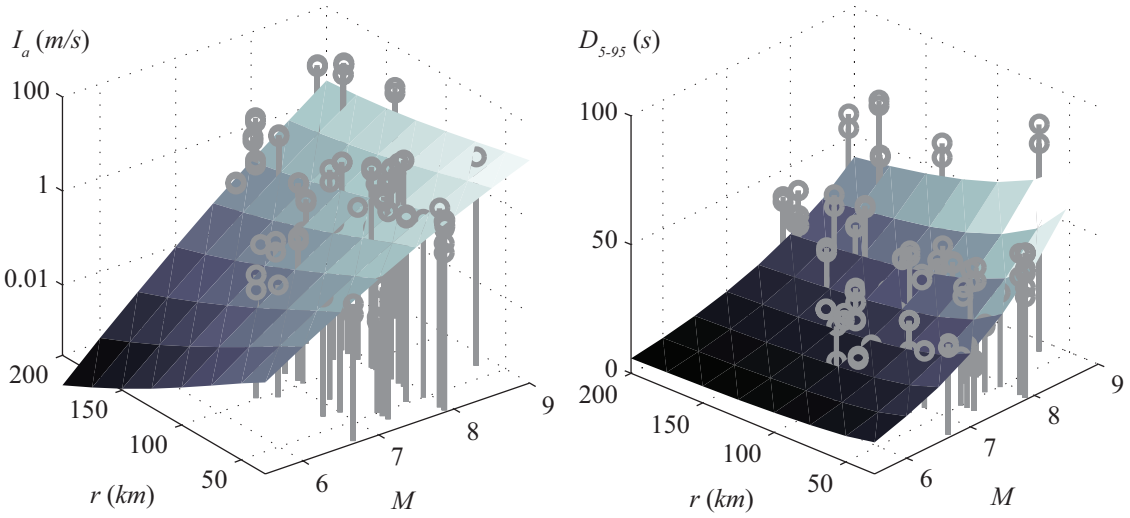

Figure 6.5 Arias intensity (left) and significant duration (right) as a function of $M - r_{rup}$ for the established ground motion model (surface plots) as well as samples from regional (for Chile) recorded ground motions

6.4 Design Optimization

The suggested multi-objective design is expressed as:

$$\mathbf{q}^* = \arg\min_{\mathbf{q}\in Q} \left\{ C(\mathbf{q}) = C_i(\mathbf{q}) + C_l(\mathbf{q}), C_{thresh}(\mathbf{q}) \right\}^T \quad \text{such that } P[C_r > C_{thresh}(\mathbf{q}) \mid \mathbf{q}, t_{life}] = p_o \tag{6.9}$$

where C [first objective] is the life-cycle cost and C_{thresh} [second objective] is the repair cost threshold with probability of being exceeded p_o over the lifetime of the structure. This multi-objective formulation leads ultimately to a set of points (also known as dominant designs) that lie on the boundary of the feasible objective space and they form a manifold, which is called Pareto front. A point belongs to the Pareto front and it is called Pareto optimal point if there is no other point that improves one objective without detriment to the other. As discussed previously, the motivation behind the

multi-objective formulation of the problem is that the decision-maker (e.g. building owner) can choose among a range of TLD-FR configurations (Pareto optimal solutions) that describe different decision making attitudes towards risk (from risk neutral to risk averse designs).

Since both performance objectives involved in the multi-objective optimization are estimated through stochastic simulation, the existence of the prediction error within the optimization (resulting in a so-called stochastic optimization problem) is addresses by adopting an exterior sampling approach (Spall 2005), utilizing the same, sufficiently large, number of samples throughout all iterations in the optimization process, i.e. $\{\boldsymbol{\theta}^j; j=1,...,N\}$ for Equation (6.8) is chosen the same for each damper design configuration examined, therefore reducing the importance of the estimation error in the comparison of different design choices (creating a consistent error in these comparisons).

Furthermore, for supporting an efficient optimization while additionally allow for a straightforward incorporation of different assumptions for the upfront damper cost, an approach relying on kriging surrogate modeling is adopted following the guidelines discussed first in (Gidaris and Taflanidis 2015). A large set of design configurations (1000 in the case study discussed later) for the TLD-FR is first established to serve as support points for the kriging, utilizing a latin hypercube sampling in Q. The system response is then evaluated through time-history analysis for all of them. The design is facilitated through the following approach. First the risk quantities C_l and C_{thresh} are estimated for

all the design configurations. Using this information a kriging metamodel is established to provide a highly efficient approximation to the system risk. The kriging implementation is identical to the one discussed in Section 5.3.1 and presented in Appendix C, the only difference being that the input in this case is the design vector $\mathbf{q}$ and the output is the different risk quantifications, C_l and C_{thresh}. The kriging metamodel allows a highly efficient estimation of these risk measures (thousands of evaluations within minutes) and is then used within the optimization in Equation (6.9), coupled with an appropriate assumption for the upfront damper cost (used to calculate the overall cost C). Note that the metamodel is independent of the upfront damper cost assumptions so needs to be built only once for all the cases considered with respect to the latter. The multi-objective problem of Equation (6.9) can be then solved through any appropriate means, for example though blind-search (Coello et al. 2007) or through genetic algorithm implementation (Deb et al. 2000).

The proposed design approach ultimately facilitates an efficient optimization for (i) different assumptions for the upfront damper cost [the surrogate-modeling-based assessment of the performance objectives facilitates this ability] and (ii) different design scenarios related to the seismic hazard description [this is facilitated through the stochastic-simulation-based evaluation of the different risk measures]. Coupled with the capability to adopt complex numerical and probability models to quantify seismic risk [facilitated through the simulation-based modeling approach] the overall multi-criteria framework for life-cycle based design discussed here supports a comprehensive

analysis/design of TLD-FR addressing cost/benefit issues as well as different attitudes towards risk.

6.5 Case Study

As case study the design for a TLD-FR for a 21-story structure located in Santiago is considered. The building corresponds to an existing structure (Zemp et al. 2011) and has already a TMD installed in its last floor across its slender axis. First the numerical and probability models adopted for the seismic hazard and the structure are discussed, then the optimization framework is validated and finally the results are presented incorporating different assumptions for the upfront cost, ranging from typical values for TMDs to anticipated cost for TLDs-FR.

6.5.1 Seismic Hazard

For the seismic hazard, the model discussed in Section 6.3 is utilized. A stochastic ground motion model is established that matches the GMPE of (Boroschek and Contreras 2012) for the peak ground acceleration (PGA) and the peak spectral acceleration S_{pa} for 5% damped elastic SDOFs with period T_{sd} 2 s, for values for M and r_{rup} in ranges [5.5 9] and [30 250] km.

Seismic events are assumed to occur following a Poisson distribution and so are independent of previous occurrences. The uncertainty in moment magnitude M is modeled by the Gutenberg-Richter relationship truncated on the interval [M_{min}, M_{max}] = [5.5, 9.0], (events smaller than M_{min} are not expected to contribute to the seismic risk)

which leads to $p(M) = b_M e^{-b_M M} / (e^{-b_M M_{min}} - e^{-b_M M_{max}})$ and expected number of events per year $v = e^{a_M - b_M M_{min}} - e^{a_M - b_M M_{max}}$. The regional seismicity factors b_M and a_M are chosen by averaging the values for the seismic zones close to Santiago based on the recommendations in (Leyton et al. 2009). This results to b_M=$0.8\log_e(10)$ and a_M=$5.65\log_e(10)$. Regarding the uncertainty in the event location, the closest distance to the fault rupture, r_{rup}, for the earthquake events is assumed to follow a beta distribution in [30 250] km with median r_{med}=100 km and coefficient of variation 35%.

The probability of exceedance of different thresholds over 50 years for the peak ground acceleration and the spectral acceleration of a 5% damped elastic SDOF with period 2 s (closest available prediction of GMPE to the fundamental period of the structure of interest) is shown in Figure 6.6. The results in this Figure 6.6 are compatible with the results reported in Figure 6.3 or in (Ordaz et al. 2014) for the seismic hazard in the greater Santiago area.

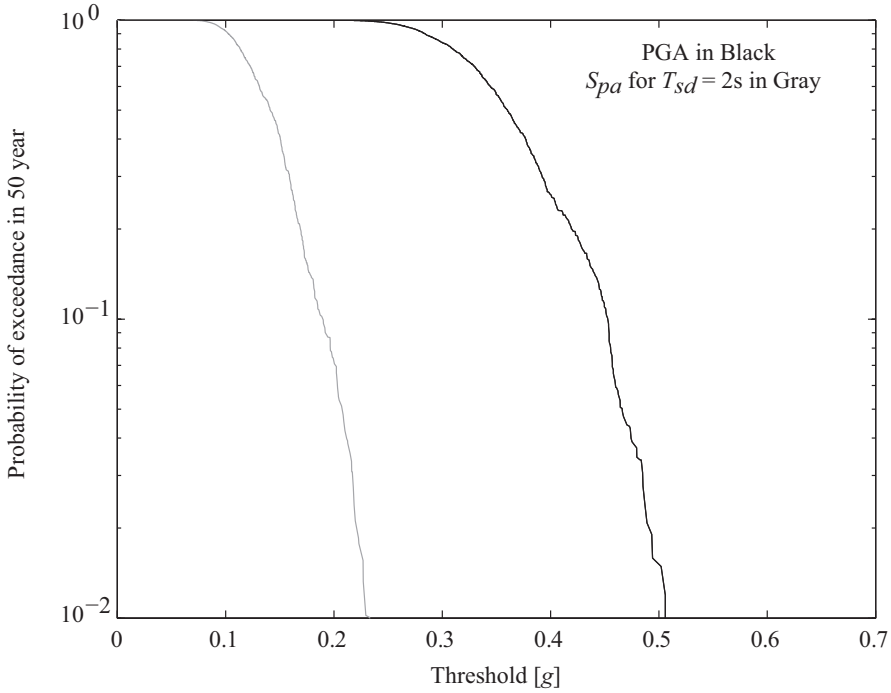

Figure 6.6 Probability of exceedance of different thresholds for peak ground acceleration PGA and spectral acceleration S_{pa} of a 5% damped elastic SDOF with period T_{sd} 2 s.

6.5.2 Structural and Loss Evaluation Models

Details about the structure may be found in (Zemp et al. 2011). It corresponds to a 21-story structure with dimensions 76.2x15.6 m with lamped mass per floor having nominal values 1124ton for ground level, 1805ton for 2nd-5th story, 1753ton for 6th-9th, 1675ton for 10th story, 1616ton for 11th-14th story, 1579ton for 15th-18th story, 1527ton for 19th story, 1158ton for 20th story and 710ton for 21th story. The damper is applied along the long axis of the structure (as the current implementation in the building) and a planar structural model is established with a single degree of freedom per floor. A linear structural model is assumed since, as explained earlier based on

observations from recent earthquakes most Chilean (EERI Special Earthquake Report, 2010) buildings exhibit predominantly linear response even under larger magnitude excitations (minimal damages to structural components). The mass and stiffness matrices for the structure are obtained through the use of a commercial structural analysis software and then structurally condensed to a planar model considering the lateral displacement for each floor. This condensed stiffness matrix is then adjusted to take into account the effect of cracked concrete section and match the experimental fundamental period reported in (Zemp et al. 2011) which is 2.1 s. The damping matrix is modeled through Rayleigh assumption by assigning an equal damping ratio for the first and second mode with a nominal value equal to 3%. For this nominal model the first three modes (and participation factors in parenthesis) are 2.10s (77%), 0.54s (16%) and 0.25s (5%).

To examine the impact of structural uncertainties on the damper design two cases are examined for the structural model. The first case utilized no uncertainties in the structural model, simply directly adopts the nominal values discussed above. This is referenced herein as nominal structure and denoted by abbreviation *NS*. The second case additionally considers uncertainty in the structural model description, particularly in the damping and stiffness matrices. This is referenced herein as probabilistic structure and denoted by abbreviation *PS*. For the uncertainty in the damping characteristics each damping ratio is modeled as Gaussian random variable with coefficient of variation 10% and mean value the nominal one discussed above. For the uncertainty in the stiffness

matrix, rather than adopting complex descriptions (Soize 2000) a simplified characterization is adopted, understanding that the main dynamic property impacting the efficiency of mass dampers are the modal frequencies (since they are directly related to the tuning of the damper). Each modal frequency is treated as a Gaussian random variable with mean value the one resulting from the nominal structural model described above and coefficient of variation 10% .

Moving now to the loss evaluation model, fragility and repair cost information is included in Table 6.1, where the fragility function is a conditional cumulative lognormal distribution with median β_f and standard deviation σ_f, which leads to

$$P_e[d_{fj} \mid EDP_j] = \Phi\left[\frac{\ln(EDP_j / \beta_{fj})}{\sigma_{fj}}\right] \tag{6.10}$$

Note that damages to structural components are not included in this study since as discussed earlier are expected to have minimum contribution (behavior remains elastic even for stronger events). n_e in this table corresponds to the number of elements assumed per story whereas for each of the three different damageable assemblies different damage states are considered (total repair cost per assembly is obtained by considering the contribution from all damage states). The fragility function parameters for the partitions and the suspended ceiling system are based on the recommendations in (FEMA-P-58 2012) whereas for the contents damageable subassembly the fragility curve used is similar to the one selected in (Taflanidis and Beck 2009).

The discount rate is taken equal to 1.5% and the lifetime t_{life} is assumed to be 50 years. The repair cost threshold is taken to correspond to probability p_o =10% over t_{life}. The life-cycle cost and C_{thresh} for the uncontrolled structure (without the dampers) are, respectively, \$2.11x10^6 and \$1.22x10^6 for the probabilistic structure (PS) and \$2.02x10^6 and \$1.13x10^6 for the nominal structure (NS).

Table 6.1 Characteristic of the cost estimation. Values for fragility curves related to partitions, contents and acoustical ceiling

State	β_f	σ_f	n_e	\$/ n_e
Partitions				
Small	0.21%	0.60	350m^2	22.3
Moderate	0.71%	0.45	350m^2	60.3
Severe	1.20%	0.45	350m^2	92.7
Contents				
Damage	0.70g	0.30	150	1000
Acoustical Ceiling				
Small	0.55g	0.40	1500m^2	15.2
Extensive	1.00g	0.40	1500m^2	120.1
Severe	1.50g	0.40	1500m^2	237.7

6.5.3 Damper Cost

The total life-cycle cost for the structure is estimated as the sum of the repair cost due to the earthquake losses over the life-cycle of the structure and the initial cost of the TLD-FR. For the initial cost of the damper a simplified assumption is established here; the cost is assumed to depend linearly to the damper mass $C_i=b_c m_{liq}$ and three different cases are examined for this proportionality, b_c=[1000 1750 2500] $/ton. The higher upfront cost case is assumed to correspond to a TMD, with cost estimate based on the TMD application in Taipei 101 (Gutierrez Soto and Adeli 2013). The other two, with lower installation cost, are representatives of a TLD-FR application.

6.5.4 Details for Optimization and Validation of Pareto Front

The analysis is performed for three different efficiency indexes. The optimization is then established over the remaining design variables (r, α and ξ_m). The ranges assumed for developing the kriging metamodel are [0.2 1.2]% for r (it is assumed that greater than 1.2% mass ratios are impractical to be achieved) [1 8]% for ξ_m and [0.94 1] for α. The frequency ratio α is defined as the ratio between damper frequency and frequency corresponding to the fundamental mode of the nominal structural model (i.e. ignoring uncertainties in the model description). Due to the simplified assumption that the initial cost is related only to the total liquid mass (and not the exact tank geometry) incorporation of the efficiency index as a design variable was redundant since it is well-understood that larger efficiency index would yield better results and therefore

correspond to the optimal design. N=10000 samples are used for the stochastic simulation and importance sampling densities q_{is} are formulated only for M and r_{rup} which are expected to be the uncertain model parameters influencing more seismic risk. The densities are chosen as truncated Gaussians in the range of each model parameter with mean and standard deviation of 7.3 and 1, respectively, for M and 70 and 70, respectively, for r_{rup}. These selections result in high accuracy estimation of the different risk characterizations with coefficient below 3% for all cases examined. The surrogate model to guide the optimization is established utilizing 1000 support points, following Latin hypercube sampling in Q, whereas a blind-search approach is adopted for solving the multi-objective optimization problem.

The accuracy of the developed surrogate model is preliminary evaluated by calculating different error statistics using the leave-one-out cross-validation approach (Meckesheimer et al. 2002). The accuracy established is ultimately high with coefficient of determination over 97% for most approximated response quantities and average error below 3%. This discussion though, refers to the overall accuracy of the metamodel. What is more important for the implementation examined here is the accuracy in estimating the different probabilistic performance objectives and performing the design optimization, which is examined next. This is performed with respect to the objective function space and is reported in Figure 6.7, which shows the predictions by the kriging metamodel and the high-fidelity model for design case corresponding to value of γ=0.7 and upfront cost assumption of 1750 $/ton (identical trends hold foal l other cases) for

both the nominal and probabilistic structure. The comparison is performed for 11 characteristic Pareto optimal solutions selected from the complete Pareto front. The close agreement of the curves in this figure validate the proposed kriging-supported design optimization approach. Ultimately, the curve that corresponds to the exact numerical model predictions (high-fidelity) is simply a slightly shifted one (when compared to the one corresponding to the kriging predictions) that corresponds still to a Pareto-front. This demonstrates that the overall approach can efficiently identify Pareto-optimal configurations.

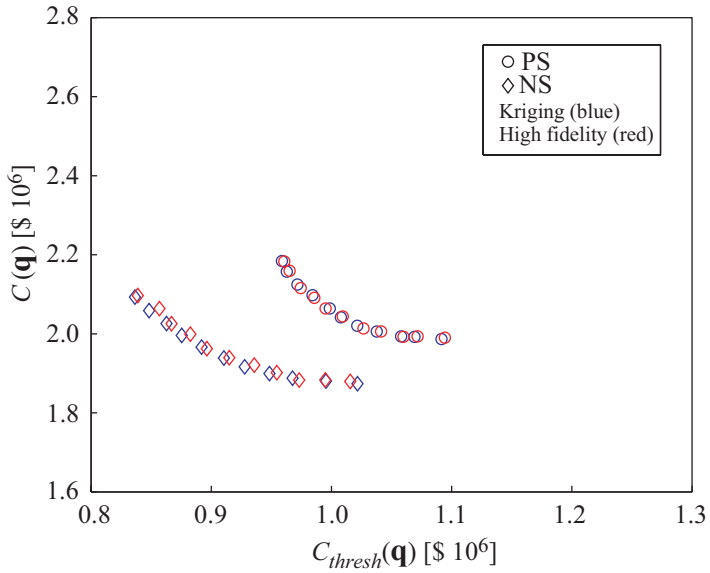

Figure 6.7. Comparison between the estimated performance through the kriging metamodel and the high-fidelity model for the Pareto optimal solutions for design case corresponding to value of γ=0.7 and upfront cost assumption of 1750 $/ton

6.5.5 Results and Discussion

With a validated optimization framework, the discussion moves now to the results. The Pareto fronts are reported in Figure 6.8 (for probabilistic structure) and Figure 6.9 (for the nominal structure) which shows the Pareto fronts for the different γ (subplots for each figure) and b_c values (curves within each plot). All potential combinations are shown for γ and b_c though for practical applications γ=1 is related to the high upfront cost b_c=2500 \$/ton (TMD) whereas the lower γ values are associated with lower upfront cost b_c=[1000 1750] \$/ton (TLD-FR). In the Pareto front the mass ratio under optimal design is also reported in some instances (extremes of the front) since this is the main design variable distinguished along the front (frequency and damping ratio simply take proper tuning values for that *r* as will be shown later). For the same extreme cases of the front the decomposition of the total cost (ratio) to upfront and repair cost is also shown (in parenthesis). Note that the scales for the axis in both these figures are kept the same to facilitate easier comparison. This comparison across different efficiency indexes as well as the nominal or probabilistic structure is also depicted in Figure 6.10 which shows the Pareto front for value of b_c=1000 \$/ton (similar trend holds for other upfront cost cases).

The overall behavior is similar for the two cases with respect to the structural configuration (probabilistic and nominal structure) with the former resulting to larger associated life-cycle cost and life-cycle losses threshold. This demonstrates that for the probabilistic structure detuning effects for the damper, stemming from the variability in

the modal characteristics of the building, impact its efficiency. This clearly shown in the comparison in Figure 6.10, especially for larger values of the efficiency index γ, which is something anticipated. For such larger values of γ the mass damper has greater potential impact against suppressing structural vibrations, so any detuning has a more profound effect on its performance.

The overall results demonstrate that the addition of mass dampers can provide a considerable reduction for both C and C_{thresh} (compare these values to the one reported above for the structure without the damper). As expected, larger values for the TLD-FR efficiency indexes yield better performance whereas reduction of the upfront cost for the damper also contributes to similar trends. In this case the optimal design corresponds to larger mass ratios (since upfront cost is reduced larger dampers can be adopted) which contributes to the better performance while also yielding a smaller distribution of the Pareto-front. The efficiency index seems to also have a similar effect on reducing the spread of the Pareto front.

The stakeholder can ultimately make a choice then among the different candidate solutions along the Pareto front by prioritizing the different competing objectives. This ultimately boils down to selection of the damper mass; larger masses yield greater reduction of C_{thresh} but a larger overall life-cycle cost (due to increase of upfront cost). Based on the Pareto-optimal solution selection the tank geometry can be chosen based on the process discussed in Section 5.3. Note that, especially for larger

values of upfront cost b_c, moving towards risk-averse designs (smaller values for C_{thresh}) leads ultimately to an increase in the total life cycle cost C.

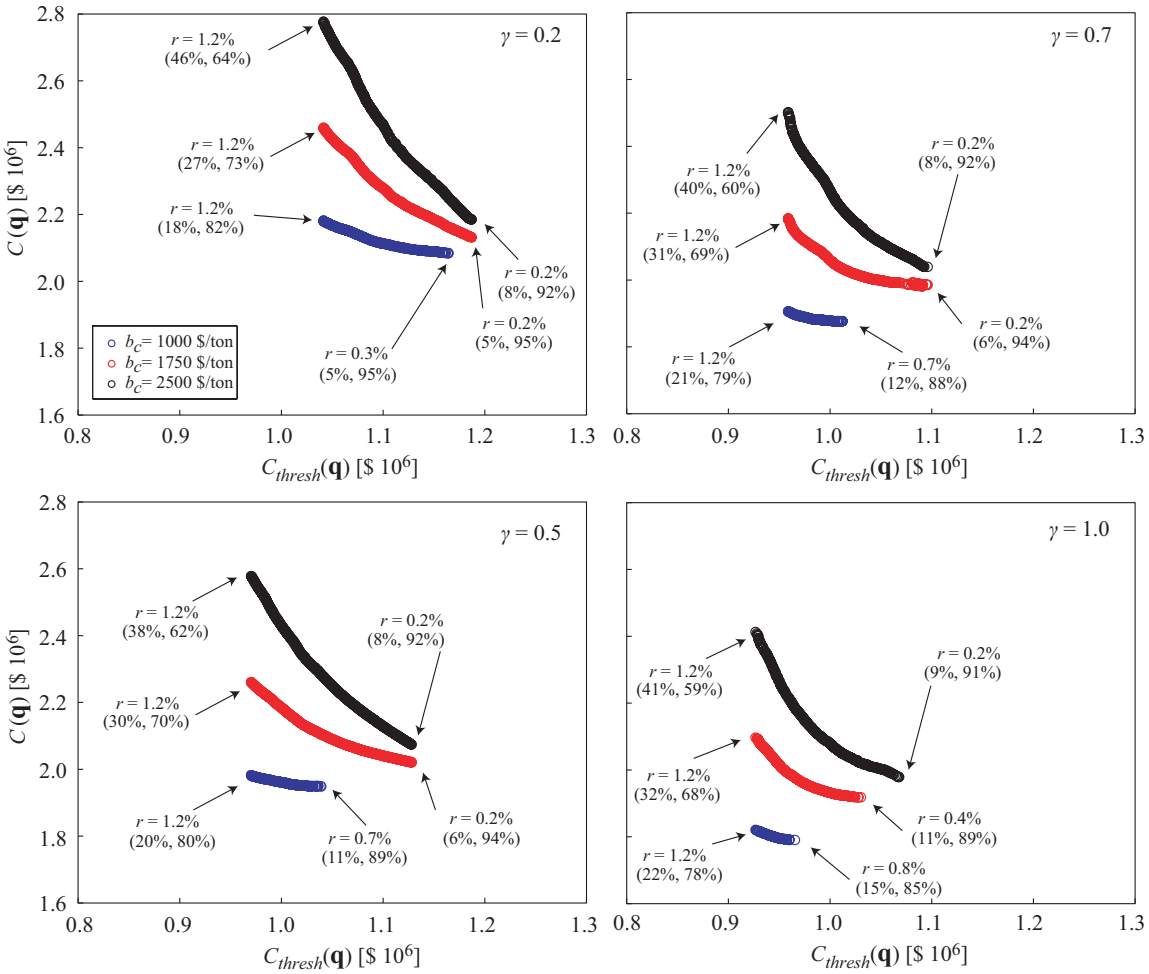

Figure 6.8 Pareto front for the total life-cycle cost C and repair cost threshold with probability of exceedance 10% in 50 years, C_{thresh}, for different efficiency indexes and different assumptions for upfront damper cost (blue is low damper cost, red is medium and black is high). Results correspond to probabilistic structure. Mass ratio under optimal design and decomposition of total cost to upfront cost and life-cycle repair cost is also shown in parenthesis.

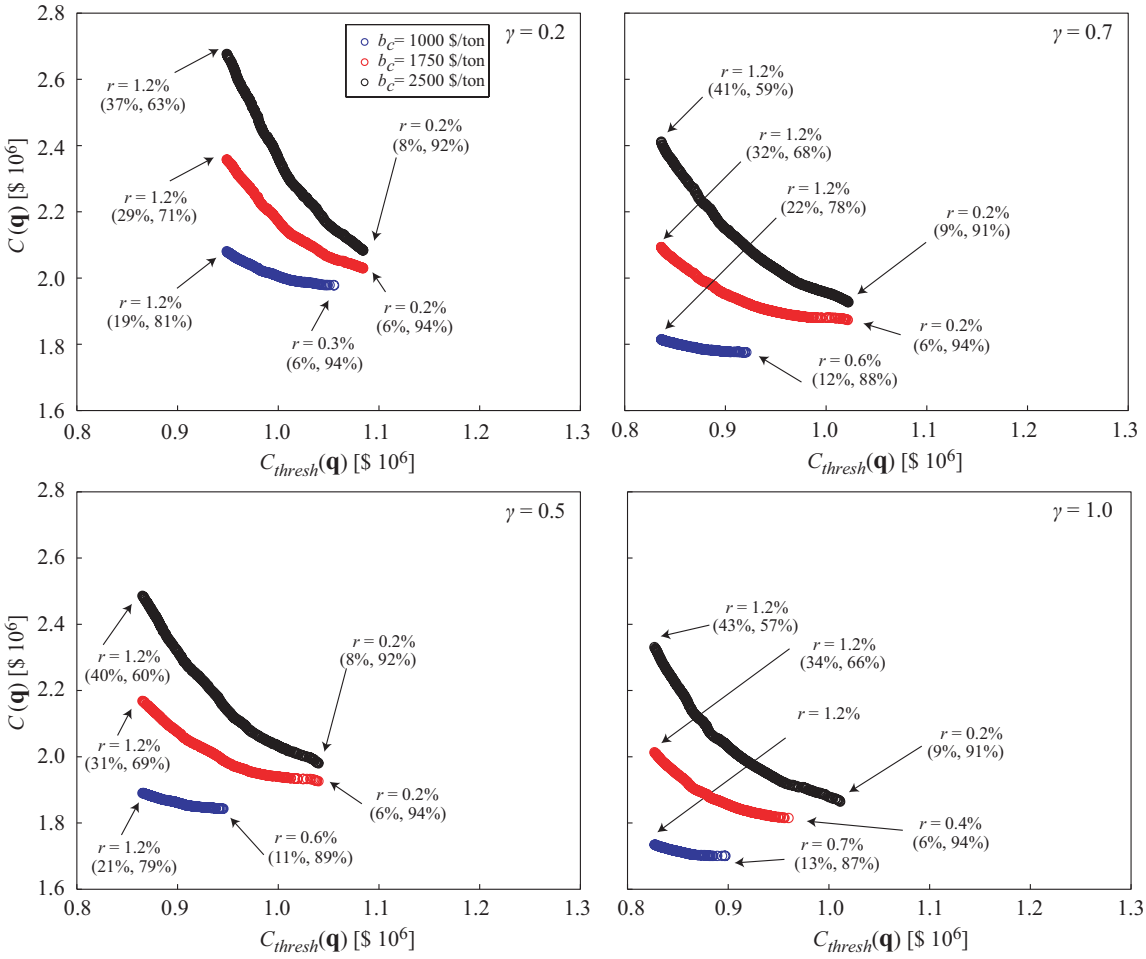

Figure 6.9 Pareto front for the total life-cycle cost C and repair cost threshold with probability of exceedance 10% in 50 years, C_{thresh}, for different efficiency indexes and different assumptions for upfront damper cost (blue is low damper cost, red is medium and black is high). Results correspond to nominal structure. Mass ratio under optimal design and decomposition of total cost to upfront cost and life-cycle repair cost is also shown in parenthesis.

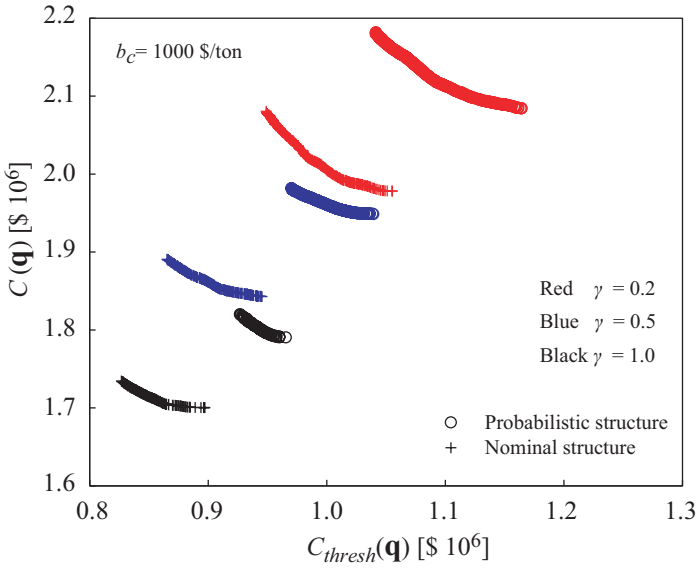

Figure 6.10. Pareto front for the total life-cycle cost C and repair cost threshold with probability of exceedance 10% in 50 years, C_{thresh}, for different efficiency indexes and and an upfront damper cost of 1000$/ton. Results for both the nominal structure and probabilistic structure are shown.

These results can be also utilized to facilitate the intended comparison between TMDs and TLDs-FR. As discussed previously, this is established by comparing the solutions for γ=1 is corresponding to high upfront cost b_c=2500 $/ton (TMD) against the solution for lower γ values associated with lower upfront cost b_c=[1000 1750] $/ton (TLD-FR). It is evident in this case that the TLD-FR offers better life-cycle performance, meaning overall reduced cost or better protection (reduction of life-cycle losses threshold or of portion of total cost stemming from necessary repairs over the lifetime) for the same overall cost, as long as a reasonable efficiency index (not too small -0.2 in the case here) is established. Even when comparing moderate cost for TMD (1750 $/ton) to lower cost for TLD-FR (1000 $/ton) the latter offers a compatible solution. This

discussion shows that TLDs-FR should be considered as an economically competitive option to TMDs for enhancement of seismic performance as long as proper design (avoidance of low efficiency indexes) can be accomplished. It also stresses the importance of the proposed framework for (i) establishing a comparison of different type of dampers based on life-cycle cost concepts and (ii) explicitly addressing the upfront cost of the dampers in the analysis.

Other interesting comparisons can be established by looking the variation across the Pareto front of different characteristics. For the mass ratio r the results are shown in Figure 6.11 for PS (probabilistic structure) and Figure 6.12 for NS (nominal structure) considering variation with respect to C across the Pareto front and in Figure 6.13 for PS and Figure 6.14 for NS considering variation with respect to C_{thresh} across the Pareto front. It is evident, especially from Figure 6.13 and Figure 6.14, that the main design variable distinguishing the behavior across the Pareto front is the mass ratio; each mass ratio is uniquely associated with a performance level, especially when that performance level is not impacted by the upfront cost (different curves in Figure 6.13 and Figure 6.14 lay on top of one another). This is expected as discussed also earlier since this is the characteristic that directly impacts both the upfront cost as well as the damper efficiency. Based on this trend results for the remaining design variables are reported as variation with respect to the mass ratio, not C_{thresh} or C.

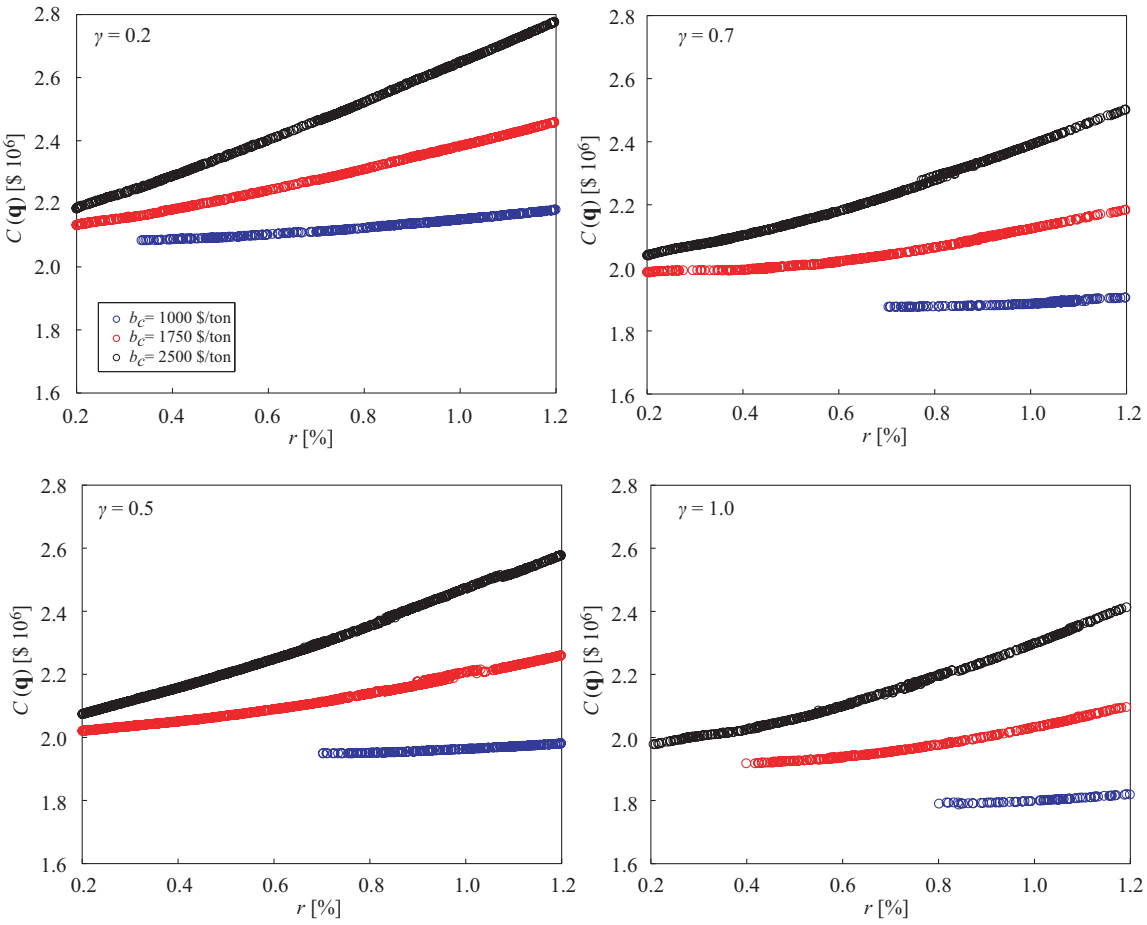

Figure 6.11. Variation of mass ratio r corresponding to optimal solution against the total life-cycle cost C across the Pareto front for different efficiency indexes and different assumptions for upfront damper cost (blue is low damper cost, red is medium and black is high). Results correspond to probabilistic structure.

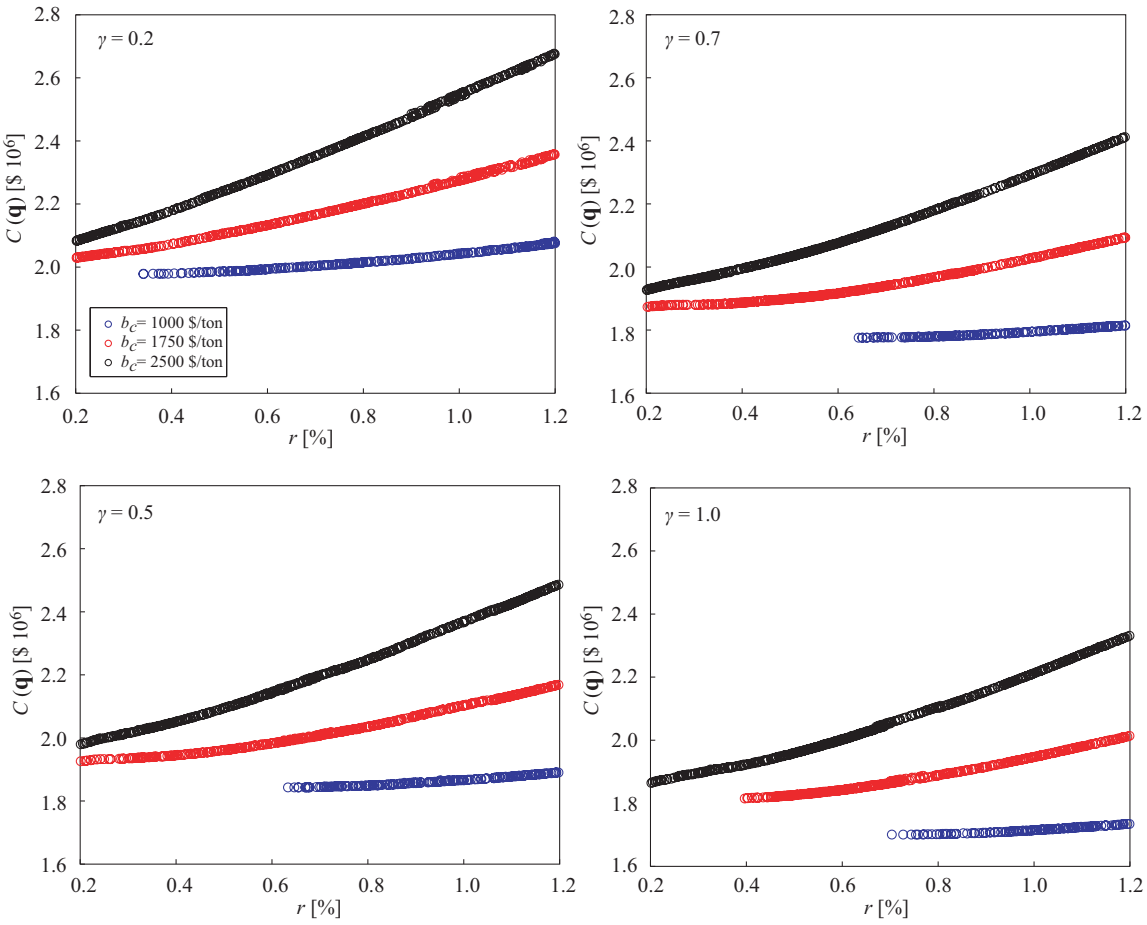

Figure 6.12. Variation of mass ratio r corresponding to optimal solution against the total life-cycle cost C across the Pareto front for different efficiency indexes and different assumptions for upfront damper cost (blue is low damper cost, red is medium and black is high). Results correspond to nominal structure

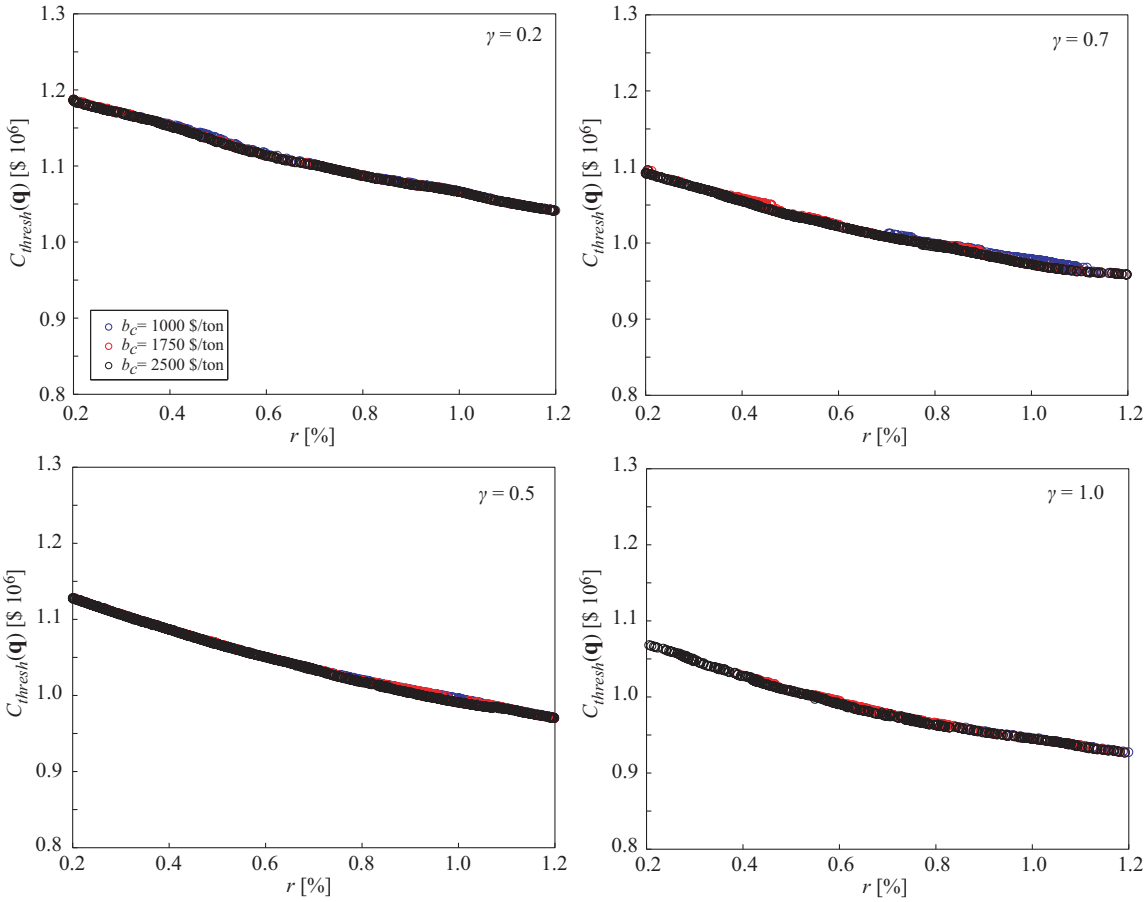

Figure 6.13. Variation of mass ratio *r* corresponding to optimal solution against repair cost threshold with probability of exceedance 10% in 50 years C_{thresh} across the Pareto front for different efficiency indexes and different assumptions for upfront damper cost (blue is low damper cost, red is medium and black is high). Results correspond to probabilistic structure.

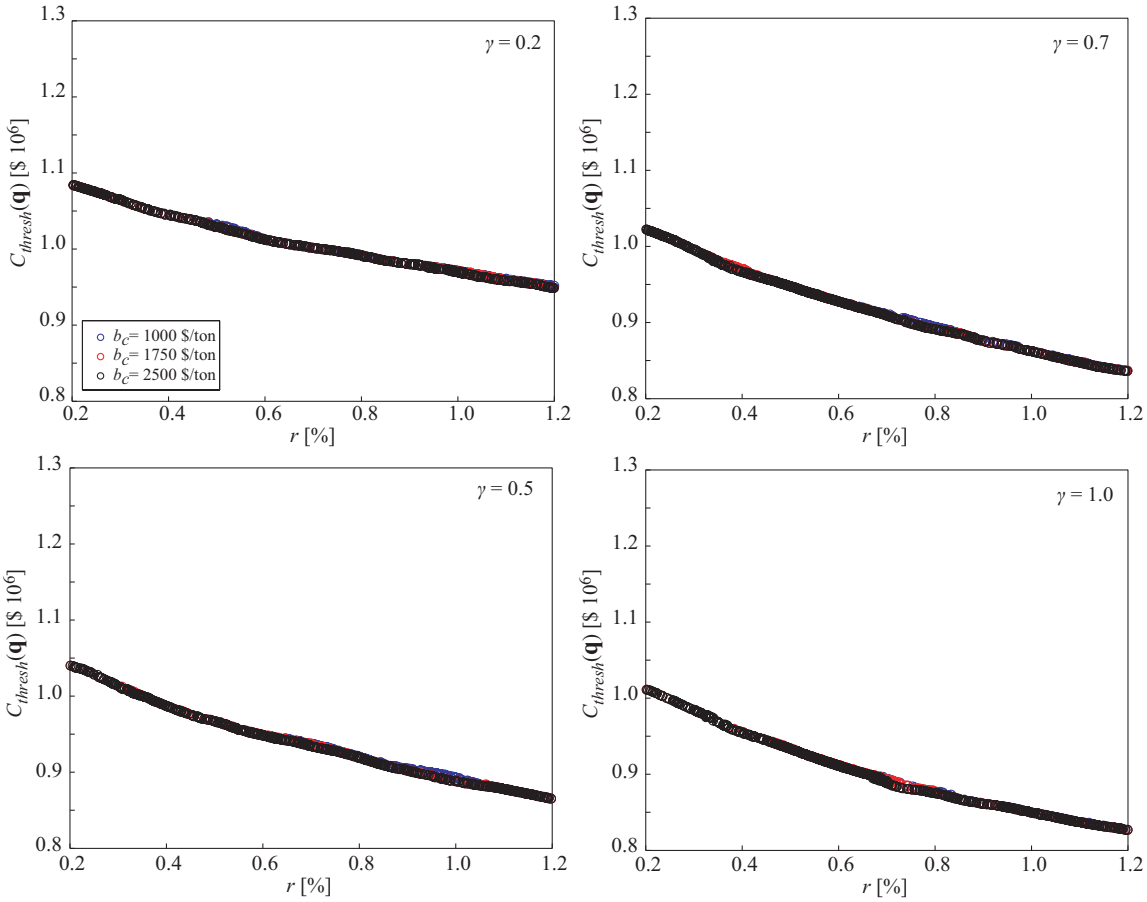

Figure 6.14. Variation of mass ratio *r* corresponding to optimal solution against repair cost threshold with probability of exceedance 10% in 50 years C_{thresh} across the Pareto front for different efficiency indexes and different assumptions for upfront damper cost (blue is low damper cost, red is medium and black is high). Results correspond to nominal structure.

Results for the optimal damping ratio are reported in Figure 6.15 for PS (probabilistic structure) and Figure 6.16 for NS (nominal structure) and for the optimal frequency ratio in Figure 6.17 for PS and Figure 6.18 for NS. It is evident that the optimal design configuration corresponds to near-optimal values for the respective mass ratio

and efficiency index, something that is well anticipated based on design trends for mass dampers (Chang 1999; Soong and Dargush 1997). The near-optimality stems from the fact that values for the frequency and damping ratio close to the optimal yield very similar efficiency, as also demonstrated in Figure 2.2 earlier, whereas these values do not impact the upfront cost directly (recall only the mass ratio does so). This leads to similar performance in the considered here objective space. Note also that for the PS greater dispersion is demonstrated for the frequency ratio. This should be attributed to the variability in the fundamental period of the structure, leading to a greater range of values for the damper frequency that yield comparable performance.

The variation of the ratio of upfront to total cost (C_i/C) against C_{thresh} across the Pareto front is then shown Figure 6.19. Especially for the cases corresponding to larger values of the upfront cost (which, recall, represent the TMD case) the initial cost from installation of the dampers is a dominant portion of the total life-cycle cost. This percentage increases as risk-averse designs are prioritized (i.e. for smaller values of the C_{thresh} threshold), since these cases correspond to installation of larger dampers. Same pattern (larger percentage for the initial damper cost) also holds for higher values of the efficiency index; for dampers with the same mass and the same initial cost characteristics, larger efficiency indexes imply greater damper efficiency, leading to bigger reduction in earthquake losses and therefore to a more dominant contribution of the damper installation cost against the total life-cycle cost.

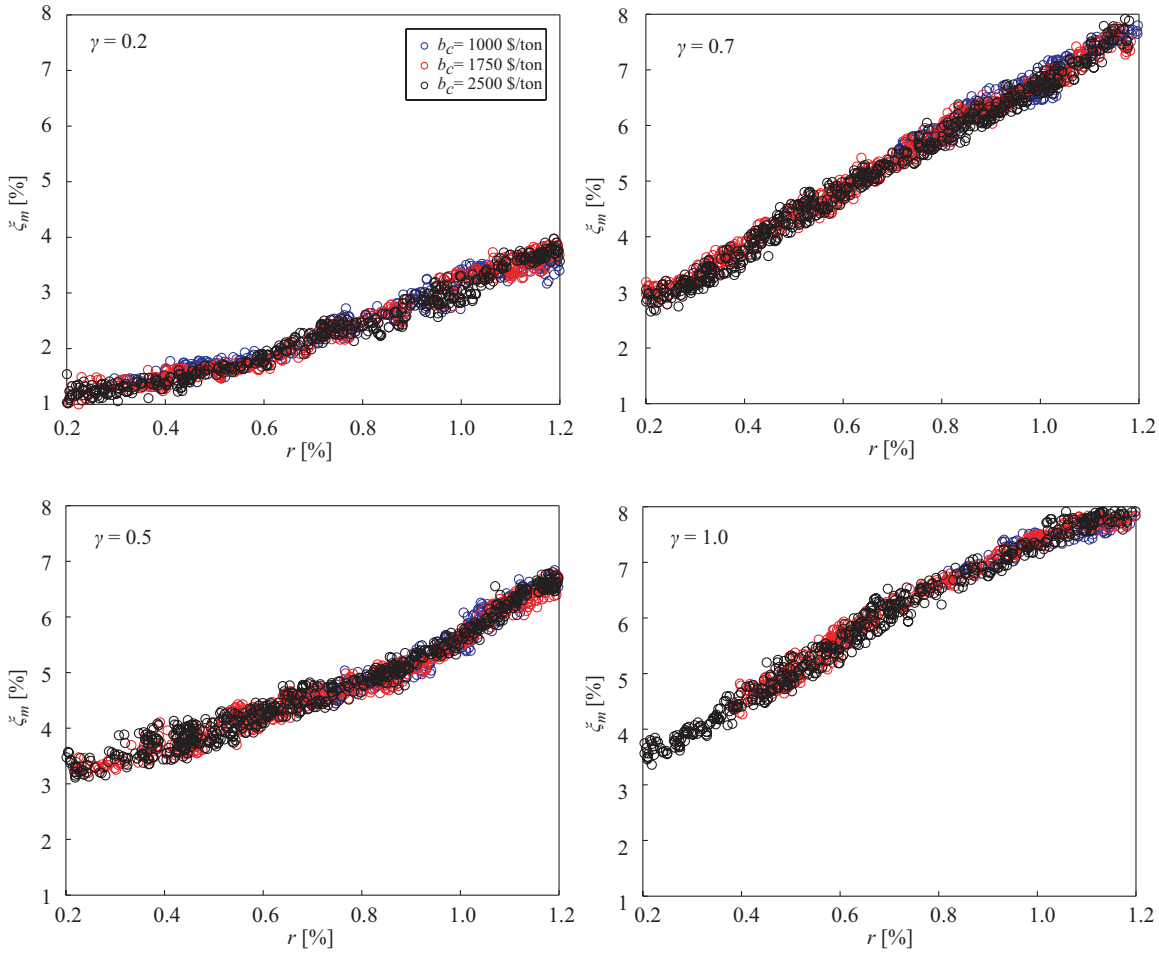

Figure 6.15. Variation of damping ratio ξ_m corresponding to optimal solution across the Pareto front against the corresponding optimal mass ratio r for different efficiency indexes and different assumptions for upfront damper cost (blue is low damper cost, red is medium and black is high). Results correspond to probabilistic structure.

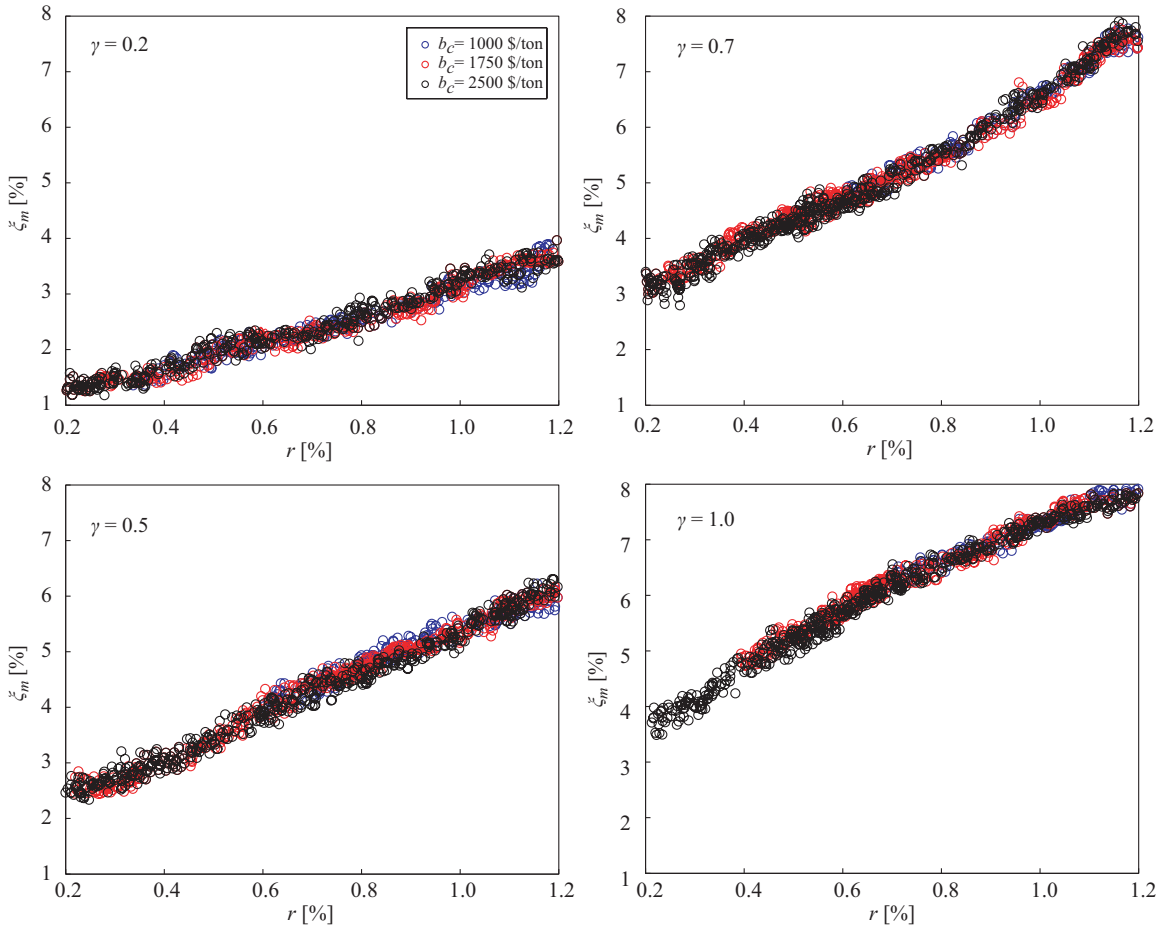

Figure 6.16. Variation of damping ratio ξ_m corresponding to optimal solution across the Pareto front against the corresponding optimal mass ratio r for different efficiency indexes and different assumptions for upfront damper cost (blue is low damper cost, red is medium and black is high). Results correspond to nominal structure.

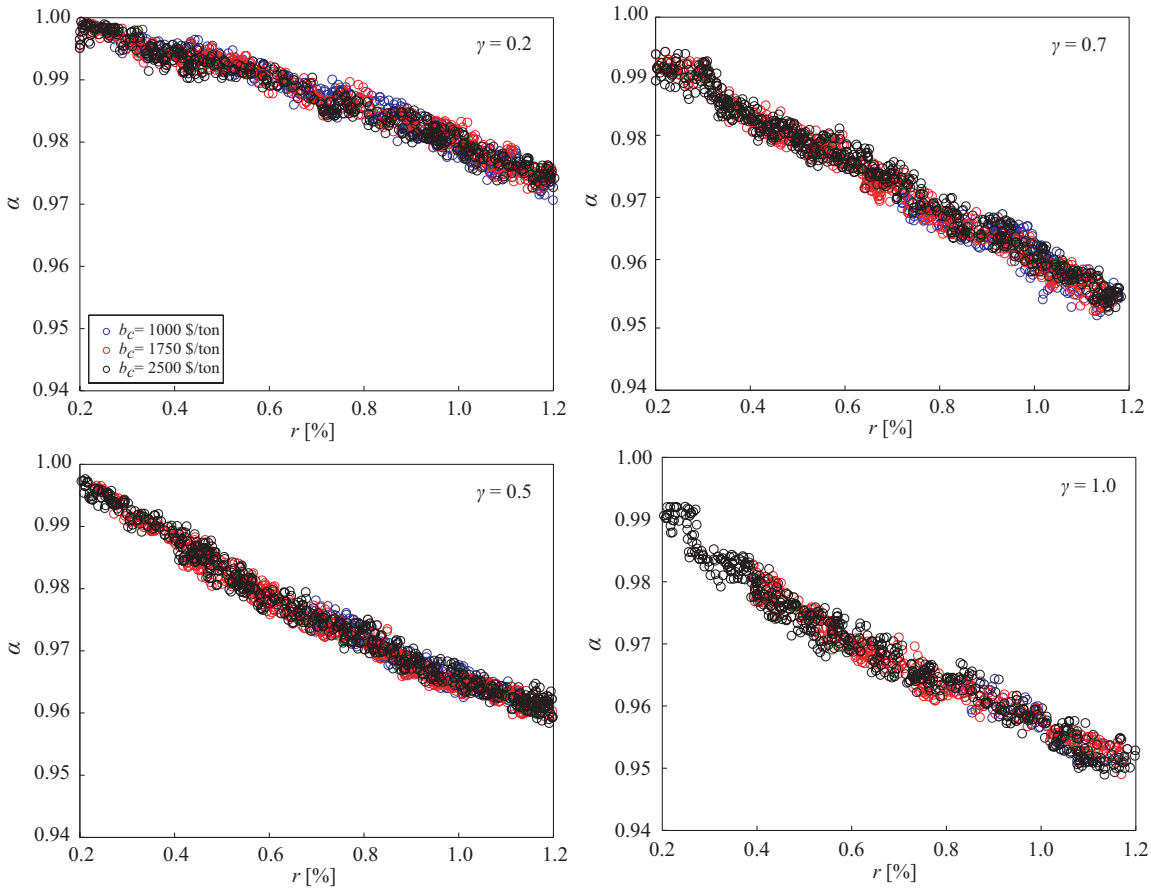

Figure 6.17. Variation of frequency ratio *a* corresponding to optimal solution across the Pareto front against the corresponding optimal mass ratio *r* for different efficiency indexes and different assumptions for upfront damper cost (blue is low damper cost, red is medium and black is high). Results correspond to probabilistic structure.

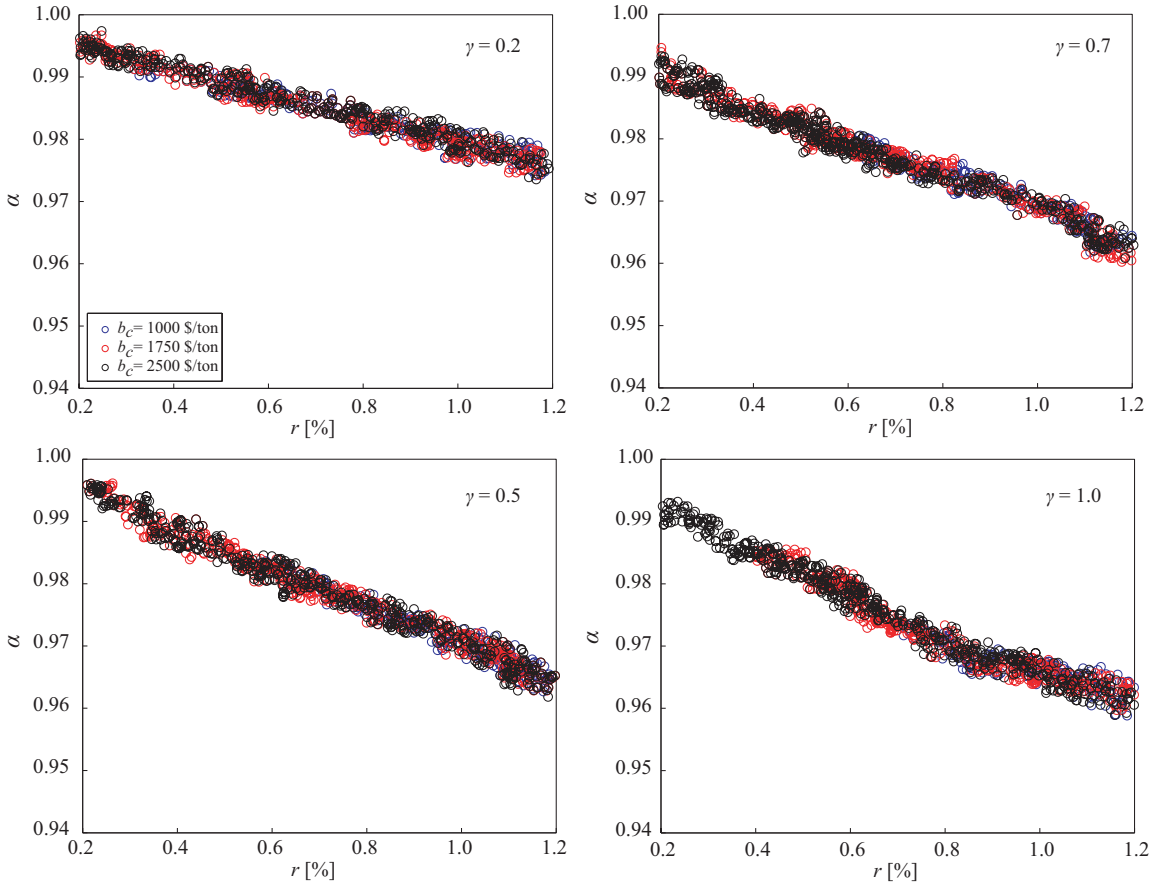

Figure 6.18. Variation of frequency ratio a corresponding to optimal solution across the Pareto front against the corresponding optimal mass ratio r for different efficiency indexes and different assumptions for upfront damper cost (blue is low damper cost, red is medium and black is high). Results correspond to nominal structure.

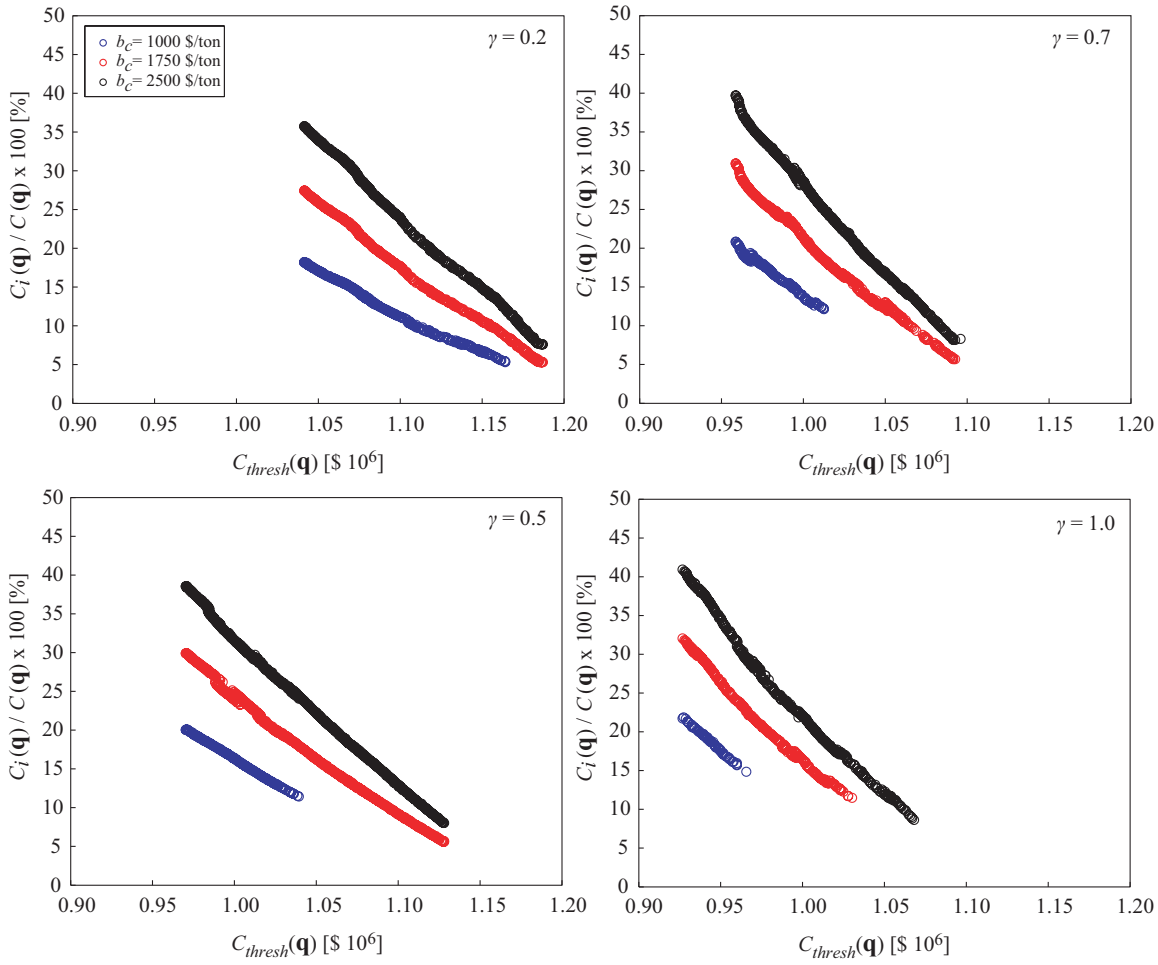

Figure 6.19. Variation of ratio of upfront to total cost against the corresponding optimal repair cost threshold with 10% of probability of exceedance in 50 years C_{thresh} across the Pareto front of optimal solutions for different efficiency indexes and different assumptions for upfront damper cost (blue is low damper cost, red is medium and black is high).

The decomposition of the total repair cost to the different damageable assemblies is also of interest. In general very small variations are reported across the Pareto front and the trends are ultimately a function of the damper efficiency (meaning

mass ratio and efficiency index). Characteristic results are shown in Figure 6.20 which demonstrates this decomposition for four representative optimal design configurations [case correspond to with high upfront cost (2500 $/ton)]. The decomposition for the structure without the dampers (unretrofitted case) are also shown. The results demonstrate anticipated patterns; introduction and increase of the efficiency of the damper (increase of mass ratio or efficiency index) provides a greater benefit for drift-sensitive components.

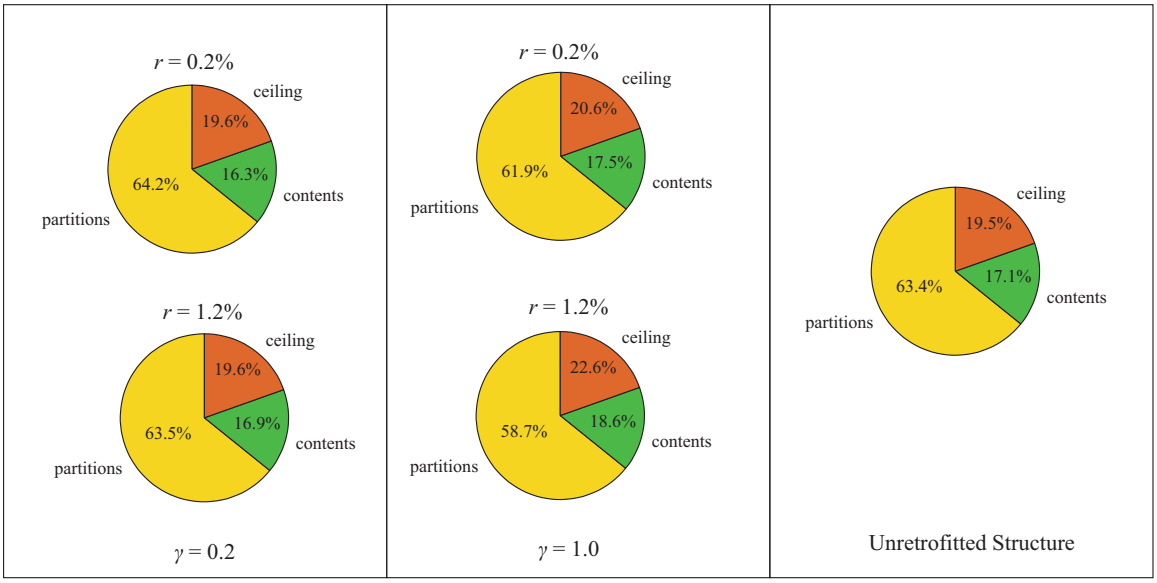

Figure 6.20. Repair cost decomposition for some representative configurations corresponding to optimal solutions across the Pareto front. Results for structure without damper also shown (unretrofitted structure).

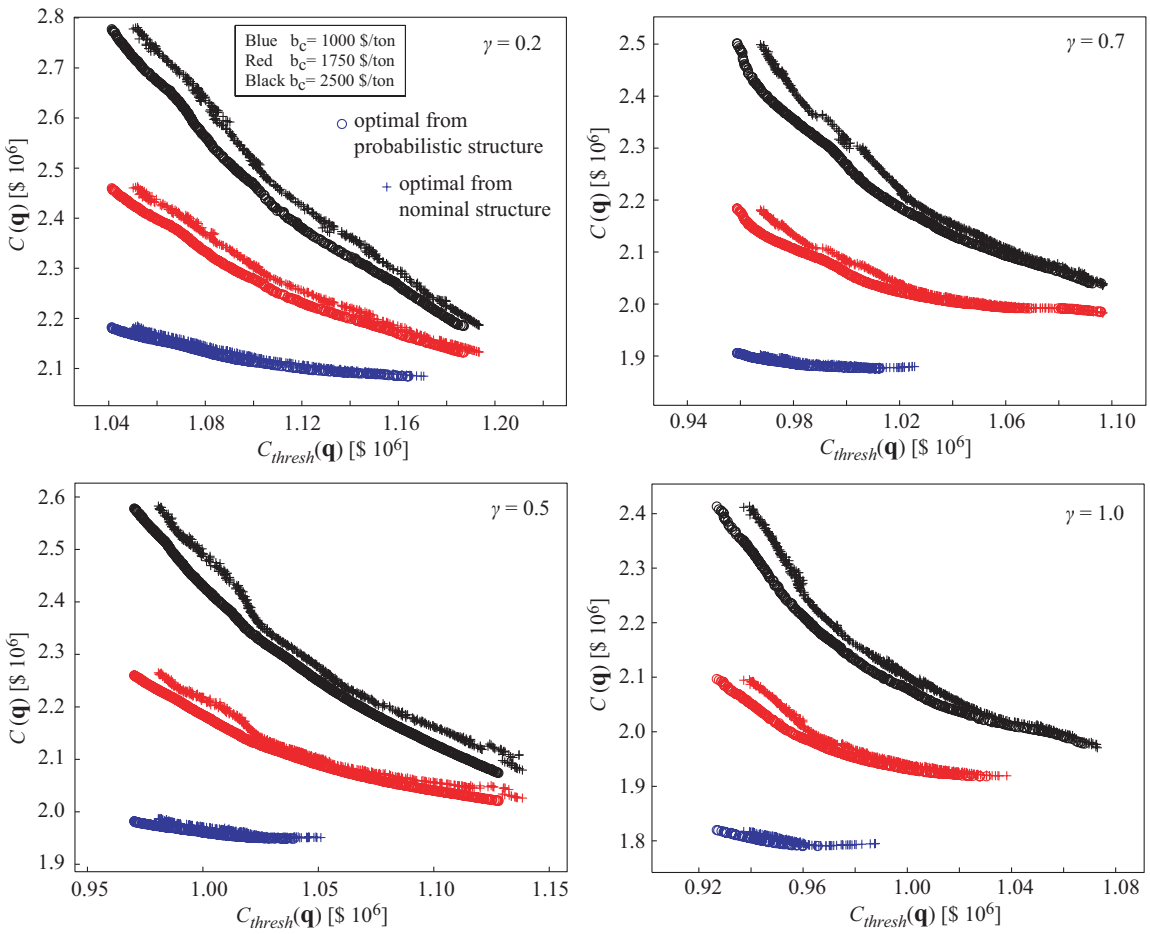

Figure 6.21. Impact of neglecting structural uncertainties in the design stage. Performance (total life-cycle cost C and repair cost threshold with probability of exceedance 10% in 50 years, C_{thresh}) for different efficiency indexes and different assumptions for upfront damper cost (blue is low damper cost, red is medium and black is high) for the probabilistic structure is shown. Pareto front for this case as well as performance for the optimal solution corresponding to the nominal structure are shown.

Finally the effect of neglecting structural uncertainties is examined in Figure 6.21 This figure shows the performance established for the probabilistic structure for the respective Pareto front as well as the design corresponding to the optimal solution from the nominal structure. The comparison answers the question; what would have been

the performance degradation if structural uncertainties were neglected at the design stage (utilize design from NS) but really existed (evaluate performance for the PS and compare to the respective Pareto front)? The results show that the explicit consideration of uncertainties does improve the robustness of the performance (Pareto curves are indeed different) with the effect being greater (larger discrepancies between the curves) when the efficiency of the damper is greater (meaning larger values of the efficiency index or smaller values for the C_{thresh} which, recall, corresponds to larger mass ratios). This result stresses the importance of a design framework that can explicitly incorporate uncertainties related to the structural characteristics within the problem formulation. The simulation-based approach discussed here can seamlessly facilitate this goal since it poses no constraints on the probability and numerical models adopted.

6.6 Summary

In this Chapter the life-cycle based assessment/design of TLDs-FR (or more generally mass dampers) was discussed considering risk characterizations appropriate for the Chilean region. A multi-objective problem was formulated considering the total life-cycle cost and consequences (repair cost) under low-likelihood events and a simulation-based probabilistic framework was adopted for quantifying/assessing these criteria. Within this framework structural performance is described through time-history analysis, adopting a comprehensive, assembly-based vulnerability approach to quantify seismic losses in a detailed, component level. To characterize the seismic hazard a

stochastic ground motion models was calibrated to provide predictions that are compatible with ground motion prediction equations (attenuation relationships) that have been recently published for Chile. For performing the design optimization a surrogate modeling formulation was adopted. The overall approach offers some unique advantages

- Simulation-based assessment allows for adoption of complex numerical and probability models, facilitating a comprehensive hazard characterization. The hazard-compatibility to the Chilean region was established by exploiting this opportunity as well as recent advances in stochastic ground motion modeling.
- Approach also allows for explicitly considering all important sources of uncertainty in the model description. For mass dampers this means that uncertainties related to the dynamic characteristics of the primary structure can be easily considered
- The surrogate modeling approach allows for an efficient optimization for different assumptions for the upfront damper cost.

Exploiting these features the life-cycle based assessment/design of mass dampers for a 21-story structure was examined in the illustrative example. The multi-objective formulation provided in the context of this example a range of Pareto optimal solutions, allowing the building stakeholder to make the final choice prioritizing between the two competing objectives; reduction of the total cost or

improved protection against low likelihood but high potential impact seismic events. Additionally by considering different upfront damper cost, a comparison between TMDs and TLDs-FR was established. Even though TMDs offer enhanced performance for the same mass ratio, when considering the higher upfront cost for them it was demonstrated that TLDs-FR ultimately outperforms them (at least in the context of this example); for the same life-cycle cost their application corresponds to better protection. Therefore TLDs-FR should be considered as an economically competitive option to TMDs for enhancement of seismic performance as long as proper design (avoidance of low efficiency indexes for them) can be accomplished. In addition, explicitly considering uncertainties related to structural dynamic characteristics was shown to provide enhanced robustness in the damper performance.

CONCLUSIONS AND FUTURE WORK

7.1 Summary of Completed Work

This research introduces a new type of mass damper, corresponding to a variation of the traditional TLD but having a relatively simple, easy-to-model, linear behavior. The basis of the new configuration is the introduction of a floating roof that imposes a kinematic constraint on the surface of the liquid and additionally allows the placement of devices to adjust the level of damping in the liquid vibration (to establish the desired optimal damping values). The research also examines the potential of this device in effectively controlling earthquake-induced vibration of structures.

The specific objectives of the research, as stated in Chapter 1, are:

1) Develop a simplified, computationally efficient framework for describing the dynamic behavior of arbitrary geometry liquid storage tanks under base excitation.
2) Extend the previous framework to describe the dynamic behavior of TLDs-FR under base excitations as well as the coupling with the structure that supports them.

3) Validate the numerical models through scaled experiments and evaluate the accuracy of the proposed modeling framework to predict the behavior of TLDs-FR under seismic excitation.
4) Propose a parametric formulation to describe the TLD-FR dynamics only through its fundamental vibratory characteristics (participating mass, frequency and damping of equivalent mass damper) in order to establish a direct comparison with other mass dampers like TMDs, TLCDs and LCVAs.
5) Propose a methodology to establish a mapping between tank geometries and the resultant vibratory characteristics of the TLD-FR and through this approach establish a practical design methodology for selecting the tank characteristics of TLDs-FR.
6) Validate the potential of mass dampers for the Chilean region and establish a multi-objective life-cycle analysis/design process for the TLD-FR considering a risk-description that is relevant for this region. The latter refers to both an appropriate characterization of seismic hazard as well as the adoption of risk-criteria that beyond the total life-cycle cost incorporate risk-averse criteria for describing life-cycle performance.

Chapter 2 offered a quick review of the equations of motion of common type of mass dampers (TMDs, and liquid column mass dampers, TLCDs and LCVAs) and briefly

discussed the behavior/design characteristics for them. It also presented the common tank geometries used in this dissertation for TLDs (or TLDs-FR). Then each of the subsequent Chapters addressed one of more of the aforementioned objectives. Chapter 3 addressed Objective 1, Chapter 4 Objectives 2 and 3, Chapter 5 Objectives 4 and 5, and finally Chapter 6 Objective 6.

7.1.1 Development of an Efficient Computational Procedure to Describe the Dynamic Behavior of Liquid Storage Tanks (Objective 1)

A relatively simple and efficient computational approach, based on a potential-variables-formulated FEM, was developed in Chapter 3 to model the dynamic behavior of liquid storage tanks subjected to base excitations; the methodology was named as Simplified Sloshing Model (SSM). The numerical procedure expresses the linear sloshing problem as a second order lineal system of equations, where the independent variables are the vertical elevations of the free surface and the excitation is directly related to the base acceleration. In this formulation the fluid is assumed ideal, and rigid. These assumptions were exploited to establish a numerical procedure significantly simpler to implement than other comprehensive procedures found in the literature. The SSM was then validated against experimental, analytical and high-fidelity numerical results available in the literature in terms of the predictions for the sloshing period, harmonic response and dynamic response under arbitrary base excitation (seismic response) for rectangular and non-rectangular tanks. Additionally, the ability of the proposed

numerical procedure to predict the response of traditional TLDs placed within a multistory structure was also validated through a direct comparison to an ANSYS implementation.

Although the overall methodology is somewhat standard, the numerical procedure offers significant advantages and physical insight as: (1) the equations are expressed in terms of physical variables (free surface elevation and base acceleration); (2) the system of equations is analogous to that of a mass-spring system; (3) it is applicable to tanks having any geometry; (4) the formulation is suitable for dynamic and frequency analysis; (5) if the tank rests on a supporting structure (i.e., an elevated tank or a TLD), the coupling between the tank and the supporting structure is straightforward; (6) it is relatively easy to implement and to understand; and (7) it is more advanced than the models suggested by current seismic design codes for liquid storage tanks.

7.1.2 Numerical Model for TLD-FR, Experimental Validation and Examination of Fundamental Vibratory Characteristics (Objectives 2 and 3)

In Chapter 3, the TLD-FR was introduced; this pertained to both the development of a numerical model for predicting its behavior as well as an extensive experimental validation through shake table experiments. For the numerical model, the floating roof and the liquid were modeled separately; a typical FEM approach was used to model the floating roof as a flexible beam while the SSM developed in Chapter 3 was used to

model the liquid. The two models were then combined through the pressure in the interface of the liquid and the floating-roof, generating the numerical model proposed for TLDs-FR, termed as Simplified Sloshing Model with Floating Roof (SSM-FR). The experimental investigation, established considering a variety of dynamic excitations and rectangular tank geometries for the TLD/TLD-FR, validated the SSM-FR and additionally offered some important insights. Contrary to the behavior of TLDs, the response of the TLD-FR is practically linear and does not exhibit a significant amplitude dependency. Also, the TLD-FR behaves essentially as a single-degree-of-freedom system, which is a consequence of the floating roof preventing wave breaking and suppressing higher modes of vibrations. Finally the TLD-FR possesses an important level of inherent damping, possibly related to friction and/or drag forces in the gap between the walls and the roof. This is an important consideration for design purposes since it means that external dampers should be selected to provide only a portion of the total optimal damping for the TLD-FR (the remaining portion contributed by the inherent damping).

Ultimately the results in this Chapter show that TLD-FR should be considered an attractive protection device since: a) has a reliable linear behavior, b) it can be equivalently modeled as a single-DOF (easy to model and understand mathematical description), c) supplemental damping devices can be easily added to the roof, d) maintains all advantages of traditional TLDs.

7.1.3 Parametric Formulation of TLD-FR Vibration and Design Procedure (Objective 4 and 5)

In Chapter 5 the fact that the TLD-FR was identified to operate linearly and in a predominant mode was exploited (assumption that only fundamental sloshing mode is important) to establish a parametric representation for its behavior. Through modal truncation and proper normalization of the equation of motion for the TLD-FR and of the force transmitted to its base (facilitating the coupling with the supporting structure), its behavior was described through only four parameters: the mass, frequency and damping ratio and the efficiency index. The first three are parameters used to describe all types of mass dampers whereas the latter is related to the portion of the total liquid mass that participates in the sloshing in the fundamental mode, and is similar to a term (with the same name) used to describe the behavior of liquid column mass dampers. For the latter dampers this index is related to the portion of the total liquid mass participating in the vibration in the horizontal direction. Through this parameterization equivalence of TLDs-FR to liquid column mass dampers was established, meaning that all results for liquid column mass dampers available in the literature are directly extendable to the behavior of TLD-FR. Higher values for the efficiency index provide always better performance under optimal design (and for same mass ratio).Additionally, it was shown through parametric investigation for different tank geometries that higher values of the efficiency index are easy to obtain for the TLD-FR, something that provides a distinct advantage over liquid column mass dampers. Through the same investigation

it was identified that the efficiency index depends only on the transversal shape of the tank, while the frequency can be adjusted by scaling this shape to a specific size (length of tank selection). For complex tank geometries, it is possible to find different shapes that lead to the same efficiency index, creating a mapping that does not correspond to a one-to-one relationship. The total mass of the damper can be adjusted by properly choosing the width of the tank. Multiple tanks can be used if constraints exist for this width, such as architectural constraints or desire to use the TLD-FR to control the motion in both directions (meaning that that dimensions of the tank needs to be also optimally tuned/selected).

The optimization of the TLD-FR should be performed using the parametric formulation, which is desirable since the SSM-FR based on FEM is avoided saving significant computational time. Of course the parametric formulation needs to be mapped in the end to a specific tank geometry and a design procedure was proposed for this task. The targeted mass ratio (or more generally mass) can be established through proper selection of the tank width whereas the optimal damping ratio through proper dimensioning of the external dampers. In the latter case a conservative estimate of the inherent damping can be used to avoid damping values lower than the optimum one (feature that leads to significant deterioration of performance).The efficiency index and optimal frequency can be then chosen based on the cross-sectional tank geometry through a blind-search approach, so that all possible solutions can be identified. These solutions correspond, though, to different displacements for the liquid, so

considerations for the maximum allowable displacement to avoid collisions of the floating roof to the walls or bottom of the tank can provide an additional preference between these solutions. To support the blind-search a surrogate modeling approach was adopted; a highly efficient kriging metamodel was first developed to approximate the relationship between tank geometry and vibratory characteristics and this metamodel was then utilized for all evaluations required within the blind-search.

This procedure was demonstrated for the design of a TLD-FR considering stationary earthquake excitation. It was shown in this example that the TLD-FR can offer a significant level of vibration suppression while the established design approach offers a range of potential solutions all with same performance with respect to the primary structure but with different associated floating roof displacements, allowing the designer to make the final choice bases on considerations for the latter.

7.1.4 Life-cycle Analysis of mass dampers for Chilean buildings (Objective 6)

In Chapter 6 a proper life-cycle analysis was established to investigate the benefits from the addition of TLDs. It is well known that TLDs offer lower installation and maintenance cost than TMDs, so proper comparison of such devices needs to consider the life-cycle performance over their entire lifetime, incorporating the different level of vibration suppression (and thus benefits from reduction of seismic) offered by each. A simulation-based, probabilistic framework was established to estimate and optimize the life cycle cost of Chilean buildings with TLDs-FR. Within this framework structural

performance was described through time-history analysis, adopting a comprehensive, assembly-based vulnerability approach to quantify seismic losses in a detailed, component level. To characterize the seismic hazard a stochastic ground motion models was calibrated to provide predictions that are compatible with ground motion prediction equations (attenuation relationships) that have been recently published for Chile. A multi-objective problem was formulated considering two different criteria: the first one, representing the direct benefits from the damper implementation, was the life-cycle cost of the system, whereas the second criterion, consequences from low likelihood events, was the repair cost with a specific probability of exceedance over the lifetime of the structure. Stochastic simulation was utilized to calculate risk whereas for performing the design optimization a surrogate modeling formulation was adopted.

The overall approach allows for adoption of complex numerical and probability models, while it facilitates an efficient design under different scenarios for the seismic hazard (different seismicity assumptions) or upfront damper cost characterization. Exploiting these features the life-cycle based assessment/design of mass dampers for a 21-story structure was examined as an illustrative example. It was demonstrated through this example that the multi-objective formulation facilitates enhanced decision support as it offers a range of Pareto optimal solutions, allowing the building stakeholder to make the final choice prioritizing between the two competing objectives. Additionally by considering different upfront damper cost, a comparison between TMDs and TLDs-FR was established. It was shown that even though TMDs offer enhanced

performance for the same mass ratio, when considering the higher upfront cost for them TLDs-FR ultimately outperforms them; for the same life-cycle cost their application corresponds to better protection (reduction of repairs for low-likelihood but high impact events or of portion of total cost stemming from necessary repairs over the building lifetime). In addition it was demonstrated that explicitly considering uncertainties related to structural dynamic characteristics provides enhanced robustness in the damper performance.

7.2 Future work

This dissertation established and validated numerical tools for analyzing the performance of TLDs-FR, established efficient design processes for them and examined their life-cycle seismic performance. It showcased their advantages over (i) TLDs as they have practically linear behavior (no weaving breaking or amplitude dependence), and (ii) over liquid column dampers as they can facilitate higher efficiency index values and proved that they are an economically competitive option to TMDs for enhancement of seismic performance as long as proper design (avoidance of low efficiency indexes for them) can be accomplished.

Potential direction of future research, for promoting the adoption of TLDs-FR, are

- Establish a better understanding of the inherent damping TLDs-FR are exhibiting through appropriate experimental investigations. Since proper

design of TLDs-FR requires establishment of an optimal damping, further insights on the inherent damping for TLDs-FR is essential for accomplishing this optimal damping through use of external devices.

- Establish an experimental validation of TLDs-FR for complex cross-sectional geometries. The validation established in this dissertation focused only on rectangular tanks, so additional experiments are required to validate the numerical models and findings for non-rectangular tanks.
- Investigate the bi-directional control capabilities of TLD-FRs.

APPENDIX A: EIGENVALUE PROBLEM ASSOCIATED WITH SSM

In Chapter 3, the equation of motion of a TLD is expressed by Equation (3.18) which leads to an eigenvalue problem that involves the square matrices $\mathbf{M}_s$ and $\mathbf{K}_s$. Recall that $\mathbf{J} = \mathbf{D}_{ss} - \mathbf{D}_{sr}\mathbf{D}_{rr}^{-1}\mathbf{D}_{rs}$, $\mathbf{G}$ is symmetric and given by Equation (3.12), $\mathbf{M}_s = \mathbf{J}^{-1}\mathbf{G}$ and $\mathbf{K}_s = g\,\mathbb{I}$. Matrix $\mathbf{K}_s$ is symmetric though $\mathbf{M}_s$ is not, therefore the product $\mathbf{M}_s^{-1}\mathbf{K}_s$ is not guaranteed to be symmetric which means that solution of the eigenvalue problem is not immediately guaranteed to be real. However, the product $\mathbf{M}_s^{-1}\mathbf{K}_s$ can be rewritten as $\mathbf{G}^{-1}\mathbf{J}\,\mathbf{K}_s$, where both $\mathbf{G}$ as well as the product $\mathbf{J}\,\mathbf{K}_s$ are symmetric. It is then straightforward to show that the eigenvalues (and eigenvectors) of the product of two symmetric matrices are real. Therefore despite $\mathbf{M}_s^{-1}\mathbf{K}_s$ leading to an asymmetric matrix, the associated eigenvalue problem is guaranteed to lead to real solutions for the eigenvalues and associated eigenvectors.

APPENDIX B: ADDITIONAL EXPERIMENTAL RESULTS

Additional results related to the experimental tests discussed in Chapter 4 are included here. First the free responses due to an impulsive excitation are shown in Figure B.1, Figure B.2 and Figure B.3. These results are used to identify experimentally natural periods and damping factors described in Table 4.2 and Table 4.3, respectively.

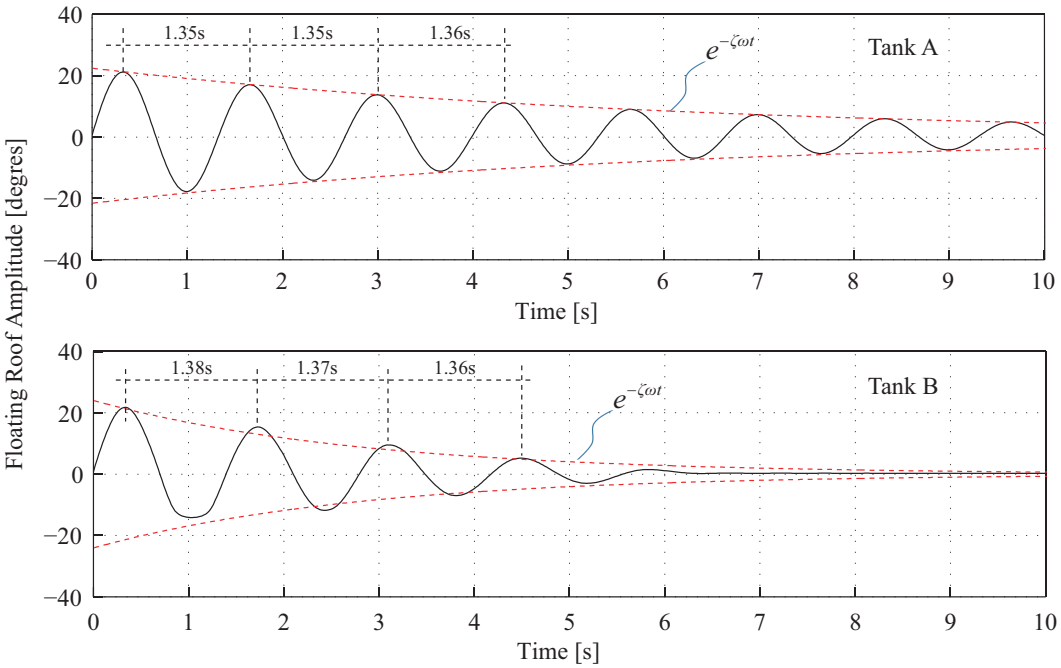

Figure B.1 Free response of the floating roof for configurations identified as Tank A and Tank B obtained after imposing a pulse-like excitation.

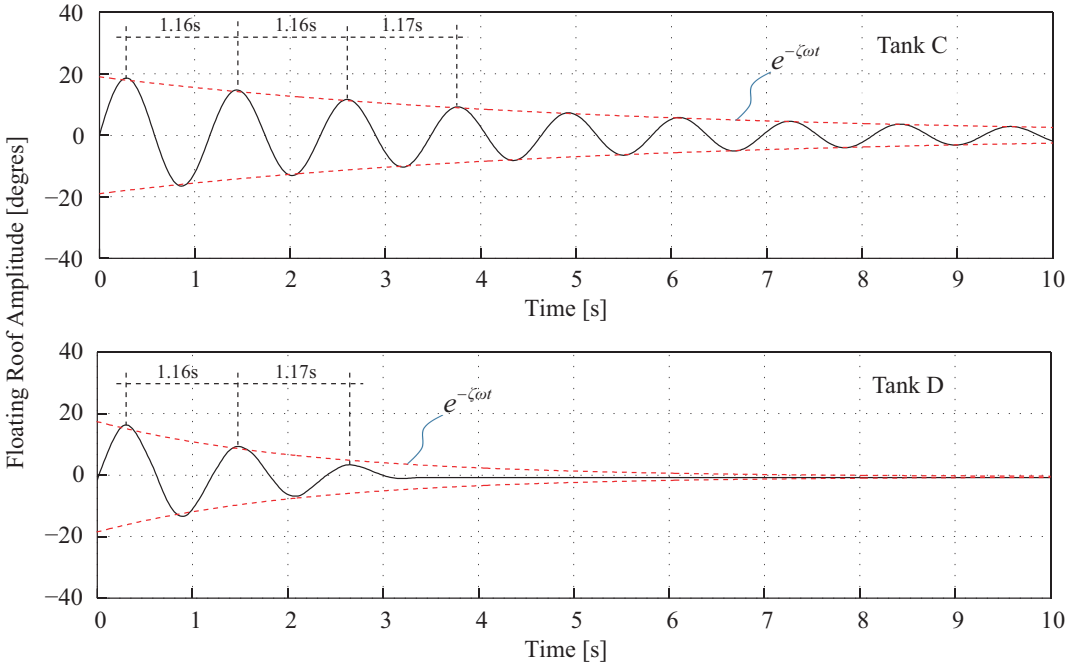

Figure B.2 Free response of the floating roof for configurations identified as Tank C and Tank D obtained after imposing a pulse-like excitation.

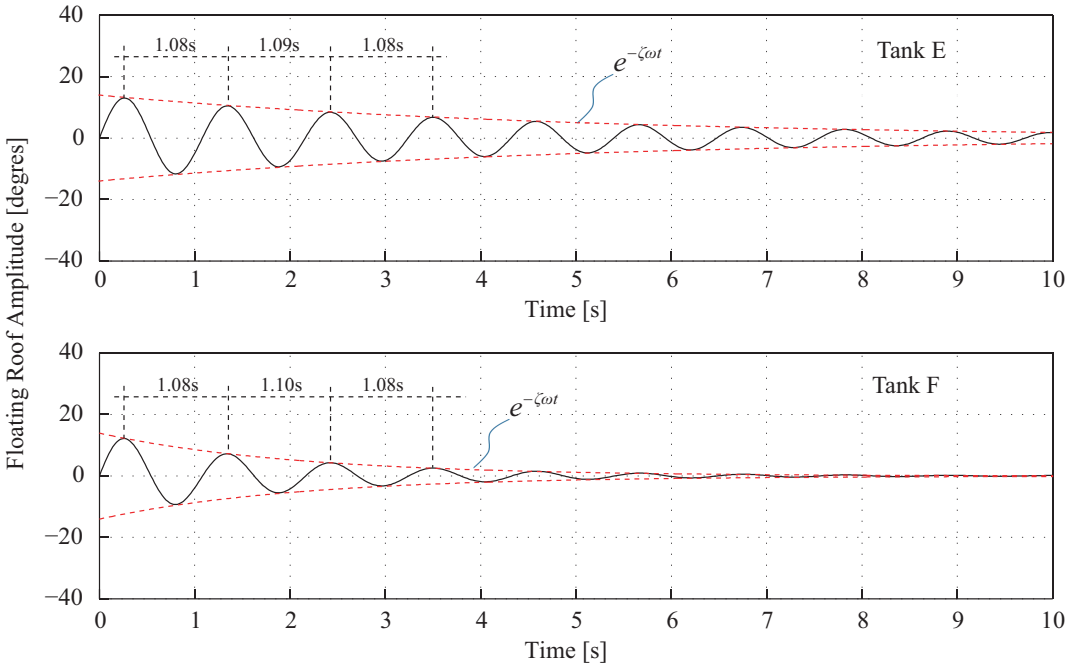

Figure B.3 Free response of the floating roof for configurations identified as Tank E and Tank F obtained after imposing a pulse-like excitation.

Next, Figure B.4, Figure B.5, Figure B.6 and Figure B.7 present, similar to Figure 4.9 and Figure 4.10, the seismic responses of the TLDs-FR identified as Tank C, D, E and F. Good agreements are again observed between numerical and experimental results.

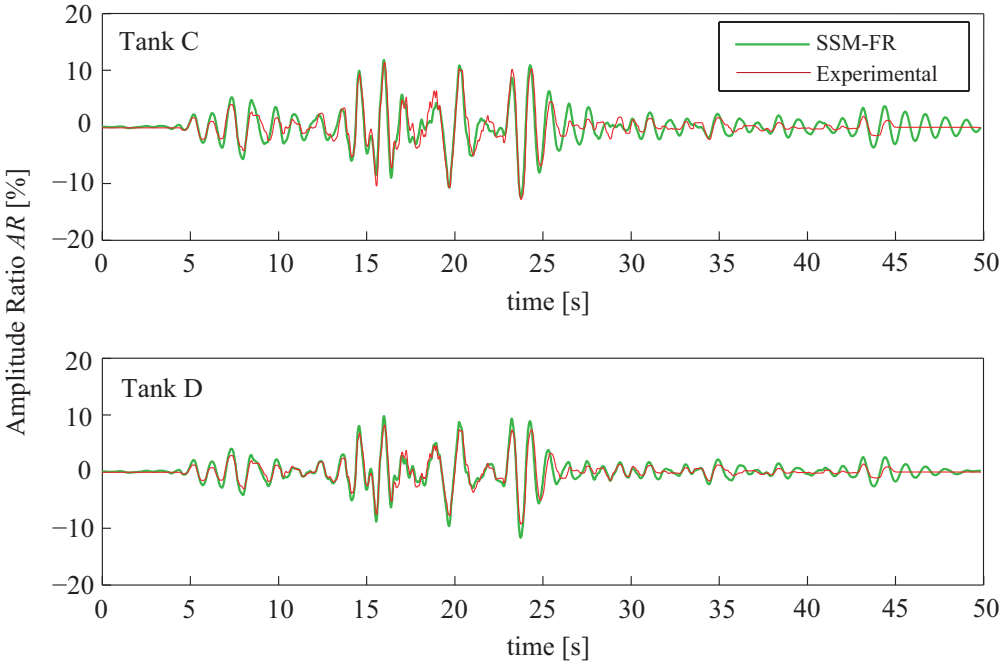

Figure B.4 Floating roof amplitude for tanks C and D under seismic excitation. Comparison between numerical and experimental results shown.

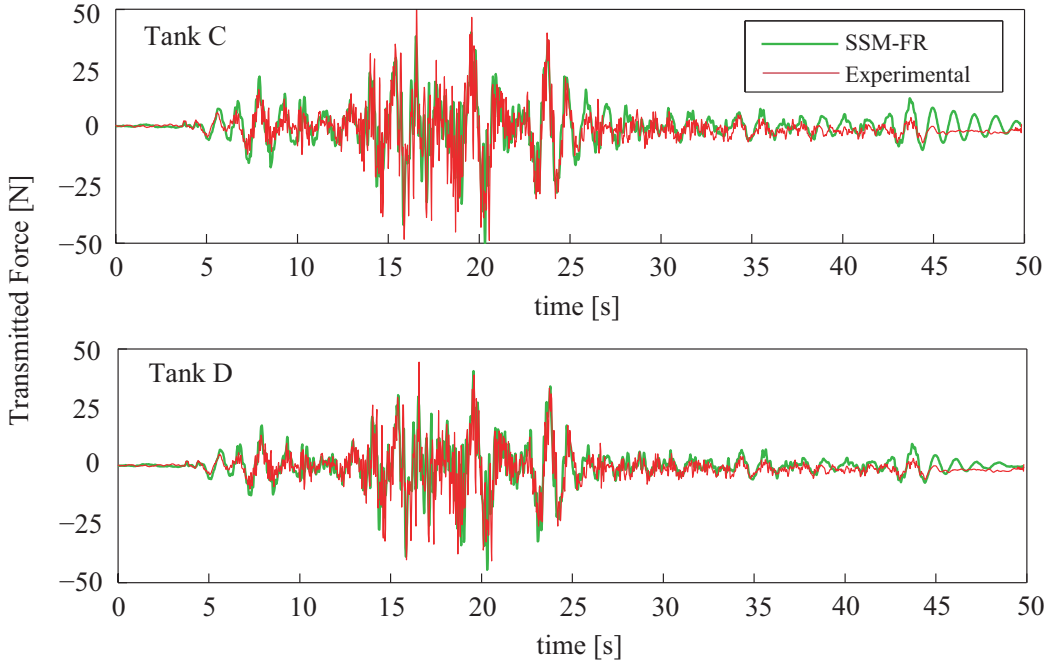

Figure B.5 Transmitted force for tanks C and D under seismic excitation. Comparison between numerical and experimental results shown.

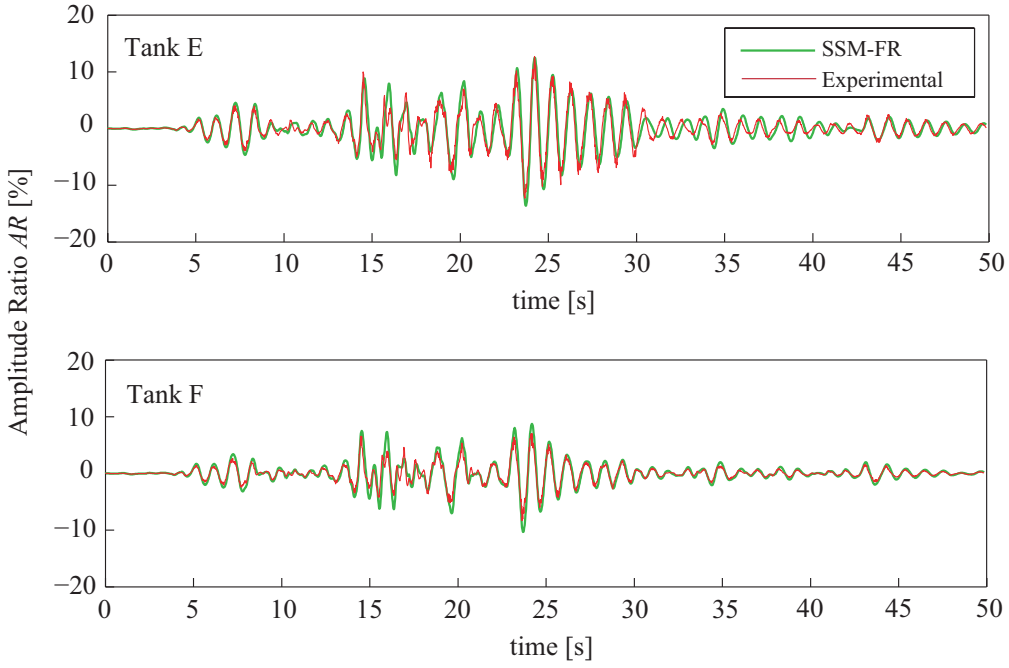

Figure B.6 Floating roof amplitude for tanks E and F under seismic excitation. Comparison between numerical and experimental results shown.

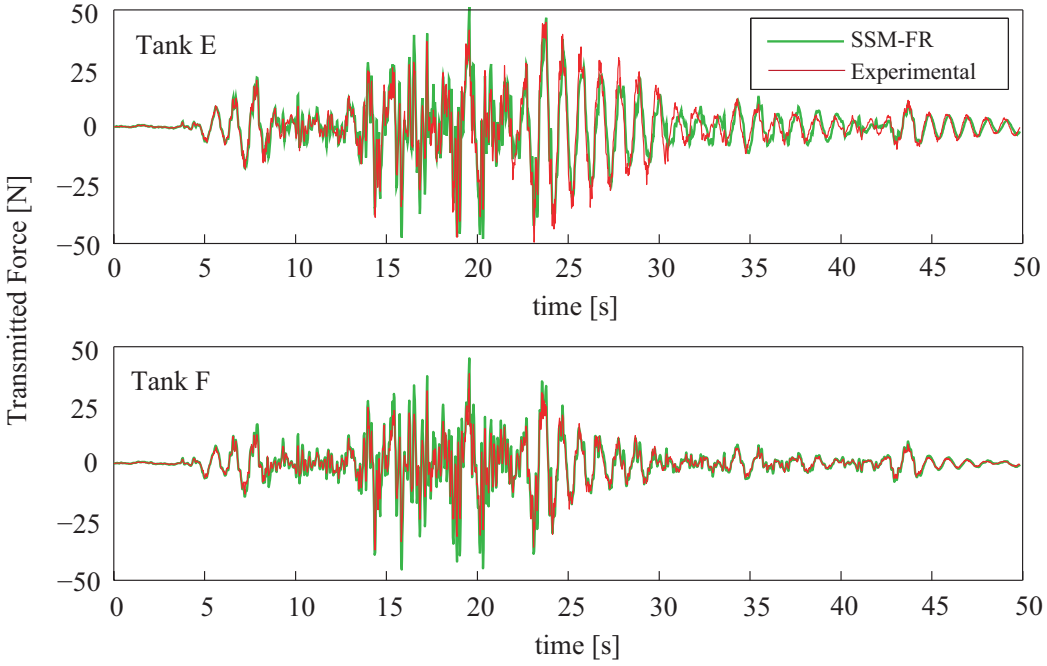

Figure B.7 Transmitted force for tanks E and F under seismic excitation. Comparison between numerical and experimental results shown.

APPENDIX C: KRIGING METAMODELING

Kriging provides a simplified relationship between the input and output of a process (for example a computational expensive simulation model) utilizing existing information (database) for them. Let $\mathbf{x} \in \mathbb{R}^{n_x}$ and $\mathbf{z}(\mathbf{x}) \in \mathbb{R}^{n_z}$ denote the input and output, respectively, following the notation for the implementation of kriging in Chapter 5 within this dissertation, and assume that a database (training set) exist of n_{sup} number of **x-z(x)** pairs (also known as support points), $\{\mathbf{x}^j - \mathbf{z}(\mathbf{x}^j) : j = 1,\ldots,n_{\text{sup}}\}$. Derivation of the database if formally known as DoE (Design of Experiments) and common approach is to use a space filling algorithm for it (such as Latin Hypercube Sampling) within the range X of possible values for $\mathbf{x}$. The fundamental building blocks of Kriging are the n_p dimensional basis vector, $\mathbf{f}(\mathbf{x})$, and the correlation function $R(\mathbf{x}^j,\mathbf{x}^k)$ with typical selections corresponding, respectively, to a full quadratic basis and a generalized exponential correlation, leading to

$$\begin{aligned} &\mathbf{f}(\mathbf{x}) = [1 \;\; x_1 \;\; \cdots \;\; x_{n_x} \;\; x_1^2 \;\; x_1x_2 \;\; \cdots \;\; x_{n_x}^2]; \quad n_p = (n_x+1)(n_x+2)/2 \\ &R(\mathbf{x}^j,\mathbf{x}^k) = \prod_{i=1}^{n_x} \exp[-s_i \,|\, \mathbf{x}_i^j - \mathbf{x}_i^k \,|^{s_{n_x+1}}]; \quad \mathbf{s} = [s_1 \;\; \cdots \;\; s_{n_x+1}] \end{aligned} \tag{C.1}$$

Then for the set of n_{sup} observations (training set) with input matrix $\mathbf{X} = [\mathbf{x}^1 \;\; \cdots \;\; \mathbf{x}^{n_{\text{sup}}}]^T$ and corresponding output $\mathbf{Z} = [\mathbf{z}(\mathbf{x}^1) \;\; \cdots \;\; \mathbf{z}(\mathbf{x}^{n_{\text{sup}}})]^T$, we define the basis

matrix $F = [f(\mathbf{x}^1) \ \ldots \ f(\mathbf{x}^{n_{sup}})]^T$ and the correlation matrix $\mathbf{R}$ with the *jk*-element defined as $R(\mathbf{x}^j,\mathbf{x}^k)$, $j,k=1, \ldots, n_{sup}$. Also for every new input $\mathbf{x}$, we define the correlation vector $\mathbf{r}(\mathbf{x}) = [R(\mathbf{x},\mathbf{x}^1) \ \ldots R(\mathbf{x},\mathbf{x}^{n_{sup}})]^T$ between the input and each of the elements of $\mathbf{X}$. Then the kriging approximation is given by (Lophaven et al. 2002):

$$\begin{aligned} \mathbf{z}(\mathbf{x}) &= \mathbf{f}(\mathbf{x})^T \boldsymbol{\alpha}^* + \mathbf{r}(\mathbf{x})^T \boldsymbol{\beta}^* \\ \boldsymbol{\alpha}^* &= (\mathbf{F}^T \mathbf{R}^{-1} \mathbf{F})^{-1} \mathbf{F}^T \mathbf{R}^{-1} \mathbf{Z} \\ \boldsymbol{\beta}^* &= \mathbf{R}^{-1}(\mathbf{Z} - \mathbf{F}\boldsymbol{\alpha}^*) \end{aligned} \qquad \text{(C.2)}$$

Through the proper tuning of the parameters, $\mathbf{s}$, of the correlation function, kriging can efficiently approximate very complex functions. More details on this optimization may be found in (Lophaven et al. 2002). The accuracy of the metamodel can be evaluated considering a leave-one out cross validation approach (Meckesheimer et al. 2002).

APPENDIX D: REVIEW OF STOCHASTIC GROUND MOTION MODEL USED IN THIS STUDY

A quick overview of the stochastic ground motion model utilized in Chapter 6 is presented here. The presentation follows directly the one in (Vetter et al. 2014), with the modification of adopting the recommendations of Papadimitriou (1990) for the variation of the frequency characteristics in time (establishing the desired spectral non-stationatiry). The discretized time history of the ground motion, $\ddot{a}_g(t)$, is expressed as

$$\ddot{a}_g(t) = e(t,\boldsymbol{\theta}_g)\left\{\sum_{i=1}^{k}\frac{h[t-t_i,\boldsymbol{\theta}_g(t_i))]}{\sqrt{\sum_{j=1}^{k}h[t-t_j,\boldsymbol{\theta}_g(t_j))]^2}}w_w(i\Delta t)\right\} \quad k\Delta t < t < (k+1)\Delta t \qquad \text{(D.1)}$$

where $\mathbf{W}_w=[w_w(i\Delta t)$: $i=1,2,\ldots, N_T]$ is a white noise sequence, $\Delta t=0.005$ s is the chosen discretization interval, $e(t,\boldsymbol{\theta}_g)$ is the time-modulating function, and $h[t\text{-}\tau,\boldsymbol{\theta}_g(\tau)]$ is an impulse response function corresponding to the pseudo-acceleration response of a single-degree-of-freedom (SDOF) linear oscillator with time varying frequency $\omega_f(\tau)$ and damping ratio $\zeta_f(\tau)$, in which τ denotes the time of the pulse

$$h[t-\tau,\boldsymbol{\theta}_g(\tau))] = \frac{\omega_f(\tau)}{\sqrt{1-\zeta_f^2(\tau)}}\exp\left[-\omega_f(\tau)\zeta_f(\tau)(t-\tau)\right]\sin\left[\omega_f(\tau)\sqrt{1-\zeta_f^2(\tau)}(t-\tau)\right]; \tau \le t \qquad \text{(D.2)}$$
$$= 0; \quad \text{otherwise}$$

For the time varying characteristics an exponential decaying function for $\omega_f(\tau)$ and a linearly varying function for the bandwidth $\alpha_f(\tau) = \zeta_f(\tau)\omega_f(\tau)$, established based on comparison to recorded ground motions, are adopted, leading to parameterization

$$\omega_f(\tau) = \omega_r + (\omega_p - \omega_r)\left(\frac{\omega_s - \omega_r}{\omega_p - \omega_r}\right)^{\tau/t_{\max}}$$
$$\zeta_f(\tau) = \alpha_f(\tau)/\omega_f(\tau) \text{ where } \alpha_f(\tau) = \omega_p\zeta_p + (\omega_r\zeta_r - \omega_p\zeta_p)\tau/t_r \quad \text{(D.3)}$$

with ω_p (primary wave frequency), ω_s (secondary wave frequency), ω_r (surface wave frequency), ζ_p (primary wave damping), and ζ_r (surface wave damping) ultimately corresponding to the primary model parameters for the filter, $t_{\max}$ corresponding to the time at which maximum intensity of the ground motion is achieved and t_r to a sufficiently large time, chosen here to be proportional to the time that 95% of the Arias intensity is reached, denoted t_{95}, given by:

$$t_r = \alpha_{dur} t_{95} \quad \text{(D.4)}$$

The time envelope $e(t, \boldsymbol{\theta}_g)$ is parameterized by by

$$e(t, \boldsymbol{\theta}_g) = e(t, I_a, \alpha_2, \alpha_3) = \sqrt{I_a}\left[\sqrt{\frac{2}{\pi}\frac{(2\alpha_3)^{2\alpha_2 - 1}}{\Gamma(2\alpha_2 - 1)}}\right] t^{\alpha_2 - 1}\exp(-\alpha_3 t) \quad \text{(D.5)}$$

where $\Gamma(.)$ is the gamma function, I_a is the Arias intensity expressed in terms of g, and $\{\alpha_2, \alpha_3\}$ are additional parameters controlling the shape and total duration of the envelope that can be related to the strong motion duration, $D_{5\text{-}95}$ (defined as the duration for the Arias intensity to increase from 5% to 95% of its final value), and the

peak of the envelope function, λ_p, are used. The latter is defined as the ratio of time corresponding to the peak of the envelope to the time corresponding to 95% of its peak value. The pair {α_2, α_3} can be easily determined based on the values of {$D_{5\text{-}95}$, λ_p} through the following approach: for the chosen time-modulating function, the variance function $e^2(t, I_a, \alpha_2, \alpha_3)$ (related to Arias intensity) is proportional to a gamma probability function having shape and scale parameters, $2\alpha_2 - 1$ and $1/(2\alpha_3)$ respectively. If t_p represents the p-percentile variate of the gamma cumulative distribution function (this means that t_p is given in terms of the inverse of the gamma cumulative distribution function at probability value p %) then it follows that t_p is uniquely given in terms of the parameters α_2 and α_3, and probability $p\%$. Therefore, the strong ground motion duration is simply $D_{5-95} = t_{95} - t_5$. The value of λ_p is further defined as the ratio of time corresponding to the peak of the envelope to the time corresponding to 95% of its peak value.

Ultimately, the ground motion model has as parameters $\boldsymbol{\theta}_g = \{I_a, D_{5-95}, \lambda_p, \alpha_{dur}, \omega_p, \omega_s, \omega_r, \zeta_p, \zeta_r\}$ and the functional form for their predictive relationships are chosen based on the recommendations in (Travasarou et al. 2003; Bommer et al. 2009; Rathje et al. 2004) with an additional modification for I_a so that it matches better to the functional form of the targeted GMPE (Boroschek and Contreras 2012). This leads to the following expressions for the predictive relationships

$$\ln\left(I_a\right)=c_{1,1}+c_{1,2}M+c_{1,3}r_{rup}+c_{1,4}r_{rup}M+c_{1,5}M^2+c_{1,6}{r_{rup}}^2+c_{1,7}\ln\left(M\right)+c_{1,8}\ln\left(r_{rup}\right);$$
$$\ln\left(D_{5-95}\right)=c_{2,1}+c_{2,2}M+c_{2,3}\ln\left(\sqrt{{r_{rup}}^2+c_{2,4}^2}\right);\quad \ln\left(\lambda_p\right)=c_{3,1}+c_{3,2}M+c_{3,3}r_{rup};$$
$$\ln\left(\alpha_{dur}\right)=c_{4,1}+c_{4,2}M+c_{4,3}r_{rup};$$
$$\ln\left(\omega_p/2\pi\right)=c_{5,1}+c_{5,2}M+c_{5,3}r_{rup};\quad \ln\left(\omega_s/2\pi\right)=c_{6,1}+c_{6,2}M+c_{6,3}r_{rup};$$
$$\ln\left(\omega_r/2\pi\right)=c_{7,1}+c_{7,2}M+c_{7,3}r_{rup};$$
$$\ln\left(\zeta_p\right)=c_{8,1}+c_{8,2}M+c_{8,3}r_{rup};\quad \ln\left(\zeta_r\right)=c_{9,1}+c_{9,2}M+c_{9,3}r_{rup} \tag{D.6}$$

with the coefficients $c_{i,l}$ i=1,…,9, l=1,…,8 formulating the coefficient vector $\mathbf{c}$, representing ultimately the vector optimized to establish the desired hazard compatibility.

The optimized coefficients for a match to the GMPE presented recently in (Boroschek and Contreras 2012) for seismicity ranges for M and r_{rup} in [5.5 9] and [30 250] km, respectively, and for responses corresponding to peak ground acceleration PGA and peak spectral acceleration S_{pa} for 5% damped elastic SDOFs with periods 1.6 s or 2 s, are given in Table D.1.

Table D.1 Optimized coefficients for the predictive relationships of the stochastic ground motion model parameters to achieve GMPE compatibility

$c_{1,1}$	-17.6737	$c_{3,1}$	-1.122	$c_{7,1}$	2.3025
$c_{1,2}$	4.2932	$c_{3,2}$	-0.043	$c_{7,2}$	-0.3227
$c_{1,3}$	-0.0895	$c_{3,3}$	-0.0464	$c_{7,3}$	-0.0345
$c_{1,4}$	0.0068	$c_{4,1}$	-0.2706	$c_{8,1}$	-3.6364
$c_{1,5}$	-0.1565	$c_{4,2}$	0.0071	$c_{8,2}$	0.211
$c_{1,6}$	0.0001	$c_{4,3}$	0.027	$c_{8,3}$	-0.0195
$c_{1,7}$	-2.7709	$c_{5,1}$	3.7109	$c_{9,1}$	-1.8895
$c_{1,8}$	0.427	$c_{5,2}$	-0.0079	$c_{9,2}$	0.0904
$c_{2,1}$	0.7694	$c_{5,3}$	-0.0119	$c_{9,3}$	-0.0175
$c_{2,2}$	0.5626	$c_{6,1}$	3.1995		
$c_{2,3}$	-0.3978	$c_{6,2}$	-0.0339		
$c_{2,4}$	5.0729	$c_{6,3}$	-0.0336		

BIBLIOGRAPHY

Abe, M., and Fujino, Y. (1994). Dynamic characterization of multiple tuned mass dampers and some design formulas. Earthquake Engineering and Structural Dynamics *23*, 813–835.

Ali Goudarzi, M., and Reza Sabbagh-Yazdi, S. (2012). Investigation of nonlinear sloshing effects in seismically excited tanks. Soil Dynamics and Earthquake Engineering *43*, 355–365.

Almazan, J., Cerda, F.A., De La Llera, J., and Lopez-Garcia, D. (2007). Linear Isolation od stainless steel legged thin-walled wine tank. Engineering Structures *29*, 1596–1611.

American Petroleum Institute (API) (2003). Welded storage tanks for oil storage, API 650.

American Water Works Association (AWWA) (2005). Welded steel tanks for water storage. AWWA D-100.

Ang, A.H.-S., and Lee, J.-C. (2001). Cost optimal design of R/C buildings. Reliability Engineering and System Safety *73*, 233–238.

ANSYS, R. (2007). Release 11.0 Documentation for ANSYS.

Augusti, G., and Ciampoli, M. (2008). Performance-Based Design in risk assessment and reduction. Probabilistic Engineering Mechanics *23*, 496–508.

Baker, J.W., and Cornell, C.A. (2005). A vector-valued ground motion intensity measure consisting of spectral acceleration and epsilon. Earthquake Engineering and Structural Dynamics *34*, 1193–1217.

Balendra, T., Wang, C.M., and Cheong, H.F. (1995). Effectiveness of tuned liquid column dampers for vibration control of towers. Engineering Structures *17*, 668–668.

Banerji, P., and Samanta, A. (2011). Earthquake vibration control of structures using hybrid mass liquid damper. Engineering Structures *33*, 1291–1301.

Banerji, P., Murudi, M., Shah, A.H., and Popplewell, N. (2000). Tuned liquid dampers for controlling earthquake response of structures. Earthquake Engineering & Structural Dynamics *29*, 587–602.

Bazzurro, P., and Cornell, C.A. (1999). Disaggregation of seismic hazard. Bulletin of the Seismological Society of America *89*, 501–520.

Bermudez, A., and Rodriguez, R. (1994). Finite element computation of the vibration modes of a fluid-solid system. Computer Methods in Applied Mechanics and Engineering *119*, 355–370.

Bermudez, A., Duran, R., and Rodriguez, R. (1997). Finite element solution of incompressible fluid-structure vibration problems. International Journal for Numerical Methods in Engineering *40*, 1435–1448.

Bermudez, A., Duran, R., and Rodriguez, R. (1998). Finite element analysis of compressible and incompressible fluid-solid systems. Mathematics of Computation *67*, 111–111.

Bertoglio, C. (2007). A reduced finite element model for seismic three-dimensional fluid-structure interaction with free surface.

Biswal, K.C., Bhattacharyya, S.K., and Sinha, P.K. (2003). Dynamic characteristics of liquid filled rectangular tank with baffles. Journal of the Institution of Engineers (India): Civil Engineering Division *84*, 145–148.

Bommer, J.J., Stafford, P.J., and Alarcon, J.E. (2009). Empirical equations for the prediction of the significant, bracketed, and uniform duration of earthquake ground motion. Bulletin of the Seismological Society of America *99*, 3217–3233.

Boore, D.M. (2003). Simulation of ground motion using the stochastic method. Pure and Applied Geophysics *160*, 635–676.

Boroschek, R., and Contreras, V. (2012). Strong ground motion form the 2010 Mw 8.8 Maule Chile earthquake and attenuation relations for Chilean subduction zone interface earthquakes. In Proceedings of the International Symposium on Engineering Lessons Learned from the 2011 Great East Japan Earthquake.

Boroschek, R., Soto, P., and Leon, R. (2015). Chilean Seismic Records Database.

Boroschek, R.L., Contreras, V., Kwak, D.Y., and Stewart, J.P. (2012). Strong ground motion attributes of the 2010 Mw 8.8 Maule, Chile, earthquake. Earthquake Spectra *28*, S19–S38.

Bozorgnia, B. (2004). Earthquake Engineering: From Engineering Seismology to Performance-based Engineering (Boca Raton FL).

C. Christopoulos, A. Filiatrault (2006). Principles of Passive Supplemental Damping and Seismic Isolation.

Cerda, F.A. (2006). Proteccion sismica para estanques de acero inoxidable de pared delgada (EAIPD) con apoyos.

Cha, E.J., and Ellingwood, B.R. (2013). Seismic risk mitigation of building structures: The role of risk aversion. Structural Safety *40*, 11–19.

Chakraborty, S., and Roy, B.K. (2011). Reliability based optimum design of Tuned Mass Damper in seismic vibration control of structures with bounded uncertain parameters. Probabilistic Engineering Mechanics *26*, 215–221.

Chakraborty, S., Debbarma, R., and Marano, G.C. (2012). Performance of tuned liquid column dampers considering maximum liquid motion in seismic vibration control of structures. Journal of Sound and Vibration *331*, 1519–1531.

Chang, C.C. (1999). Mass dampers and their optimal designs for building vibration control. Engineering Structures *21*, 454–463.

Chang, C.C., and Hsu, C.T. (1998). Control performance of liquid column vibration absorbers. Engineering Structures *20*, 580–586.

Chen, H.C., and Taylor, R.L. (1990). Vibration analysis of fluid-solid systems using a finite element displacement formulation. International Journal for Numerical Methods in Engineering *29*, 683–698.

Chen, W., Haroun, M.A., and Liu, F. (1996). Large amplitude liquid sloshing in seismically excited tanks. Earthquake Engineering & Structural Dynamics *25*, 653–669.

Coello, C., Lamont, G., and van Veldhuizen, D. (2007). Evolutionary Algorithms for Solving Multi-Objective Problems (Springer).

Corotis, R. (2009). Societal issues in adopting life-cycle concepts within the political system. Structure and Infrastructure Engineering *5*, 59–65.

Daniel, Y., and Lavan, O. (2014). Gradient based optimal seismic retrofitting of 3D irregular buildings using multiple tuned mass dampers. Computers and Structures *139*, 84–97.

Deb, K., Agrawal, S., Pratap, A., and Meyarivan, T. (2000). A fast elitist non-dominated sorting genetic algorithm for multi-objective optimization: NSGA-II. Lecture Notes in Computer Science *1917*, 849–858.

Debbarma, R., Chakraborty, S., and Kumar Ghosh, S. (2010a). Optimum design of tuned liquid column dampers under stochastic earthquake load considering uncertain bounded system parameters. International Journal of Mechanical Sciences *52*, 1385–1393.

Debbarma, R., Chakraborty, S., and Ghosh, S. (2010b). Unconditional reliability-based design of tuned liquid column dampers under stochastic earthquake load considering system parameters uncertainties. Journal of Earthquake Engineering *14*, 970–988.

Deierlein, G. (2004). Overview of a comprehensive framework for earthquake performance assessment. In Proceedings of the Proceedings of an International Workshop on Performance-Based Seismic Design - Concepts and Implementation.

Den Hartog (1985). Mechanical Vibration (Dover).

Dormand, J.R., and Prince, P.J. (1980). Family of embedded runge-kutta formulae. Journal of Computational and Applied Mathematics *6*, 19–26.

EERI Special Earthquake Report (2010). Learning from Earthquakes: The Mw 8.8 Chile Earthquake of February 27, 2010.

FEMA-P-58 (2012). Seismic Performance Assessment of Buildings. American Technology Council.

Fragiadakis, M., Lagaros, N.D., and Papadrakakis, M. (2006). Performance-based multiobjective optimum design of steel structures considering life-cycle cost. Structural and Multidisciplinary Optimization *32*, 1–11.

Frahm, H. (1911). Device for damping vibrations of bodies.

Frandsen, J.B., and Borthwick, A.G.L. (2003). Simulation of sloshing motions in fixed and vertically excited containers using a 2-D inviscid -transformed finite difference solver. Journal of Fluids and Structures *18*, 197–214.

Fujii, K., Tamura, Y., Sato, T., and Wakahara, T. (1990). Wind-induced vibration of tower and practical applications of tuned sloshing damper. Journal of Wind Engineering and Industrial Aerodynamics *33*, 263–272.

Fujino, Y., Pacheco, B.M., Chaiseri, P., and Sun, L.M. (1988). Parametric studies on tuned liquid damper (TLD) using circular containers by free-oscillation experiments. Doboku Gakkai Rombun-Hokokushu/Proceedings of the Japan Society of Civil Engineers 177–187.

Gardarsson, S.M. (1997). Shallow-water sloshing. PhD Thesis, University of Washington.

Gidaris, I., and Taflanidis, A.A. (2015). Performance assessment and optimization of fluid viscous dampers through life-cycle cost criteria and comparison to alternative design approaches. Bulletin of Earthquake Engineering *13*, 1003–1028.

Gidaris, I., Taflanidis, A.A., and Mavroeidis, G.P. (2014). Multi-objective design of fluid viscous dampers using life-cycle cost criteria. In 10th U.S. National Conference on Earthquake Engineering: Frontiers of Earthquake Engineering, NCEE 2014, July 21, 2014 - July 25, 2014, (Earthquake Engineering Research Institute), p. Computers and Structures Inc. (CSI); ConocoPhillips; et al.; Federal Emergency Management Agency (FEMA); Golder Associates; State of Alaska, Division of Geological and Geophysical Surveys (DGGS).

Giuliano, F. (2013). Note on the paper “optimum parameters of tuned liquid column-gas damper for mitigation of seismic-induced vibrations of offshore jacket platforms” by Seyed Amin Mousavi, Khosrow Bargi, and Seyed Mehdi Zahrai. Structural Control and Health Monitoring *20*, 852.

Goulet, C.A., Haselton, C.B., Mitrani-Reiser, J., Beck, J.L., Deierlein, G.G., Porter, K.A., and Stewart, J.P. (2007). Evaluation of the seismic performance of a code-conforming reinforced-concrete frame building - From seismic hazard to collapse safety and economic losses. Earthquake Engineering and Structural Dynamics *36*, 1973–1997.

Grigoriu, M. (2011). To scale or not to scale seismic ground-acceleration records. Journal of Engineering Mechanics *137*, 284–293.

Grigoriu, M., and Radu, A. (2014). A comparative study on fragility analyses in earthquake engineering. In 9th International Conference on Structural Dynamics.

Gutierrez Soto, M., and Adeli, H. (2013). Tuned Mass Dampers. Archives of Computational Methods in Engineering *20*, 419–431.

Haukaas, T. (2008). Unified reliability and design optimization for earthquake engineering. Probabilistic Engineering Mechanics *23*, 471–481.

Hernandez-Barrios, H., Heredia-Zavoni, E., and Aldama-Rodriguez, A.A. (2007). Nonlinear sloshing response of cylindrical tanks subjected to earthquake ground motion. Engineering Structures *29*, 3364–3376.

Hitchcock, P.A., Kwok, K.C.S., Watkins, R.D., and Samali, B. (1997). Characteristics of liquid column vibration absorbers (LCVA) - I. Engineering Structures *19*, 126–134.

Hoang, N., Fujino, Y., and Warnitchai, P. (2008). Optimal tuned mass damper for seismic applications and practical design formulas. Engineering Structures *30*, 707–715.

Hoskins, L.M., and Jacobsen, L.S. (1934). Water Pressure in a Tank Caused by a Simulated Earthquake. Bulletin of the Seismological Society of America *24*.

Housner, G. (1957). Dynamic Pressure on Accelerated Fluid Containers. Bulletin of the Seismological Society of America *47*, 15–35.

Housner, G. (1963). The Dynamic Behavior of Water Tanks. Bulletin of the Seismological Society of America *53*, 381–387.

Housner, G.W., Bergman, L.A., Caughey, T.K., Chassiakos, A.G., Claus, R.O., Masri, S.F., Skelton, R.E., Soong, T.T., Spencer, B.F., and Yao, J.T.P. (1997). Structural control: Past, present, and future. Journal of Engineering Mechanics-Asce *123*, 897–971.

Hrovat, D., Barak, P., and Rabins, M. (1983). Semi-Active versus Passive or Active Tuned Mass Dampers for Structural Control. Journal of Engineering Mechanics *109*, 691–705.

Ibrahim, R.A. (2005). Liquid Sloshing Dynamics: Theory and Applications (Cambridge University Press).

Idir, M., Ding, X., Lou, M., and Chen, G. (2009). Fundamental frequency of water sloshing waves in a sloped-bottom tank as tuned liquid damper. pp. 831–840.

Ikeda, T., Ibrahim, R.A., Harata, Y., and Kuriyama, T. (2012). Nonlinear liquid sloshing in a square tank subjected to obliquely horizontal excitation. Journal of Fluid Mechanics *700*, 304–328.

Inokuma, A., and Nagayama, D. (2013). The 2011 Great East Japan earthquake, tsunami and nuclear disaster. Proceedings of the Institution of Civil Engineers: Civil Engineering *166*, 170–177.

Jalayer, F., and Beck, J.L. (2008). Effects of two alternative representations of ground-motion uncertainty on probabilistic seismic demand assessment of structures. Earthquake Engineering and Structural Dynamics *37*, 61–79.

Jensen, H.A., and Kusanovic, D.S. (2014). On the effect of near-field excitations on the reliability-based performance and design of base-isolated structures. Probabilistic Engineering Mechanics *36*, 28–44.

Jia, G., and Taflanidis, A.A. (2013). Kriging metamodeling for approximation of high-dimensional wave and surge responses in real-time storm/hurricane risk assessment. Computer Methods in Applied Mechanics and Engineering *261-262*, 24–38.

Kaneko, S., and Ishikawa, M. (1999). Modeling of tuned liquid damper with submerged nets. JOURNAL OF PRESSURE VESSEL TECHNOLOGY-TRANSACTIONS OF THE ASME *121*, 334–343.

Kareem, A. (1990). Reduction of wind induced motion utilizing a tuned sloshing damper. Journal of Wind Engineering and Industrial Aerodynamics *36*, 725–737.

Kareem, A., and Sun, W.-J. (1987). STOCHASTIC RESPONSE OF STRUCTURES WITH FLUID-CONTAINING APPENDAGES. Journal of Sound and Vibration *119*, 389–408.

Katsanos, E.I., Sextos, A.G., and Manolis, G.D. (2010). Selection of earthquake ground motion records: A state-of-the-art review from a structural engineering perspective. Soil Dynamics and Earthquake Engineering *30*, 157–169.

Kiefling, L., and Feng, G.C. (1976). Fluid-structure finite element vibrational analysis. AIAA Journal *14*, 199–203.

Kim, H.-S., and Kang, J.-W. (2012). Semi-active fuzzy control of a wind-excited tall building using multi-objective genetic algorithm. Engineering Structures *41*, 242–257.

Kock, E., and Olson, L. (1991). Fluid-structure interaction analysis by the finite element method. A variational approach. International Journal for Numerical Methods in Engineering *31*, 463–491.

Komatsu, K. (1987). Non-linear sloshing analysis of liquid in tanks with arbitrary geometries. International Journal of Non-Linear Mechanics *22*, 193–207.

Kramer, S. (1996). Geotechnical earthquake engineering (Prentice Hall).

Lee, D.T., and Schachter, B.J. (1980). Two algorithms for constructing a Delaunay triangulation. International Journal of Computer & Information Sciences *9*, 219–242.

Lee, C.S., Goda, K., and Hong, H.P. (2012). Effectiveness of using tuned-mass dampers in reducing seismic risk. Structure and Infrastructure Engineering *8*, 141–156.

Leyton, F., Ruiz, S., and Sepulveda, S. (2009). Preliminary re-evaluation of probabilistic seismic hazard assessment in Chile: from Arica to Taitao Península. Advances in Geosciences *22*, 147–153.

Lin, C.-C., Wang, J.-F., and Ueng, J.-M. (2001). Vibration control identification of seismically excited m.d.o.f. structure-PTMD systems. Journal of Sound and Vibration *240*, 87–115.

Lin, C.-C., Chen, C.-L., and Wang, J.-F. (2010). Vibration control of structures with initially accelerated passive tuned mass dampers under near-fault earthquake excitation. Computer-Aided Civil and Infrastructure Engineering *25*, 69–75.

Lin, G.-L., Lin, C.-C., Chen, B.-C., and Soong, T.-T. (2015). Vibration control performance of tuned mass dampers with resettable variable stiffness. Engineering Structures *83*, 187–197.

Lin, T., Haselton, C.B., and Baker, J.W. (2013). Conditional spectrum-based ground motion selection. Part I: Hazard consistency for risk-based assessments. Earthquake Engineering and Structural Dynamics *42*, 1847–1865.

Liu, M., Burns, S.A., and Wen, Y.K. (2003). Optimal seismic design of steel frame buildings based on life cycle cost considerations. Earthquake Engineering and Structural Dynamics *32*, 1313–1332.

De la Llera, J.C., Luders, C., Leigh, P., and Sady, H. (2004). Analysis, testing, and implementation of seismic isolation of buildings in Chile. Earthquake Engineering and Structural Dynamics *33*, 543–574.

Lophaven, S., Nielsen, H., and Sondergaard, J. (2002). DACE, a Matlab Kriging Toolbox.

Love, J.S., and Tait, M.J. (2010). Nonlinear simulation of a tuned liquid damper with damping screens using a modal expansion technique. JOURNAL OF FLUIDS AND STRUCTURES *26*, 1058–1077.

Lu, Z., Wang, D., and Li, P. (2014). Comparison study of vibration control effects between suspended tuned mass damper and particle damper. Shock and Vibration *2014*.

Luco, N., and Bazzurro, P. (2007). Does amplitude scaling of ground motion records result in biased nonlinear structural drift responses? Earthquake Engineering and Structural Dynamics *36*, 1813–1835.

Lutes, L.D., and Sarkani, S. (1997). Stochastic analisys of structural and mechanical vibrations (Prentice Hall).

Marano, G.C., Greco, R., Trentadue, F., and Chiaia, B. (2007). Constrained reliability-based optimization of linear tuned mass dampers for seismic control. International Journal of Solids and Structures *44*, 7370–7388.

Maravani, M., and Hamed, M.S. (2011). Numerical modeling of sloshing motion in a tuned liquid damper outfitted with a submerged slat screen. International Journal For Numerical Methods In Fluids *65*, 834–855.

Matta, E., and De Stefano, A. (2009). Robust design of mass-uncertain rolling-pendulum TMDs for the seismic protection of buildings. Mechanical Systems and Signal Processing *23*, 127–147.

Mavroeidis, G.P., and Papageorgiou, A.S. (2003). A mathematical representation of near-fault ground motions. Bulletin of the Seismological Society of America *93*, 1099–1131.

McGuire, R.K. (1995). Probabilistic seismic hazard analysis and design earthquakes: Closing the loop. Bulletin of the Seismological Society of America *85*, 1275–1275.

Meckesheimer, M., Booker, A.J., Barton, R.R., and Simpson, T.W. (2002). Computationally inexpensive metamodel assessment strategies. Aiaa Journal *40*, 2053–2060.

Mei, G., Kareem, A., and Kantor, J.C. (2004). Model predictive control of wind-excited building: Benchmark study. Journal of Engineering Mechanics *130*, 459–465.

Mellado, M., and Rodriguez, R. (2001). Efficient solution of fluid-structure vibration problems. Applied Numerical Mathematics *36*, 389–400.

Miranda, J.C. (2005). On tuned mass dampers for reducing the seismic response of structures. Earthquake Engineering and Structural Dynamics *34*, 847–865.

Modi, V.J., and Akinturk, A. (2002). An efficient liquid sloshing damper for control of wind-induced instabilities. Journal of Wind Engineering and Industrial Aerodynamics *90*, 1907–1918.

Modi, V.J., and Munshi, S.R. (1998). An efficient liquid sloshing damper for vibration control. Journal of Fluids and Structures *12*, 1055–1071.

Moehle, J., and Deierlein, G. (2004). A framework methodology for performance-based earthquake engineering. In Proceedings of the Proceedings of the 13th World Conference on Earthquake Engineering.

Morand, H., and Ohayon, R. (1979). Substructure variational analysis of the vibration of coupled fluid-structure systems. Finite element results. International Journal for Numerical Methods in Engineering *14*, 741–755.

Moutinho, C. (2012). An alternative methodology for designing tuned mass dampers to reduce seismic vibrations in building structures. Earthquake Engineering and Structural Dynamics *41*, 2059–2073.

NIST (2012). Comparison of U.S. and Chilean Building Code Requirements and Seismic Design Practice 1985–2010.

Oberguggenberger, A., and Schmelzer, B. (2014). Seismic Performance of Tuned Mass Dampers with Uncertain Parameters. Computational Engineering *Springer International Publishing*, 57–83.

Ohtori, Y., Christenson, R.E., Spencer, B.F., and Dyke, S.J. (2004). Benchmark control problems for seismically excited nonlinear buildings. J. Eng. Mech.-ASCE *130*, 366–385.

Olson, L.G., and Bathe, K.-J. (1985). Analysis of fluid-structure interactions. A direct symmetric coupled formulation based on the fluid velocity potential. Computers and Structures *21*, 21–32.

Ordaz, M., Cardona, O., Salgado-Galve, M., Bernal-Granados, G., and Zuloaga-Romero, D. (2014). Probabilistic seismic hazard assessment at global level. International Journal of Disaster Risk Reduction.

Papadimitriou, K. (1990). Stochastic characterization of strong ground motion and applications to structural response. Doctoral Dissertation, California Institute of Technology.

Park, J., and Reed, D. (2001). Analysis of uniformly and linearly distributed mass dampers under harmonic and earthquake excitation. Engineering Structures *23*, 802–814.

Park, K.-S., Koh, H.-M., and Hahm, D. (2004). Integrated optimum design of viscoelastically damped structural systems. Engineering Structures *26*, 581–591.

Petersen, M., Frankel, A., Harmsen, S., Mueller, C., Haller, K., Wheeler, R., Wesson, R., Zeng, Y., Boyd, O., Perkins, D., et al. (2008). Documentation for the 2008 update of the

United States National Seismic Hazard Maps: U.S Geological Survey Open-File Report 2008-1128.

Porter, K.A., Kiremidjian, A.S., and LeGrue, J.S. (2001). Assembly-based vulnerability of buildings and its use in performance evaluation. Earthquake Spectra *17*, 291–312.

Priestley, M.J.N., Davison, B.J., Honey, G.D., Hopkins, D.C., Martin, R.J., Ramsey, G., and et. al. (1986). Seismic design of storage tanks, recommendations from the New Zealand National Society for Earthquake Engineering.

Rathje, E.M., Faraj, F., Russell, S., and Bray, J.D. (2004). Empirical Relationships for Frequency Content Parameters of Earthquake Ground Motions. Earthquake Spectra *20*, 119–144.

Ray Clough, and Penzien, J. (1993). Dynamics of Structures (New York: McGraw Hill).

Reddy, J.N. (2005). An Introduction to the Finite Element Method (New York: McGraw Hill).

Reed, D., Yu, J.Y., Yeh, H., and Gardarsson, S. (1998). Investigation of tuned liquid dampers under large amplitude excitation. Journal of Engineering Mechanics-Asce *124*, 405–413.

Rezaeian, S., and Kiureghian, A.D. (2010). Simulation of synthetic ground motions for specified earthquake and site characteristics. Earthquake Engineering and Structural Dynamics *39*, 1155–1180.

Robert, C., and Casella, G. (2004). Monte Carlo statistical methods (New York: Springer).

Rudinger, F. (2007). Tuned mass damper with nonlinear viscous damping. Journal of Sound and Vibration *300*, 932–948.

Saatcioglu, M., Tremblay, R., Mitchell, D., Ghobarah, A., Palermo, D., Simpson, R., Adebar, P., Ventura, C., and Hong, H. (2013). Performance of steel buildings and nonstructural elements during the 27 February 2010 Maule (Chile) Earthquake. Canadian Journal of Civil Engineering *40*, 722–734.

Sadek, F., Mohraz, B., and Lew, H.S. (1998). Single- and multiple-tuned liquid column dampers for seismic applications. Earthquake Engineering and Structural Dynamics *27*, 439–463.

Sain, T., and Kishen, J.M.C. (2007). Prediction of fatigue strength in plain and reinforced concrete beams. ACI Structural Journal *104*, 621–628.

Sakai, F., Takaeda, S., and Tamaki, T. (1989). Tuned Liquid Column Damper-New Type Device for Suppresion of Building Vibrations. In Proceedings of the International Conference of High-Rise Buildings., pp. 926–931.

Samali, B. (1990). Dynamic response of structures equipped with Tuned Liquid Column Dampers. In Australian Vibration and Noise Conference 1990, September 18, 1990 - September 20, 1990, (Melbourne, Aust: Publ by IE Aust), pp. 138–143.

Shang, C.-Y., and Zhao, J.-C. (2008). Periods and energy dissipations of a novel TLD rectangular tank with angle-adjustable baffles. Journal of Shanghai Jiaotong University (Science) *13 E*, 139–144.

Shin, H., and Singh, M.P. (2014). Minimum failure cost-based energy dissipation system designs for buildings in three seismic regions - Part II: Application to viscous dampers.

Simiu, E., and Scanlan, R. (1996). Wind effects on structures: fundamentals and applications to design (New York: Wiley-Interscience).

Soize, C. (2000). Nonparametric model of random uncertainties for reduced matrix models in structural dynamics. Probabilistic Engineering Mechanics *15*, 277–294.

Soong, T.T., and Dargush, G.F. (1997). Passive Energy Dissipation Systems in Structural Engineering.

Spall, J. (2005). Introduction to stochastic search and optimization: estimation, simulation, and control.

Sun, C., and Nagarajaiah, S. (2014). Study on semi-active tuned mass damper with variable damping and stiffness under seismic excitations. Structural Control and Health Monitoring *21*, 890–906.

Sun, C., Nagarajaiah, S., and Dick, A.J. (2014). Family of smart tuned mass dampers with variable frequency under harmonic excitations and ground motions: closed-form evaluation. Smart Structures and Systems *13*, 319–341.

Sun, L., Fujino, Y., Chaiseri, P., and Pacheco, B. (1995). The properties of tuned liquid dampers using a TMD analogy. Earthquake Engineering & Structural Dynamics *24*, 967–976.

Taflanidis, A.A. (2003). Investigation of passive and active liquid column mass dampers.

Taflanidis, A.A. (2011). Soft computing applications in simulation based natural hazard risk assessment. Tsompanakis, Y, and B.H.V. Topping Eds., Soft Computing Methods for Civil and Structural Engineering.

Taflanidis, A.A., and Beck, J.L. (2008). An efficient framework for optimal robust stochastic system design using stochastic simulation. Computer Methods in Applied Mechanics and Engineering *198*, 88–101.

Taflanidis, A.A., and Beck, J.L. (2009). Life-cycle cost optimal design of passive dissipative devices. Structural Safety *31*, 508–522.

Taflanidis, A.A., and Scruggs, J.T. (2010). Performance measures and optimal design of linear structural systems under stochastic stationary excitation. Structural Safety *32*, 305–315.

Taflanidis, A.A., Beck, J.L., and Angelides, D.C. (2007). Robust reliability-based design of liquid column mass dampers under earthquake excitation using an analytical reliability approximation. Engineering Structures *29*, 3525–3537.

Tait, M.J. (2008). Modelling and preliminary design of a structure-TLD system. ENGINEERING STRUCTURES *30*, 2644–2655.

Tamboli, A., Joseph, L., Vadnere, U., and Xu, X. (2008). Tall buildings: Sustainable design opportunities. In 8th World Congress on Tall and Green: Typology for a Sustainable Urban Future, CTBUH 2008, March 3, 2008 - March 5, 2008, (Council on Tall Buildings and Urban Habitat), pp. 120–126.

Tamura, Y., Fujii, K., Ohtsuki, T., Wakahara, T., and Kohsaka, R. (1995). Effectiveness of tuned liquid dampers under wind excitation. Engineering Structures *17*, 609–621.

Travasarou, T., Bray, J.D., and Abrahamson, N.A. (2003). Empirical attenuation relationship for Arias Intensity. Earthquake Engineering and Structural Dynamics *32*, 1133–1155.

Tributsch, A., and Adam, C. (2012). Evaluation and analytical approximation of Tuned Mass Damper performance in an earthquake environment. Smart Structures and Systems *10*, 155–179.

Tubaldi, E., Barbato, M., and Dall'Asta, A. (2014). Performance-based seismic risk assessment for buildings equipped with linear and nonlinear viscous dampers. Engineering Structures *78*, 90–99.

Vetter, C., Taflanidis, A.A., and Mavroeidis, G. (2014). Development of ground motion models compatible with ground motion prediction equations. In Proceedings of the 10th National Conference in Earthquake Engineering.

Wang, W., Li, J., and Wang, T. (2006). Damping computation of liquid sloshing with small amplitude in rigid container using FEM. Acta Mechanica Sinica/Lixue Xuebao *22*, 93–98.

Warburton, G.B. (1982). Optimum absorber parameters for various combinations of response and excitation parameters. Earthquake Engineering & Structural Dynamics *10*, 381–401.

Won, A.Y.J., Pires, J.A., and Haroun, M.A. (1997). Performance assessment of tuned liquid column dampers under random seismic loading. International Journal of Non-Linear Mechanics *32*, 745–758.

Wong, K.K.F. (2008). Seismic energy dissipation of iInelastic structures with tuned mass dampers. Journal of Engineering Mechanics *134*, 163–172.

Yalla, S.K., and Kareem, A. (2000). Optimum absorber parameters for tuned liquid column dampers. Journal of Structural Engineering New York, N.Y. *126*, 906–915.

Yalla, S.K., and Kareem, A. (2001). Beat phenomenon in combined structure-liquid damper systems. Engineering Structures *23*, 622–630.

Yalla, S.K., and Kareem, A. (2003). Semiactive tuned liquid column dampers: Experimental study. Journal of Structural Engineering *129*, 960–971.

Yang, F., Sedaghati, R., and Esmailzadeh, E. (2015). Optimal design of distributed tuned mass dampers for passive vibration control of structures. Structural Control and Health Monitoring *22*, 221–236.

Zahrai, S.M., Abbasi, S., Samali, B., and Vrcelj, Z. (2012). Experimental investigation of utilizing TLD with baffles in a scaled down 5-story benchmark building. Journal of Fluids and Structures *28*, 194–210.

Zareian, F., and Krawinkler, H. (2012). Conceptual performance-based seismic design using building-level and story-level decision support system. Earthquake Engineering and Structural Dynamics *41*, 1439–1453.

Zemp, R., De La Llera, J., and Almazan, J. (2011). Tall building vibration control using a TM-MR damper assembly. Earthquake Engineering and Structural Dynamics. *40*, 339–354.